Advancing Wind Load Assessment of Low-rise Buildings: CFD and Wind Tunnel Approaches

A thesis

submitted to the Faculty of Graduate Studies
in partial fulfilment of the requirements for the
Degree of Doctor of Philosophy
in

Civil Engineering
Lakehead University
By

Raghdah Raad Al-Chalabi

Supervisor:
Dr. Ahmed Elshaer
Associate Professor
Department of Civil Engineering,

ABSTRACT

Understanding wind hazards is essential for designing low-rise buildings that are resilient over time. These structures located within the turbulent Atmospheric Boundary Layer (ABL) are particularly vulnerable to wind-induced damage. In more realistic scenarios where, low-rise buildings are surrounded by similar structures, the flow and, consequently, the pressure distribution can be significantly altered. The characteristics of incident wind flow significantly influence pressure patterns and magnitudes on building façades. During windstorms, the cladding of low-rise buildings often suffers damage due to uplift forces, compromising their structural integrity. Roof damage is typically triggered by high suction regions caused by flow separation at edges and corners, forming conical and separation bubble vortices. Most previous studies focused on tall buildings for accurately evaluating and aerodynamically mitigating the wind load experimentally and numerically. Therefore, the main objective of this research is to develop a framework to accurately evaluate and effectively mitigate the wind load on low-rise buildings to enhance safety and structural integrity. The **first objective** of this research is to investigate the impact of discontinuous corner and ridgeline parapets on stand-alone low-rise buildings with complex roof geometry located in suburban terrain in reducing wind load by displacing the flow separation zones from the corners and edges using parapets. As for the **second objective**, it aims to estimate and correlate the effective parameters controlling the accuracy of the numerical wind pressure evaluation using Large Eddy Simulations (LES) on a low-rise building based on comparing wind pressures (i.e., mean and RMS) to wind tunnel results. In the **third objective,** the thesis aims to systematically define the required computational fluid dynamics (CFD) details to produce accurate ABL flows with LES models, particularly including a discussion aimed to efficiently select turbulence maximum frequency (f_{max}) employed as an input in the turbulence flow generator concerning grid size in the refinement zones that can accurately capture the pressure fluctuation induced on the building façade. The **fourth objective** is to experimentally evaluate the effectiveness of parapets in reducing wind pressures on low-rise buildings under two different terrain roughness conditions and with two parapet configurations added to the benchmark model. To address the challenges faced during the experimental testing, the **fifth objective** is to optimally reduce the number of pressure sensors needed while maintaining accurate wind load evaluations, ultimately enhancing the resilience of buildings against wind-induced damage. This research uses multi-resolution Dynamic Mode Decomposition (mrDMD) to decompose multiscale wind pressure data into modes representing different timescales. QR-Pivoting then identifies key dynamic modes that best capture the pressure field's dynamics. Together, these techniques can help identify sensor locations that minimize the required sensors while ensuring accurate pressure field reconstruction. This research provides a comprehensive framework for enhancing the resilience of low-rise buildings against wind-induced damage by addressing numerical and experimental challenges in wind load evaluation and mitigation.

Keywords

Aerodynamic Mitigation; Low-rise buildings; Turbulence; Large Eddy Simulation (LES); Computational Fluid Dynamic (CFD); Aerodynamic Wind Profile; Complex Roof Geometry; Parapets; Corner Vortices; Peak Value analysis; Maximum Turbulence Frequency; Boundary Layer Wind tunnel (BLWT); Terrian Roughness; Optimal Sensor Placement; Dynamic Mode Decomposition (DMD); QR Pivoting.

CO-AUTHORSHIP STATEMENT

This thesis has been prepared in accordance with the regulations for an Integrated-Article format stipulated by the Faculty of Graduate Studies at Lakehead University. Information from outside sources, which has been used for analysis or discussion, has been cited where appropriate. This thesis has been co-authored as:

Chapter 2: Aerodynamic Mitigation of Low-Rise Buildings with Complex Roof Geometry

Publication: Al-Chalabi, R., and Elshaer, A., 2023. Aerodynamic mitigation of low-rise buildings with complex roof geometry. Frontiers in Built Environment, 9, p.1200383.

Candidate's Contribution: The candidate designed and conducted the numerical simulations, analyzed the data, and prepared the manuscript.

Co-Author's Contribution: Dr. Ahmed Elshaer provided supervision, conceptual guidance, and manuscript revisions.

Chapter 3: Enhancing LES Efficacy in Wind Load Evaluation of Low-Rise Buildings Using Synthesized Inflow Turbulence

Publication: Al-Chalabi, R., Elshaer, A., and Aboshosha, H., 2024. Enhancing LES efficacy in wind load evaluation of low-rise buildings using synthesized inflow turbulence. Journal of Building Engineering, 95, p.110233.

Candidate's Contribution: The candidate developed the methodology, performed LES simulations, and wrote the manuscript.

Co-Authors' Contributions: Dr. Ahmed Elshaer provided supervision and conceptual guidance, and Dr. Hany Aboshosha contributed to manuscript editing and data interpretation.

Chapter 4: The influence of terrain roughness on parapet efficiency in mitigating wind loads on low-rise buildings: An experimental study

Publication: Al-Chalabi, R., Gemayel, D., Aboshosha, H., and Elshaer, A., 2024. The influence of terrain roughness on parapet efficiency in mitigating wind loads on low-rise buildings: An experimental study (submitted as journal publication).

Candidate's Contribution: The candidate conducted experimental testing, analyzed data, and drafted the manuscript.

Co-Authors' Contributions: Dr. Ahmed Elshaer supervised the study and assisted in manuscript revisions; Dr. Haitham Aboshosha provided experimental setup guidance; D. Gemayel assisted in data collection.

Chapter 5: Impact of Maximum Turbulence Frequency on Wind Flow and Pressure Distribution for Low-Rise Buildings Using Discrete Random Flow Generator

Publication: Al-Chalabi, R., and Elshaer, A., 2024. Impact of Maximum Turbulence Frequency on Wind Flow and Pressure Distribution for Low-Rise Buildings Using Discrete Random Flow Generator (submitted as journal publication).

Candidate's Contribution: The candidate developed the numerical model, performed simulations, and wrote the manuscript.

Co-Author's Contribution: Dr. Ahmed Elshaer provided conceptual input and reviewed the manuscript.

Chapter 6: CFD-based Sensor Placement Optimization for Low-rise Buildings Using Machine Learning Algorithm

Publication: Al-Chalabi, R., Alanani, M., and Elshaer, A., 2025. Spatiotemporal Analysis and Optimization of Sensor Placement for Wind Pressure Distributions on Low-Rise Buildings (submitted as journal publication).

Candidate's Contribution: The candidate developed and implemented the optimization methodology, analyzed the results, and prepared the manuscript.

Co-Authors' Contributions: Dr. Ahmed Elshaer supervised the research and provided manuscript revisions; Dr. Alanani assisted in data analysis and manuscript editing.

DEDICATION

To my parents for raising me to believe everything is possible, and to my husband for making everything possible!

ACKNOWLEDGEMENTS

"It takes a village to raise a child" is a well-known proverb, and I firmly believe that completing a Ph.D. also requires the support of a village. I began this journey just before the onset of the COVID-19 pandemic, a period fraught with challenges and uncertainties. Despite the hurdles, I made it to the finish line!

I want to express my deepest gratitude to the exceptional individuals who played significant roles in this transformative journey, enabling me to obtain my doctorate successfully. First and foremost, I extend my heartfelt gratitude to my PhD supervisor, Dr. Ahmed Elshaer. His exceptional mentorship has been instrumental in shaping both my academic and professional growth. Dr. Elshaer's unwavering commitment to academic excellence, meticulous attention to detail, and profound insights have greatly influenced the direction and quality of this dissertation. His patient feedback and constant encouragement were pivotal throughout my research journey. I deeply appreciate his invaluable support, which extended far beyond the boundaries of this thesis, leaving a lasting impact on my personal and professional development. I immensely thank Dr. Janusz Koziński and Dr. Eltayeb, whose leadership and accessibility inspired confidence and assured me throughout my PhD journey. Their ability to create a supportive environment for students made a meaningful difference. I am also indebted to the members of my thesis committee, Dr. Ali Tarokh and Dr. Ahmed Bediwy for their scholarly insights, constructive feedback, and invaluable contributions to shaping this research.

I am deeply thankful to the SWERL research group for their collaboration and support. The discussions and unwavering support from my peers have enriched my research experience, making this journey possible and enjoyable. Special appreciation goes to Dr. Magdy Alanani for his guidance and shared learning experiences that enriched this journey.

I am profoundly grateful to my family for their unwavering support. My husband, Dr. Samer Khalil, has been my anchor, providing boundless encouragement and understanding through every challenge. Thank you for always being my rock and accompanying me through the highs and lows of this academic journey. Your support and belief in me have strengthened and motivated me. My children, Zain, Ayman, and Mina, have been my greatest motivation and source of patience as I pursued this milestone. I also express my heartfelt appreciation to my parents, Shahala and Raad Al-Chalabi, for their prayers and for raising me to believe in myself. To my siblings, Marwa, Farah, and Rafal, for their love and encouragement. To my in-laws, Khala Atarad and Amu Zuhair, thank you for your steadfast support and care. Lastly, I thank my incredible office colleagues, Aysan, Sabiha, Maral and Zahara, for the laughter, camaraderie, and shared moments that brightened even the most challenging days. They provided both distractions when needed and encouragement when it seemed impossible to continue. I also acknowledge Dr. Shumsun Saddiuqe, a fellow mother and researcher, for her resilience and companionship during the pandemic, which was a source of strength and inspiration.

As I bring my five-year-long PhD journey to a close, I can genuinely say that I am immensely proud of my accomplishments. This transformative journey has shaped me as a researcher and an individual, imparting the invaluable lesson that perseverance yields fruitful rewards in the long run. The unwavering commitment and determination displayed by those around me have profoundly influenced my character. Thank you to everyone who contributed to my journey in big and small ways. This achievement reflects the collective efforts of an extraordinary village!

LIST OF JOURNAL PUBLICATIONS

Al-Chalabi, R., and Elshaer, A., 2023. Aerodynamic mitigation of low-rise buildings with complex roof geometry. Frontiers in Built Environment, 9, p.1200383.

Al-Chalabi, R., Elshaer, A., and Aboshosha, H., 2024. Enhancing LES efficacy in wind load evaluation of low-rise buildings using synthesized inflow turbulence. Journal of Building Engineering, 95, p.110233.

Al-Chalabi, R., and Elshaer, A., 2024. Impact of Maximum Turbulence Frequency on Wind Flow and Pressure Distribution for Low-Rise Buildings Using Discrete Random Flow Generator. (submitted as a journal publication).

Al-Chalabi, R., Gemayel, D., Aboshosha, H., and Elshaer, A., 2024. The influence of terrain roughness on parapet efficiency in mitigating wind loads on low-rise buildings: An experimental study. (submitted as a journal publication).

Al-Chalabi, R., Alanani, M., and Elshaer, A., 2025. Spatiotemporal Analysis and Optimization of Sensor Placement for Wind Pressure Distributions on Low-Rise Buildings. (submitted as a journal publication).

LIST OF CONFERENCE PUBLICATIONS

Al-Chalabi, R., Elshaer, A., (2024). Mitigation of Wind Load on Low-rise Buildings Using Roof Parapets: A Numerical and Experimental Study. 9th International Colloquium on Bluff Body Aerodynamics and Applications (BBAA). Birmingham, UK.

Al-Chalabi, R., Elshaer, A. (2024). Maximum Turbulence Frequency Impact on the ABL Inflow Generation. Canadian Society of Civil Engineering (CSCE). Niagara Falls, Ontario.

Al-Chalabi, R., Elshaer, A. (2023). Toward an efficient practice for computational wind load evaluation of low-rise buildings. Canadian Society of Civil Engineering (CSCE). Moncton, New Brunswick.

Al-Chalabi, R., Ibrahim, M., Elshaer, A. (2022). Computational Wind Load Evaluation and Aerodynamic Mitigation of Low-Rise Building with Complex Roof Geometry Canadian Society of Civil Engineering (CSCE). Whistler, Canada.

Al-Chalabi, R., Elshaer, A. (2021). Aerodynamic mitigation of low-rise building roofs. Canadian Society of Civil Engineering (CSCE) Conference, Niagara Falls.

Table of Contents

LIST OF TABLES

LIST OF FIGURES

CHAPTER 1

Introduction to Wind Load Evaluation and Aerodynamic Mitigation

1.1. Background

The significance of buildings' aerodynamic performance has grown in recent decades, primarily due to the heightened intensity and frequency of windstorms [1]. Understanding wind hazards is critical for the design of low-rise buildings to enhance their structural resilience and longevity. In Canada, the majority of constructed buildings fall under the category of low-rise structures, predominantly serving residential and commercial purposes. In fact, according to Census Canada in 2016, the overall housing stock was classified as single detached houses, with more than 53.4% of the total buildings in Canada [2]. Environment and Climate Change Canada has reported that Canada is affected by climate change at more than twice times the average worldwide rate. According to the post-damage surveys, wind catastrophes inflected mostly on personally categorized structures (i.e., housing, sheds, etc.), and the damages exceeded 69.5% of all total losses [3]. As demonstrated in Fig. 1.1. The latter trend is increasing the risk of wind hazards, which has a higher risk compared to the past, and it is expected to increase more in the future.

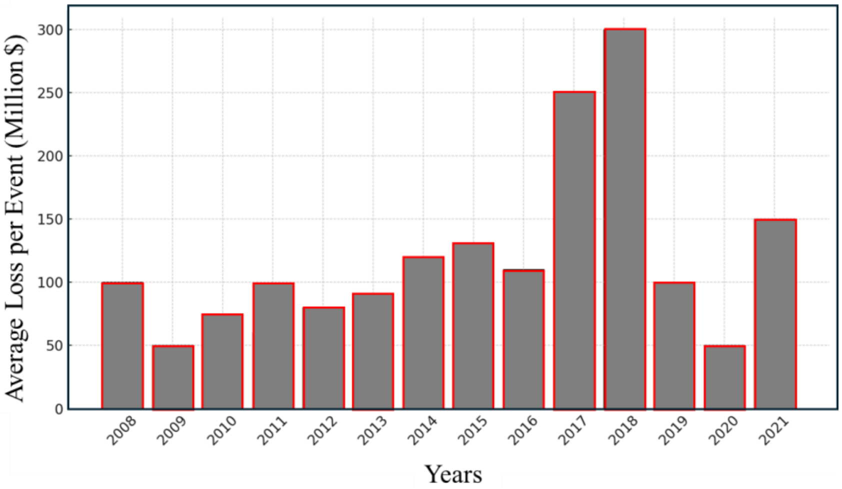

Fig. 1.1 The yearly trend of average loss per event for Ontario, Canada [4].

Wind-induced damages for roofs demonstrated in Fig. 1.2 are typically initiated due to the high suction regions caused by flow separations at edges and corners, leading to the development of conical and separation bubbles vortices, which are demonstrated in Fig. 1.3. The extreme suction initiated by the vortices can lead to cladding or total roof failure [5]. Any breach of the building envelope, in addition to causing water intrusion and interior damage, can alter the aerodynamics of the building by adversely affecting the internal pressure that increases wind forces on roofs, doors, and windows [6,7].

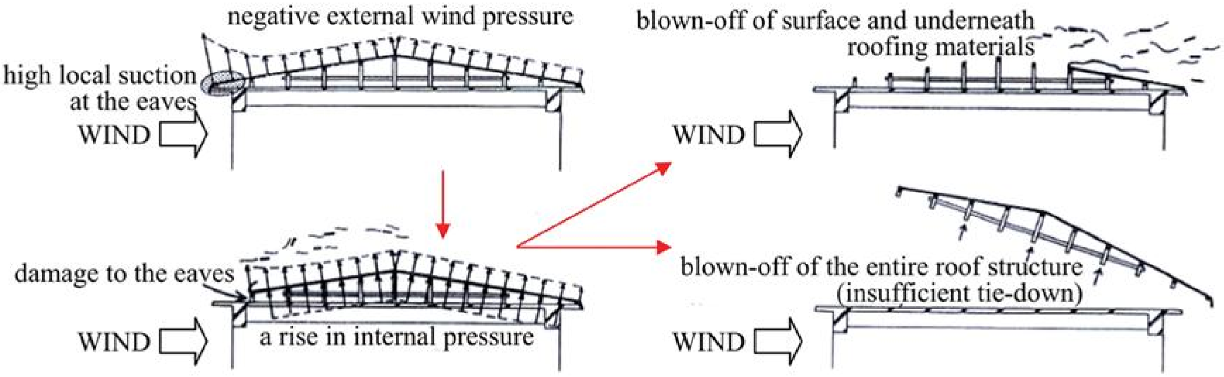

Fig. 1.2 Schematic Damage Chain for the roof during wind event [8].

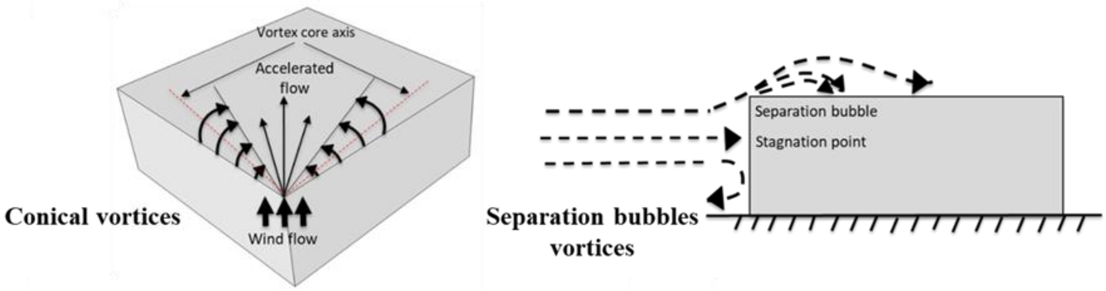

Fig. 1.3 The formation of conical vortices and separation bubbles over building roofs [9].

Many studies have investigated modifying the roof shape by utilizing roof mitigation techniques that can change the roof flow pattern, reduce wind loads, and decrease the damage risk to low-rise buildings. Introducing aerodynamic mitigation techniques for roofs of low-rise buildings can bring answers in the area of wind-induced hazards, where the wind load can be lowered or mitigated instead of strengthening the structure to sustain a higher wind impact. Many previous studies investigated the efficiency of modifying the roof corners or edges by adding various aerodynamic modifications to reduce the severity of vortex-induced uplift initiated on the roof of low-rise buildings [7,10–16] as shown in Fig. 1.4. A summary of previous studies' scope and main findings is provided in Chapter 2. Based on the findings of previous studies, the modification techniques can effectively reduce the magnitude of wind load on simple roof geometry design, subsequently reducing the wind-induced risk of damage to roofs of low-rise buildings and the building cost.

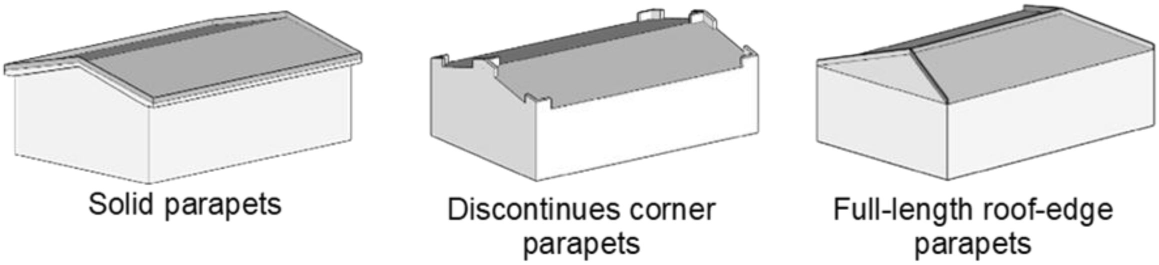

Fig. 1.4 various aerodynamic modification techniques on the roof [9].

Accurate wind load evaluation is crucial for mitigating risks to low-rise buildings. Considering the design variability inherent to these structures, computational wind load assessment can be effectively utilized during the preliminary design phase. Over the past decades, CFD has proved its value in wind-related studies by obtaining reliable quantitative and qualitative wind-induced load data [6,17–21]. The CFD technique draws its strength from being practically available and in its ability to consider parameters that are difficult to implement, such as temperature, scalability, and repeatability, in addition to the ability of fast execution on high-performance computers [22]. Moreover, the CFD can capture fluctuations at a large number of points on the surfaces of a building; hence, more crucial information about separation zones will be captured [17,23–25]. Additionally, the development of numerical modelling has empowered Large Eddy Simulation (LES) to accurately simulate the wind flows around buildings and structures under conditions very close to the actual state with full-scale modelling [18]. However, many factors can play a vital role in establishing the efficacy of numerical wind load evaluation, which are explained in detail in both chapter 3 and chapter 4.

Numerous wind tunnel experimental studies have examined the aerodynamic efficiency of the parapets installed at various locations on the roof surfaces of low-rise buildings in an open terrain exposure. These studies have helped to understand better and predict the working mechanism of aerodynamic mitigation techniques in reducing the wind pressures on mainly the roof surfaces of low-rise buildings. Several studies have found that the efficacy of a parapet in reducing the magnitude of wind pressures highly depends on the parapet's height and wind direction [13,26,27]. While other studies concluded that roof geometrical configurations are critical in determining the parapet's efficiency in reducing the pressure's mean and RMS [28,29]. Other studies examined the impact of parapet's porosity installed on gable roofs of low-rise buildings embedded in open terrain on their aerodynamic mitigation efficiency [14,16]. The current design codes for wind loads are evaluated, while the aerodynamic pressure coefficients are based on wind-tunnel measurements on isolated buildings [32,33]. Isolated buildings are uncommon, especially for low-rise structures, which are typically arranged in clusters within populated areas. The presence of neighboring buildings disrupts wind flow, significantly altering pressure distribution compared to isolated low-rise structures [34]. Chapter 5 details the experimental testing conducted to examine the terrain impact of the most common parapet’s shape and orientation on efficiency in reducing wind load on the roof of low-rise buildings.

A key component of experimental wind tunnel testing for low-rise structures is the strategic placement and quantity of pressure sensors, as they are vital for collecting the data necessary to design wind-resistant buildings effectively. Therefore, a reliable approach is required to enhance data collection procedures in the Boundary Layer Wind Tunnel test (BLWT). Initially, sensor placement methodologies deployment, utilization and management are proposed for structural diagnosis (i.e., structural health monitoring), particularly in the design phase [35] and field measurement [36,37]. In the field of structural health monitoring, Yuan et al. and Worden et al. suggested using advanced techniques like optimization algorithms and machine learning to determine optimal sensor locations. In these studies, sensors are placed sequentially at positions that provide high entropy values in model predictions, improve the performance of the system and avoid the use of an additional number of sensors and the related wiring that can add significant weight to the system, which can directly affect the operating costs [38,39]. Driven by the need to balance cost and the quality of information when determining sensor positions, Optimal Sensor Placement (OSP) remains a central challenge in designing, predicting, estimating, and controlling high-dimensional systems, particularly in fields such as wind engineering. This study introduces a framework for wind pressure analysis that leverages advancements in computational wind load evaluations during the preliminary design process to enhance structural safety. Techniques such as multi-resolution Dynamic Mode Decomposition (mrDMD) are employed to extract dominant dynamic features from wind pressure data, capturing multiscale phenomena. The QR pivoting algorithm is then used to rank and select sensor locations based on their contribution to measurement accuracy. This approach reduces the number of required sensors while maintaining precise wind load evaluations. More details are provided in Chapter 6. By combining numerical simulations with experimental validations, this thesis advances the understanding of wind-induced hazards and aerodynamic mitigation for low-rise buildings. The findings aim to inform cost-effective design strategies that enhance resilience against extreme wind events while addressing critical gaps in wind engineering practices.

1.2. Research Gap

While extensive research has examined the impact of parapets on uplift forces for typical roof geometries such as gable and hip roofs, their effectiveness on complex roof structures has been largely underexplored. The role of discontinuous corner and ridgeline parapets in reducing wind loads by displacing flow separation zones requires further investigation, particularly for low-rise buildings in suburban terrains. Additionally, parapets may increase loads on interior roof zones, as noted in previous studies, potentially influencing their overall effectiveness as a mitigation technique. It is also critical to assess the loads generated on parapets themselves to ensure they do not become sources of flying debris, posing risks to life and surrounding structures. In numerical wind load evaluations, key parameters such as the turbulence maximum frequency used in inflow generation, computational domain size, and grid discretization remain inadequately defined in existing guidelines. There is no established approach to determining the value of the maximum turbulence frequency or the corresponding grid refinement needed to capture pressure fluctuations accurately. The influence of computational domain dimensions and grid discretization, including size, shape, and scheme, on wind pressure accuracy has not been systematically correlated with building dimensions or validated against experimental results.

Existing parapet studies have predominantly focused on buildings in open terrains, with limited exploration of their effectiveness in suburban environments. Prior research has largely examined parapets on roofs with slopes around 3:12 and heights between 0.75 and 0.9 meters, while this study investigates low-sloped gable roofs and practical parapet heights of 0.6 meters under varying terrain roughness. The performance of perimetric and corner parapets will be evaluated based on mean, root mean square, and peak pressures across critical locations identified in post-damage surveys, using models tested at multiple wind angles of attack. For sensor placement employed in wind tunnel testing, traditional methods rely on heuristics and empiricism, deploying sensors at critical locations identified through prior damage surveys. However, this approach may miss essential locations, resulting in incomplete data collection. The high cost of sensors, time-consuming deployment, and accessibility constraints in complex geometries further complicate the sensor placement challenge. Optimizing sensor placement to maximize the information captured about wind pressures and flow dynamics remains a significant challenge.

This research addresses these gaps by investigating the aerodynamic performance of parapets for complex roof geometries in suburban terrains, systematically defining the parameters required for accurate numerical wind load evaluation using large eddy simulation models, evaluating the performance of low-height parapets across different terrains and roof configurations, and introducing an optimal sensor placement framework to enhance data accuracy and reduce redundancy while minimizing costs. These efforts aim to provide practical insights and improve wind load evaluation and mitigation strategies for low-rise buildings in realistic environments.

1.3. Thesis Scope

This thesis focuses on enhancing the resilience of low-rise buildings against wind-induced damages by investigating aerodynamic mitigation techniques and improving the efficacy of wind load numerical methods and experimental wind tunnel test evaluation. The scope of this work encompasses:

I. **Aerodynamic Mitigation Techniques:**
   - Investigating the aerodynamic behaviour of low-rise buildings under smooth and turbulent wind conditions.
   - Developing and assessing roof mitigation strategies, such as parapets with various orientations and geometrical configurations, to reduce wind loads.
   - Analyzing the efficiency of different orientation aerodynamic techniques on complex roof geometry.

II. **Wind Load Evaluation:**
   - Employing Computational Fluid Dynamics (CFD) simulations, particularly Large Eddy Simulation (LES), to model wind flows around low-rise buildings.

- Validating CFD results against experimental data from Boundary Layer Wind Tunnel (BLWT) tests.
- Addressing the challenges of numerical modeling, including inflow turbulence synthesis, boundary conditions, and scalability.

III. **Enhancing Aerodynamic Performance of Parapets on Low-Rise Buildings Using Wind Tunnel Testing:**
  - Developing wind tunnel-based methodologies tailored for open and suburban terrains.
  - Investigating aerodynamic mitigation strategies to reduce wind loads on parapets.
  - Offering design recommendations for improved wind resistance in varying terrain conditions.

IV. **Optimal Sensor Placement:**
  - Developing methodologies to optimize the placement and number of pressure sensors for wind load evaluation.
  - Utilizing advanced algorithms such as mrDMD and QR pivoting to improve data collection efficiency and reduce experimental costs.
  - Demonstrating the applicability of optimized sensor placement in experimental setups studies.

This thesis aims to advance the field of structural wind engineering by providing cost-effective, efficient, and scalable strategies to mitigate wind-induced risks for low-rise buildings. The findings are intended to contribute to the development of safer and more sustainable housing solutions, particularly in the face of increasing windstorm severity due to climate change.

1.4. Organization of the Thesis

1.4.1. Chapter 1

This chapter (the current chapter) introduces the motivation, research gap and objectives of the thesis, along with providing brief background relevant to the research project.

1.4.2. Chapter 2

Chapter 2 examines wind-induced forces on low-rise buildings with complex roof geometries, focusing on accurate wind load evaluation and aerodynamic mitigation. Using Large Eddy

Simulation (LES) validated against wind tunnel results, the study evaluates pressure coefficients and wind impacts at various angles of attack. Aerodynamic mitigation techniques, such as 500 mm parapets placed at roof corners and ridgelines, are analyzed, showing a 29% reduction in extreme corner suction and a 5.6% decrease in overall roof uplift. These findings demonstrate the effectiveness of parapets in enhancing the resilience of complex roof designs against wind damage.

1.4.3. Chapter 3

Chapter 3 explores the factors influencing the accuracy of numerical wind load evaluation for low-rise buildings using Large Eddy Simulation (LES). The chapter investigates the impact of turbulence inflow parameters, computational domain (CD) size, and grid discretization on the reliability of wind load predictions. Parametric studies are conducted to identify the optimal maximum turbulence frequency (f_{max}) for accurately capturing pressure fluctuations while balancing computational cost. The study also examines the effects of CD dimensions, boundary condition distances, and grid schemes (e.g., grid size and shape) on error margins. Key findings include identifying errors of up to 21% due to insufficient CD specifications and 14% errors in mean roof pressure from tetrahedral grid shapes. The results propose recommendations for improved domain and grid design, addressing gaps in current standards, particularly for low-rise buildings in oblique wind orientations. These insights aim to enhance the efficacy and reliability of LES for wind load evaluations.

1.4.4. Chapter 4

Chapter 4 focuses on enhancing turbulent inflow generation for Large Eddy Simulation (LES) to improve wind load evaluations on low-rise buildings situated in the lower Atmospheric Boundary Layer (ABL). The study investigates the impact of turbulence characteristics, including wind speed profile, turbulence intensity, and eddy scales, which are influenced by surface roughness and ground-generated turbulence. This study focuses on defining the effective range of the maximum frequency (f_{max}) for generating realistic inflow conditions across varying terrain types. The scope includes examining the impact of f_{max} as an input into the inflow generator, ranging from 1 to 100 Hz on turbulence intensity, spectra, and coherence. Comparing numerical simulation results with experimental data, achieving 92% accuracy in predicting wind-induced responses. The findings provide computationally efficient and adaptable methods for improving LES in computational wind engineering, offering insights for enhancing the structural resilience of low-rise buildings and advancing safer design practices in wind-prone regions.

1.4.5. Chapter 5

Chapter 5 examines the influence of surrounding terrain and building configurations on the aerodynamic performance of low-rise buildings with gable roof geometries, focusing on the efficiency of parapets as wind mitigation techniques. The study evaluates how open and suburban terrains affect wind-induced pressures, with particular emphasis on mean, RMS, and peak pressure variations caused by disrupted flow from nearby buildings. Using scaled wind tunnel tests at a 1:60 model scale, the chapter compares the performance of solid perimetric and corner parapets under different terrain conditions and wind directions. Results show that surrounding buildings reduce mean suction on the roof while increasing peak suction, significantly impacting parapet efficiency. For example, at oblique wind directions in suburban terrain, the efficiency of perimetric parapets is reduced by over 50%, while corner parapets show a 40% reduction in effectiveness. These findings underscore the importance of accounting for terrain effects in wind load evaluations, as real-life low-rise buildings often exist in rough and complex terrain scenarios, which can diminish the performance of aerodynamic mitigation strategies like parapets.

1.4.6. Chapter 6

Chapter 6 focuses on optimizing the placement and number of pressure sensors for accurate wind load evaluation on low-rise buildings, addressing practical and cost limitations associated with extensive sensor deployments. Low-rise buildings, located in the lower Atmospheric Boundary Layer, are exposed to high turbulence and peak pressures, making precise wind load measurement essential for ensuring structural safety. This study introduces a framework for Optimal Sensor Placement (OSP) that strategically reduces monitoring costs while maintaining accuracy. Using Large Eddy Simulation (LES), a 4-minute (full-scale) wind load time history on a 1:60 scale gable roof model is analyzed for four wind angles of attack. The time steps are decomposed into snapshots using multi-resolution Dynamic Mode Decomposition (mrDMD), capturing multiscale wind pressure features, including dominant trends and high-frequency variations. The QR pivoting algorithm is employed to rank and select sensor locations based on their contribution to overall measurement accuracy. The study highlights that the accuracy of predicted pressures depends on factors such as the number of dynamic modes, input maximum cycle frequency and truncation rates. Results demonstrate that the proposed framework can reduce the number of sensors by over 80%, significantly lowering experimental costs without compromising wind load evaluation accuracy. By integrating computational advancements with experimental approaches, this framework facilitates more efficient and effective wind pressure analysis during the preliminary design stages, contributing to improved structural safety and mitigation strategies for low-rise buildings.

1.4.7. Chapter 7

This chapter presents a summary of the key findings, insights, and contributions of the research, highlighting significant results and their implications in the context of aerodynamic mitigation and accurate wind load evaluation for low-rise buildings. It also discusses the challenges encountered during the research process and provides recommendations for future studies to expand on the current findings.

1.5. References

[1] A.M. Aly, N. da Fonseca Yousef, High Reynolds number aerodynamic testing of a roof with parapet, Eng. Struct. 234 (2021) 112006. https://doi.org/10.1016/J.ENGSTRUCT.2021.112006.

[2] Census, Census Topic: Housing, (2016). https://www12.statcan.gc.ca/census-recensement/2016/rt-td/hous-loge-eng.cfm.

[3] Insurance of Bureau of Canada, Welcome to Insurance Bureau of Canada, (2022). http://www.ibc.ca/on/.

[4] M. Hadavi, L. Sun, D. Romanic, Normalized insured losses caused by windstorms in Quebec and Ontario, Canada, in the period 2008–2021, Int. J. Disaster Risk Reduct. 80 (2022) 103222. https://doi.org/10.1016/J.IJDRR.2022.103222.

[5] J.X. Lin, D. Surry, H.W. Tieleman, The distribution of pressure near roof corners of flat roof low buildings, J. Wind Eng. Ind. Aerodyn. 56 (1995) 235–265. https://doi.org/10.1016/0167-6105(94)00089-V.

[6] A. Elshaer, G. Bitsuamlak, H. Abdallah, Variation in wind load and flow of a low-rise building during progressive damage scenario, Wind Struct. An Int. J. 28 (2019) 389–404. https://doi.org/10.12989/WAS.2019.28.6.389.

[7] G.T. Bitsuamlak, M. Asce, W. Warsido, ; Edward Ledesma, A.G. Chowdhury, Aerodynamic Mitigation of Roof and Wall Corner Suctions Using Simple Architectural Elements, Ascelibrary.Org. 139 (2013) 396–408. https://doi.org/10.1061/(ASCE)EM.1943-7889.0000505.

[8] Y. Uematsu, N. Isyumov, Wind pressures acting on low-rise buildings, J. Wind Eng. Ind. Aerodyn. 82 (1999) 1–25. https://doi.org/10.1016/S0167-6105(99)00036-7.

[9] R. Al-Chalabi, A. Elshaer, Aerodynamic mitigation of low-rise building with complex roof geometry, Front. Built Environ. 9 (2023) 1200383. https://doi.org/10.3389/FBUIL.2023.1200383/BIBTEX.

[10] A. Baskaran, T. Stathopoulos, Roof corner wind loads and parapet configurations, J. Wind Eng. Ind. Aerodyn. 29 (1988) 79–88. https://doi.org/10.1016/0167-6105(88)90147-X.

[11] D. Surry, J.X. Lin, The effect of surroundings and roof corner geometric modifications on roof pressures on low-rise buildings, J. Wind Eng. Ind. Aerodyn. 58 (1995) 113–138. https://doi.org/10.1016/0167-6105(95)00016-K.

[12] S. Pindado, J. Meseguer, Wind tunnel study on the influence of different parapets on the roof pressure distribution of low-rise buildings, J. Wind Eng. Ind. Aerodyn. 91 (2003) 1133–1139. https://doi.org/10.1016/S0167-6105(03)00055-2.

[13] G.A. Kopp, D. Surry, C. Mans, Wind effects of parapets on low buildings: Part 1. Basic aerodynamics and local loads, J. Wind Eng. Ind. Aerodyn. 93 (2005) 817–841. https://doi.org/10.1016/j.jweia.2005.08.006.

[14] W. Suaris, P. Irwin, Effect of roof-edge parapets on mitigating extreme roof suctions, J. Wind Eng. Ind. Aerodyn. 98 (2010) 483–491. https://doi.org/10.1016/j.jweia.2010.03.001.

[15] A.M. Aly, J. Bresowar, Aerodynamic mitigation of wind-induced uplift forces on low-rise buildings: A comparative study, J. Build. Eng. 5 (2016) 267–276. https://doi.org/10.1016/j.jobe.2016.01.007.

[16] Z. Azzi, F. Habte, A. Elawady, A. Gan Chowdhury, M. Moravej, Aerodynamic Mitigation of Wind Uplift on Low-Rise Building Roof Using Large-Scale Testing, Front. Built Environ. 5 (2020) 149. https://doi.org/10.3389/FBUIL.2019.00149/BIBTEX.

[17] K. Nozawa, T. Tamura, Large eddy simulation of the flow around a low-rise building immersed in a rough-wall turbulent boundary layer, J. Wind Eng. Ind. Aerodyn. 90 (2002) 1151–1162. https://doi.org/10.1016/S0167-6105(02)00228-3.

[18] T. Tamura, K. Nozawa, K. Kondo, AIJ guide for numerical prediction of wind loads on buildings, J. Wind Eng. Ind. Aerodyn. 96 (2008) 1974–1984. https://doi.org/10.1016/J.JWEIA.2008.02.020.

[19] A. Elshaer, H. Aboshosha, G. Bitsuamlak, A. El Damatty, A. Dagnew, LES evaluation of wind-induced responses for an isolated and a surrounded tall building, Eng. Struct. 115 (2016) 179–195. https://doi.org/10.1016/J.ENGSTRUCT.2016.02.026.

[20] A.M. Aly, H. Gol-Zaroudi, A.M. Aly, G. Zaroudi, Peak pressures on low rise buildings: CFD with LES versus full scale and wind tunnel measurements, 30 (2020) 99–117. https://doi.org/10.12989/was.2020.30.1.099.

[21] R.H. Ong, L. Patruno, D. Yeo, Y. He, K.C.S. Kwok, Numerical simulation of wind-induced mean and peak pressures around a low-rise structure, Eng. Struct. 214 (2020) 110583. https://doi.org/10.1016/J.ENGSTRUCT.2020.110583.

[22] K. Wijesooriya, D. Mohotti, C.K. Lee, P. Mendis, A technical review of computational fluid dynamics (CFD) applications on wind design of tall buildings and structures: Past, present and future, J. Build. Eng. 74 (2023) 106828. https://doi.org/10.1016/J.JOBE.2023.106828.

[23] F. Xing, D. Mohotti, K. Chauhan, Study on localised wind pressure development in gable roof buildings having different roof pitches with experiments, RANS and LES simulation models, Build. Environ. 143 (2018) 240–257. https://doi.org/10.1016/J.BUILDENV.2018.07.026.

[24] C.S. Yuan, The Effect of Building Shape Modification on Wind Pressure Differences for Cross-Ventilation of a Low-Rise Building, Int. J. Vent. 6 (2007) 167–176. https://doi.org/10.1080/14733315.2007.11683775.

[25] J.O.P. Cheung, C.H. Liu, CFD simulations of natural ventilation behaviour in high-rise buildings in regular and staggered arrangements at various spacings, Energy Build. 43 (2011) 1149–1158. https://doi.org/10.1016/J.ENBUILD.2010.11.024.

[26] G.A. Kopp, C. Mans, D. Surry, Wind effects of parapets on low buildings: Part 2. Structural loads, Undefined. 93 (2005) 843–855. https://doi.org/10.1016/J.JWEIA.2005.08.005.

[27] C. Mans, G.A. Kopp, D. Surry, Wind effects of parapets on low buildings: Part 3. Parapet loads, J. Wind Eng. Ind. Aerodyn. 93 (2005) 857–872. https://doi.org/10.1016/J.JWEIA.2005.08.007.

[28] W. Shan, Q. Yang, K. Guo, Y. Tamura, Effects of slope curvature, ridge height and layered roofs on wind pressures on traditional-Chinese-style gable-hip and gable roofs, J. Build. Eng. 70 (2023) 106300. https://doi.org/10.1016/J.JOBE.2023.106300.

[29] G.T. Bitsuamlak, W. Warsido, E. Ledesma, A.G. Chowdhury, Aerodynamic Mitigation of Roof and Wall Corner Suctions Using Simple Architectural Elements, J. Eng. Mech. 139 (2013) 396–408. https://doi.org/10.1061/(ASCE)EM.1943-

[30] S. Gan, G. Li, Z. Dong, H. Li, M. Zhao, Numerical study on aeroelastic behavior of spoiler on low-rise building based on fluid-structure interaction method, J. Build. Eng. 59 (2022) 105115. https://www.sciencedirect.com/science/article/pii/S2352710222011238 (accessed October 25, 2023).

[31] Y. Weng, S.G. Paal, Extrapolating wind pressures on roof soffits of low-rise buildings using few-shot learning, J. Build. Eng. 82 (2024) 108110. https://doi.org/10.1016/J.JOBE.2023.108110.

[32] X.J. Wang, Q.S. Li, J.W. Yang, Nonstationary near-ground wind characteristics and wind-induced pressures on the roof of a low-rise building during a typhoon, J. Build. Eng. 53 (2022) 104492. https://doi.org/10.1016/J.JOBE.2022.104492.

[33] H. Kiefer, E.J. Plate, Modelling of mean and fluctuating wind loads in built-up areas, J. Wind Eng. Ind. Aerodyn. 74–76 (1998) 619–629. https://doi.org/10.1016/S0167-6105(98)00056-7.

[34] S. Kim, N. Alinejad, S. Jung, H.K. Kim, The effect of open-to-suburban terrain transition on wind pressures on a low-rise building, J. Build. Eng. 85 (2024) 108651. https://doi.org/10.1016/J.JOBE.2024.108651.

[35] S. Hassani, M. Mousavi, A.H. Gandomi, Structural Health Monitoring in Composite Structures: A Comprehensive Review, Sensors 2022, Vol. 22, Page 153. 22 (2021) 153. https://doi.org/10.3390/S22010153.

[36] X. Luo, A. Kareem, S. Yoo, Optimal sensor placement for reconstructing wind pressure field around buildings using compressed sensing, J. Build. Eng. 75 (2023) 106855. https://doi.org/10.1016/J.JOBE.2023.106855.

[37] H. Gao, J. Liu, P. Lin, G. Hu, L. Patruno, Y. Xiao, K.T. Tse, K.C.S. Kwok, An optimal sensor placement scheme for wind flow and pressure field monitoring, Build. Environ. 244 (2023) 110803. https://doi.org/10.1016/J.BUILDENV.2023.110803.

[38] Y. Yuan, F.T.K. Au, D. Yang, J. Zhang, Active learning structural model updating of a multisensory system based on Kriging method and Bayesian inference, Comput. Civ. Infrastruct. Eng. 38 (2023) 353–371. https://doi.org/10.1111/MICE.12822.

[39] K. Worden, C.R. Farrar, G. Manson, G. Park, The fundamental axioms of structural health monitoring, Proc. R. Soc. A Math. Phys. Eng. Sci. 463 (2007) 1639–1664. https://doi.org/10.1098/RSPA.2007.1834.

CHAPTER 2

Aerodynamic Mitigation of Low-rise Buildings with Complex Roof Geometry

2.1. Introduction

It is crucial to perceive wind hazards in the design of low-rise buildings to improve their structural resiliency over time. Most structures built in Canada are categorized as low-rise buildings used mainly for residential and commercial purposes. In fact, according to Census Canada in 2016, the overall housing stock was classified as single detached houses, with more than 53.4% of the total buildings in Canada [1]. Wind loads rather than seismic loads typically govern the lateral strength of the low-rise building; hence, they are more susceptible to wind-induced damage than other structures [2]. Wind-induced damages in the past 40 years represented over 60% of the total insured losses due to natural catastrophes [3]. For instance, Barrie's recent tornado in July 2021 is a sobering reminder of the catastrophic damages that wind may cause [4]. Increasing population densities and expanding development into extreme wind-prone regions, such as coastlines, will increase the likelihood that structures will continue to encounter extreme wind events. In addition, wind hazard has a higher risk compared to the past, and it is expected to increase more in the future [5]. Wind-induced damages for roofs are typically initiated due to the high suction regions caused by flow separations at edges and corners, leading to the development of conical and separation bubbles vortices, which are demonstrated in Fig. 2.1(a). The extreme suction initiated by the vortices can lead to cladding or total roof failure [6]. Any breach of the building envelope, in addition to causing water intrusion and interior damage, can alter the aerodynamics of the building by adversely affecting the internal pressure that increases wind forces on roofs, doors, and windows [1,7].

Many studies have investigated modifying the roof shape by utilizing roof mitigation techniques that can change the roof flow pattern, reduce wind loads, and decrease the damage risk to low-rise buildings. These modification techniques, such as pergolas and parapets, can be installed on edges and corners and used as permanent architectural features or for rehabilitation. Parapets were commonly used with flat-roof versions of the early Mediterranean revival-style homes [1]. The parapets installed at the roof edges and corners aim to change the wind flow pattern on the roof by disrupting the formation of corner vortices or diverting the flows in the separation zone, as demonstrated in Fig. 2.1(b). They are often mounted on the edge and corner areas, as shown Fig. 2.1(c), where their height and orientation are crucial factors impacting their efficiency [8–10]

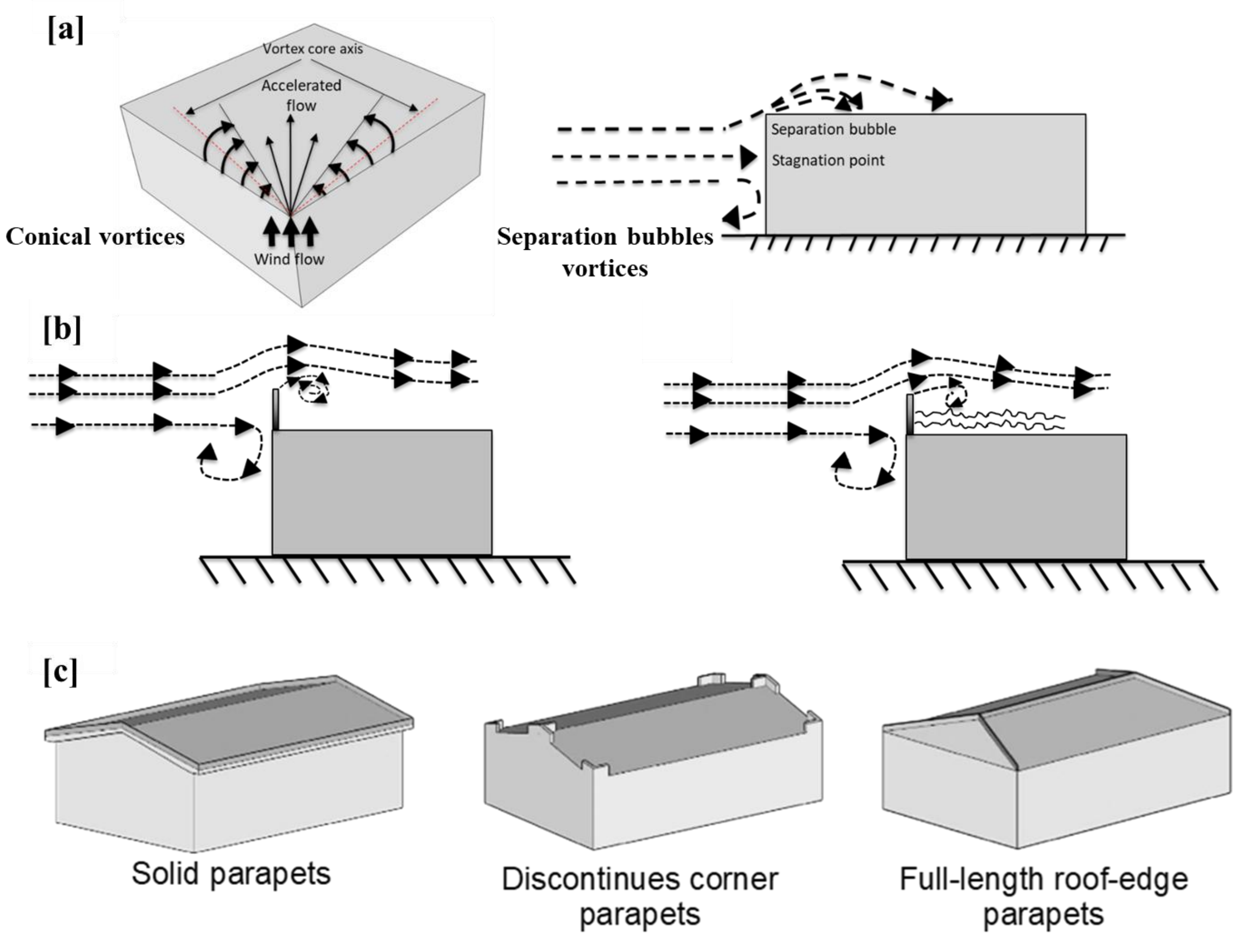

Fig. 2.1 (a) The formation of conical vortices and separation bubbles over building roofs, (b) the parapet's mechanism of working over a flat roof using solid and porous parapets, and (c) various aerodynamic modification techniques on the roof.

Introducing aerodynamic mitigation techniques for roofs of low-rise buildings can bring answers in the area of wind-induced hazards, where the wind load can be lowered or mitigated instead of strengthening the structure to sustain a higher wind impact. Many previous studies investigated the efficiency of modifying the roof corners or edges by adding various aerodynamic modifications to reduce the severity of vortex-induced uplift initiated on the roof of low-rise buildings [1,11–17]. A summary of previous studies' scope and main findings is provided in

Table 2.1. Based on the findings of previous studies, it was found that the modification techniques can effectively reduce the magnitude of wind load on various components, subsequently reducing the wind-induced risk of damage to roofs of low-rise buildings and the building cost. Furthermore, some previous studies have adopted the concept of linking the mitigation techniques to an optimization algorithm to find the optimal configuration of the mitigation techniques in terms of reducing wind load [18–21]. Studying wind load on parapets is crucial since these loads must be included in the design of the main wind force-resisting systems of buildings, in addition to being essential for the design of parapets themselves, including their connection to the roof surface. Parapet failures caused by strong wind forces can become sources of flying debris that can damage other buildings. Wind standards and codes provide very little guidance regarding quantifying the wind load on parapets. It is worth mentioning that the ASCE-7 (2005) [22] standards estimate the wind loads on parapets conservatively based on the net pressure coefficients on both windward and leeward parapet surfaces.

While the impact of parapets on the uplift forces for typical roof geometry (i.e., gable or hip) has been the topic of numerous experimental and numerical studies, the effect of parapets on complex roof structures has remained largely less examined. Therefore, there is a need to investigate the impact of discontinuous corner and ridgeline parapets on stand-alone low-rise buildings with complex roof geometry located in suburban terrain in reducing wind load by displacing the flow separation zones from the corners and edges. Parapets located at the corners and edges can increase the load on interior roof zones, thus influencing the overall effectiveness of parapets as a mitigation technique. Therefore, this study will evaluate wind load on the interior roof zones as the parapets may increase the load on these locations, as previously stated and found by Sarkar et al. (2001) [23]. As mentioned earlier, there is also a need to study the loads generated on the added parapets to prevent them from becoming a source of flying debris, injuring life, and damaging surrounding structures.

Table 2.1 Scope and the main findings of previous studies focused on building aerodynamic mitigation.

Reference	Roof type	Mitigation technique	Findings/comments
Baskaran and Stathopoulos, 1988 [11]	Flat	One-side parapets Perimetric parapets	One-side parapet increases the edge suctions in comparison to the no-parapet case. Corner peak suctions increase even for high parapets. Increase the corner suctions in the presence of low perimetric parapets at an oblique wind direction.
Lin et al., 1995 [12]	Flat	Sawtooth partial parapets Porous parapets	Sawtooth parapets tend to stabilize the corner vortices, filtering out the high peaks. Porous parapets reduced the peak, RMS, and mean Cp near the corner by 70% and lowered the pressure distribution over the roof.
Pindado and Meseguer, 2003 [13]	Flat	Perimetric solid and porous parapets	Load reduction between solid and porous parapets at low heights parapets is smaller as the relative parapet height grows. Perimetric solid parapets effectively reduce corner suctions at high turbulence intensity flow.
Kopp et al., 2005 [14]	Gable	Perimetric parapet and an isolated parapet on one wall	Tall perimetric parapets resulted in a significant reduction in the peak corner suctions and uniform pressure distribution. Isolated parapets strengthen the flow separation at the sharp vertical edge as flow curves around the parapet.
Suaris and Irwin, 2010 [15]	Gable	Solid and 33% porous corner and ridgeline parapets	60% decrease in corner suction pressures with a parapet designed with a length of 10% of the shortest dimension of the model. Perimetric parapets lead to a 50% reduction in pressure coefficients at the corner zone.
Bitsuamlak et al., 2013 [1]	Gable and hip	roof extensions of gable ends, ridgeline extensions, and	The critical suction at the ridge resulted in a 60% reduction on both roof geometries after introducing the ridgeline extension.

		sideways extensions of walls	Gable end extension leads to a 65% reduction of the peak pressure close to the gable end zone.
Aly-Mousaad and Bresowar, 2016 [16]	Flat	Barrier, barrier with an outer slope, barrier with an inner slope, circular device concaved out, circular device concaved in, and airfoil	Barriers, slope-in, circular-in, and airfoils reduced the uplift of the whole structure by 20%, 22%, 24%, and 28%, respectively. Mitigation techniques increased the drag forces on the structure by 32.8 %.
Azzi et al., 2020 [17]	Gable	Discontinuous 33% porous parapets	Discontinued parapets reduced the extreme suction at the corner by 45%, indicating that full perimeter parapets are not obligatory to mitigate the extreme suction on the roof.

This paper is divided into four sections. Section 1(the current section) presents an introduction that includes a review of the related literature examining the impact of adding aerodynamic modifications to the roof perimeter and interior zones and elaborating on the existing gap in studying complex roof geometries and wind-induced forces on parapets. Section 2.2 presents the methodology of validating the CFD model with the experimental results and describes the mitigation techniques and extreme value analysis adopted in the study. Section 2.5 discloses this study's main findings in terms of the effectiveness of corner and edge parapets in reducing wind load on the complex roof geometry, including an assessment of the wind load generated by the mitigation techniques themselves. Finally, Section 2.6 will conclude the main findings of adding parapets in reducing both extreme corners and edges suction pressure and forces acting on the roof surfaces without substantially increasing the loads on the roof's internal zones while producing minimum wind load on the mitigation techniques.

2.2. Methodology Framework

Since this study aims to investigate the effectiveness of adding aerodynamic mitigations (i.e., parapets) to a complex roof of a low-rise building to minimize the wind-induced loads and pressures, the aerodynamic performances of a non-modified model will be compared to two configurations of modifications (i.e., Config-1 and Config-2), which will be described in sub-section 2.3. The modified configurations are designed by adding corner and ridgeline parapets to the original roof configuration to displace the high local edge suctions over a much larger area, hence lowering the pressure magnitudes at these locations. The original non-modified model has a complex roof geometry with varieties of roof slopes and a chimney, occupying a total footprint of $20.88\ \mathrm{m}\ \times\ 21.7\ \mathrm{m}$ with a total height of 5.5 m and an eave height (H) of 2.34 m in full scale. The low-rise building model utilized in this study was experimentally tested by Kopp et al. [24]. The overall model dimensions and 3D view layout are illustrated in Fig. 2.2(a) and (b), respectively. This study starts with a validation step to ensure the accuracy of the adopted Large Eddy Simulation (LES) used in evaluating wind load for a complex roof of a low-rise building by comparing the extracted data with wind tunnel test data from the literature. Once the model is validated, the same LES details and assignments will be used to examine the modified models. Mitigation techniques (i.e., parapets) will then be added to the non-modified roof in two scenarios, namely, "Config-1" and "Config-2", as will be explained in the following sub-section (Section 2.3). To count for the wind directionality, evaluating the peak wind loads and pressures on the roof surface will require repeating the previous procedure for eight wind angles of attack ranging from 0° to 315° with an increment of 45°. The wind load on the roof surfaces is evaluated by dividing the complex geometry's roof surface into six surfaces, namely R1, R2, R3, R4, R5, and R6, as shown in Fig. 2.2 (c). In addition, corner probes (i.e., tabs) are added to the roof corners to extract pressure time histories for the peripheral and interior corners of the roof. The pressure probes are located within the expected flow separation zones, as shown in Fig. 2.2 (c). The wind load on the building is evaluated by extracting the time histories of the wind loads and pressure coefficients in x, y, and z directions from corner probes for both Config-1 and Config-2. The critical values of the mean pressure that can govern the design of the aerodynamically modified complex roof geometry are extracted after comparing eight wind angles of attack for all probes. The extreme statistical values of the pressure and wind load for a design return period of 50 years are evaluated using the Gumbel approach to conduct a fully probabilistic assessment of wind loads for the critical wind angle of attack. The Extreme value analysis gives suitable predictions within the range of the data and extrapolates to risks of exceedance beyond [25]. Details of the extreme value analysis approach will be explained in sub-section 2.4.1, where the critical values of the mean pressure are extracted from all the peripheral and interior probes. The proposed procedure is concluded by conducting a comparative study between the original roof configuration and the modified roof configurations (i.e., Config-1 and Config-2) in terms of wind-load induced to examine the effectiveness of adding the parapets to complex roof geometry in reducing the suction-acting on the roof surfaces and corners. Fig. 2.3 summarizes the framework proposed in the study.

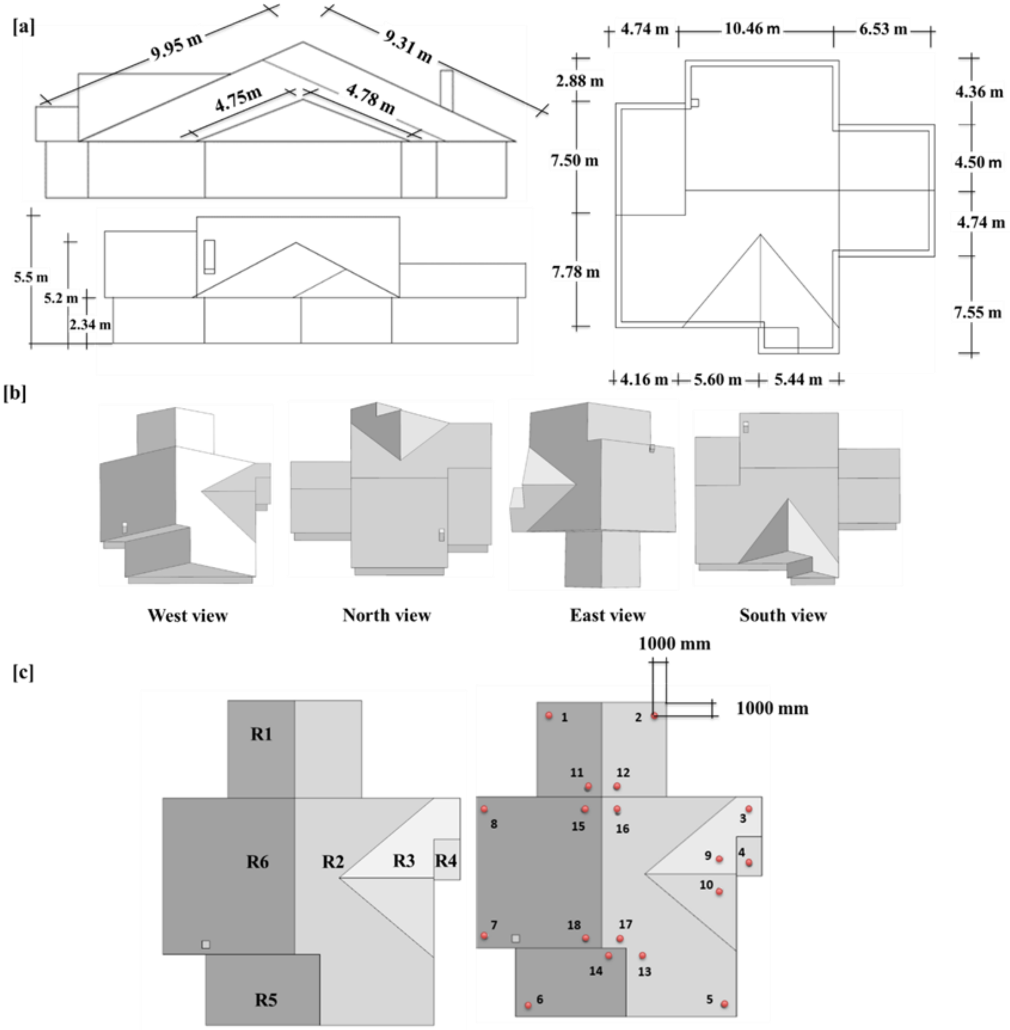

Fig. 2.2 The original building geometry used in this study is (a) dimensions, (b) 3D view layout, and (c) pressure probe locations and roof surfaces.

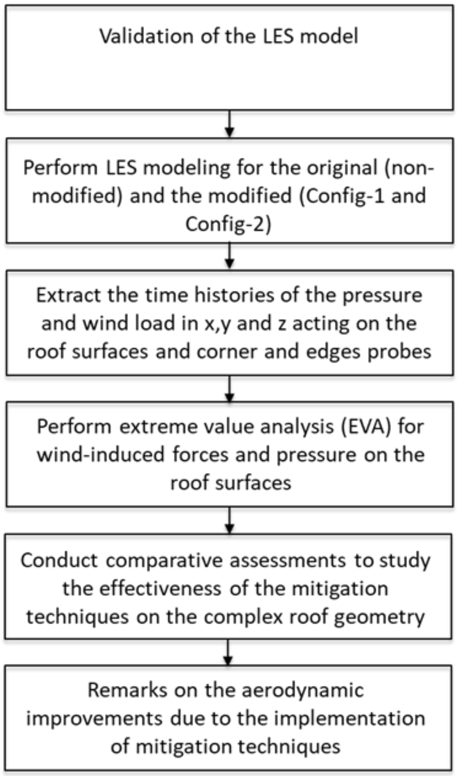
Validation of the LES model

Perform LES modeling for the original (non-modified) and the modified (Config-1 and Config-2)

Extract the time histories of the pressure and wind load in x,y and z acting on the roof surfaces and corner and edges probes

Perform extreme value analysis (EVA) for wind-induced forces and pressure on the roof surfaces

Conduct comparative assessments to study the effectiveness of the mitigation techniques on the complex roof geometry

Remarks on the aerodynamic improvements due to the implementation of mitigation techniques

Fig. 2.3 The framework of the aerodynamic mitigation technique for complex roof geometry.

2.3. Aerodynamic Mitigation Techniques

This subsection introduces the layout and dimensions for the original building configuration and the modified roof configurations. The current study is carried out using a parapet height of 500 mm installed on the roof at corners (for Config-1) and at both edges and corners (for Config-2). The parapet dimensions are chosen to be of low height and smaller length to ensure cost-effectiveness, ease of installation, and architectural aesthetics to the retrofitted building while lowering the wind forces initiated on the parapets. The first roof modification (Config-1) is developed by adding parapets at the peripheral corners of the complex roof geometry with a height of 500 mm, a width of 160 mm, and a length of 1000 mm on each side, as shown in Fig. 2.4(a). The aerodynamic improvement intended from the placement of corner parapets is to displace the conical vortices, reducing the suction at these damage-prone locations [1,14,16]. The second roof modification (Config-2) is carried out by employing the same eight corner parapets as Config-1 while adding additional parapets along the ridgeline to avoid the creation of high negative pressure zones at the interior surfaces of the roof, as illustrated in Fig. 2.4(b).

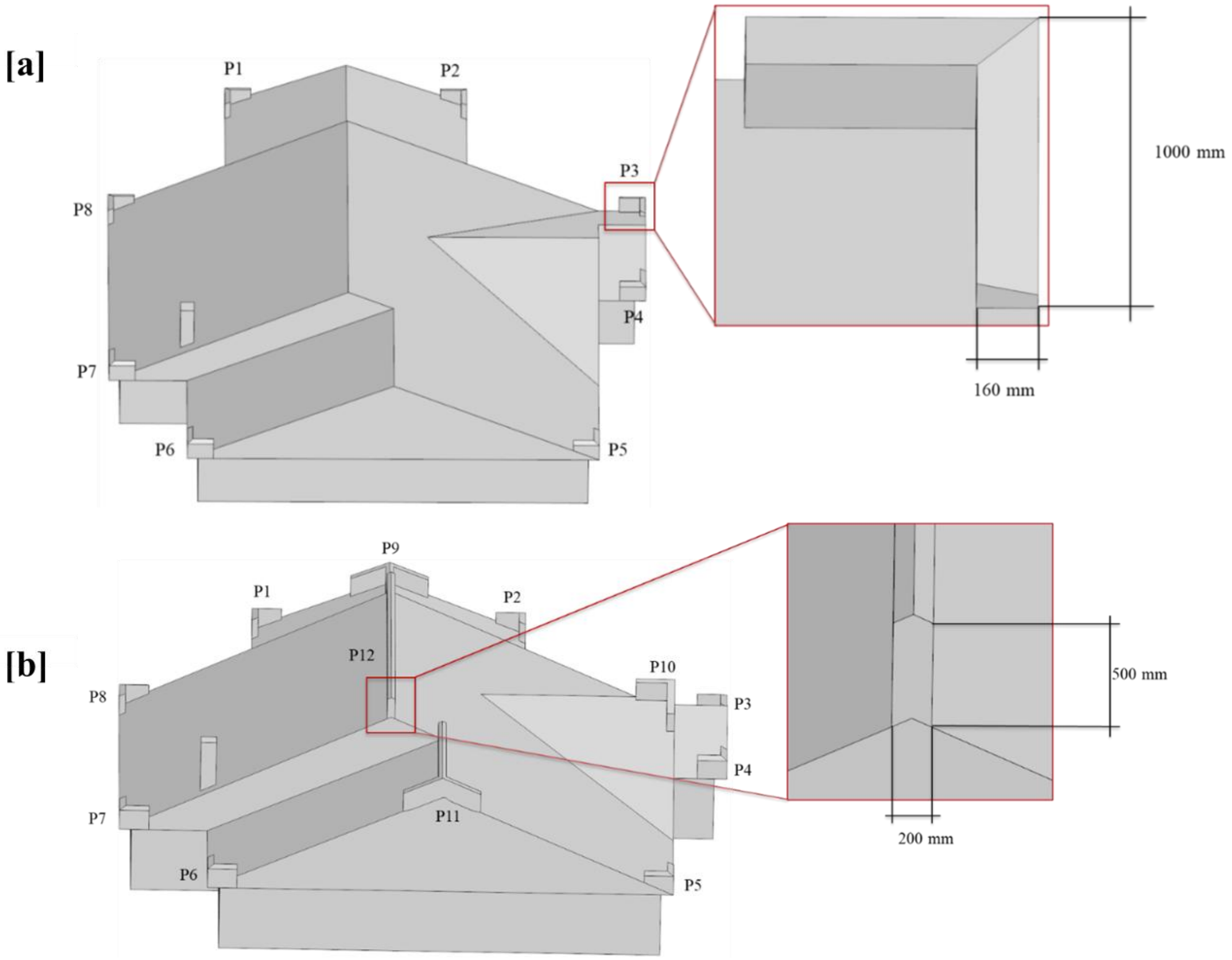

Fig. 2.4 (a) location and dimensions of the parapets used in Config-1, and (b) location and dimensions of the parapets used in Config-2.

2.4. Model Validation

This subsection will present the validation process and results for the numerical model adopted in this study. The adopted CFD model, presented in Fig. 2.2, is validated by comparing the mean and RMS of pressure coefficient values for the taps located at the roof of the east end of the building geometry to the experimentally obtained data presented by Kopp et al. (2010) [24]. The mean velocity profile obtained from the wind tunnel experimental test compared well with the inlet velocity profile corresponding to suburban terrain roughness, z_o of 23 mm and $1/\alpha$ is 0.14, as given in Equation [1] and shown in Fig. 2.5(a). The turbulence intensity profile demonstrated in Fig. 2.5(b) obtained from the wind tunnel experimental test also matches the turbulence profile shown in Equation [2].

$$U_z = \overline{U}_{10}\left(\frac{z}{10}\right)^{1/\alpha} \qquad [1]$$

$\overline{\mathrm{U}}_{10}$ is the reference wind velocity at 10 m height is 9.25 m/s, and z is referred to as the height in m at the evaluated corresponding wind velocity.

$$I_u = c_u\left(\frac{z_{ref}}{z}\right)^{bu} \qquad [2]$$

$\mathrm{C_u}$and $\mathrm{b_u}$ are the curvature fitting paraments and $\mathrm{z_{ref}}$ is the reference height (i.e., 4.3 m). Similar to the wind tunnel testing, the CFD is modeled at a scale of 1:50, where the utilized reference wind velocity ($\mathrm{V_{ref}}$) of 1.6 m/s (8.2 m/s in full scale), corresponding to a mean roof height of 0.086 m (4.3 m in full scale), which matches the reference height and velocity adopted in the wind tunnel experimental testing. Fig. 2.5(c) represents a comparison of longitudinal spectra for the current LES and wind tunnel experiment data. It is worth mentioning that the inflow condition must satisfy the spectra in terms of correlations and magnitudes. Any discrepancy in the resulting spectra can lead to inaccurate wind-induced structural responses, particularly if this discrepancy occurs close to the natural frequencies of the structure. Furthermore, Fig. 2.5 shows that both simulated mean velocity and turbulence intensity profiles have been reasonably maintained throughout the examined computational domain. This can be evident from comparing the inlet profiles to the profiles at the building locations without the influence of the building aerodynamics.

The computational domain dimensions and boundary conditions are shown in Fig. 2.6. As observed, the computational domain size satisfied the minimum values set by Franke et al. (2011) [26]. The boundary conditions at the top and side surfaces of the computational study domain are set as symmetry plane boundary conditions. The ground and building surfaces are defined as a non-slip wall boundary condition, while the outlet surface is defined as an outflow. The inlet wall was defined as a time-varying inlet velocity boundary condition using the CDRFG technique described by Aboshosha et al. (2015) [27] and adopted by Elshaer et al. (2017) [20]. Since the building is located within a rough terrain, accurately modelling the turbulence impacting the model is crucial. Therefore, the effects of turbulence on wind flow will be initiated using turbulence modeling methods, namely Large Eddy Simulation (LES). LES is a reliable and applicable than other turbulence modelling methods [5]. A mesh sensitivity analysis is conducted by examining the impact of the mesh refinements zones on the mean and RMS of the pressure across a gable roof model. The results are then compared to experimental data presented by Ho et al. (2005) [28], where the discrepancies are evaluated by using the RMSE. The mesh refinement zones ranged from coarse, medium, and fine, yielding 1, 2.1, and 3 million mesh cells, respectively. Overall, when compared to the experimental testing, the pressure parameters (i.e., mean and RMS of pressure), presented in Table 2.2, show consistent numerical results with a maximum of 4.5% discrepancy recorded for RMS readings of the pressure when a medium-mesh size is adopted compared to 3.3% for the fine meshing scheme. The coarse mesh scheme recorded a discrepancy of 8% in RMS of pressure compared to the experimental results. Therefore, all the numerical simulations of CFD models were performed by adopting the medium mesh scheme.

Table 2.2. Results of the mesh sensitivity analysis using three mesh size schemes

Numerical model	RMSE Mean Cp	RMSE RMS Cp
Coarse	10%	8%
Medium	4.2%	4.5%
Fine	3.7%	3.3%

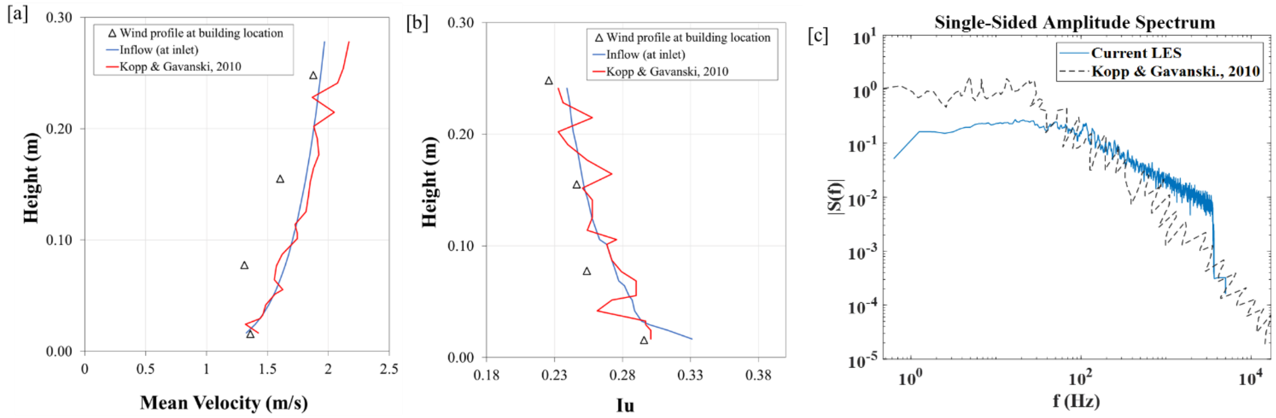

Fig. 2.5 (a) mean velocity profile (b) turbulence intensity profile, and (c) longitudinal spectra at the roof reference height.

The adopted computational domain was discretized to a hexahedral ranging from 10 mm to 40 mm and further refined near the building to a mesh size of 4 mm to capture smaller-scale turbulence near the building of interest, yielding a total mesh of 2.02 M cells, as shown in Fig.

2.6(b). The adopted CFD model employed Star CCM+ (15.04.008-R8) and utilized the LES turbulence model while using the dynamic WALE sub-grid scale, as previous studies found that it can reduce the computational time by up to 64% [29]. The conditional transient analysis with LES is crucial to ensure the convergence of a numerical method for partial differential equations. This condition is known as the Courant-Friedrichs-Lewy (CFL) [30]. The latter aims to provide numerical convergence within each time step by maintaining the Courant-Friedrichs-Lewy (CFL) below 1.0. CFL is calculated based on velocity, cell size, and the time step at each cell. Accordingly, the time step was chosen to be equal to 0.5 milliseconds. The numerical simulations are conducted for 8000-time steps and four inner iterations. The first 1600 time steps are disregarded to ensure the stability of the aerodynamic quantities. The values of y+ utilized for the computational domain boundary layers were chosen to be 1. SharcNet high-performance computer (HPC) is utilized for conducting numerical simulations [31].

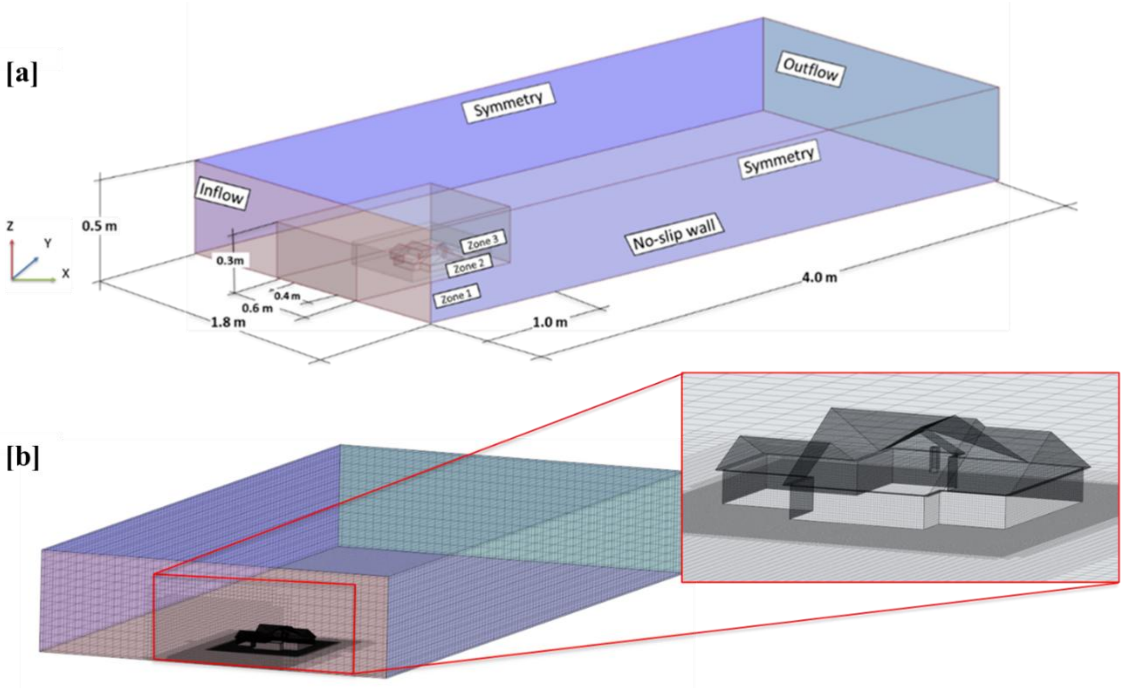

Fig. 2.6 (a) computational domain dimensions (in model-scale), boundary conditions, and (b) grid resolution utilized in the CFD simulations.

The validation was performed on the study model corresponding to a wind angle of attack of 130°, which was repeated 30 times where each test lasted for 360 seconds, with a time scale of 1:10. It is worth mentioning that the pressure coefficient was obtained by referencing the data to the dynamic pressure at mean roof height, which is typical for aerodynamic data. The mean and RMS of the pressure coefficient for the probe location, shown in Fig. 2.7(a), at 130° wind angle of attack, shows an average difference of 14 % and 10 % for all the probes, respectively, as demonstrated in Fig. 2.7(b). The fluctuation in the pressure coefficient beyond the separation point is found to be lower than that of the experimental results. This can be attributed to the lower resolution in pressure monitoring in experimental testing versus the numerical results, as in wind tunnel testing, fewer pressure taps are used to represent a region with a larger pressure gradient, while in CFD, it can be represented by multiple mesh grids. In addition, the experimental mean and RMS values are as shown in the range obtained from repeating the test 30 times, which could impact the maximum difference when compared to experimental values. Furthermore, the complex roof geometry examined in this study has many features that may implicate the pressure readings at various locations. For example, three various roof slopes can intensify the wind flow separation or even act as a shield and hence reduce the pressure depending on the wind angle of attack.

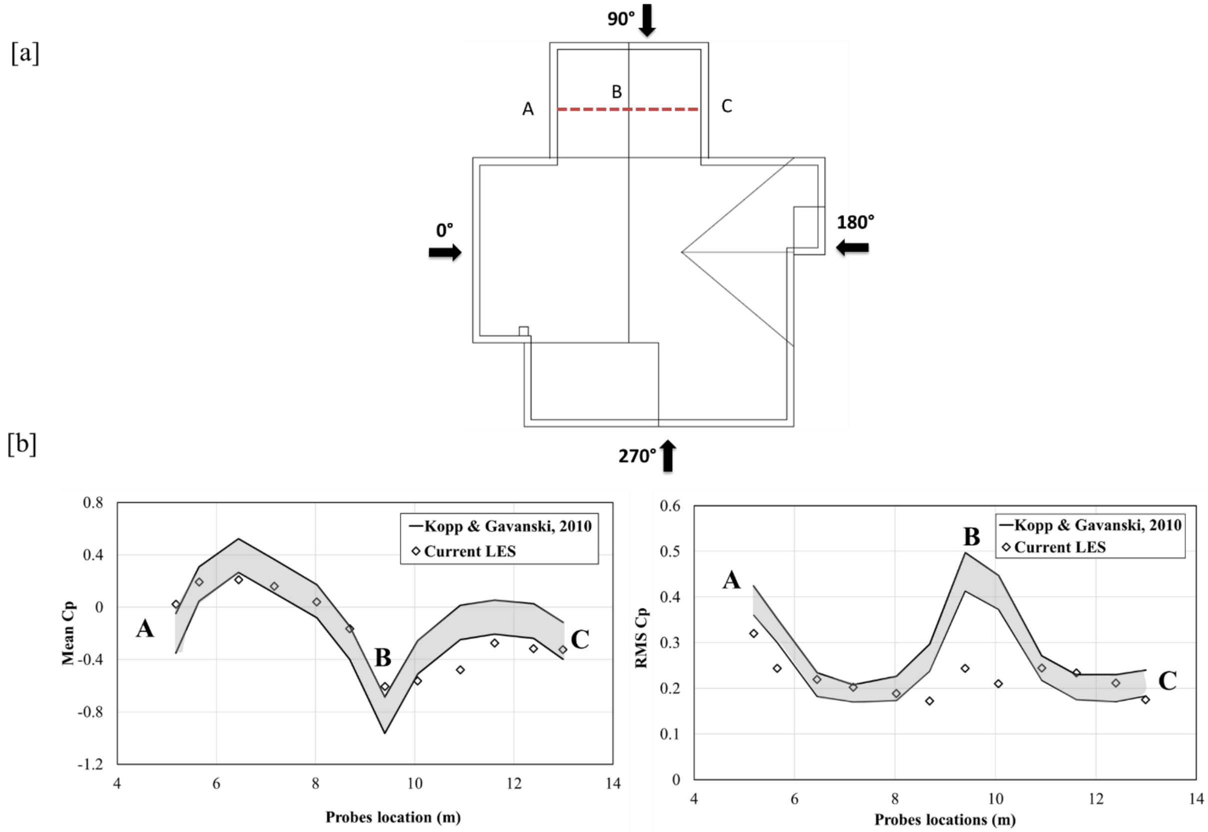

Fig. 2.7 (a) locations of the pressure taps on the east side used for validation, and (b) mean and RMS of the pressure coefficient at a wind angle of attack of 130°.

2.4.1. Method for Determining the Extreme Values

This subsection will briefly explain the extreme value analysis (EVA) followed in this study to obtain the extreme statistical values for wind load and pressure acting on the roof. To ensure the safety and reliability of designed structures, accurate estimation of the extreme values of externally applied load effects attributable to the wind is vital [32]. In principle, this study employs EVA analysis using the Gumbel approach to evaluate extreme values for wind forces and pressure [25]. A sample of time history for turbulence can be divided into subintervals of sufficient duration that peak values occurring can be treated as independent events. In this study, a total of 4200 data points are divided into 22 segments, each of 190 data points. For each segment, the peak value is selected to be used to perform extreme value analysis using the Gumbel method. The following analysis is applied throughout this study to find the extreme values of the pressure and forces [25]. In turbulence simulation, we can estimate the probability that the peak pressure coefficient will not exceed the value $\hat{C}_p$ in a subinterval. The data are ordered from smallest to largest and allocated a Gumbel plotting position, given by Equation [3]:

$$p = \frac{m}{1+N} \qquad [3]$$

m is the order, and N is the total number of values. Then, the plotted parameter was transformed into a reduced variate by $-\ln(-\ln(1-p))$ and the recorded extreme pressure coefficients are plotted against the reduced variate and a straight line fitted by linear regression. The extreme pressure values evaluated are higher than the most significant pressure coefficients recorded during the tests.

2.5. Results and Discussion

This section studies the effectiveness of adding corner and ridgeline parapets to reduce the wind load on roof surfaces. The study compares the mean and extreme pressure values between the original roof configuration and both modified roof configurations. The wind load assessment applies to 18 probs locations on peripheral and internal corners, edges, and six roof surfaces (subsections 3.1 and 3.2). Furthermore, this study presents a wind load evaluation on the parapets (subsection 3.3) as a step to prevent these mitigation techniques from dislodging and becoming flying hazardous debris to the surroundings.

2.5.1. Wind-induced pressure on corners and edges

A total of 18 probes located on the roof are examined in this section to investigate the impact of the mitigation technique on extreme pressure for probes located at the corners/ridges for non-modified and modified roof configurations. The probe's locations are selected as they are the most prone locations for roof damage to initiate during a windstorm. To demonstrate the impact of the parapets without the consideration of various wind angles of attack, the oblique wind angle of attack of 135° is selected for the non-modified and modified models to display the contour plot for the different mean and RMS of the pressure coefficient for the roof surfaces, as shown in both Fig. 2.8(a), and (b). Although the later comparison will take into account all wind angles of attack, it can be observed from the selected angle of attack (i.e., 135°) that the roof surface edges and corners for both modified configurations exhibit lower mean and RMS pressure coefficients compared to its counterpart on the left (non-modified case). This is due to the fact that parapets have successfully displaced the wind flow separation zone and, therefore, reduced the suction in these locations. Overall, the pressure testing demonstrated that modifications effectively lower the roof pressure distribution, reducing the risk of wind damage to the roof. Although the reduction of negative pressure is generally applied to the entire roof, it can be concluded that the decrease in pressure is higher in zones located on the edges and corners of the roof (e.g., where the parapets are installed) than in internal areas, which is also concluded by Azzi et al. (2020) [17].

In addition to reducing the negative pressure (suction) at the leading corners and edges of the building, parapets are also found to cause significant positive or downward pressures. These observations are found along the leading roof surfaces and interior zones. The latter observation is believed to act as a stabilizing force on the roof; however, it may also be governing when combined with other gravity loads (e.g., snow load and dead load) [14]. Furthermore, in the wake zones of the ridgeline parapets, it is found that 500 mm height increases the intensity of pressure in the cornering wind direction. The latter finding may probably be due to the interaction between the small vortices of the wake of the parapet and the conical vortex of high-intensity core occurring at the flow separation along the roof edge, which was previously noted by Baskaran and Stathopoulos, 1988 [11]. To reduce the aggravated pressure, increasing the height of the parapets may be required, as was recommended by previous studies [11,33].

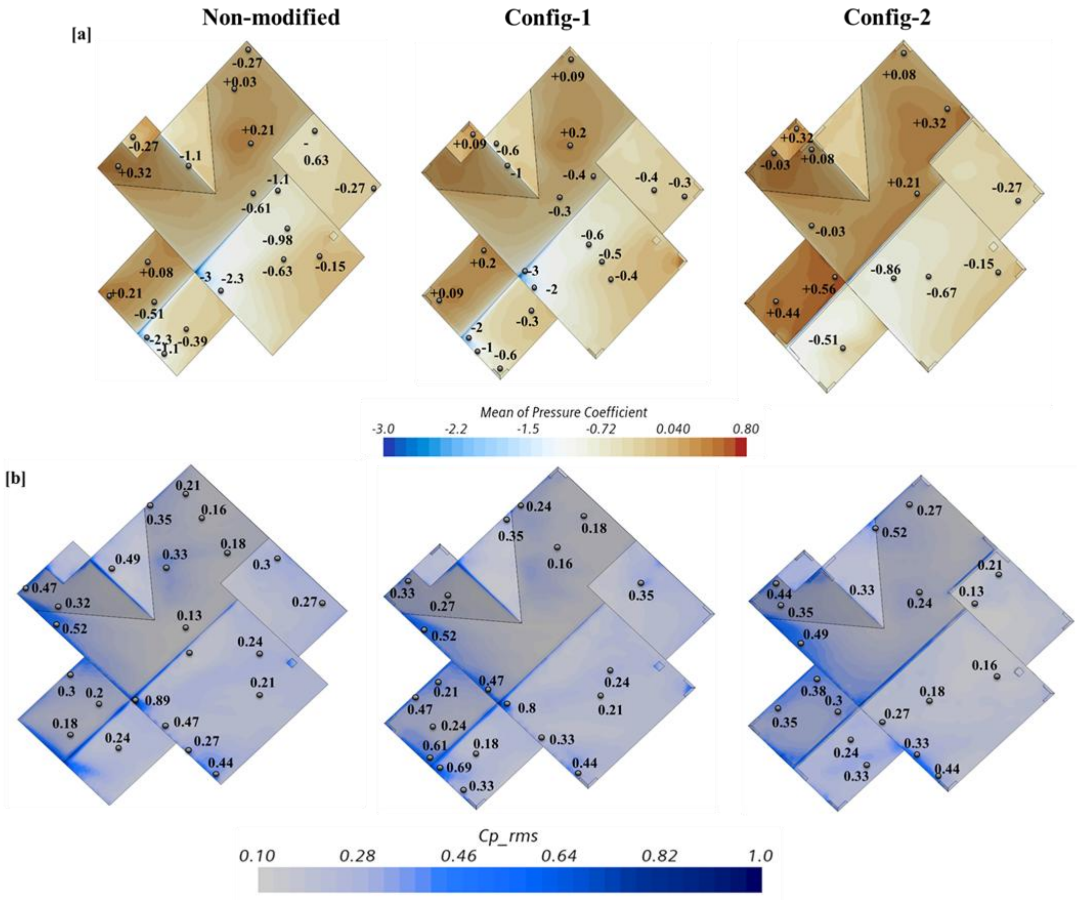

Fig. 2.8 (a) mean and (b) RMS of the pressure coefficient for the wind angle of attack of 135° for the non-modified and modified building configurations.

Additionally, it was observed that pressure coefficients measured on the interior zones for Config-1 are similar to those estimated on roofs without modifications. The latter indicates that a modified roof with peripheral corner parapets may not significantly mitigate suction at the interior zones. This was also concluded by Surry and Tieleman, 1995 [6]. The latter finding supported the idea of adding ridgelines for the Config-2 roof design. The extreme pressure values recorded for the three models in this study are displayed in Fig. 2.9 (a). It is found that the extreme values of the suction are decreased when compared to the values evaluated at the corners of the non-modified roof configuration. The reduction reached a maximum of 29% and 9.4% for both config-1 and Config-2, respectively. To further investigate the effect of adding parapets on the pressure of interior zones within the complex roof configuration, Fig. 2.9(b) displays the extreme pressure readings for ten probs at the corners of the internal roof zones. The values of the intense pressure coefficients extracted from probs 11 and 12 located on roof surface R1 showed that the ridgeline addition of

500 mm height induced higher suction compared to the other models. This can be attributed to trapped vortices on the parapets wake zone's location; hence, higher parapets on the ridgeline may eliminate these vortices. Corner probs located on roof surfaces, namely (R5 and R6), witnessed a significant decrease in the pressure values when introducing parapets on the ridgeline of both roof surfaces, reaching 53%. Overall, it is found that the Config-2 models significantly decrease the pressure at corners and edges compared to the non-modified roof and Config-1 configurations.

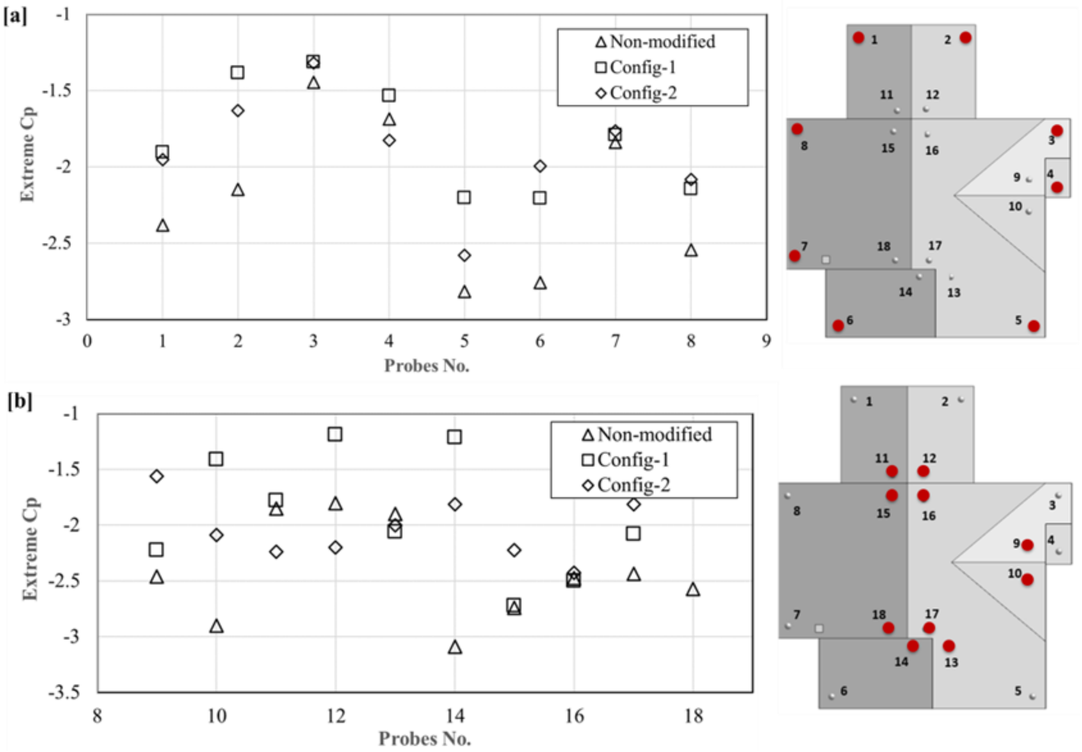

Fig. 2.9 Extreme pressure coefficient values extracted from probes located at the (a) peripheral corners and (b) interior corners.

Fig. 2.10 displays the mean and RMS of the critical pressure coefficient values extracted from the probes investigated in this study. It can be observed that critical RMS of the pressure coefficients for the internal and peripheral corner probs are reduced by a maximum of 25% when both roof modifications are applied to the non-modified roof. However, the parapet arrangement in Config-1 reduced the critical mean pressure by a maximum of 13%.

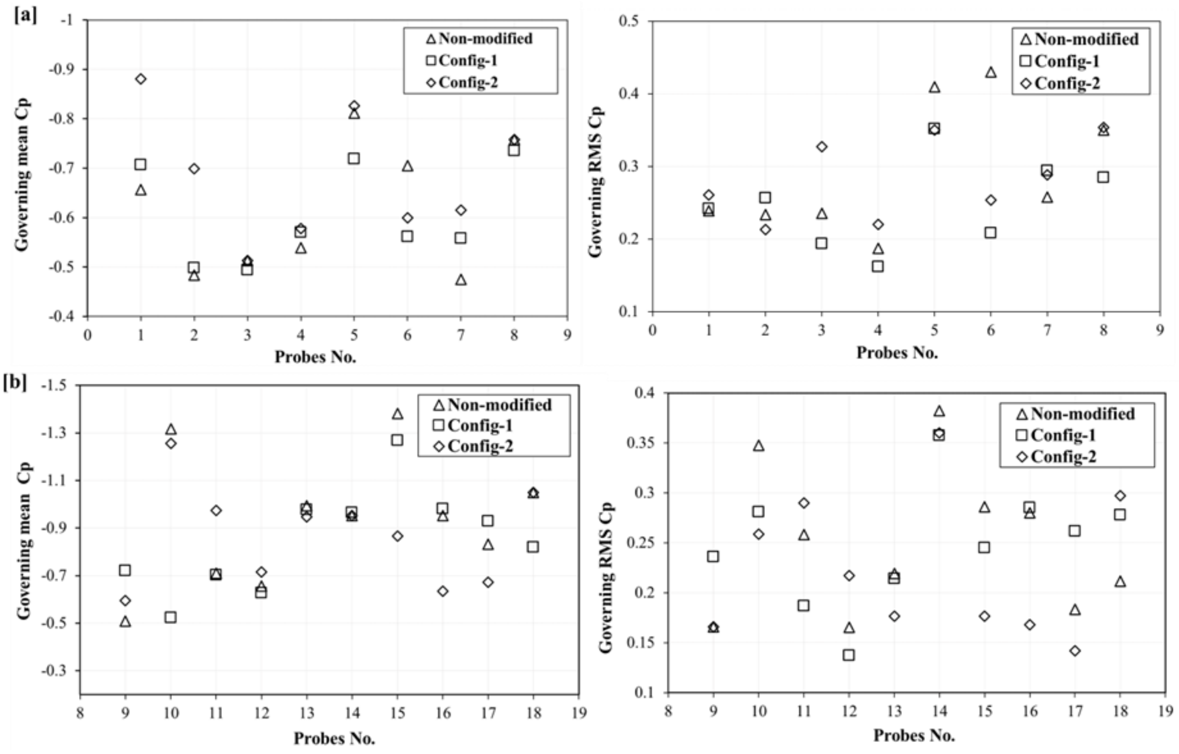

Fig. 2.10 Critical mean and RMS of the pressure coefficient extracted from probes located at the (a) peripheral corners and (b) interior corner.

2.5.2. Wind-induced Forces on Surfaces of the Roof

As expected, the change in pressure distribution on roof surfaces has resulted in a consequence change in the uplift forces, which can also show the effectiveness of adding parapets on the studied complex roof. Fig. 2.11 shows the normalized extreme uplift force of the entire roof surface at various wind angles of attack ranging from 0° to 315°. The normalized wind loads ($\mathrm{F_N}$) is calculated using the Equation [4].

$$\mathrm{F_{x,z-N}} = \frac{\mathrm{F_z}}{\frac{1}{2}\rho_{\mathrm{air}} \mathrm{v}^2 \mathrm{A_s}} \qquad [4]$$

$\mathrm{F_z}$ is the extreme statistical force values in both x and z directions, the ρ_{air} is the air density, which has been used as $1.2929\ \mathrm{kg/m^3}$, v is the wind velocity at roof reference height, and $\mathrm{A_s}$ is the surface area of the roof. As it can be noticed, oblique wind directions are the most critical (i.e., highest) and, therefore, will govern the design of the roof. In fact, the non-modified roof configuration at the wind angle of attack of 315° induced the highest uplift force on the entire roof surface. Furthermore, the normalized roof uplift at an oblique wind angle of attack, 315°, is reduced when adding ridgeline parapets (i.e., Config-2) by 5.6%. In contrast, adding only peripheral corner parapets (i.e., Config-1) led to a total reduction of the extreme uplift force on the entire roof by 3.6% compared to the non-modified configuration. Fig. 2.12 shows that parapets can reduce the standard deviation of the uplift force by up to 7%, which can be attributed to the added down-acting stabilizing pressure on the interior zones of the roof, as remarked in sub-section 3.1.

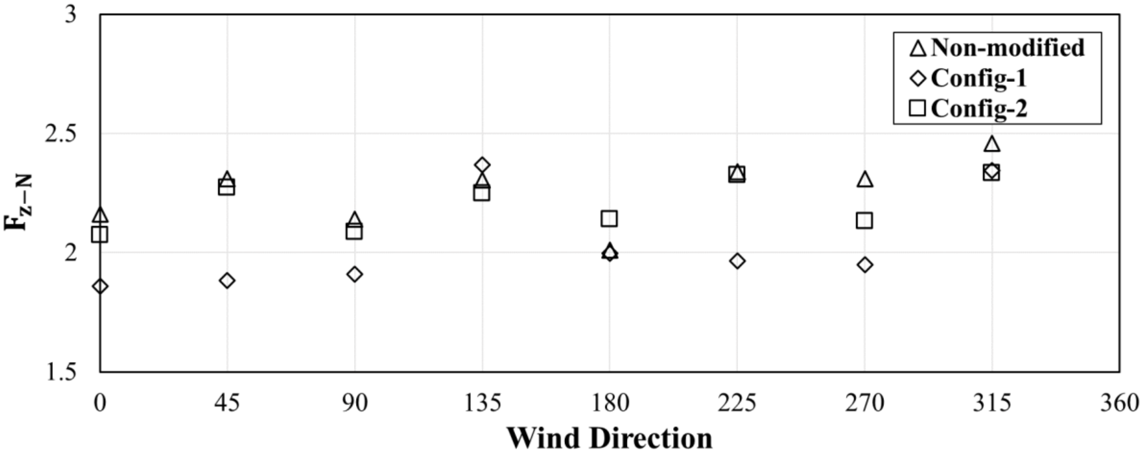

Fig. 2.11 Normalized roof uplift for non-modified and modified roof surfaces for wind angle of attack ranging from 0° to 315°.

It is worth mentioning that the uplift wind forces on individual surfaces resulting from Config-2 have shown a decrease in magnitude, which is detailed in Fig. 2.13. The maximum reduction of extreme wind pressure on the roof is found to be 11% on R1. However, it is noticed that roof surfaces R3 and R4 substantially increase the wind uplift force when the corner parapets are the only peripheral of the roof configuration (i.e., Config-1). This increase in the uplift is probably due to redirecting the flow by the added parapets, magnifying the separation bubble at these roof surfaces. The latter can initiate corner damage during a windstorm. However, adding a 500 mm ridgeline (in Config-2) is found to reduce the uplift forces by 5% compared to the original roof configuration on roof surface R4.

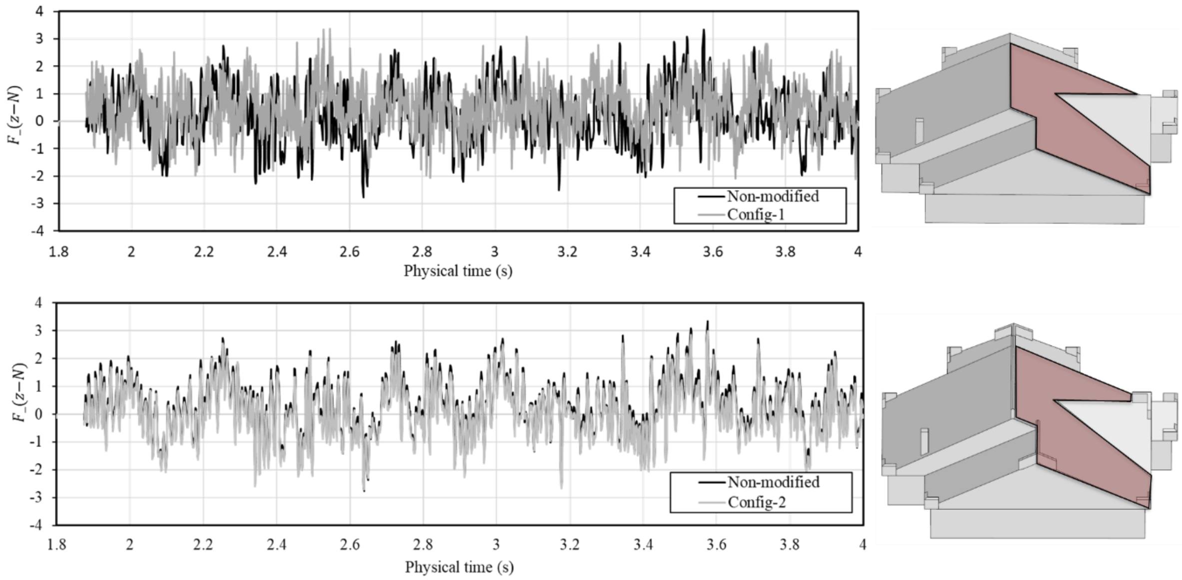

Fig. 2.12 Time history for the roof surface (R2) uplift at a wind angle of 135 ° for modified roof configurations.

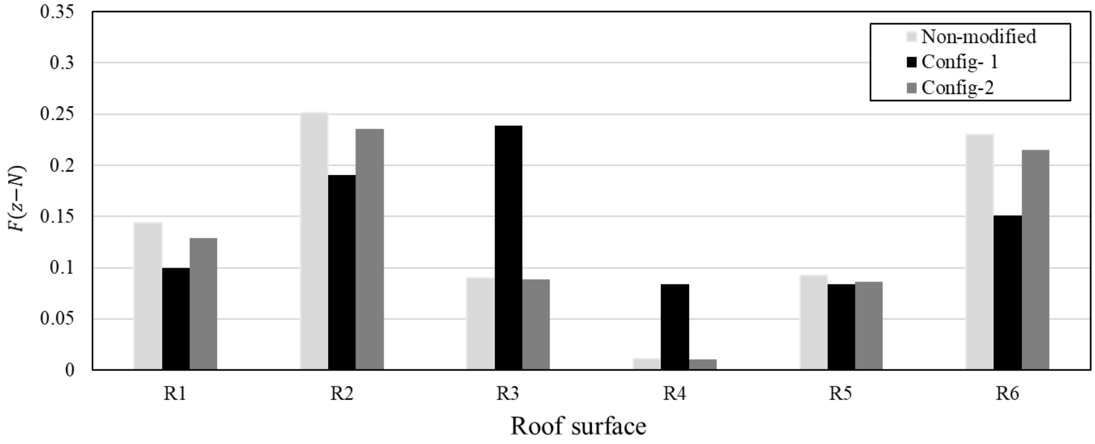

Fig. 2.13 Normalized extreme roof uplift force on individual surfaces for Non-modified and modified roof configurations.

2.5.3. *Wind Loads on the Parapets*

Adding parapets to low-rise buildings can cause an additional risk of attracting elevated wind forces on the roof surfaces. Accordingly, this subsection evaluates the wind loads on parapets for the studied configurations to better understand the added damage risk from the implementation of parapets and avoid them becoming flying hazards to the surroundings [16]. Since the parapets can alter the flow over the roof, evaluating the loads on parapet surfaces is crucial to be accounted for in designing the main wind force-resisting system (MWFRS) [14]. Fig. 2.14 shows an example of time histories for forces in the x, y, and z directions acting on parapet "P11", subjected to an oblique wind angle of attack of $225°$. It is known that the wind load on the parapets is governed by both along and uplift forces; therefore, they are evaluated for all the parapets in Config-1 and Config-2. The loads developed on the parapets are obtained using force time histories extracted from the numerical simulation, and then the EVA is applied to find the extreme statistical values. The normalized wind loads ($\mathrm{F_N}$) are then calculated using the Equation [5] below:

$$\mathrm{F_{x,z-N}} = \frac{\mathrm{F_{x,z}}}{\frac{1}{2}\rho_{\mathrm{air}} \mathrm{v}^2 \mathrm{A_p}} \qquad [5]$$

$\mathrm{F_{x,z}}$ is the extreme statistical forces values in both x and z directions, the ρ_{air} is the air density, which has been used as $1.2929\ \mathrm{kg/m^3}$, v is the wind velocity at the roof reference height and $\mathrm{A_p}$ is the surface area of the parapets.

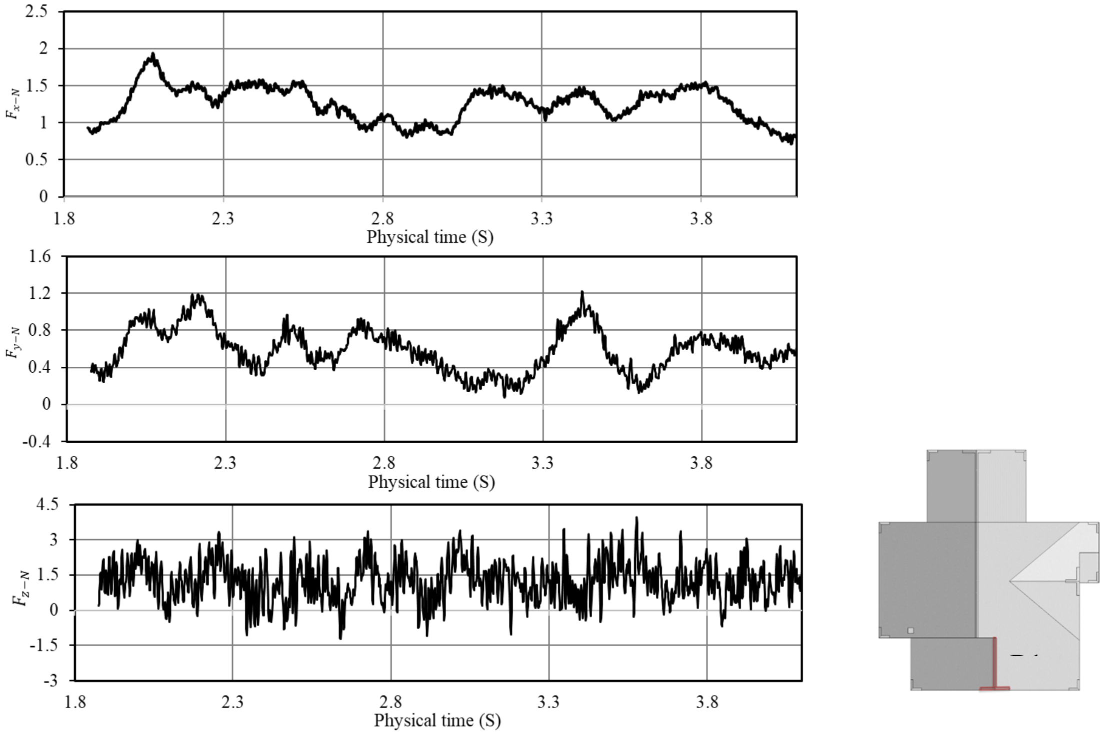

Fig. 2.14 Forces acting on parapet "P11" at wind angle of attack 225°.

A comparison of the extreme along and uplift force impacting the parapets in both modified configurations is presented in Fig. 2.15. The overall extreme uplift wind forces acting on the parapets located on the ridgeline are found to be higher than those of the along wind forces. In other words, the extreme uplift force reached a value of 1.02 for the $135°$ wind direction acting on the parapets along the ridgeline. In comparison, the normalized extreme along force recorded an extreme value of 0.95 for the 0° wind direction impacting corner parapets. The high suction impacted on the parapet surface is initiated due to flow separation at the parapet’s edges and corners. Therefore, choosing the parapet's manufacturing material and its connection to the roof is crucial because it determines its functionality during a wind event. Although parapets can be made in various materials such as steel, metal, wood, or even stucco masonry; However, using the steel/metal material for the parapets is recommended as it can be designed into any form that the building requires.

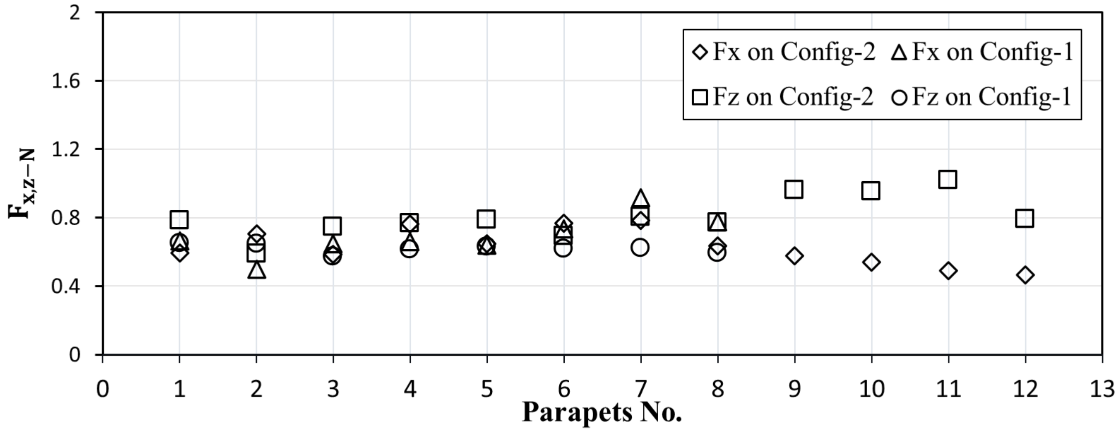

Fig. 2.15 Normalized extreme forces impact parapets in different configurations.

2.6. Summary and Conclusion

This study presents preliminary but promising results aiming at mitigating damages for low-rise buildings with complex roof geometry to enable them to withstand windstorms. The current study proposes aerodynamic mitigation techniques for a low-rise building with complex roof geometry. The procedure utilized Computational Fluid Dynamics (CFD) to examine the effectiveness of adding corner and ridgeline parapets. The mitigation techniques aim to reduce wind loads at corners, edges, and interior roof surfaces by weakening the vortices responsible for initiating damages. In addition, the study investigated the wind load on the parapets to assess the optimal parapet configuration design. It is found that parapets located at the peripheral corners have reduced extreme suction by a maximum of 29% compared to the non-modified roof design. Probes located on the interior roof corners showed a significant decrease in the pressure values when introducing parapets on the ridgeline (i.e., Config-2), reaching 53%. The latter indicates that adding ridgeline parapets is crucial to reducing wind load on the interior zone surfaces of the complex roof geometry. Furthermore, the extreme roof uplift is decreased by a maximum of 5.6% when adding ridgeline parapets compared to the non-modified roof. It was also found that extreme uplift occurs when wind approaches the roof in an oblique direction to the parapet face. After examining both along and uplift forces impacting the parapets, it is concluded that uplift forces are the governing ones in the design, thus impacting the design of the parapet. The study showed that corner and ridgeline parapets can be utilized to successfully enhance the roof aerodynamic performance (i.e., reduce wind load) on complex roof geometry for retrofitting and new construction purposes. These techniques can alleviate roof damage, which is considered one of the biggest concerns during windstorms. It is worth mentioning that adding parapets to low-rise building roofs poses a risk of its own if the parapets are insufficiently anchored to the roofing system. Hence, they can dislodge and become a source of flying hazard debris, impacting the neighbouring building. Furthermore, insulations installed at the locations where the parapet walls meet with the roof can increase the risk of water leaks if they are breached. In addition, parapets may require a drainage system and regular maintenance throughout the seasons.

2.7. References

[1] G.T. Bitsuamlak, M. Asce, W. Warsido, Edward Ledesma, A.G. Chowdhury, Aerodynamic Mitigation of Roof and Wall Corner Suctions Using Simple Architectural Elements, Ascelibrary.Org. 139 (2013) 396–408. https://doi.org/10.1061/(ASCE)EM.1943-7889.0000505.

[2] NBCC, "Supplement to the National Building Code of Canada"., Association; Committee on the National Building Code; National Research Council of Canada, Ottawa, Ont. Norris, 2005.

[3] D. Sandink, G. Kopp, S. Stevenson, N. Dale, Increasing High Wind Safety for Canadian Homes: A Foundational Document for Low-Rise Residential and Small Buildings Institute for Catastrophic Loss Reduction Building resilient communities, (2019).

[4] Insurance of Bureau of Canada, Welcome to Insurance Bureau of Canada, (2022).

[5] Z. Mansouri, R.P. Selvam, A.G. Chowdhury, Maximum grid spacing effect on peak pressure computation using inflow turbulence generators, Results Eng. 15 (2022) 100491. https://doi.org/10.1016/J.RINENG.2022.100491.

[6] J.X. Lin, D. Surry, H.W. Tieleman, The distribution of pressure near roof corners of flat roof low buildings, J. Wind Eng. Ind. Aerodyn. 56 (1995) 235–265.

https://doi.org/10.1016/0167-6105(94)00089-V.

[7] A. Elshaer, G. Bitsuamlak, H. Abdallah, Variation in wind load and flow of a low-rise building during progressive damage scenario, Wind Struct. An Int. J. 28 (2019) 389–404. https://doi.org/10.12989/WAS.2019.28.6.389.

[8] T. Stathopoulos, A. Baskaran, P.A. Goh, Full-scale measurements of wind pressures on flat roof corners, J. Wind Eng. Ind. Aerodyn. 36 (1990) 1063–1072. https://doi.org/10.1016/0167-6105(90)90103-J.

[9] C. Mans, G.A. Kopp, D. Surry, Wind effects of parapets on low buildings: Part 3. Parapet loads, J. Wind Eng. Ind. Aerodyn. 93 (2005) 857–872. https://doi.org/10.1016/J.JWEIA.2005.08.007.

[10] R. Al-Chalabi, M. Ibrahim, A. Elshaer, Computational Wind Load Evaluation and Aerodynamic Mitigation of Low- rise Building with Complex Roof Geometry | Request PDF, in: Proc. Can. Soc. Civ. Eng. Annu. Conf., 2022.

[11] A. Baskaran, T. Stathopoulos, Roof corner wind loads and parapet configurations, J. Wind Eng. Ind. Aerodyn. 29 (1988) 79–88. https://doi.org/10.1016/0167-6105(88)90147-X.

[12] D. Surry, J.X. Lin, The effect of surroundings and roof corner geometric modifications on roof pressures on low-rise buildings, J. Wind Eng. Ind. Aerodyn. 58 (1995) 113–138. https://doi.org/10.1016/0167-6105(95)00016-K.

[13] S. Pindado, J. Meseguer, Wind tunnel study on the influence of different parapets on the roof pressure distribution of low-rise buildings, J. Wind Eng. Ind. Aerodyn. 91 (2003) 1133–1139. https://doi.org/10.1016/S0167-6105(03)00055-2.

[14] G.A. Kopp, D. Surry, C. Mans, Wind effects of parapets on low buildings: Part 1. Basic aerodynamics and local loads, J. Wind Eng. Ind. Aerodyn. 93 (2005) 817–841. https://doi.org/10.1016/j.jweia.2005.08.006.

[15] W. Suaris, P. Irwin, Effect of roof-edge parapets on mitigating extreme roof suctions, J. Wind Eng. Ind. Aerodyn. 98 (2010) 483–491. https://doi.org/10.1016/j.jweia.2010.03.001.

[16] A.M. Aly, J. Bresowar, Aerodynamic mitigation of wind-induced uplift forces on low-rise buildings: A comparative study, J. Build. Eng. 5 (2016) 267–276. https://doi.org/10.1016/j.jobe.2016.01.007.

[17] Z. Azzi, F. Habte, A. Elawady, A. Gan Chowdhury, M. Moravej, Aerodynamic Mitigation of Wind Uplift on Low-Rise Building Roof Using Large-Scale Testing, Front. Built

Environ. 5 (2020) 149. https://doi.org/10.3389/FBUIL.2019.00149/BIBTEX.

[18] S. Bobby, S.M.J. Spence, E. Bernardini, A. Kareem, Performance-based topology optimization for wind-excited tall buildings: A framework, Eng. Struct. 74 (2014) 242–255. https://doi.org/10.1016/J.ENGSTRUCT.2014.05.043.

[19] E. Bernardini, S.M.J. Spence, D. Wei, A. Kareem, Aerodynamic shape optimization of civil structures: A CFD-enabled Kriging-based approach, J. Wind Eng. Ind. Aerodyn. 144 (2015) 154–164. https://doi.org/10.1016/J.JWEIA.2015.03.011.

[20] A. Elshaer, G. Bitsuamlak, A. El Damatty, Enhancing wind performance of tall buildings using corner aerodynamic optimization, Eng. Struct. 136 (2017) 133–148. https://doi.org/10.1016/J.ENGSTRUCT.2017.01.019.

[21] A. Elshaer, A.M. Asce, G. Bitsuamlak, Multiobjective Aerodynamic Optimization of Tall Building Openings for Wind-Induced Load Reduction, J. Struct. Eng. 144 (2018) 04018198. https://doi.org/10.1061/(ASCE)ST.1943-541X.0002199.

[22] ASCE-7, Minimum Design Loads on Buildings and Other Structures, in: American, S. of C. Engineers. (Eds.), 2005.

[23] P. Sarkar, F. Wu, P.P. Sarkar, K.C. Mehta, Article in Wind and Structures An International Journal ·, Wind Struct. 4 (2001) 131–146. https://doi.org/10.12989/was.2001.4.2.131.

[24] Gregory A. Kopp, Eri Gavanski, Wind tunnel pressure measurements on two FCMP houses, (2010) 1–30.

[25] J.E. Gumbel, Statistics of extremes, Eng. Econ. 7 (1961) 36–38. https://doi.org/10.1080/00137916108928620.

[26] J. Franke, A. Hellsten, K.H. Schlünzen, B. Carissimo, The COST 732 Best Practice Guideline for CFD simulation of flows in the urban environment: A summary, Int. J. Environ. Pollut. 44 (2011) 419–427. https://doi.org/10.1504/IJEP.2011.038443.

[27] H. Aboshosha, A. Elshaer, G.T. Bitsuamlak, A. El Damatty, Consistent inflow turbulence generator for LES evaluation of wind-induced responses for tall buildings, J. Wind Eng. Ind. Aerodyn. 142 (2015) 198–216. https://doi.org/10.1016/j.jweia.2015.04.004.

[28] T.C.E. Ho, D. Surry, D. Morrish, G.A. Kopp, The UWO contribution to the NIST aerodynamic database for wind loads on low buildings: Part 1. Archiving format and basic aerodynamic data, J. Wind Eng. Ind. Aerodyn. 93 (2005) 1–30.

https://doi.org/10.1016/J.JWEIA.2004.07.006.

[29] M.F. Khaled, A.M. Aly, A. Elshaer, Computational efficiency of CFD modeling for building engineering: An empty domain study, J. Build. Eng. 42 (2021) 102792. https://doi.org/10.1016/J.JOBE.2021.102792.

[30] R. Courant, K. Friedrichs, H. Lewy, Über die partiellen Differenzengleichungen der mathematischen Physik, Math. Ann. 100 (1928) 32–74. https://doi.org/10.1007/BF01448839.

[31] SHARCNET, is a consortium of colleges, universities and research institutes operating a network of high-performance computer clusters across south western, central and northern Ontario, (2022). www.sharcnet.ca.

[32] J.D. Holmes, W.W. Moriarty, Application of the generalized Pareto distribution to extreme value analysis in wind engineering, J. Wind Eng. Ind. Aerodyn. 83 (1999) 1–10. https://doi.org/10.1016/S0167-6105(99)00056-2.

[33] G.A. Kopp, C. Mans, D. Surry, Wind effects of parapets on low buildings: Part 4. Mitigation of corner loads with alternative geometries, J. Wind Eng. Ind. Aerodyn. 93 (2005) 873–888. https://doi.org/10.1016/J.JWEIA.2005.08.004.

CHAPTER 3

Enhancing LES efficacy in wind load evaluation of low-rise buildings using synthesized inflow turbulence

3.1.Introduction

3.1.1. Background and Study Motivation

Single detached residential low-rise buildings in Canada represent over 53.6% of the private dwellings, which occupy over 14M of the Canadian population [1]. Low-rise buildings are located in the Atmospheric Boundary Layer (ABL), where wind flow is highly turbulent, and hence, they are more prone to wind damage than other structures (NBCC, 2005). According to previous studies, wind catastrophes inflected mostly on personally categorized structures (i.e., housing, shed, etc.) where the damages exceeded 69.5% of all total losses [2]. During windstorms, claddings of low-rise buildings can be subject to damage due to uplift forces, which can jeopardize the integrity of low-rise buildings [3]. Multiple studies have found that uplift forces resulting from pressure variations can initiate roof failure [4–6]. Hence, accurate wind load prediction at critical locations in low-rise buildings (i.e., separation location) is vital for low-rise buildings to build high-wind resilient structures. Currently, the boundary layer wind tunnel test is utilized to evaluate the wind-induced aerodynamic load; however, it is not necessarily affordable for residential buildings, especially given that the design varies from one building to another. Experimental wind tunnel affordability is associated with the cost of manufacturing a model under various experimental conditions and the time and labor-consumption limitations [7]. The overall challenges in wind engineering testing and the importance of accurate wind load evaluation are pointed out in several studies [8,9]. To reduce the cost associated with design variables and model design limitations, the computational wind load evaluation using Computational Fluid Dynamic (CFD) can be utilized as a complementary tool to the experimental testing that can provide preliminary directions through the design process of the built environment, where wind tunnel testing can be conducted when the conceptual design is identified.

Over the past decades, CFD has proved its value in wind-related studies by obtaining reliable quantitative and qualitative wind-induced load data [10–15]. The CFD technique draws its strength from being practically available and in its ability to consider parameters that are difficult to implement, such as temperature, scalability, and repeatability, in addition to the ability of fast execution on high-performance computers [16]. Moreover, the CFD can capture fluctuations at a large number of points on the surfaces of a building; hence, more crucial information about separation zones will be captured [10,17–19]. Additionally, the development of numerical modelling has empowered Large Eddy Simulation (LES) to accurately simulate the wind flows around buildings and structures under conditions very close to the actual state with full-scale modelling [11]. The Architectural Institute of Japan (AIJ) has examined the CFD technique's applicability in wind load evaluation. AIJ permits using the CFD approach like wind tunnel testing as long as guidelines concerning three-dimensional LES and inflow simulation are followed and the work performed is supervised by a wind engineering expert [20]. However, many factors can play a vital role in establishing the efficacy of numerical wind load evaluation. Franke et al. [21] have specified that numerical wind load evaluations' accuracy includes the computational domain size, domain discretization, size of the time step, and the geometric boundary conditions. The latter findings also have been concluded by Bruno et al. [22] following the large benchmark study of 70 experimental and numerical studies, where it was found that estimation of the lift forces showed discrepancies due to domain size and discretization as well as the turbulence models. In addition, accurately generating the wind flow parameters using inflow generators can be highly influenced by the input parameters, such as the maximum and minimum turbulence frequency range that needs to be resolved (i.e., f_{max}, f_{min}).

The following sub-sections (1.2-1.4) will present more details about the current knowledge in selecting the maximum frequency content for small-scale structures and the current code of practice in choosing computational domain size and discretization.

3.1.2. Capturing Frequency Content of the Turbulence for Small-scale Structures

Achieving accurate turbulence characteristics is often challenging due to the significantly smaller geometrical configurations compared to the ABL height [18]. Typically, experimental and computational wind load evaluation studies rely on replicating the wind profile within the ABL around buildings. For low-rise buildings in the ABL, turbulence is crucial to aerodynamic loading. Large-scale turbulence can increase the gust speeds, which alters the overall loading [25]. In contrast, small-scale turbulence controls the aerodynamic loading by altering the flow around the building, leading to a significant increase in the magnitude of high negative surface pressures located under reattaching shear layers [24]. Melbourne [26] has established that capturing small-scale turbulence at a reduced frequency, fh/U, where f is turbulence frequency, U is wind velocity and h is roof height, equals to 10, is critical to ensure the accuracy of capturing flow features around a low-rise building. Adjacently, Morrison and Kopp [27] argued that for low-rise buildings, the vital turbulence scales are the ones captured at a reduced frequency that varies between 0.1 and 2.0. It is also worth noting that the "small scales" of turbulence that are controlling the wind loads on the roof are up to 10 times larger than the height of the (low-rise) building and about 50 times larger than the width of the separated shear layer [28]. Hence, to accurately model wind loading on low-rise buildings, incoming turbulence must be resolved up to a frequency corresponding to the characteristic scale of the building, which requires proper modelling of small-scale turbulence, particularly at the separation locations [24]. To accurately model the turbulence, maintaining the spectral content of the incident flow is critical and often found challenging in small-scale structures [29,30].

In wind tunnel testing, determining the critical frequency range spectrum, which contributes to generating wind loads, is required for small-scale structures. In LES, the turbulent flow injected into the computational domain is typically generated by matching ABL flow statistically using numerous methods such as (i) Random Flow Generation methods (RFG) [31–35], (ii) Digital Filtering Methods (DFM) [36], and (iii) Synthetic Eddy Methods (SEM) [37]. The RFG method requires an input range of dimensional frequency that varies between minimum (f_{min}) and maximum frequency (f_{max}). The latter defines the largest frequency that a grid can resolve. In order to perform highly accurate LES simulation, the majority of the turbulence (e.g., 80% of turbulence) has to be resolved rather than being modelled, which can be controlled by defining f_{max} shown in Fig. 3.1 [38]. Generally, the value of f_{max} at is used, as input in the turbulence flow generator, is typically resembles the frequency range employed in the experimental testing. However, this frequency range is not necessarily resolved as it highly depends on the grid refinement and accordingly, the minimum resolved wavelength. Aboshosha et al. developed and employed one of the RFG methods (i.e., Consistent Discrete Random Flow Generation CDRFG) [39] to study tall building aerodynamics. Later, several studies utilized the same method to study low-rise building aerodynamics [40–44]. Despite that, there are no clear guidelines on the way of defining the value of f_{max} required for the inflow generation for low-rise buildings.

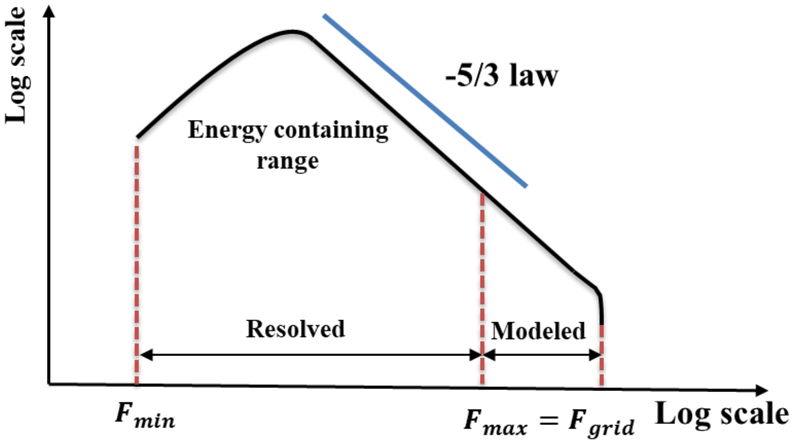

Fig. 3.1 The correlation between a power density spectrum and turbulence modelling in LES.

3.1.3. The Influence of Computational Domain Size on Wind Load Evaluation for Low-Rise Building

Franke et al., COST (European Corporation in Science and Technology) action 732 guidelines [21], suggested that for LES, the computational domain's (CD) overall size must be large enough to contain the largest and energetically significant flow around structures to accommodate all flow features that have an impact on the characteristics of the flow field within the region of interest. The guideline is merely based on simulating obstacles such as generic bluff bodies rather than buildings, specifically low-rise buildings. In general, the extension of the CD in the longitudinal, lateral, and vertical directions depends on the type of boundary conditions used. Consequently, Franke et al. [21] recommended that a building with height (H) may have a marginal influence if its distance from the region of interest exceeds 5H to 10H, which will ensure the ABL fully develops. Most previous studies have utilized building height, H, as a reference to find the suitable size for the computational domain. Table 3.1 broadly sheds light on the various computational domain sizes employed in previous studies. However, relying on the building height to define the computational domain dimensions can be suitable for tall buildings. The latter can be attributed to the fact that once the wind flow reaches the building, the airflow reaches furthest at the maximum structure height, whereas it is not necessarily adequate for low-rise buildings. In addition, the current CFD practice in selecting the computation domain size is founded on guidelines that have approximately used the knowledge created from experimental tests, such as using the blockage ratio to determine the computational domain's width and height. Hence, precise guidelines for identifying the computational domain size are believed to be limited. Therefore, computational domain dimensions can be a source of error in CFD simulations, current common practice, or at least overly sized for low-rise buildings.

Table 3.1 List of computational domain sizes followed by previous studies.

Authors	Building dimensions (L, W, H)	Computational domain size		
		Domain Length	**Domain width**	**Domain Height**
Geleta and Bitsuamlak [45]	274.4×183×80 mm	130H	15H	12.5H
Qiu et al. [46]	150×150×75 mm	42 H	26H	8H
Aly and Bresowar [47]	301×198×88 mm	16.4 H	10H	5.5H
Yang et al. [48]	240×160×120 mm	28H	15H	8H
Rack-woo Kim et al. [7]	2200×175×350 mm	15H	5H	5H
Ricci and Miranda [49]	240×160×80 mm	65.5 H	27.5H	22.5H
Singh and Roy [50]	562×562×180 mm	20H	10H	6H
Amini and Memari [51]	500 ×250×200 mm	18H	10H	6H
Shi Gan et al. [52]	600×600×600 mm	20H	9.3H	7.5H
Y. Ozmen et al. [53]	100×50 ×40 mm	14.5H	8.8H	6H
Tominaga and Stathopoulos [54]	100 ×100 ×100 mm	15H	13H	6.7H

3.1.4. The Influence of Computational Domain Spatial Discretization on Wind Load Evaluation for Low-Rise Building

Another vital source of error in the numerical wind load evaluation is spatial and temporal discretization. The accurate computational discretization reflects the precision of capturing important wind phenomena such as important turbulence structures, shear layers, and vortices with sufficient resolution, particularly at the location of wind flow separation (i.e., at edges and corners). High grid density within multiple refinement zones is therefore crucial for maintaining horizontal homogeneity and accurate pressure predictions; however, it can require higher memory size and speed of the computational hardware [56]. Moreover, the time step required to accurately execute LES is highly dependent on the smallest cell size to maintain a Courant Friedrichs Lewy (CFL) number less than 1. This greatly affects the total number of time steps needed to resolve the flow. For low-rise buildings, the range of eddy sizes that manifest the turbulent flow around structures typically dictate the grid sizes. In turbulent flow, capturing eddies with a wavelength smaller than the grid size (Δx) cannot be resolved and will be modelled using a sub-grid model (SGS) such as WALE, as presented in Fig. 3.2. Previous studies indicated that the error resulted in wind load evaluation using minimum grid size to transport a sine or cosine wave of a length of $2\Delta x$ is significantly high (i.e. 90%) compared to utilize a grid size resolving a wavelength of $10\Delta x$ (i.e. 10%) [57,58]. However, executing LES with very fine grid cells that can resolve a wavelength of

$10\Delta x$ will require a long running time (i.e., 10 times more simulation under the same computational resources), and, therefore, computational cost. The common practice in unsteady LES simulations is to maintain the balance between the selected grid size and time step by maintaining a stable Courant-Friedrichs-Lewy (CFL) condition, as presented in Eq. (1) [59]. The maximum CFL of 1.0 is ideal for most flow problems.

$$CFL = \frac{U\Delta t}{\Delta x} < 1.0 \qquad (1)$$

Where U is the velocity magnitude at roof reference height, Δt and Δx are the time-step and the grid size, respectively.

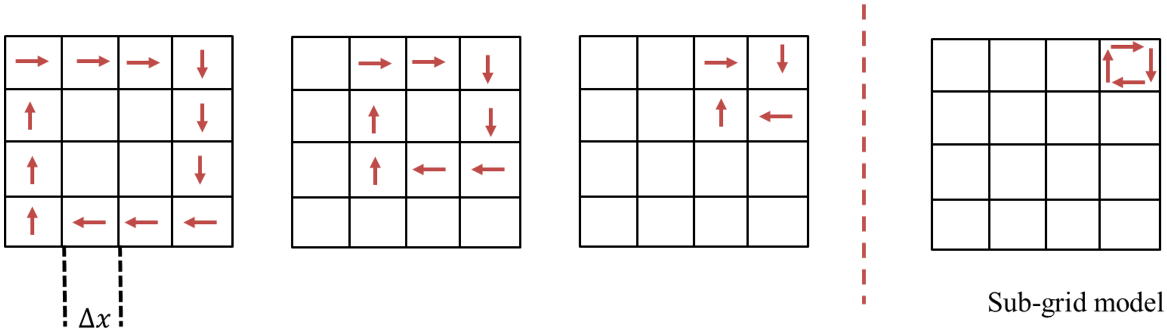

Fig. 3.2 Various eddy sizes resolved by the grid size.

Several previous studies have utilized the building dimensions to select the grid size, such as Ricci et al. [49]. The latter employed three grid refinement zones around the gable roof low-rise building, where the grid sizes are adopted with respect to the building height. It was found that the pressure coefficient achieved a good accuracy for 90% of monitored probe points compared to the experimental test data, while the rest of the probe points, mainly the ones located at edges, showed numerical predictions lower than the experimental by 30%. Yan and Li [60] verified the accurate estimations of wind effects on the tall building when a very fine mesh is utilized, where the grid size near the building of interest was B/200 along the surface and B/2000 in the perpendicular direction to the surface, where B is the shortest side of the building. Additionally, the AIJ building code (2017) presented a recommendation for mesh generation when employing LES in numerical wind engineering. The guidelines recommended a fine grid with a size of B/100 in the horizontal direction. Aboshosha et al. [39] tested two grid sizes adjacent to the target building corresponding to B/10 and B/15, where B is the shortest side of the building. They found no significant deviation between the two simulations, and the numerical simulations showed good agreement with the experimental tests regarding wind pressure prediction. In LES, various refinement zone arrangements have been utilized in previous studies to capture the crucial aerodynamic wind phenomena. The grid refinement's zones can be located between the inlet and around the building of interest, while others are found to be extended from the inlet to the outlet and from the building to the symmetry boundary conditions. Previous studies have grid refinement zone arrangements within the computational domain to enhance the accuracy of capturing wind load on low-rise buildings without correlating the specific scheme to the accuracy of numerical wind load evaluation. Huang et al. [61], Al-Masoodi et al. [62], Chen et al. [63], and Ben Mou et al. [64] have introduced a refinement zone extended from the inlet to the outlet and another from the building to the symmetry boundary conditions. Another study conducted by Marie et al. [65] aimed to evaluate wind load on tall buildings has adopted six refinement zones. All the refinement zones were located between the inlet and around the target building, where each zone had a slightly lower width than the other.

Previous studies, such as Ong and Patruno [66], have used refinement zones extended from the inlet and around the target building and two grid refinement zones around the building. Aly et al. [47] have utilized refinement zones that adapted to the gable roof low-rise building located at an oblique wind angle of attack. The refinement zones were extended parallelly from each side wall of the study building to the inlet, outlet, and symmetry boundary conditions. All the above studies have adopted a hexahedral grid shape, while studies such as Nourhan et al. [67], Biswas et al. [68], Lou and Kim [69] have adopted a tetrahedral grid shape to evaluate wind pressure on the low-rise building facade. Based on this discussion, it can be noticed that there is a vast variation in the adopted relative grade size, grid scheme, and grid shape, which will consequently affect the accuracy and the computational cost of simulations. Accordingly, there is a need to specify the required grid details that can fulfill both the accuracy and the computational affordability requirements.

3.1.5. Study Objectives

In light of the above-mentioned discussion, the objective of this study aims to estimate and correlate the effective parameters controlling the accuracy of wind pressure evaluation on a low-rise building based on comparing wind pressures (i.e., mean and RMS) to wind tunnel results conducted by Ho et al. [70]. This study aims to systematically define the required CFD details to produce accurate ABL flows with Large Eddy Simulation (LES) models. It includes a discussion about the efficient selection of turbulence maximum frequency (f_{max}) used as an input in the turbulence flow generator concerning grid size in the refinement zones that can accurately capture the pressure fluctuation induced on the building façade. Furthermore, this study aims to examine the current code of practice for selecting the computational domain size (CD) by examining multiple models independently using computational domain sizes that vary in length, width, and height and correlating that to the relevant building dimensions. Computational domain discretization is also examined, and the pressure parameters were utilized to correlate the efficient grid in terms of size, scheme, and shape with accurate wind load evaluation. The findings will be based on a quantitative assessment of the aerodynamic parameters, such as mean and fluctuating pressure for critical flow separation locations on the roof, which are crucial for resilient wind design.

The current study is divided into seven sections. Section 1 (this section) was divided into four subsections where the main motive behind this study was stated. In addition, it examined the relationship between the maximum frequency and the size of the computational domain grid refinement zones. Moreover, the section sheds light on the current code of practice in selecting computational domain size and spatial discretization is examined. Section 2 provides a detailed description of the utilized study model and the validation of the pressure parameter readings by comparing them to the experimental wind tunnel test. Section 3 presents the overall methodology framework that is undertaken throughout the study, which includes a full description of the numerical models simulated and the technique followed to examine the model's accuracy of wind load evaluation. The following section, section 4, examines models that adopt a range of maximum turbulence frequency (f_{max}) in the turbulence generator. The models are compared using the generated wind profile (i.e., mean velocity, turbulence intensity, longitudinal spectra) at the inlet location and building location (empty domain study). Section 5 examines the computational domain dimensions (length, width, and height) and presents findings based on comparing pressure parameters with wind tunnel tests. Similarly, section 6 examines the impact of computational discretization on pressure evaluation in terms of grid size, scheme, and shape. Section 7 summarizes and concludes the findings of this study by highlighting the correlation between the maximum turbulence frequency (f_{max}) used as input in the turbulence inflow generator with the grid refinements utilized. Besides, the most efficient computational domain size and discretization in terms of the grid size, scheme, and shape in accurately evaluating wind load on low-rise buildings.

3.2. Numerical Model Validation

This section presents the numerical model validation for the flow aerodynamics and pressure reading across the roof of a low-rise building. To validate the turbulence content in the flow and to ensure horizontal homogeneity, two models (including an empty domain study) are performed where the flow characteristics, such as mean velocity, turbulence intensity, and velocity spectra, are examined. The CFD model for this study is validated with the experimental testing performed in the Boundary Layer Wind Tunnel II at the University of Western Ontario (UWO) by Ho et al. [70]. Consequently, the validated CFD model will be used as a benchmark for assessing the efficiency of CFD characteristics. A gable roof low-rise building with a roof slope of $1:12$ and footprint dimensions of 38.1×24.4 m^2 with a roof total height of $13.2\ m$ in full-scale is utilized in the validation of the numerical model. The validation is conducted by comparing the mean and RMS of pressure coefficient values for the 12 taps located across the gable roof, as presented in Fig. 3.3. The mean velocity and turbulence intensity profiles are generated to match an open-terrain exposure with a roughness height, z_o, of $30\ mm$ (in the full scale) with a reference velocity of $37.6\ m/s$ at a reference height of 10 m in full-scale. The current model is set to match the wind tunnel experimental model adopted at a length scale and timescale of $1:100$ and $1:25$, respectively.

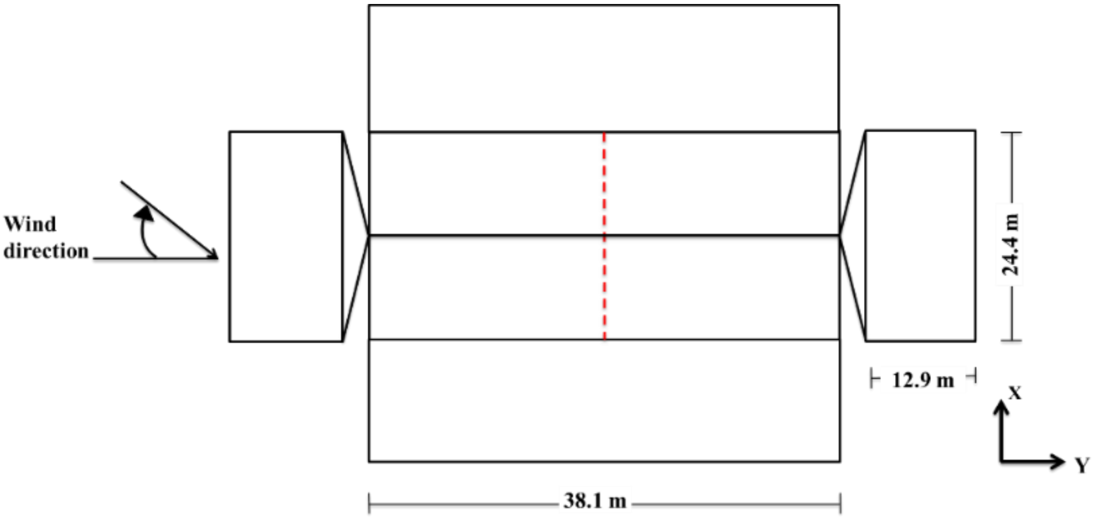

Fig. 3.3 Exploded view of the study model building with a gable roof slope of 1:12 and the location of test probes (12 probes in total).

The equations proposed and published by the Engineering Sciences Data Unit (ESDU) are followed in this study to compare vertical profiles for mean velocity and turbulence intensity [71,72]. This study's velocity and intensity profiles agree with the wind tunnel experimental data using the Power Law (i.e., Eq. 2) for the mean wind velocity. The $\overline{U}_{10}$ refers to the wind velocity at 10 m height with a value of $37.6\ m/s$. The z refers to the height in meters corresponding to the reference wind velocity, while the terrain roughness for open exposure ($1/\alpha$) is 0.13, as employed by Ho et al. (2005). The turbulence intensity is calculated for the target profile using the equation below (Eq. 3).

$$U_z = \overline{U}_{10}\left(\frac{z}{10}\right)^{1/\alpha} \tag{2}$$

$$I_u = c_u\left(\frac{z_{ref}}{z}\right)^{bu} \tag{3}$$

To ensure the accuracy of numerical results, it is essential to validate and verify relevant models [73]. To validate the numerical model, STAR-CCM+ 2020.2 (15.04.008-R8) is employed where Large Eddy Simulation (LES) is utilized to conduct the numerical wind load evaluation. A computational domain of dimensions of 3.4 m × 2.5 m × 0.7 m (in model scale) is used, as shown in Fig. 3.4. The boundary conditions at the top and side surfaces of the computational study domain are set as symmetry plane boundary conditions. The ground and building surfaces are defined as a non-slip wall boundary condition, while the outlet surface is defined as an outflow. Consistent discrete random flow generation (CDRFG) is utilized to generate the inflow [39]. The inlet wall is defined as a time-varying inlet velocity boundary condition using the CDRFG technique described by Aboshosha et al. and later adopted by Elshaer et al. [12,39]. The building is placed 0.8 m away from the inlet; hence, pressure data collection started after 800 time steps to ensure flow stabilization. The Reynolds number (Re) utilized in the CFD is calculated using $U_H H/\nu$, whee the viscosity, v, is $1.3 \times 10^{-5}\ m/s^2$. Accurate near-wall modeling is crucial for CFD simulation because the solution gradients are high in a wall-bounded flow; thus, y+ values are considered to find the most suitable first cell height from the adjacent wall for a value less than 5 [74].

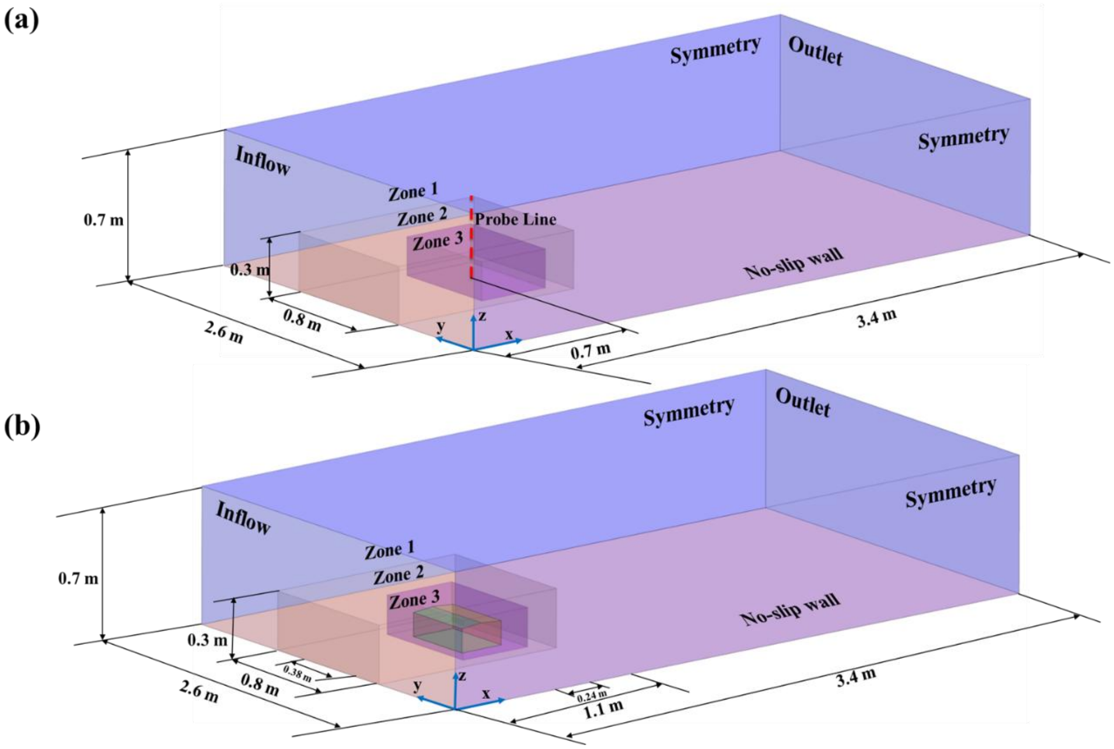

Fig. 3.4 Computational domain dimensions (in model-scale) and boundary conditions (a) an empty computational domain (b) study building in the computational domain.

The computational domain is discretized into three zones using hexahedral mesh cells. Zone 1 adopted a base mesh size of 15 mm, while 8.0 mm and 6.0 mm for zones 2 and 3, respectively, which yielded 1.45 M of the total mesh cells, as presented in Fig. 3.5. The sub-grid model WALE is utilized as it is found by previous studies to reduce the computational time by about 35 to 60% compared to other SGS models without affecting the accuracy of the simulation [75–77]. This is due to its ability to correctly model the asymptotic behaviour of turbulent eddy-viscosity near the walls and generate ABL flow with accuracy comparable to LES with the dynamic one-equation SGS model [76]. The mean wind velocity and turbulence intensity profiles adopted in the wind tunnel experiment compared to numerical profiles showed good agreement with wind tunnel data presented in Fig. 3.6. Moreover, the latter figure demonstrates a good agreement for the longitudinal spectra for open terrain at 9.75 m height (full scale) when compared with the ESDU (47031) and the validation wind tunnel data. Additionally, Fig. 3.6(c) indicates the ability to simulate ABL flow in an empty domain as an indication of the horizontal homogeneity in the vertical profiles of mean velocity and turbulence intensity at the building location.

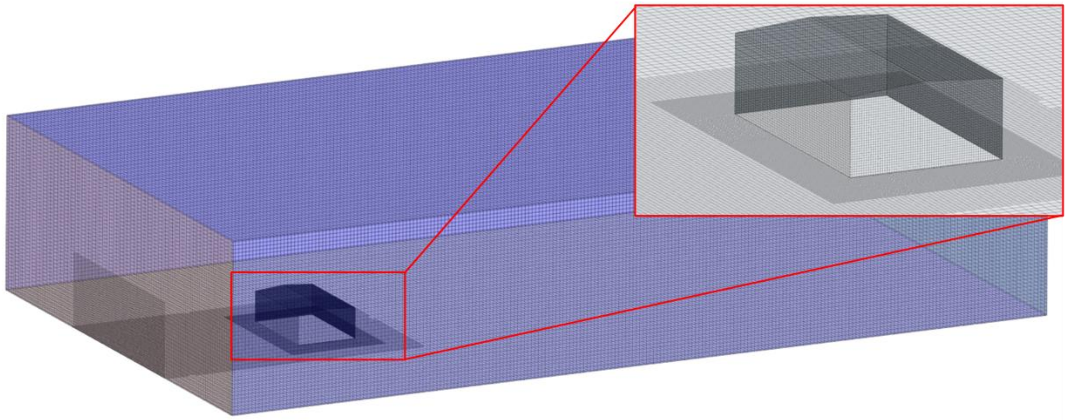

Fig. 3.5 Mesh discretization of the validation model.

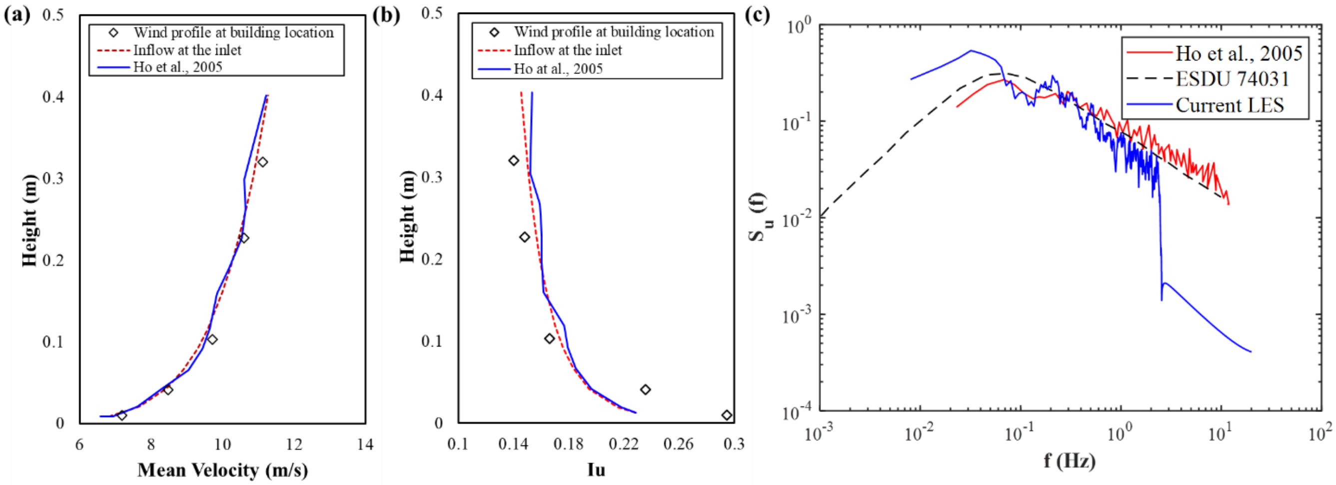

Fig. 3.6 (a) Mean velocity profile and (b) Turbulence intensity profile (c) Longitudinal wind spectra at 9.75 m (full scale) above ground.

The simulation duration is 8.0 seconds (in model scale) with a time-step of 0.5 milli-seconds with total time-steps of 16,000. The total sampling duration chosen was adequate for obtaining sufficiently accurate numerical results that balances the relationship between computational accuracy and efficiency. Similar approach was used by Zhixiang Liu et al. [78]. The time step is selected based on the velocity scale and the minimum cell size to satisfy the Courant-Friederichs-Lewy (CFL) number to be below unity to ensure the solution convergence (see Eq. (1)) [59]. As for the reference pressure used to calculate Cp, a probe point is placed in the domain at the midpoint of the inlet before the building at the height of 0.48 m (model scale). After running the validation model, the mean and RMS of the pressure coefficient across the ridgeline are compared to the wind tunnel test, as shown in Fig. 3.7(a) and Fig. 3.7(b**)**, respectively. The validation model results show a good agreement between the reading numerical and experimental pressure parameters, where the mean Cp results showed root mean square error (i.e., RMSE, defined in Section 4. Eq. (4)) of 1.65 %. In contrast, the pressure fluctuations showed a 4.3 % difference when compared to the experimentally obtained data.

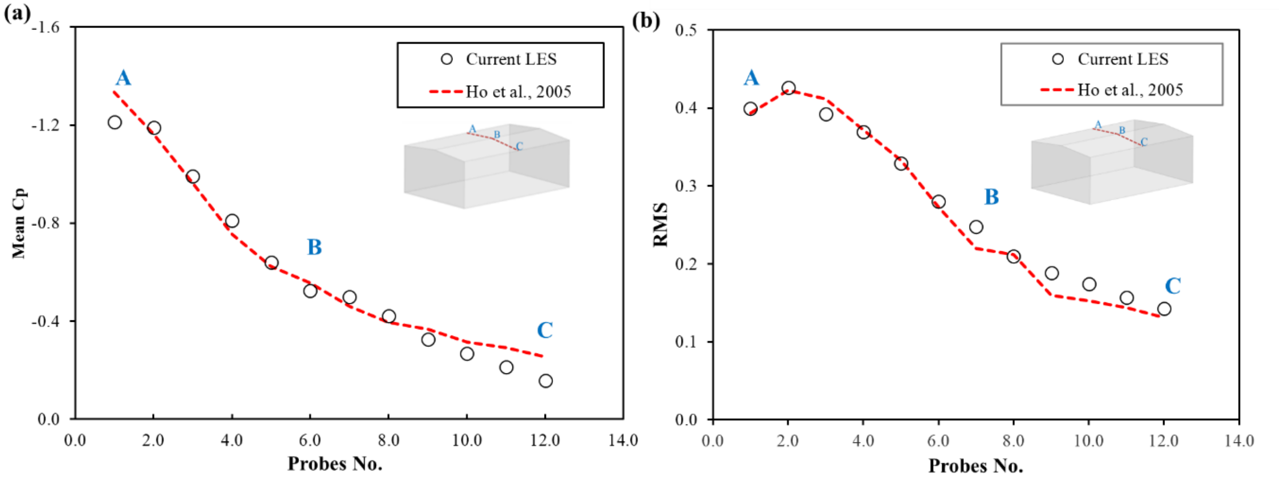

Fig. 3.7 (a) Mean and (b) RMS of the pressure for probes located at the building roof.

3.3. Methodology Framework

Structured analysis is conducted based on the validated LES model by systematically varying a single parameter and evaluating the discrepancies in computational wind load compared to the wind tunnel test. The examined parameters include the maximum frequency resolved by the grid employed in LES, the computational domain size and computational domain discretization. The mean and RMS of the pressure coefficient (Cp) are extracted from the probes across the building roof, as shown in Fig. 3.8. The accuracy of the CFD model is examined by evaluating the Root Mean Square of Error (RMSE), as shown in Eq. (4).

$$RMSE = \sqrt{\frac{\Sigma\left(R_{Exp}-R_{LES}\right)^2}{n}} \tag{4}$$

Where R_{Exp} refers to pressure readings extracted from the experimental wind tunnel test, R_{LES} refers to pressure readings extracted from numerical simulation, and n is the number of readings.

Generally, in the benchmark model, the computational domain length (DL) and width (DW) are adopted with respect to the building length (L) with values of 6.5L and 3L, respectively. The study building location is at 1.6L from the inlet (i.e., 0.7 m remains unchanged throughout the study. The height of the domain (DH) is selected to be 6H based on the study building roof reference height (H). The computational domain size parameters examined in this study (i.e., DL, DW, and DH) are shown in Fig. 3.8.

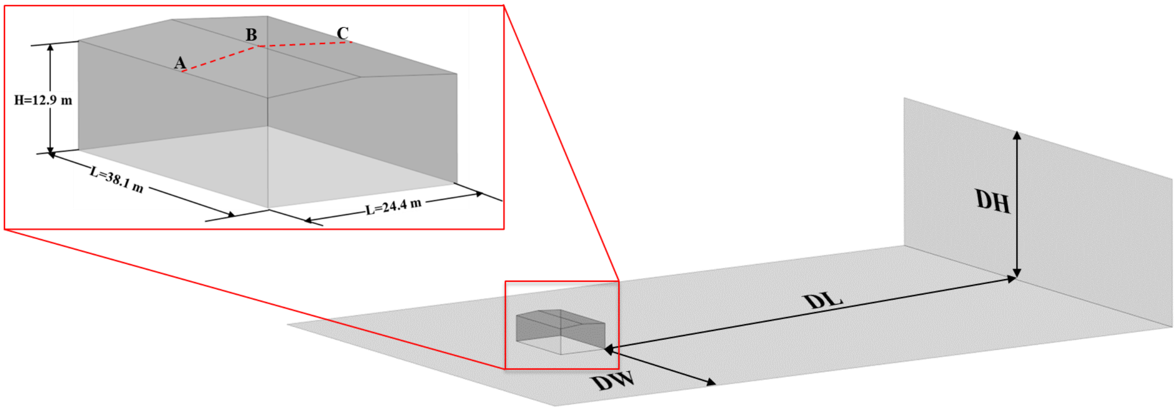

Fig. 3.8 The computational domain size parameters and probe's (12 in total) locations.

Throughout the study (unless stated otherwise), the computational domain spatial discretization utilized three grid refinement zones with the size selected based on the building roof reference height. The sizes of the grid refinement zones and their location for the benchmark model are listed in Table 3.2. As mentioned earlier, this study utilizes the turbulence inflow generator technique, based on synthesizing random divergent free turbulent velocities where the input parameters were modified to enforce the generated turbulent velocity components to match the properties required for the LES study. Generally, this study adopted a maximum frequency of 100 Hz input to generate the turbulent inflow mimicking the open terrain wind profile setup. The input data details for this study are utilized as input in the MATLAB code and are detailed in Table 3.3.

Table 3.2 Grid size and location within the computational domain

Zones	Mesh Count	Grid size
Zone1	515,625	$H/8$
Zone 2	718,920	$H/16$
Zone 3	221,666	$H/22$

The velocity information for each cell at the inlet is supplied using the CDRFG technique, as proposed by Aboshosha et al. [39]. For the benchmark model, the velocity profile produced corresponds to 9,728 cells at the inlet. The code is run for a sampling period corresponding to 8.0 seconds in the model-scale to generate the inflow velocity fluctuations. Fig. 3.9 below summarizes the individual cases conducted to find the efficient parameters in synthesizing turbulent wind pressure parameters on low-rise buildings.

Table 3.3 Parameters used to generate velocity field.

Parameters	Definition/Value
Exposure	Open terrain
Reference height	H=0.13m
Mean velocity U_{av}	$U_{av} = U_{avef}\left(\frac{z}{z_{ref}}\right)^{\alpha}$ $U_{avef} = 9.67\frac{m}{s}, z_{ref} = 0.13m, \alpha = 0.13$
Turbulence intensity	$I_j = k_{efj}\left(\frac{z}{z_{ref}}\right)^{-dj} \quad ,j = u, v, w$ $I_{refj} =$ 0.174, 0.153, 0.095 in the u, v, and w directions, respectively [79]
Von Karman turbulent spectra S_u, S_v, S_w	$S_u = \frac{4(I_u\, U_{av})^2(L_u/U_{av})}{(1 + 70.8(fL_u/U_{av})^2)^{5/6}}$ $S_v = \frac{4(I_u\, U_{av})^2(L_u/U_{av})(1 + 188.4(2fL_v/U_{av})^2)}{(1 + 70.8(2fL_v/U_{av})^2)^{11/6}}$ $S_w = \frac{4(I_v\, U_{av})^2(L_w/U_{av})(1 + 188.4(2fL_w/U_{av})^2)}{(1 + 70.8(2fL_w/U_{av})^2)^{11/6}}$ where $L_j = L_{refj}\left(\frac{z}{z_{refL}}\right)^{\varepsilon j}$ εj=0.593, 0.952, and 1.834 in the x, y, z directions respectively
Coherency function	$Coh(f_m) = \left(-\frac{C_j f_m d_{xj}}{U_{av}}\right)$, [80] where C_j is coherency decay constant

Number of frequency segments	nm= 50
Number of random frequencies	nf= 100
Number of time steps	nt= 6000
Time step	dt= 0.0005 seconds

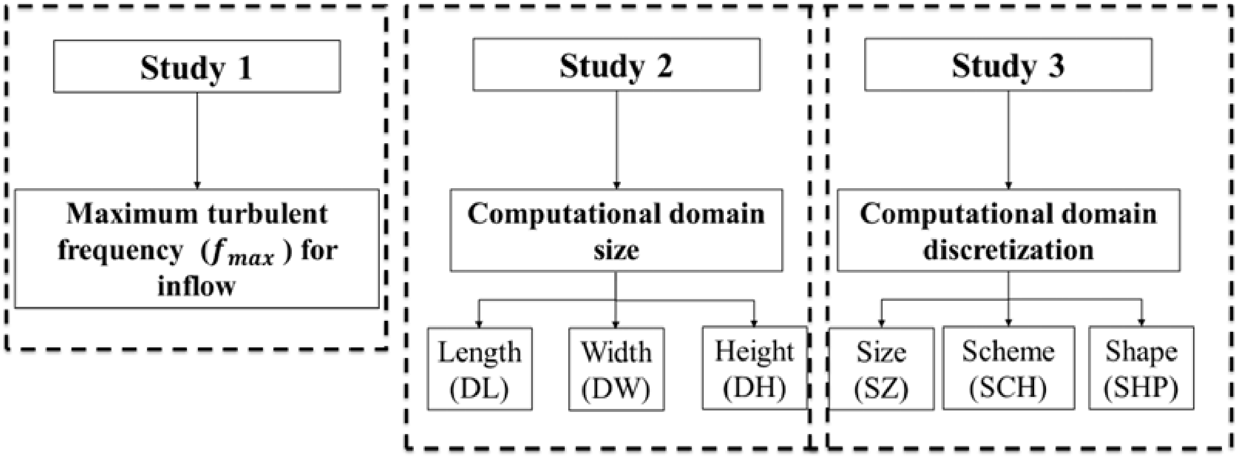

Fig. 3.9 A flow chart for the overall methodology employed in this study.

3.4. Maximum Turbulence Frequency

This section discusses the role of maximum frequency values used as an input to generate synthetic turbulent flow that mimics the atmospheric boundary layer. Nine numerical models are examined in this study, where the generic numerical model adopts identical computational domain size and spatial discretization. The inflow was generated using multiple values of f_{max}, to correlate the maximum frequency employed in the synthetic turbulence method to the turbulent energy resolved by the various grid sizes in the refinement zones (i.e., zone 2, which is extended from the inlet and around the building). The input values for the inflow generator for f_{max} ranges from 0.5, 1, 10, 25 to 100 Hz. Hence, f_{min}, is given by $2f_{max}/nm$ is equal to 0.02, 0.04, 0.4, 1.0, and 4.0 Hz, respectively.

The range of the values of the maximum frequencies is based on Melbourne [26] and Morrison and Kopp [28], where it was concluded that wind load is impacted when the small-scale turbulence is resolved up to a reduced frequency ranging from 10 and from 0.1 to 2.0, respectively. In other words, the maximum frequency expected to impact the wind load on low-rise buildings ranges from 0.3 to 30 Hz. Fig. 3.10 presents a comparison between numerical wind profiles generated at various maximum frequencies and the longitudinal spectrum generated at a height of 9.75m (full-scale) with the ones obtained from the experimental wind tunnel study and the measured ESDU formulation. The latter profiles are injected into the computational domain to simulate wind flow in an open terrain setup. It is worth mentioning that identical grid refinement zones are selected for all the examined cases for a consistent comparison and to demonstrate their efficacy in resolving large and small eddies velocity spectra. Overall, the velocity spectrum at the inlet complies with the experimental and ESDU formulation over the entire frequency range when the maximum input frequency in the turbulence generator ranges between 10 and 100 Hz.

The energy maintenance of capturing the wide range frequencies in the longitudinal spectrum is evidently correlated with the grid resolution and f_{max} the cut-off frequencies are found to increase with the increase of maximum frequency used in the turbulence generator. The latter is found to be caused by the increased energy of the streamwise velocity fluctuations [27]. Generally, it can be deduced that the maximum cut-off frequencies varied between 2 Hz and 6 Hz for numerical models adopted f_{max} of 10, 25, and 100 Hz, as an input in the turbulence generator. In contrast, the spectra profile at 9.75 m decreases for frequencies lower than 1.0 Hz, indicating that the energy is not maintained in the flow with frequencies below this range. Similar results were obtained by Yan and Li where power spectra density generated with the RFG method, drops compared to the ones with high frequencies, due to not satisfying the Von Karman spectrum [60]. To examine the computational discretization efficiency in resolving the turbulence flow generated, the wind flow profiles (i.e., mean velocity and turbulent intensity) at each corresponding height are computed from LES at the building location (i.e., at 0.7 m from the inlet in an empty domain), as shown in Fig. 3.10**.**

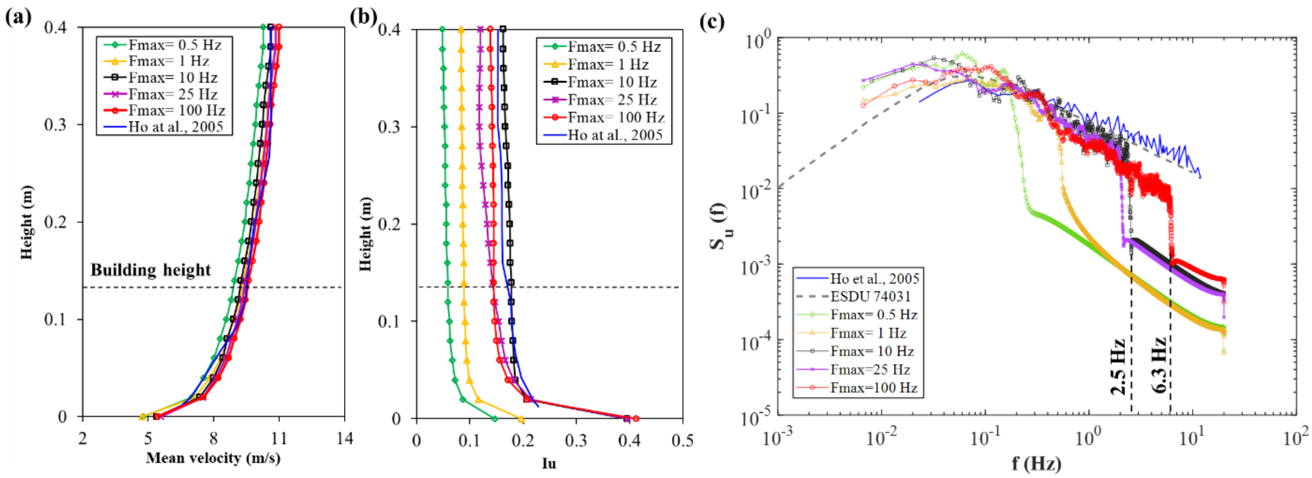

Fig. 3.10 Wind flow profiles at the inlet (a) Mean velocity, (b) Turbulence intensity, and (c) Longitudinal frequency spectrum at a height of 9.75m (full-scale).

Wind flow profiles for the probe line located at the building location in the computational domain undergo considerable evolution as the values of the maximum frequency increase. In other words, the turbulent intensity keeps growing from what is supplied at the inlet. A similar trend is observed for mean velocity profile cases. Broadly concluding, the LES cases with turbulence generated at frequencies higher than 25 Hz, show a good correlation between the experimental and numerical mean velocity and turbulence intensities. Besides, it can be noticed that the high-frequency end of the simulated velocity spectra possesses lower energy because of grid filtering. Moreover, upon using low f_{max}, we neglected (filtered) part of the turbulence magnitude, and therefore, the wind speed profiles injected at the inlet got adjusted to a smoother profile to reflect the lower turbulence intensity. Hence, it is crucial to precisely model the proper turbulence by selecting. f_{max} and grid size.

In light of the above, to resolve the spectral frequency at roof reference height, the following steps demonstrate guidance toward evaluating grid size that resolves specific frequencies and vice versa. In other words, the following steps can be utilized either to estimate the required mesh size Δx that resolves the turbulence up to the maximum frequency, f_{max} or to determine f_{max} that can be resolved by a pre-designed grid of size Δx. The steps are merely based on the size of the grid located in the grid refinement zone located between the building and around the target building. This maximum frequency is calculated based on the grid size of $H/16$ (i.e., zone 2) in the building height of H = 12.9 m, and UH = 37.6 m/s (full-scale). The grid size employed in zone 2 is chosen based on resolving the targeted cut-off frequency that impacts the wind load estimation on low-rise buildings as found by Melbourne [26] and Morrison and Kopp [28].

1. Define the minimum grid refinement size (Δx) concerning building height (H), for example $\left(\frac{H}{16}\right)$, precisely for the refinement zones extended from the inlet and around the study building.
2. Define the minimum wavelength that is required to be resolved based on the minimum grid size utilized around the bluff body; for example, if the minimum wavelength is $4\Delta x$, therefore grid size is given by $4 \times \frac{H}{16}$.
3. Evaluate the non-dimensional frequency that can be solved by LES denoted by f_{grid}, which resolves eddies with a wavelength of 4Δx by calculating $f_{grid} = \frac{H}{4\Delta x}$.
4. Evaluate the maximum dimensional frequency, $f_{max} = \frac{f_{grid} U_H}{H}$ where U_H is the mean velocity (m/s) in the full scale. The value of f_{max} represents the maximum frequency that will be captured by the employed grid refinement zones. This will result in $f_{max} = \frac{U_H}{4\Delta x}$.

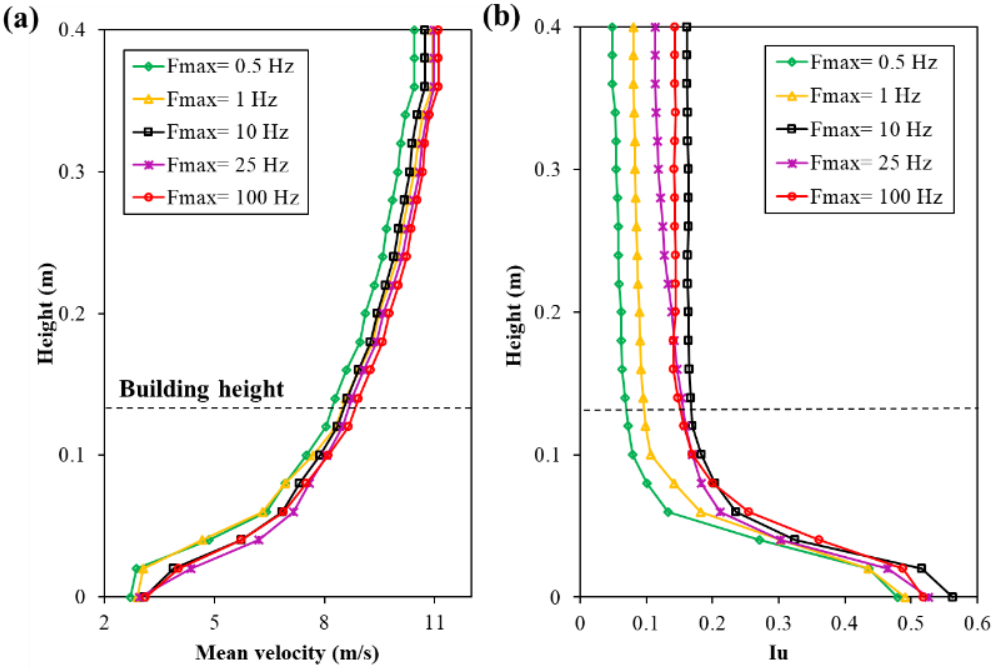

Fig. 3.11 Wind flow profiles at building location (Empty domain) (a) Mean velocity, (b) Turbulence intensity.

Overall, it is found that the minimum grid spacing Δx utilized in the computational domain (i.e., in zone 2) determines the highest non-dimensional frequency of the fluctuations transported by the grid (f_{grid}) from the inflow. In the study, the suggested highest frequency transported in the flow using LES was defined by $f_{grid} = H/4\Delta x$, where 4 Δx is the smallest wavelength resolved by the grid in the zone extending from the inlet and around the building. The velocity spectra agreement with ESDU formulation over the low-frequency part is very encouraging for the computation of the peak pressure on low-rise buildings in future studies using this numerical CFD model. A qualitative assessment presented in Fig. 3.12 shows that in models simulated using frequencies ranging between 25 Hz and 100 Hz, both the mean and pressure fluctuation on the roof were found to encounter minimal changes with a high degree of accuracy compared to the wind tunnel test. The RMSE recorded for the mean and pressure fluctuating were 3.1% and 2.6% for a model with a maximum frequency input of 100 Hz, respectively. In contrast, the mean pressure is found to be estimated with RMSE of >13%, while the pressure fluctuation error is found to be >8 when the utilized input values of F_{max} the turbulence generator was 0.5 Hz.

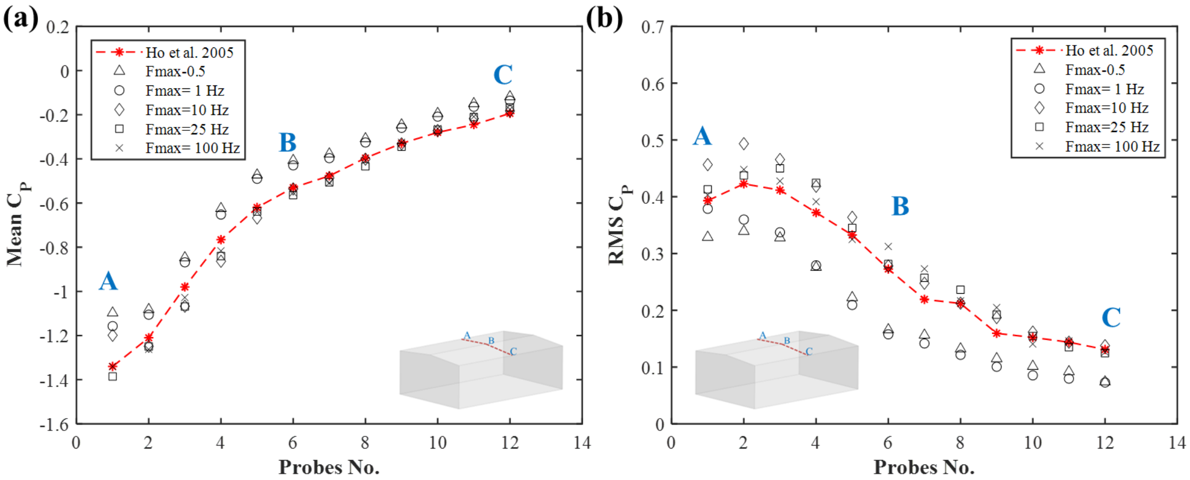

Fig. 3.12 (a) Mean and (b) RMS of the pressure coefficients for probe points across the roof examining a range of maximum turbulent frequencies.

3.5. Computational Domain Size

This section examines the computational domain lateral and vertical domain extensions to assess their impact on wind load evaluation on the walls and roofs of low-rise buildings by comparing the extracted pressure data to the experimental wind tunnel test. As mentioned earlier, the common practice in CFD to select the domain extension and width is based on the study building height, which may not be sufficient for the flow to fully develop and for the simulation to converge. It is merely based on the ratio between the model facade's frontal area and the computational domain's cross-section (i.e., blockage ratio). In CFD, a maximum blockage of 3% is recommended. In contrast, Franke et al. [21] suggested that the minimum distance equals 5 times the height (H) between the building and boundary conditions and 15 H between the building and the outlet to avoid interference of the domain size on the numerical simulation results. These guidelines can jeopardize the efficacy of CFD in wind load evaluation, particularly for low-rise buildings. Apart from the upstream length, which is selected to be two times the building length, the investigated computational domain size considered the downstream, side and upper distances. The examined computational domain length (DL) and the domain width (DW) are selected based on the study model length (L). In contrast, the computational domain height (DH) is selected based on the building height (H). The numerical models examined in this section are termed by 3 parts. The first part of the term is denoted by CD, symbolizing the computational domain study. The second part reflects the examined domain parameter (i.e., DL, DW, and DH), while the third part is the computational domain value being examined. Both second and third terms will vary depending on the model tested. In other words, the name code has the abbreviation of CD-D**X**-**Y**L or CD-D**X**-**Y**H, where **X** denotes the type of study in which it could be either L, W or H, while **Y** is the value of the computational domain study parameter.

3.5.1. Computational Domain Length Study

This subsection discusses the impact of computational domain length on the numerical wind load evaluation based on comparing the mean and RMS of the pressure concerning the experimental wind tunnel test. As mentioned earlier, the pressure parameters are extracted from probes located at the center section of the roof and across the ridgeline, where wind flow separation is recognized to be at its highest magnitude. The dimensions of the numerical model tested in this study are listed in Table 3.4. Since the study building is at a fixed location throughout the study, the domain length (DL) changes only involve the region behind (wake) the model. To begin with this inquiry in the search for the most efficient computational domain size that produces a high-accuracy solution without the need to expand it to unnecessary size, which may later impact the computational cost, the computational domain length is examined. The study adopted computational domain length ranging from 5L to 8L, knowing that the current practice recommended the CD extension to be not less than 15H (i.e., 5L) for a single study model. As can be observed from Fig. 3.13, although the minimum downstream current code of practice (i.e., CD-DL-5L) has yielded a good agreement of RMS of pressure compared to the wind tunnel test, the mean pressure values deviated explicitly at the leading roof and separation locations. In fact, the RMSE of the mean pressure is found to be

10%. The latter error is probably because the flow in the wake zone (i.e., behind the building) did not develop fully. On the other hand, all the other models with domain lengths ranging from 6.5-8L have yielded stable good agreement for both mean and pressure fluctuation with RMSE recorded of 5% and 3%, respectively.

Table 3.4 Computational domain (CD) study models with different lengths

Model	**Length**	**Width**	**Height**
CD-DL-5L	5L	3L	6H
CD-DL-6.5L	6.5L	3L	6H
CD-DL-7L	7L	3L	6H
CD-DL-8L	8L	3L	6H

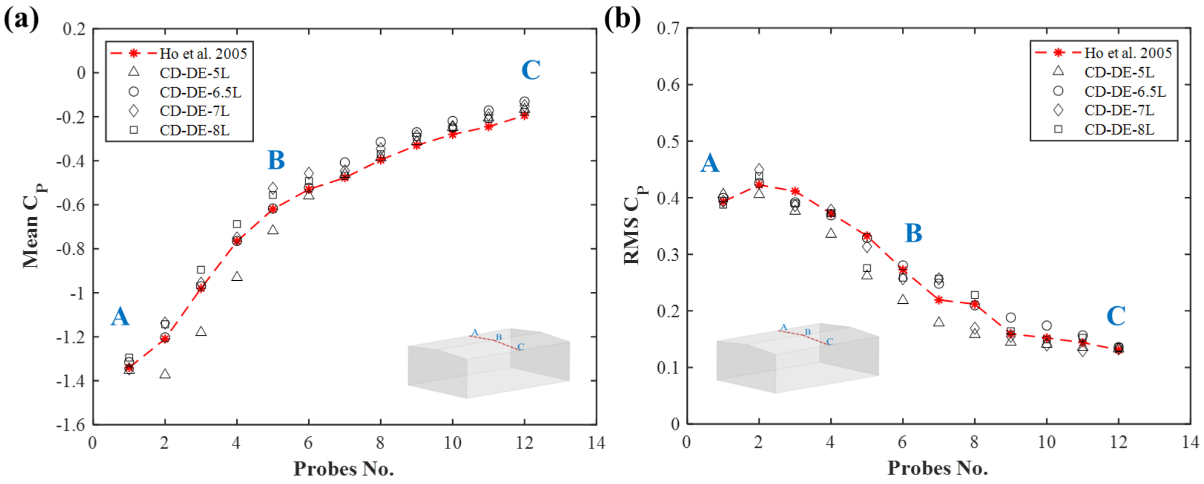

Fig. 3.13 (a) Mean and (b) RMS of the pressure coefficients for probe points across the roof examining the computational domain extension.

3.5.2. Computational Domain Width Study

The computational width in this study is examined using two scenarios. The first scenario is accomplished by locating the study building at a 270° wind angle of attack, while the second scenario considers the impact of the study building located at an oblique wind angle of attack (i.e., 315°). It is worth noting that with the change in the domain width, the values of the inlet coordinates are subsequently changed. Therefore, the inflow turbulence has been generated individually for the numerical models listed in Table 3.4 while adopting identical inflow parameters. For the first scenario, Fig. 3.14 indicates a relatively high error for both mean and RMS pressure values, particularly at separation locations when the CD width is equal to building length (i.e., CD-DW-L) and is equal to the minimum requirement by the current code of practice (i.e., CD-DW-1.7L). The discrepancy in the mean pressure is higher than 8% for a domain width of 1.7L compared to a 1.5% error for a domain width of 3L. In contrast, the models with a width of 1.7L led to an error in the mean pressure readings that reached 22% compared to 4% for the model with a width of 3L.

Table 3.5 Computational domain (CD) study models with different widths

Model	Length	Width	Height
CD-DW-L	6.5L	L	6H
CD-DW-1.7	6.5L	1.7L	6H
CD-DW-2L	6.5L	2L	6H
CD-DW-3L	6.5L	3L	6H

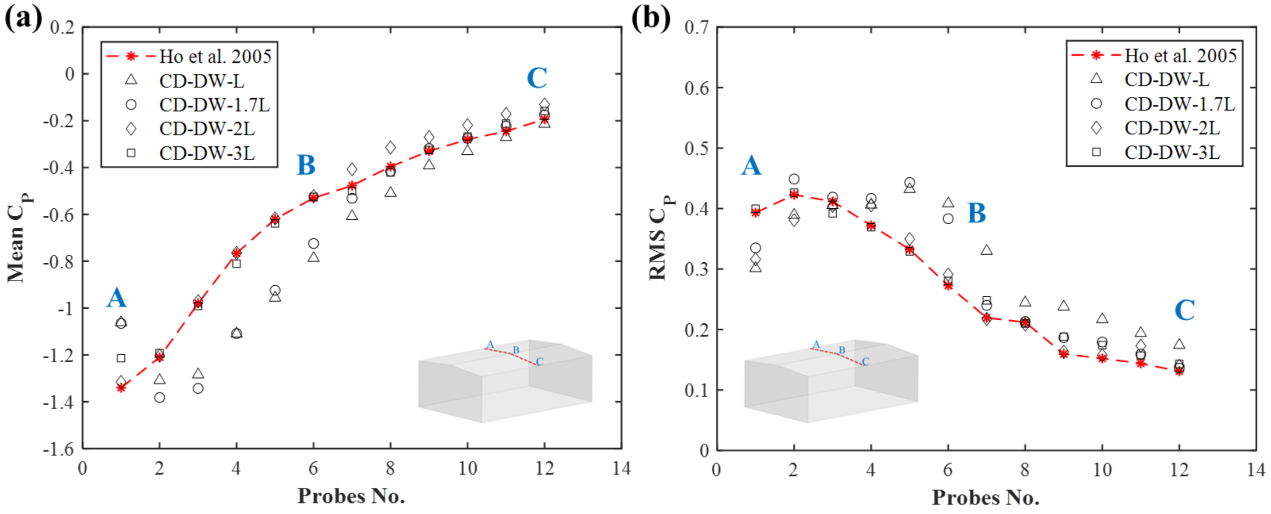

Fig. 3.14 (a) Mean and (b) RMS of the pressure coefficients for probe points across the roof examining the computational domain width for the building located at 270°.

The second scenario examines the computational width for the same study building located at a wind angle of attack of 315° where discrepancies are estimated with respect to the numerical model with a computational domain of 4L. Fig. 3.15 displays the pressure parameters (i.e., mean and RMS) for models with computational domain widths ranging from L to 4L. The mean and RMS of pressure produce high discrepancies compared to the benchmark model (i.e., CD-DW-4L). The model with a width of 1.7L (current code of practice) led to an overall substantial mean pressure RMSE of 9% compared to less than 3.5% for the model that adopted a width of 3L. The high RMSE is probably due to the insufficient distance between the symmetry boundary conditions and the building, which, therefore, impacted the convergence of the wind flow, as demonstrated in Fig. 3.16.

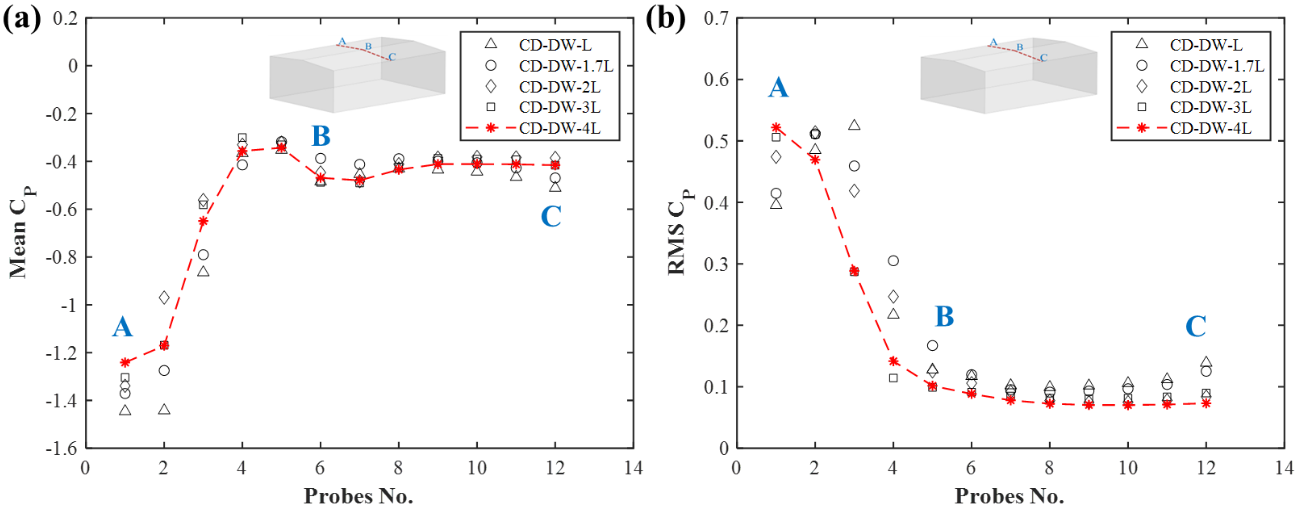

Fig. 3.15 (a) Mean and (b) RMS of the pressure coefficients for probe points across the roof examining the computational domain width for the building located at 315°.

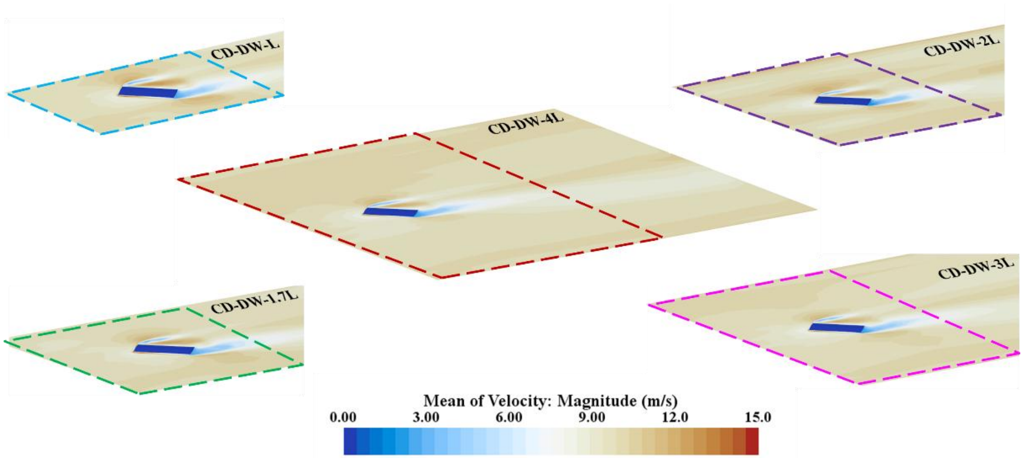

Fig. 3.16 Mean velocity contours for a building located at 315° for different computational domain width.

3.5.3. Computational Domain Height Study

For a single building, the height of the computational domain is recommended to be at least 5H (i.e., 5 times the building height). The latter recommendation is based on a blockage ratio of 3%. Four models are tested to study the required computational domain height, and the dimensions of the computational domain are listed in Table 3.6. The inflow generator is generated individually for each tested model, as changing the computational domain height alters the inlet coordinates required in the inflow generator. The mean velocity contours for the four examined models are illustrated in Fig. 3.17. In contrast, Fig. 3.18 displays the results that verify the current code of practice that examines the computational domain height by utilizing mean and RMS pressure values. It was found that employing a domain with a height higher than 6H led to producing RMS with an error of less than 2%, compared to 5% for models simulated at domain height <5H. Furthermore, the later models produced mean pressure values along the roof with discrepancies ranging between 10 and 13%. Overall, the recorded RMSE values were found to be of lower values for a computational domain height of 5H and above.

Table 3.6 Computational domain (CD) study models with different heights

Model	**Length**	**Width**	**Height**
CD-DH-4H	6.5L	3L	4H
CD-DH-5H	6.5L	3L	5H
CD-DH-6H	6.5L	3L	6H
CD-DH-7H	6.5L	3L	7H

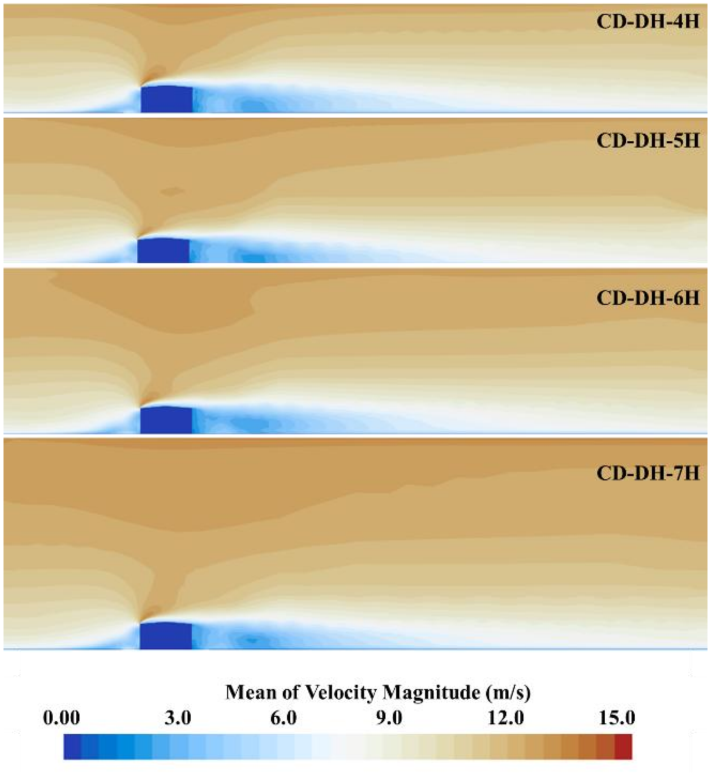

Fig. 3.17 Mean velocity contours for a building located at 270° for different computational domain heights.

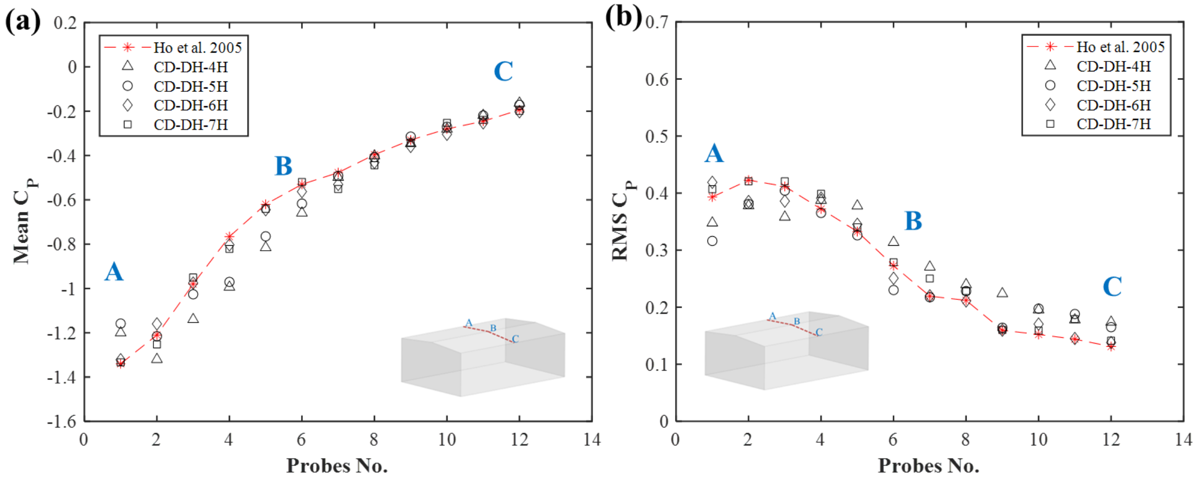

Fig. 3.18 (a) Mean and (b) RMS of the pressure coefficients for probe points across the roof examining the height of the computational domain.

3.6. Computational Domain Discretization

The adopted computational domain discretization is also known to have a significant impact not only on the accuracy of the inflow generation but also its impact extends to precision in resolving the turbulence through the computational domain; hence, it signifyingly influences the accuracy of the wind load on buildings. This section will include examining the grid scheme (SCH), size (SZ), and shape (SHP) adopted. Both grid schemes and shapes are selected based on the most commonly used in previous studies, as mentioned in the literature review. The inflow for models with various grid schemes and sizes is generated for each case separately, as the inlet coordinates for the grid vary from one model to another. As a result, three independent studies were conducted, where the mean and fluctuation of the pressure were used to evaluate the discrepancies by comparing them to the experimental test.

3.6.1. Computational domain grid size study

The grid sizes for the refinement zones employed in the study for four models are demonstrated in Table 3.7. It is worth mentioning that the model donated by CD-GSZ-3 adopted an identical mesh refinement zone as the validated study model. To examine the discrepancies in the computational wind load evaluation triggered by domain discretization, RMSE calculations were evaluated relative to the experimental values. Upon examining the computational domain grid size for the four models employed, a high discrepancy in the mean pressure is estimated with an error of 12% when a coarse grid is utilized (i.e., CD-GSZ-1) as shown in Fig. 3.19 . In contrast, less than 4%

error was found when the grid size for the same refinement zones was refined (i.e., CD-GSZ-3 and CD-GSZ-4). Besides, the pressure fluctuation shows a good agreement with the experimental wind tunnel test, where discrepancies were below 3% for models that adopted a fine refinement grid around the study building (i.e., CD-GSZ-2,3, and 4).

Table 3.7 Computational domain discretization for refinement zones

Numerical model	Zone 1	Zone 2	Zone 3	Total number of mech cells
CD-GSZ-1	H/6	H/11	H/15	580,000
CD-GSZ-2	H/7	H/14	H/18	930,000
CD-GSZ-3	H/8	H/16	H/22	1,450,000
CD-GSZ-4	H/10	H/22	H/30	2,500,000

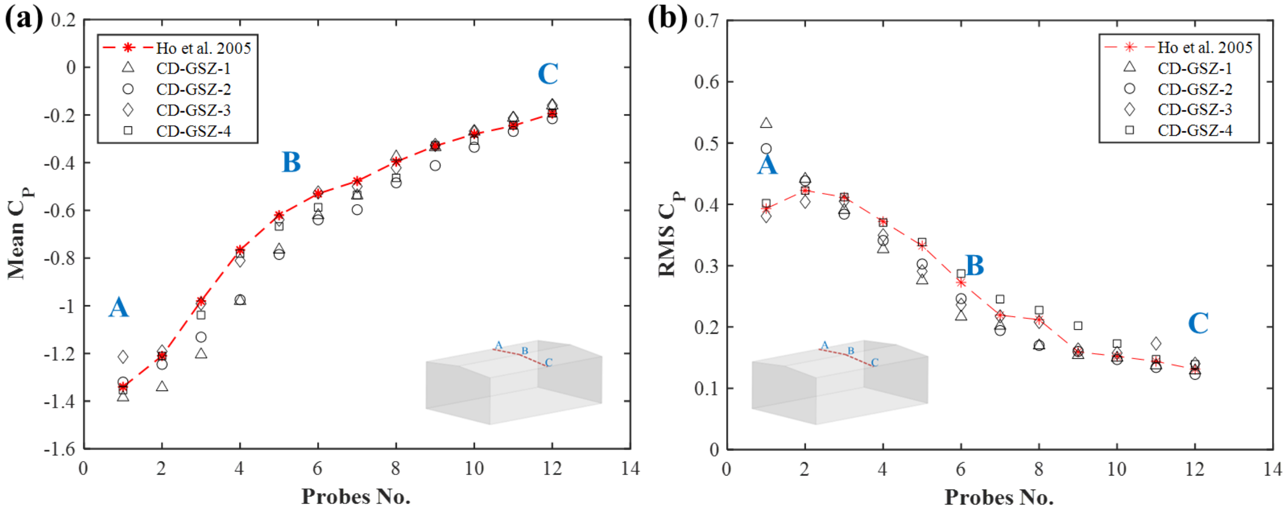

Fig. 3.19 (a) Mean and (b) RMS of the pressure coefficients for probe points across the roof examining the size of the computational domain discretization.

3.6.2. Computational Domain Grid Scheme Study

The location of the refinement zones within the computational domain is crucial in capturing the vital flow characteristic. Fig. 3.20 shows the four grid schemes examined in this study, where the results can signify the efficient scheme in wind load evaluation. It can be noted from Fig. 3.21 that both grid schemes 2 and 4 (i.e., CD-GSCH-2 and CD-GSCH-4) displayed high accuracy for the mean and RMS of the pressure when compared to the wind tunnel test. The later models have recorded discrepancies (i.e., RMSE) for the mean and RMS of the pressure values lower than 4% and 2%, respectively. This is probably attributed to the fact that these grid schemes introduce refined mesh zones in the crucial areas around the building of interest. The latter secured the accurate capturing of the shear layer and the vortices around and in the wake of the target building; therefore, they were sufficiently resolved. This is probably attributed to the fact that these grid schemes introduce the refinement zones where vital wind characteristics are captured within crucial areas around the study building.

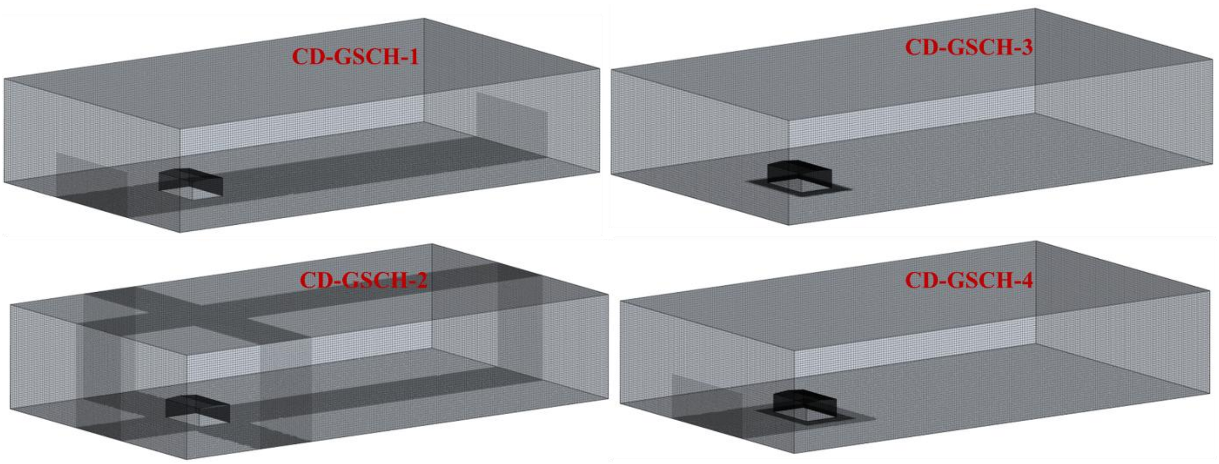

Fig. 3.20 Computational domain discretization schemes examined in this study.

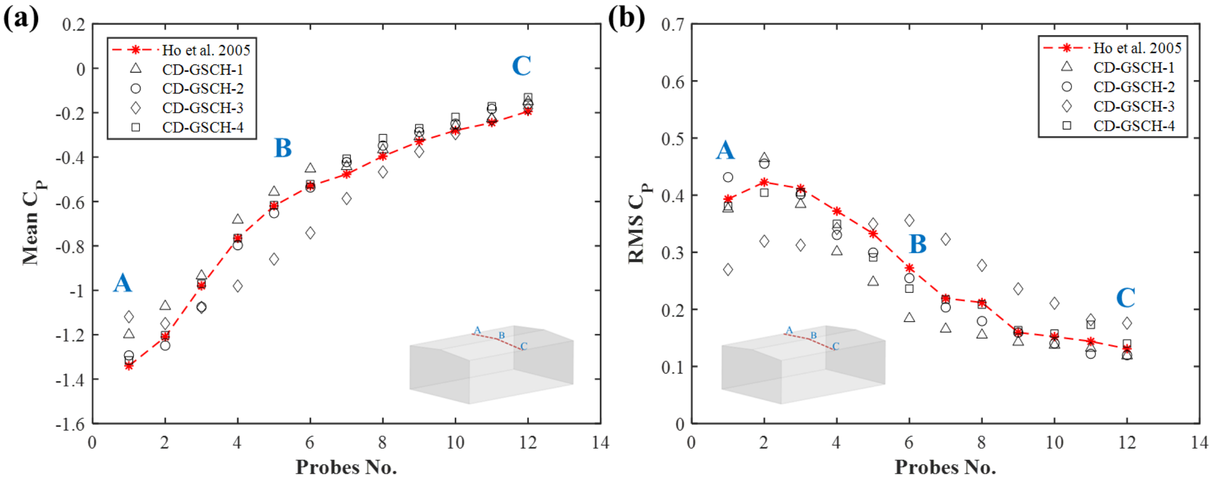

Fig. 3.21 (a) Mean and (b) RMS of the pressure coefficients for probe points across the roof examining the scheme employed in refinement zones.

3.6.3. Computational Domain Grid Shape Study

To examine the impact of the grid shape on the wind load computational evaluation, three common shapes of grid cells are assessed in this study: tetrahedral, hexahedral, and polyhedral, as shown in Fig. 3.22. Fig. 3.23 shows that using a tetrahedral mesh shape to discretize the entire domain resulted in a significant error of 11-14 % compared to 2 and 3% when using a hexahedral grid shape for both mean and pressure fluctuation on the roof, respectively. This is due to the large skewness of its grid cells and the presence of multiple edges [68]. This highlights the fact that the tetrahedral grid is deficient in accurately resolving the flow field within the computational domain. The latter is in line with the study presented by Hirsch et al. [81] and Wang et al. [82], where it was found that when the mesh shape hexahedral is employed for the computational grid, it will introduce minor truncation errors compared to the tetrahedral, as the former is known to display better iterative convergence. Hexahedral ability to refine the mesh makes a tremendous difference when directional flow features are present. Overall, polyhedral grid cells are found to produce results close to that of the hexahedral grid, and more accurate than that of the tetrahedral grid. This is because the grid lines of polyhedral cells have better orthogonality to the wall compared to tetrahedral [82].

The mean pressure is found to be overestimated at the separation locations, leading to an RMSE of 10% when a polyhedral grid is employed compared to the experimental wind tunnel test. It is noted that model discretizing using polyhedral requires approximately double the storage and CPU time in creating the mesh continuum than hexahedral. Hence, considering both the accuracy of wind load evaluation and the computational time consumed, the hexahedral computational domain is found to be the most efficient grid shape. Therefore, it can be concluded that the advantages of hexahedral grid adaptation exceed both polyhedral and tetrahedral grid cells.

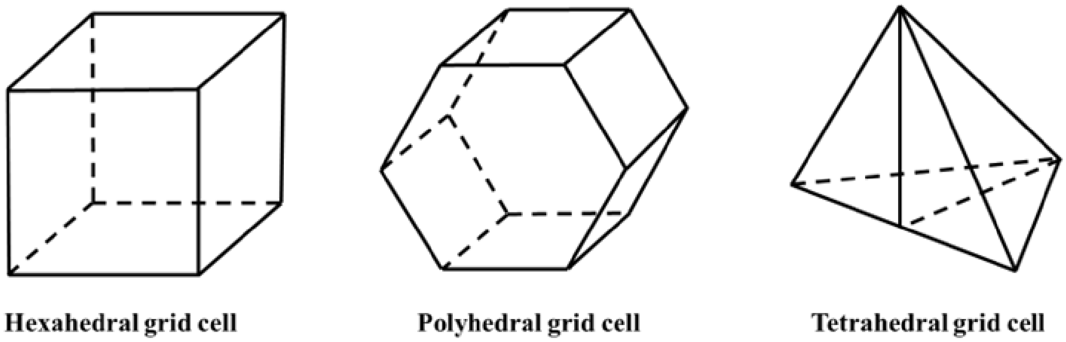

Fig. 3.22 Grid cell shapes examined in the study.

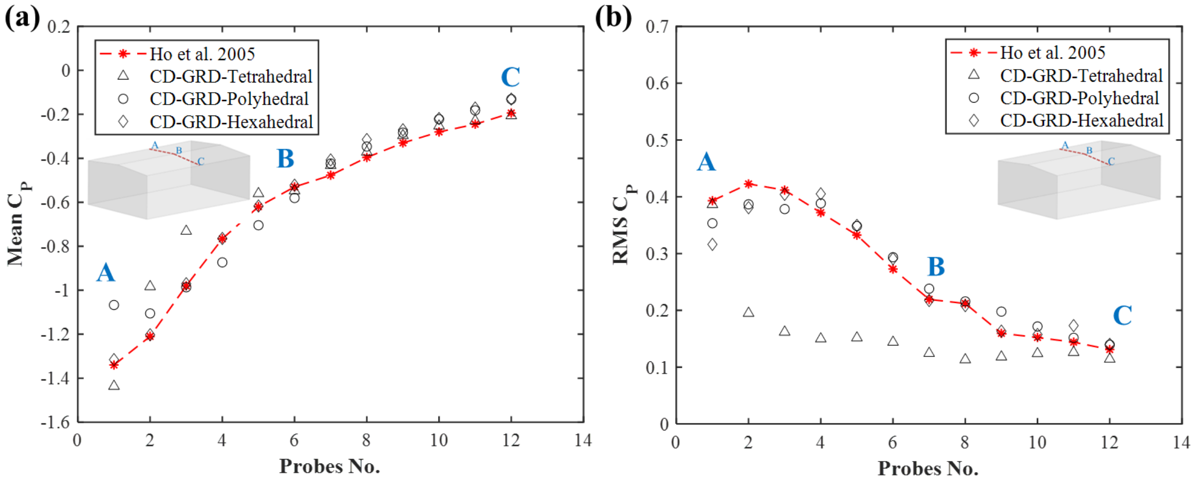

Fig. 3.23 Mean and RMS of the pressure coefficients for probe points across the roof examining the shape of the grid employed in the refinement zones.

3.7. Summary and Conclusion

This paper aims to enhance the accuracy of LES evaluation of wind load on low-rise buildings by efficiently defining the inflow synthesizing and computational domain specifications. Qualitative and quantitative assessments of flow parameters are performed on forty LES models by comparing them to wind tunnel tests. The simulation accuracy is assessed based on the value of the RMSE for the pressure readings (i.e., mean and RMS). The study investigates the relationship between the maximum turbulence frequency resolved by LES and the employed grid in the crucial refinement zones around the building model. Furthermore, this study examines the current code of practice impacting the selection of the computational domain size. Also, a study was performed to examine the computational domain grid discretization size selected based on the study model height and the most commonly used schemes for the grid refinement zones and grid shapes. The following findings are concluded.

I. The suitable maximum dimensional frequency used for inflow generation can be evaluated based on the grid size, building height and velocity at the reference height, $f_{max} = \frac{f_{grid}\, U_H}{H}$. By utilizing a computational domain with grid refinement zones with sizes ranging from $H/16$ to $H/22$, and f_{max} of 100 Hz, a minimum RMSE value was found for the mean and RMS of the pressure of 3% and 2%, respectively.

II. The current practice utilized to determine the minimum domain is found to slightly overestimate the mean pressure along the leading part of the roof, leading to an RMSE of 10% compared to 4.7% for models that adopted a domain length of over 6.5L.

III. The current code of practice recommended that the minimum computational domain width be 5H (i.e., 1.7L). However, this will lead to substantial discrepancies in the values of the mean pressure estimated by 21% compared to 4.7% when using a model with a computational domain of a width of 3L.

IV. The computational domain adopted a height greater than or equal $6H$ (i.e., CD-DH-6H and CD-DH-7H), found to result in minimum discrepancies when compared to the wind tunnel test. Mean and RMS pressure values yielded maximum RMSE of 3% and 1.8%, respectively.

V. The computational domain adopted fine grid size for the refinement zones around the building ranging from $H/10$, to $H/30$, which have led to minimum discrepancies when compared to the wind tunnel test for the mean and RMS of the pressure, which yielded 4% and 1.5%, respectively.

VI. The model adopted two grid refinement zones extended from the inlet and around the building and another located around the building (i.e., CD-GSCH-4), which is found to produce accurate pressure readings at both roof edges and across the ridgeline where the maximum RMSE is found to be maximum for the mean pressure at the value of 4.7%.

VII. The computational domain discretized with tetrahedral mesh shape produced the maximum error for the pressure reading on the roof by above 11% and 14% for mean and pressure fluctuation compared to 4% and 3% for the model discretized with hexahedra grid, respectively.

3.8. References

[1] Census, Census Topic: Housing, (2016). https://www12.statcan.gc.ca/census-recensement/2016/rt-td/hous-loge-eng.cfm.

[2] M. Hadavi, L. Sun, D. Romanic, Normalized insured losses caused by windstorms in Quebec and Ontario, Canada, in the period 2008–2021, Int. J. Disaster Risk Reduct. 80 (2022) 103222. https://doi.org/10.1016/J.IJDRR.2022.103222.

[3] P.R. Sparks, S.D. Schiff, T.A. Reinhold, Wind damage to envelopes of houses and consequent insurance losses, J. Wind Eng. Ind. Aerodyn. 53 (1994) 145–155. https://doi.org/10.1016/0167-6105(94)90023-X.

[4] R.N. Banks, D. and Meroney, A model of roof-top surface pressures produced by conical vortices: Evaluation and implications, Wind Struct. 4(4), p.2 (2001).

[5] H. Kawai, G. Nishimura, Characteristics of fluctuating suction and conical vortices on a flat roof in oblique flow, J. Wind Eng. Ind. Aerodyn. 60 (1996) 211–225. https://doi.org/10.1016/0167-6105(96)00035-9.

[6] D. Surry, J.X. Lin, The effect of surroundings and roof corner geometric modifications on roof pressures on low-rise buildings, J. Wind Eng. Ind. Aerodyn. 58 (1995) 113–138. https://doi.org/10.1016/0167-6105(95)00016-K.

[7] R. woo Kim, S. Woon Hong, I. bok Lee, K. Seok Kwon, Evaluation of wind pressure acting on multi-span greenhouses using CFD technique, Part 2: Application of the CFD model, Biosyst. Eng. 164 (2017) 257–280. https://doi.org/10.1016/J.BIOSYSTEMSENG.2017.09.011.

[8] A.M. Aly, G. Bitsuamlak, Aerodynamics of ground-mounted solar panels: Test model scale effects, J. Wind Eng. Ind. Aerodyn. 123 (2013) 250–260. https://doi.org/10.1016/J.JWEIA.2013.07.007.

[9] M. Abdelwahab, T. Ghazal, K. Nadeem, H. Aboshosha, A. Elshaer, Performance-based wind design for tall buildings: Review and comparative study, J. Build. Eng. 68 (2023) 106103. https://doi.org/10.1016/J.JOBE.2023.106103.

[10] K. Nozawa, T. Tamura, Large eddy simulation of the flow around a low-rise building immersed in a rough-wall turbulent boundary layer, J. Wind Eng. Ind. Aerodyn. 90 (2002) 1151–1162. https://doi.org/10.1016/S0167-6105(02)00228-3.

[11] T. Tamura, K. Nozawa, K. Kondo, AIJ guide for numerical prediction of wind loads on

buildings, J. Wind Eng. Ind. Aerodyn. 96 (2008) 1974–1984. https://doi.org/10.1016/J.JWEIA.2008.02.020.

[12] A. Elshaer, H. Aboshosha, G. Bitsuamlak, A. El Damatty, A. Dagnew, LES evaluation of wind-induced responses for an isolated and a surrounded tall building, Eng. Struct. 115 (2016) 179–195. https://doi.org/10.1016/J.ENGSTRUCT.2016.02.026.

[13] A. Elshaer, G. Bitsuamlak, H. Abdallah, Variation in wind load and flow of a low-rise building during progressive damage scenario, Wind Struct. An Int. J. 28 (2019) 389–404. https://doi.org/10.12989/WAS.2019.28.6.389.

[14] A.M. Aly, H. Gol-Zaroudi, A.M. Aly, G. Zaroudi, Peak pressures on low rise buildings: CFD with LES versus full scale and wind tunnel measurements, 30 (2020) 99–117. https://doi.org/10.12989/was.2020.30.1.099.

[15] R.H. Ong, L. Patruno, D. Yeo, Y. He, K.C.S. Kwok, Numerical simulation of wind-induced mean and peak pressures around a low-rise structure, Eng. Struct. 214 (2020) 110583. https://doi.org/10.1016/J.ENGSTRUCT.2020.110583.

[16] K. Wijesooriya, D. Mohotti, C.K. Lee, P. Mendis, A technical review of computational fluid dynamics (CFD) applications on wind design of tall buildings and structures: Past, present and future, J. Build. Eng. 74 (2023) 106828. https://doi.org/10.1016/J.JOBE.2023.106828.

[17] F. Xing, D. Mohotti, K. Chauhan, Study on localised wind pressure development in gable roof buildings having different roof pitches with experiments, RANS and LES simulation models, Build. Environ. 143 (2018) 240–257. https://doi.org/10.1016/J.BUILDENV.2018.07.026.

[18] C.S. Yuan, The Effect of Building Shape Modification on Wind Pressure Differences for Cross-Ventilation of a Low-Rise Building, Int. J. Vent. 6 (2007) 167–176. https://doi.org/10.1080/14733315.2007.11683775.

[19] J.O.P. Cheung, C.H. Liu, CFD simulations of natural ventilation behaviour in high-rise buildings in regular and staggered arrangements at various spacings, Energy Build. 43 (2011) 1149–1158. https://doi.org/10.1016/J.ENBUILD.2010.11.024.

[20] F. Ding, A. Kareem, J. Wan, Aerodynamic Tailoring of Structures Using Computational Fluid Dynamics, Https://Doi.Org/10.1080/10168664.2018.1522936. 29 (2019) 26–39. https://doi.org/10.1080/10168664.2018.1522936.

[21] J. Franke, A. Hellsten, H. Schlünzen, B. Carissimo, Best practice guideline for the CFD simulation of flows in the urban environment cost action 732 quality assurance and improvement of microscale meteorological models, (2007).

[22] L. Bruno, M.V. Salvetti, F. Ricciardelli, Benchmark on the Aerodynamics of a Rectangular 5:1 Cylinder: An overview after the first four years of activity, J. Wind Eng. Ind. Aerodyn. 126 (2014) 87–106. https://doi.org/10.1016/J.JWEIA.2014.01.005.

[23] A. Jafari, F. Ghanadi, M.J. Emes, M. Arjomandi, B.S. Cazzolato, Measurement of unsteady wind loads in a wind tunnel: Scaling of turbulence spectra, J. Wind Eng. Ind. Aerodyn. 193 (2019) 103955. https://doi.org/10.1016/J.JWEIA.2019.103955.

[24] H.W. Tieleman, Wind tunnel simulation of wind loading on low-rise structures: a review, J. Wind Eng. Ind. Aerodyn. 91 (2003) 1627–1649. https://doi.org/10.1016/J.JWEIA.2003.09.021.

[25] S. Li, Y. Liu, M. Li, W. Zeng, S. Gu, Y. Gao, The effect of turbulence intensity on the unsteady gust loading on a 5:1 rectangular cylinder, J. Wind Eng. Ind. Aerodyn. 225 (2022) 104994. https://doi.org/10.1016/J.JWEIA.2022.104994.

[26] W.H. Melbourne, Turbulence effects on maximum surface pressures-a mechanism and possibility of reduction, Zement-Kalk-Gips. 1 (1980) 541–551. https://doi.org/10.1016/B978-1-4832-8367-8.50055-3.

[27] M.J. Morrison, G.A. Kopp, Effects of turbulence intensity and scale on surface pressure fluctuations on the roof of a low-rise building in the atmospheric boundary layer, J. Wind Eng. Ind. Aerodyn. 183 (2018) 140–151. https://doi.org/10.1016/J.JWEIA.2018.10.017.

[28] M.J. Morrison, G.A. Kopp, Effects of turbulence intensity and scale on surface pressure fluctuations on the roof of a low-rise building in the atmospheric boundary layer, J. Wind Eng. Ind. Aerodyn. 183 (2018) 140–151.

[29] M. Asghari Mooneghi, R. Kargarmoakhar, Aerodynamic Mitigation and Shape Optimization of Buildings: Review, J. Build. Eng. 6 (2016) 225–235.

[30] H. Gol-Zaroudi, A.M. Aly, Open-jet boundary-layer processes for aerodynamic testing of low-rise buildings, Wind Struct. 25 (2017) 233–259. https://doi.org/10.12989/WAS.2017.25.3.233.

[31] R.H. Kraichnan, Diffusion by a random velocity field, Phys. Fluids. 13 (1970) 22–31. https://doi.org/10.1063/1.1692799.

[32] A. Li, G. Ahmadi, R.G. Bayer, M.A. Gaynes, Aerosol particle deposition in an obstructed turbulent duct flow, J. Aerosol Sci. 25 (1994) 91–112. https://doi.org/10.1016/0021-8502(94)90184-8.

[33] J. Fung, J. Hunt, … N.M.-J. of F., U. 1992, Kinematic simulation of homogeneous turbulence by unsteady random Fourier modes, J. Fluid Mech. 281-318. (1992).

[34] A. Smirnov, S. Shi, I. Celik, Random flow generation technique for large eddy simulations and particle-dynamics modeling, J. Fluids Eng. 123 (2001) 359–371.

[35] P. Batten, U. Goldberg, S. Chakravarthy, Interfacing Statistical Turbulence Closures with Large-Eddy Simulation, Https://Doi.Org/10.2514/1.3496. 42 (2012) 485–492. https://doi.org/10.2514/1.3496.

[36] M. Klein, A. Sadiki, J. Janicka, A digital filter based generation of inflow data for spatially developing direct numerical or large eddy simulations, J. Comput. Phys. 186 (2003) 652–665. https://doi.org/10.1016/S0021-9991(03)00090-1.

[37] N. Jarrin, S. Benhamadouche, D. Laurence, R. Prosser, A synthetic-eddy-method for generating inflow conditions for large-eddy simulations, (2006). https://doi.org/10.1016/j.ijheatfluidflow.2006.02.006.

[38] H. Tieleman, Wind tunnel simulation of wind loading on low-rise structures: a review, J. Wind Eng. (2003). https://www.sciencedirect.com/science/article/pii/S0167610503001326

[39] H. Aboshosha, A. Elshaer, G.T. Bitsuamlak, A. El Damatty, Consistent inflow turbulence generator for LES evaluation of wind-induced responses for tall buildings, J. Wind Eng. Ind. Aerodyn. 142 (2015) 198–216. https://doi.org/10.1016/j.jweia.2015.04.004.

[40] J. Chen, A. Elshaer, H. Aboshosha, G. Pedro, Calibrated consistent flow generator for tall building aerodynamics using large eddy simulation, Results Eng. 16 (2022) 100634.

[41] M. Alanani, A. Elshaer, ANN-based optimization framework for the design of wind load resisting system of tall buildings, Eng. Struct. 285 (2023) 116032. https://doi.org/10.1016/J.ENGSTRUCT.2023.116032.

[42] Q. Yang, T. Wang, B. Yan, T. Li, M.L.-J. of W.E. and, undefined 2021, Nonlinear motion-induced aerodynamic forces on large hyperbolic paraboloid roofs using LES, Elsevier. (n.d.). https://www.sciencedirect.com/science/article/pii/S0167610521001859

[43] R. Al-Chalabi, A. Elshaer, Aerodynamic mitigation of low-rise building with complex roof geometry, Front. Built Environ. 9 (2023) 1200383.

https://doi.org/10.3389/FBUIL.2023.1200383/BIBTEX.

[44] Y. Zhang, S. Cao, J. Cao, An improved consistent inflow turbulence generator for LES evaluation of wind effects on buildings, Build. Environ. 223 (2022) 109459. https://doi.org/10.1016/J.BUILDENV.2022.109459.

[45] T.N. Geleta, G. Bitsuamlak, Validation metrics and turbulence frequency limits for LES-based wind load evaluation for low-rise buildings, J. Wind Eng. Ind. Aerodyn. 231 (2022) 105210. https://doi.org/10.1016/J.JWEIA.2022.105210.

[46] Y. Qiu, B. San, Y. Zhao, Numerical Simulation and Optimization of Wind Effects of Porous Parapets on Low-Rise Buildings with Flat Roofs, Adv. Civ. Eng. 2019 (2019). https://doi.org/10.1155/2019/3402613.

[47] A.M. Aly, J. Bresowar, Aerodynamic mitigation of wind-induced uplift forces on low-rise buildings: A comparative study, J. Build. Eng. 5 (2016) 267–276. https://doi.org/10.1016/j.jobe.2016.01.007.

[48] W. Yang, Y. Quan, X. Jin, Y. Tamura, M. Gu, Influences of equilibrium atmosphere boundary layer and turbulence parameter on wind loads of low-rise buildings, J. Wind Eng. Ind. Aerodyn. 96 (2008) 2080–2092. https://doi.org/10.1016/J.JWEIA.2008.02.014.

[49] M. Ricci, L. Patruno, S. de Miranda, Wind loads and structural response: Benchmarking LES on a low-rise building, Eng. Struct. 144 (2017) 26–42. https://doi.org/10.1016/J.ENGSTRUCT.2017.04.027.

[50] J. Singh, · Amrit, K. Roy, Effects of roof slope and wind direction on wind pressure distribution on the roof of a square plan pyramidal low-rise building using CFD simulation, Int. J. Adv. Struct. Eng. 11 (2019) 231–254. https://doi.org/10.1007/s40091-019-0227-3.

[51] M. Amini, A.M. Memari, CFD-Based Evaluation of Elevated Coastal Residential Buildings under Hurricane Wind Loads, J. Archit. Eng. 27 (2021). https://doi.org/10.1061/(ASCE)AE.1943-5568.0000472.

[52] S. Gan, G. Li, Z. Dong, H. Li, M. Zhao, Numerical study on aeroelastic behavior of spoiler on low-rise building based on fluid-structure interaction method, J. Build. Eng. 59 (2022) 105115. https://www.sciencedirect.com/science/article/pii/S2352710222011238

[53] Y. Ozmen, E. Baydar, J.P.A.J. van Beeck, Wind flow over the low-rise building models with gabled roofs having different pitch angles, Build. Environ. 95 (2016) 63–74.

https://doi.org/10.1016/J.BUILDENV.2015.09.014.

[54] Y. Tominaga, T. Stathopoulos, Numerical simulation of dispersion around an isolated cubic building: Model evaluation of RANS and LES, Build. Environ. 45 (2010) 2231–2239. https://doi.org/10.1016/J.BUILDENV.2010.04.004.

[55] S. Gan, G. Li, Z. Dong, H. Li, M. Zhao, Numerical study on aeroelastic behavior of spoiler on low-rise building based on fluid-structure interaction method, J. Build. Eng. 59 (2022) 105115. https://doi.org/10.1016/J.JOBE.2022.105115.

[56] Z. Mansouri, R.P. Selvam, A.G. Chowdhury, Maximum grid spacing effect on peak pressure computation using inflow turbulence generators, Results Eng. 15 (2022) 100491. https://doi.org/10.1016/J.RINENG.2022.100491.

[57] J.P. Boris, F.F. Grinstein, E.S. Oran, R.L. Kolbe, New insights into large eddy simulation, Fluid Dyn. Res. 10 (1992) 199–228. https://doi.org/10.1016/0169-5983(92)90023-P/META.

[58] RP. Selvam, cfd as tool for assessing wind loading selvam - Google Scholar, Bridg. Struct. Eng. (2017).

[59] R. Courant, K. Friedrichs, H. Lewy, Über die partiellen Differenzengleichungen der mathematischen Physik, Math. Ann. 100 (1928) 32–74. https://doi.org/10.1007/BF01448839.

[60] B.W. Yan, Q.S. Li, Inflow turbulence generation methods with large eddy simulation for wind effects on tall buildings, Comput. Fluids. 116 (2015) 158–175. https://doi.org/10.1016/J.COMPFLUID.2015.04.020.

[61] S. Huang, Q.S. Li, S. Xu, Numerical evaluation of wind effects on a tall steel building by CFD, J. Constr. Steel Res. 63 (2007) 612–627. https://doi.org/10.1016/J.JCSR.2006.06.033.

[62] A.H.H. Al-Masoodi, Y.M. Abbas, F. Alkhatib, M.I. Khan, N. Shafiq, M. ElGawady, Aerodynamic optimization for corner modification of octagonal-shape tall buildings using computational approach, J. Build. Eng. 76 (2023) 107017. https://www.sciencedirect.com/science/article/pii/S2352710223011968

[63] B. Chen, Y. Sun, M. Liu, F. Alkhatib, N. Kasim, W.I. Goh, N. Shafiq, M. Amran, E.V. Kotov, M.A. Albaom, Computational aerodynamic optimization of wind-sensitive irregular tall buildings, Build. 2022, Vol. 12, Page 939. 12 (2022) 939.

https://doi.org/10.3390/buildings12070939.

[64] B. Mou, B.J. He, D.X. Zhao, K.W. Chau, Numerical simulation of the effects of building dimensional variation on wind pressure distribution, Eng. Appl. Comput. Fluid Mech. 11 (2017) 293–309. https://doi.org/10.1080/19942060.2017.1281845.

[65] M.S. Thordal, J.C. Bennetsen, S. Capra, H.H.H. Koss, Towards a standard CFD setup for wind load assessment of high-rise buildings: Part 1 – Benchmark of the CAARC building, J. Wind Eng. Ind. Aerodyn. 205 (2020) 104283. https://doi.org/10.1016/J.JWEIA.2020.104283.

[66] R.H. Ong, L. Patruno, D. Yeo, Y. He, K.C.S. Kwok, Numerical simulation of wind-induced mean and peak pressures around a low-rise structure, Eng. Struct. 214 (2020) 110583. https://www.sciencedirect.com/science/article/pii/S0141029619336193

[67] N.S. Fouad, G.H. Mahmoud, N.E. Nasr, Comparative study of international codes wind loads and CFD results for low rise buildings, Alexandria Eng. J. 57 (2018) 3623–3639. https://doi.org/10.1016/J.AEJ.2017.11.023.

[68] R. Biswas, R.C. Strawn, Tetrahedral and hexahedral mesh adaptation for CFD problems, Appl. Numer. Math. 26 (1998) 135–151. https://doi.org/10.1016/S0168-9274(97)00092-5.

[69] Y.L. LLo, Y.C. Kim, Y.C. Li, Downstream interference effect of high-rise buildings under turbulent boundary layer flow, J. Wind Eng. Ind. Aerodyn. 159 (2016) 19–35. https://www.sciencedirect.com/science/article/pii/S0167610516302525

[70] T.C.E. Ho, D. Surry, D. Morrish, G.A. Kopp, The UWO contribution to the NIST aerodynamic database for wind loads on low buildings: Part 1. Archiving format and basic aerodynamic data, J. Wind Eng. Ind. Aerodyn. 93 (2005) 1–30. https://doi.org/10.1016/J.JWEIA.2004.07.006.

[71] J.M. Denmark, Atmospheric turbulence, Breeze.Colorado.EduJ MannDTU Wind Energy, Tech. Univ. Denmark, Denmark, DK, 2012•breeze.Colorado.Edu. (2012). https://breeze.colorado.edu/ftp/RSWE/Jakob_Mann.pdf.

[72] R.A. Sanni, D. Surry, A.G. Davenport, Wind loading on intermediate height buildings, Can. J. Civ. Eng. 19 (1992) 148–163. https://doi.org/10.1139/L92-015.

[73] F.Q. Meng, B.J. He, J. Zhu, D.X. Zhao, A. Darko, Z.Q. Zhao, Sensitivity analysis of wind pressure coefficients on CAARC standard tall buildings in CFD simulations, J. Build. Eng. 16 (2018) 146–158. https://doi.org/10.1016/J.JOBE.2018.01.004.

[74] B. Blocken, T. Stathopoulos, J. Carmeliet, CFD simulation of the atmospheric boundary layer: wall function problems, Atmos. Environ. 41 (2007) 238–252. https://www.sciencedirect.com/science/article/pii/S135223100600834X

[75] F. Bazdidi-Tehrani, S. Masoumi-Verki, P. Gholamalipour, M. Kiamansouri, Large eddy simulation of pollutant dispersion in a naturally cross-ventilated model building: Comparison between sub-grid scale models, Build. Simul. 12 (2019) 921–941. https://doi.org/10.1007/S12273-019-0525-5/METRICS.

[76] P. Kakka, K. Anupindi, Assessment of subgrid-scale models for large-eddy simulation of a planar turbulent wall-jet with heat transfer, Int. J. Heat Mass Transf. 153 (2020) 119593. https://doi.org/10.1016/J.IJHEATMASSTRANSFER.2020.119593.

[77] M.F. Khaled, A.M. Aly, A. Elshaer, Computational efficiency of CFD modeling for building engineering: An empty domain study, J. Build. Eng. 42 (2021) 102792. https://doi.org/10.1016/J.JOBE.2021.102792.

[78] Z. Liu, Z. Yu, X. Chen, R. Cao, F. Zhu, An investigation on external airflow around low-rise building with various roof types: PIV measurements and LES simulations, Build. Environ. 169 (2020) 106583. https://doi.org/10.1016/J.BUILDENV.2019.106583.

[79] Y. Zhou, T. Kijewski, A. Kareem, Aerodynamic Loads on Tall Buildings: Interactive Database, J. Struct. Eng. 129 (2003) 394–404. https://doi.org/10.1061/(ASCE)0733-9445(2003)129:3(394).

[80] A.D.- And, How can we simplify and generalize wind loads?, Jouranl Wind Eng. (1995). https://www.sciencedirect.com/science/article/pii/016761059400079S

[81] Hirsch C., V. Bouffioux, V. and W.F. Bouffioux, CFD simulation of the impact of new buildings on wind comfort in an urban area, in: CSTB, Nantes, 2002: pp. 164–171.

[82] W. Wang, Y. Cao, T. Okaze, Comparison of hexahedral, tetrahedral and polyhedral cells for reproducing the wind field around an isolated building by LES, Build. Environ. 195 (2021) 107717. https://doi.org/10.1016/J.BUILDENV.2021.107717.

CHAPTER 4

Impact of Maximum Turbulence Frequency on Wind Flow and Pressure Distribution for Low-Rise Buildings Using Discrete Random Flow Generator

4.1. Introduction

Evaluating wind loads is crucial for maintaining buildings' structural integrity and safety, particularly in areas prone to severe weather conditions. Wind-induced forces can heavily impact low-rise buildings as they are located within the Atmospheric Boundary Layer (ABL), which is characterized by turbulent wind flow, making them more susceptible to wind damage than other structures. During windstorms, claddings can be damaged due to uplift forces, which can jeopardize the integrity of low-rise buildings. Numerous studies have found that uplift forces resulting from pressure variations can initiate roof failure [1–3]. Thus, precisely predicting wind loads at critical locations on low-rise buildings, such as separation locations, is crucial for constructing resilient structures capable of withstanding high winds. With the development of computational fluid dynamics (CFD) techniques, large eddy simulation (LES) has been widely applied to simulate turbulent flows of engineering interest. For instance, Tominaga and Stathopoulos employed both Large Eddy Simulation (LES) and Reynolds-Averaged Navier-Stokes (RANS) models to investigate pollution dispersion around buildings and within street canyons [4,5]. Similarly, Gousseau et al. applied LES to examine pollution dispersion in an urban city center [6]. Furthermore, LES has been widely adopted in numerous studies to investigate the wind aerodynamics of low-rise buildings, providing a detailed understanding of wind-induced pressures, vortex formation, and flow separation that are difficult to model with traditional methods like RANS equations [7–10]. In addition, it has been particularly useful in studying the complex wind phenomena associated with tall buildings, including vortex shedding, pressure distributions, and the interaction of wind with surrounding urban environments [11–14]. Experimental and computational studies evaluating wind loads typically focus on replicating the wind profile within the buildings surrounding the Atmospheric Boundary Layer (ABL). In the case of low-rise buildings, large-scale turbulence can potentially elevate gust speeds, thereby modifying the overall loading conditions. In contrast, small-scale turbulence can dictate the aerodynamic loading by reshaping the flow patterns around the structure, causing a substantial amplification of high negative surface pressures occurring beneath the reattached shear layers [15].

The accuracy of LES results in wind load evaluation significantly depends on the accuracy of the injected turbulent inflow. Accurate modelling of turbulent inflow boundary conditions (BC) is essential for the reliable evaluation of building aerodynamic forces and building responses, which requires accurate matching of turbulent spectra, correlation and magnitudes with respect to the appropriate upstream conditions [15–17]. The turbulent flow injected into the computational domain is typically generated by matching ABL flow statistically using numerous methods such as (i) Random Flow Generation methods (RFG) [16–20], (ii) Digital Filtering Methods (DFM) [21], and (iii) Synthetic Eddy Methods (SEM) [22]. Existing Random Flow Generator (RFG) techniques face a challenge in that turbulent profiles degrade with increasing distance from the inlet. Many of these methods overlook the distance between the inlet and the incident location (i.e., test location), adversely impacting the quality of the incoming turbulence at the test location. The latter method requires an input range of dimensional frequency that varies between minimum (f_{min}) and maximum frequency (f_{max}). The latter defines the largest frequency that a grid can resolve. In order, to perform highly accurate LES simulation, the majority of the turbulence (e.g., 80% of turbulence) has to be resolved rather than being modelled, which can be controlled by defining f_{max} shown in Fig. 4.1 [23]. Generally, the value of f_{max} is used, as input in the turbulence flow generator, typically resembles the frequency range employed in the experimental testing. However, this frequency range is not necessarily resolved as it highly depends on the refinement, and accordingly, the minimum resolved wavelength. Aboshosha et al. developed and employed one of the RFG methods (i.e., Consistent Discrete Random Flow Generation CDRFG) to study tall building aerodynamics [24]. Later, several studies utilized the same method to study low-rise building aerodynamics [10,25–27]. Melbourne [28] has established that capturing small-scale turbulence at a reduced frequency, fh/U, where f is turbulence frequency, U is wind velocity , and h is roof height, equals to 10, is critical to ensure curacy of capturing flow features around a low-rise building. Adjacently, Morrison and Kopp [29] argued that for low-rise buildings, the vital turbulence scales are the ones captured at a reduced frequency that varies between 0.1 and 2.0. Hence, to accurately model wind loading on low-rise buildings, incoming turbulence must be resolved up to a frequency corresponding to the characteristic scale of the building, which requires proper modelling of small-scale turbulence, particularly at the separation locations [30].

Despite that, there are no clear guidelines on the way of defining the value of f_{max} required for the inflow generation, leading to accurate wind load evaluation for low-rise buildings. In light of the discussion above, this study aims to systematically define the required CFD details to produce accurate ABL flows with Large Eddy Simulation (LES) models, particularly including a discussion aims at efficiently selecting turbulence maximum frequency (f_{max}) employed as an input in the turbulence flow generator concerning grid size in the refinement zones that can accurately capture the pressure fluctuation induced on the building façade. The efficient selection of the value of f_{max} will depend on assessing the mean and RMS pressure values across the gable roof of the low-rise structure, and the accuracy of the wind load evaluation will be correlated to the experimental wind tunnel test conducted by Ho et al. [31].

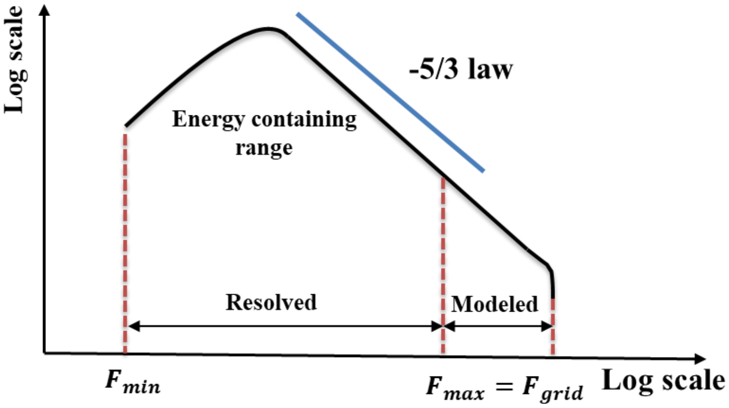

Fig. 4.1 The correlation between a power density spectrum and turbulence modelling in LES [15].

This section (Section 1) provides a review of prior large eddy simulation (LES) studies that have employed different inflow generators, focusing primarily on low-rise buildings. Section 2 outlines the numerical model validation with the wind tunnel experimental test conducted by Ho et al. (2005). Section 3 presents the methodology framework followed to find the efficient approach to evaluate the maximum turbulent frequency as an input in the turbulent generator CDRFG. Section 4 presents mesh sensitivity analysis to validate the mesh resolution utilized in the study as well as compares the accuracy of the inflow generated using CDRFG against experimental wind tunnel results for low-rise buildings using a range of values for maximum input frequency, F_{max}, between $0.5\ Hz\ to\ 100\ Hz$. Finally, Section 5 concludes with a summary of the study's findings and implications.

4.2. Numerical Model Validation

Two models are employed to validate the turbulence content and ensure horizontal consistency, one involving an empty domain study. These models analyze flow characteristics such as mean velocity and turbulence intensity. The CFD model used in this study is validated against experimental testing conducted at the Boundary Layer Wind Tunnel II at the University of Western Ontario by Ho et al. [31]. The validation is performed using a gable roof low-rise building with dimensions of 38.1×24.4 m^2 (i.e., $B \times L$)with a roof total height (h) of $13.2\ m$ in full-scale. The validated CFD model serves as a benchmark for evaluating CFD efficiency. This validation involves comparing the mean and RMS pressure coefficient values for 12 taps located across the gable roof, as depicted in Fig. 4.2. Mean velocity and turbulence intensity profiles are generated to match an open-terrain exposure with a roughness height, z_O, of 30 mm (in the full scale) with a reference velocity of $37.6\ m/s$ at a reference height of 10 m in full-scale. The current model is set to match the wind tunnel experimental model adopted at a length scale and timescale of $1{:}\ 100$ and $1{:}\ 25$, respectively.

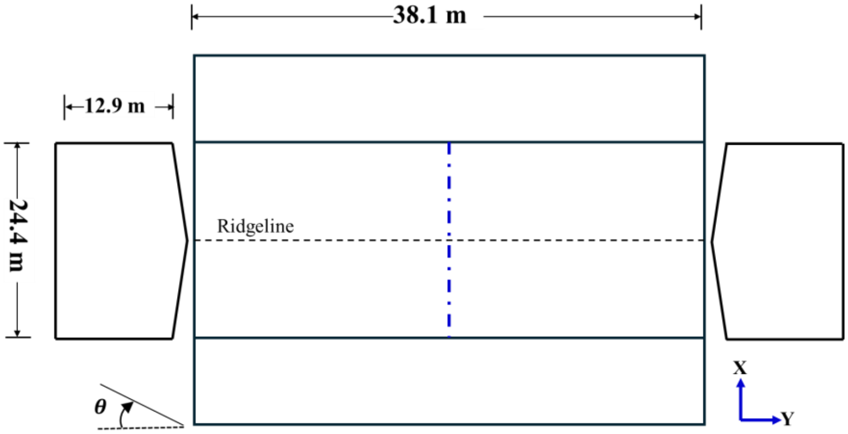

Fig. 4.2 Exploded view of the study model building with a gable roof slope of 1:12 and test probe's location (12 probes in total).

This study follows the equations proposed and published by the Engineering Sciences Data Unit (ESDU) intensity [32,33] to compare vertical profiles for mean velocity and turbulence intensity. This study's velocity and intensity profiles align with wind tunnel experimental data using the Power Law (Eq. 2) for mean wind velocity. The $\overline{U}_{10}$ represents the wind velocity at a height of 10 m, with a value of $37.6\ m/s$. The variable "z" denotes the height in meters corresponding to the reference wind velocity, while the terrain roughness for open exposure ($1/\alpha$) is 0.13, consistent with the approach used by Ho et al. (2005). Turbulence intensity is calculated using the equation provided (Eq. 2) for the target profile.

$$U_z = \overline{U}_{10}\left(\frac{z}{10}\right)^{1/\alpha} \tag{3}$$

$$I_u = c_u\left(\frac{z_{ref}}{z}\right)^{bu} \tag{4}$$

To verify the numerical model, STAR-CCM+ 2020.2 (15.04.008-R8) is utilized with LES for wind load assessment. A computational domain measuring $3.4\,m\ \times\ 2.5\,m\ \times\ 0.7\,m$ (in model scale) is employed, depicted in Fig. 4.3. Symmetry plane boundaries are set for the top and side surfaces. Non-slip wall boundaries are assigned to the ground and building surfaces, while the outlet is designated as an outflow boundary. Consistent Discrete Random Flow Generation (CDRFG) is used for inflow generation [24]. The inlet wall is defined as a time-varying inlet velocity boundary condition using the CDRFG technique described by Aboshosha et al. and later adopted by Elshaer et al. [14,24]. The building is placed 0.6 m away from the inlet; hence, pressure data collection started after 800-time steps to ensure flow stabilization. The computational domain is divided into three refinement zones using hexahedral mesh cells. Zone 1 employs a base mesh size of 15 mm, while zones 2 and 3 use 8.0 mm and 6.0 mm, respectively, resulting in a total of 1.45 million mesh cells, as depicted in Fig. 4.3. The mean wind velocity and turbulence intensity profiles utilized in the wind tunnel experiment demonstrated favorable agreement with the numerical profiles, as depicted in Fig. 4.4. This alignment with wind tunnel data suggests the capability to simulate Atmospheric Boundary Layer (ABL) flow within an empty domain, indicating horizontal homogeneity in the vertical profiles of mean velocity and turbulence intensity at the building location.

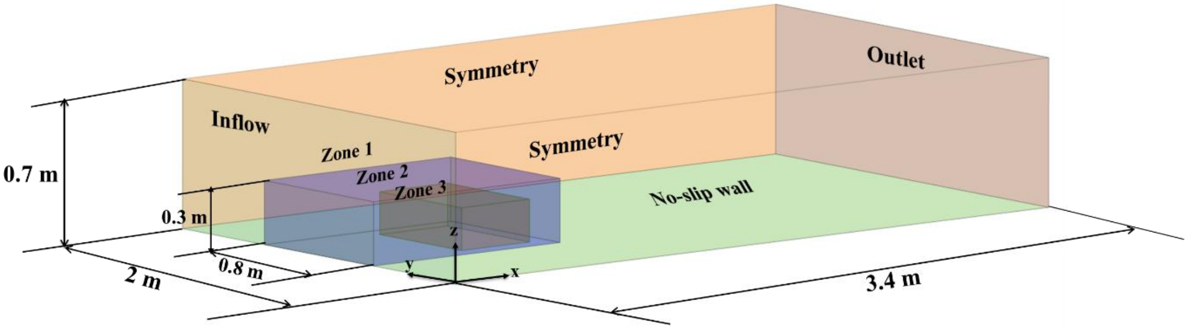

Fig. 4.3 Computational domain dimensions (in model-scale) and boundary conditions.

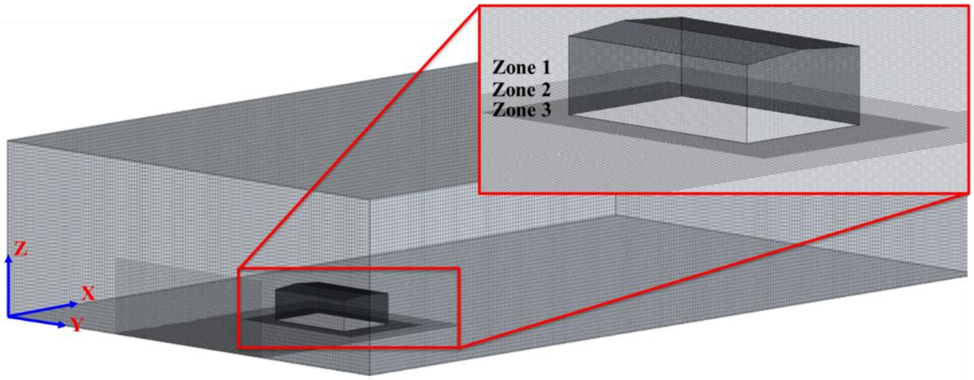

Fig. 4.4 Mesh discretization of the validation model.

The simulation duration is 8.0 seconds (in model scale), employing a time-step of 0.5 milliseconds, resulting in a total of 16,000-time steps. The time step is chosen based on the velocity scale and the minimum cell size to ensure the Courant-Friedrichs-Lewy (CFL) number remains below unity for solution convergence [34]. For reference pressure used in calculating Cp, a probe point is positioned at the midpoint of the inlet before the building at a height of 0.48 m (model scale). Upon running the validation model, the mean and RMS of the pressure coefficient across the ridgeline are compared to wind tunnel test results, as illustrated in Fig. 4.5 (a) and (b), respectively. The validation model exhibits good agreement between numerical and experimental pressure parameters, as shown in Fig. 4.6. Mean Cp results demonstrate a root mean square error (RMSE) (see Eq. 3) of 1.65%, while pressure fluctuations exhibit a 4.3% difference compared to experimentally obtained data.

$$RMSE = \sqrt{\frac{\Sigma\left(R_{Exp}-R_{LES}\right)^2}{n}} \tag{5}$$

where R_{Exp} refers to pressure readings extracted from the experimental wind tunnel test, R_{LES} refers to pressure readings extracted from numerical simulation, and n is the number of readings.

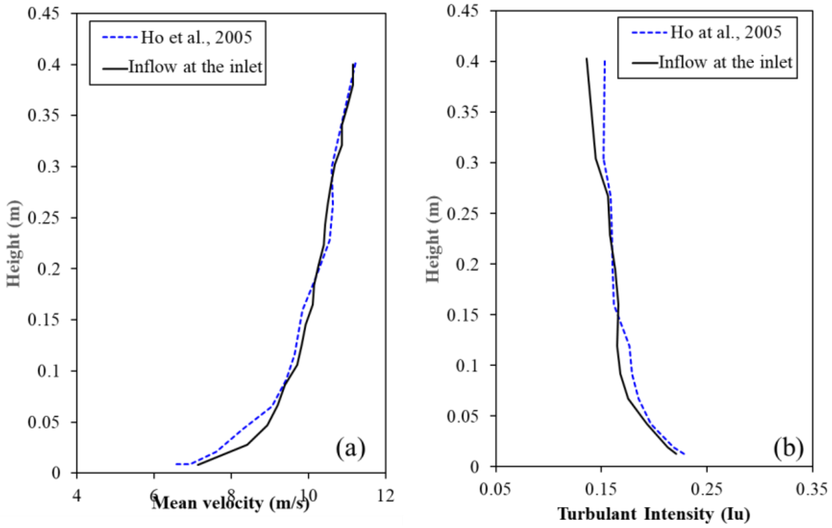

Fig. 4.5 (a) Mean velocity profile and (b) Turbulence intensity profiles.

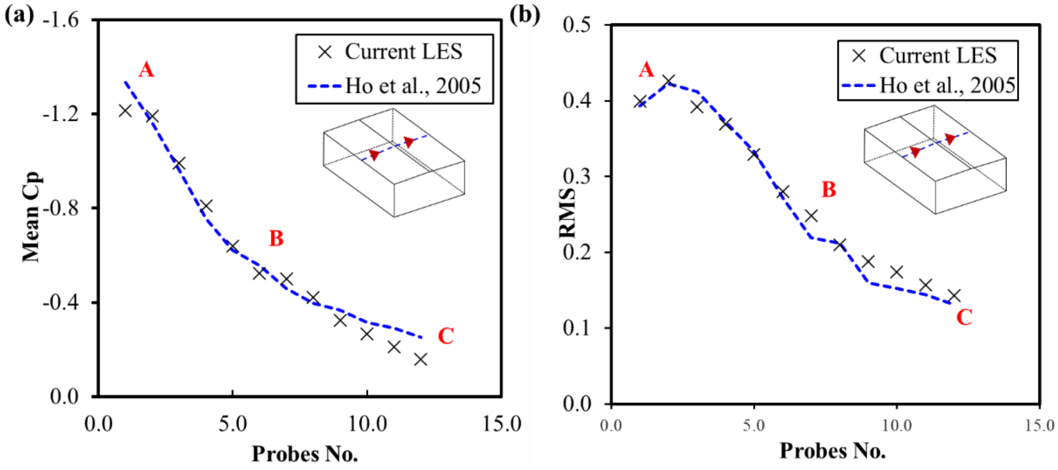

Fig. 4.6 (a) Mean and (b) RMS of the pressure for probes located at the building roof.

4.3.Methodology Framework

Structured analysis is conducted based on the validated LES model by systematically varying a single parameter and evaluating the discrepancies in computational wind load compared to the wind tunnel test. The examined parameters include the maximum frequency resolved by the grid employed in LES, the computational domain size and computational domain discretization. The mean and RMS of the pressure coefficient (Cp) are extracted from the probes across the building roof, as shown in Fig. 4.7. The accuracy of the CFD model is examined by evaluating the Root Mean Square of Error (RMSE), as shown in Eq. (3).

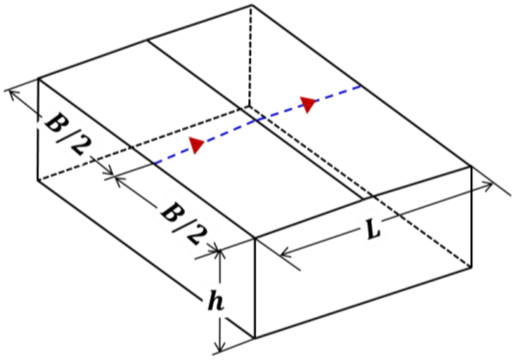

Fig. 4.7 The probe's (12 in total) locations are examined in this study.

Throughout the study, the computational domain spatial discretization utilized three grid refinement zones with the size selected based on the building roof reference height. The sizes of the grid refinement zones and their location for the benchmark model are listed in Table 4.1. As mentioned earlier, this study utilizes the turbulence inflow generator technique, based on synthesizing random divergent free turbulent velocities where the input parameters are modified to enforce the generated turbulent velocity components to match the properties required for the LES study.

Table 4.1 Grid size with reference to building height (h) the computational domain.

Zones	**Grid size**
Zone1	$h/8$
Zone 2	$h/16$
Zone 3	$h/22$

Generally, this study adopted a maximum frequency of 100 Hz input to generate the turbulent inflow mimicking the open terrain wind profile setup. The input data details for this study are utilized as input in the MATLAB code and are detailed in. The velocity information for each cell at the inlet is supplied using the CDRFG technique, as proposed by Aboshosha et al. [24]. The benchmark model's velocity profile corresponds to 9,728 cells at the inlet. The code is run for a sampling period of 8.0 seconds in the model scale to generate the inflow velocity fluctuation. The methodology followed by this study is summarized in Fig. 4.8.

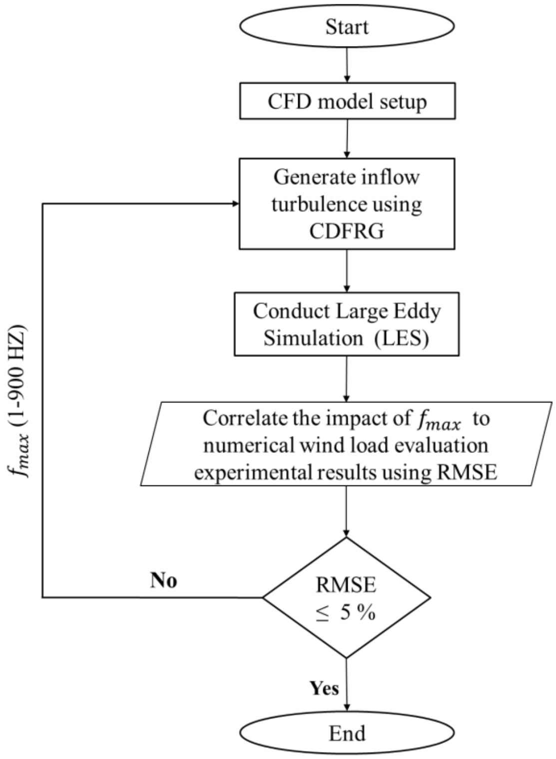

Fig. 4.8 Methodology framework adopted in this study.

4.4. Results and Discussion

4.4.1. Mesh Sensitivity Analysis

In computational fluid dynamics (CFD) simulations, mesh resolution is critical in capturing the intricate details of fluid flow, particularly in the context of turbulent flows and their interaction with building surfaces. To ensure the accuracy and reliability of the results, it is essential to conduct a mesh sensitivity analysis. This process involves evaluating how the resolution of the computational grid affects key flow characteristics, such as pressure distributions on the surfaces of interest. In this study, four numerical models with varying mesh resolutions are utilized to assess the impact of mesh size on the simulation outcomes as shown in Fig. 4.9 and Table 4.2. Each model employed a different level of refinement, from coarse to fine (i.e., Mod-1 to Mod-4), to determine the extent to which the mesh resolution influences the accuracy of wind flow and pressure predictions on low-rise buildings. The objective is to identify the optimal mesh resolution that balances computational efficiency with the ability to resolve key turbulent features, especially in regions of high flow complexity, such as near the roof and windward wall of the structure. This section presents a comparative analysis of the results obtained from these models, focusing on the mean and root mean square (RMS) values of velocity and pressure distributions across the building roof surfaces, RMSE calculations are evaluated relative to the experimental values. Upon examining the computational domain grid resolution for the four models employed (as it can be seen in Fig. 4.10), a high discrepancy in the mean pressure is estimated with an error of 12% when a coarse grid is utilized (i.e., Mod-1). In contrast, less than 4% error in the mean pressure is found when the grid size for the same refinement zones adopted higher mesh resolution (i.e., Mod-1 and Mod-4). Besides, the pressure fluctuation shows a good agreement with the experimental wind tunnel test, where discrepancies are below 3% for models that adopted a fine refinement grid around the study building (i.e., Mod-3 and Mod-4). To balance computational accuracy and cost, Mod-3 is selected to examine the impact of the maximum frequency (f_{max}) on wind flow characteristics and pressure distribution. This model offers an optimal trade-off, ensuring sufficient resolution to capture essential flow features while minimizing computational expenses.

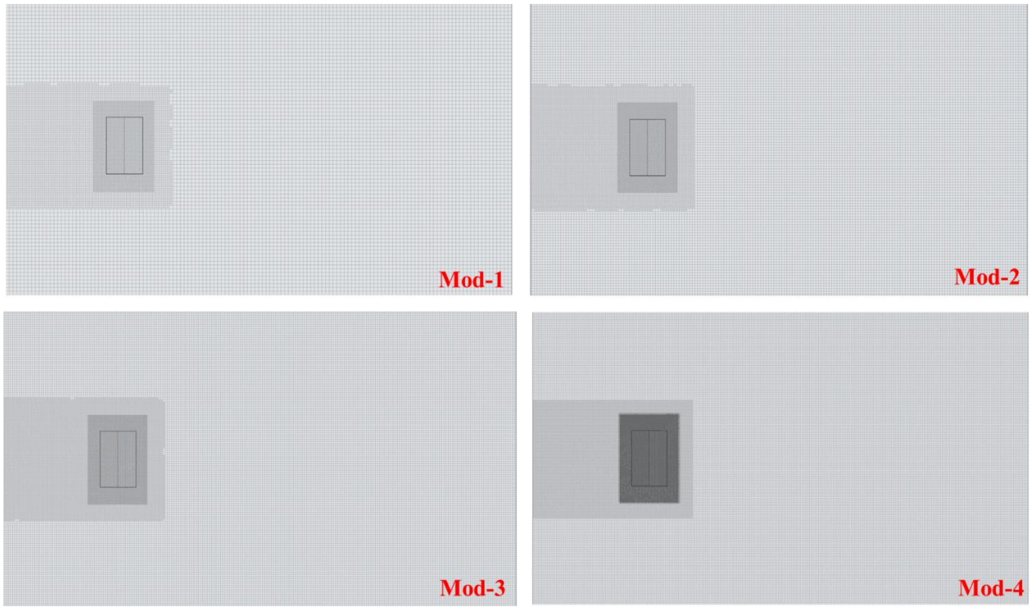

Fig. 4.9 Computational domain discretization for refinement zones.

Table 4.2 Computational domain discretization for refinement zones

Numerical model	Zone 1	Zone 2	Zone 3	Total number of mech cells
Mod-1	H/6	H/11	H/15	580,000
Mod-2	H/7	H/14	H/18	930,000
Mod-3	H/8	H/16	H/22	1,450,000
Mod-4	H/10	H/22	H/30	2,500,000

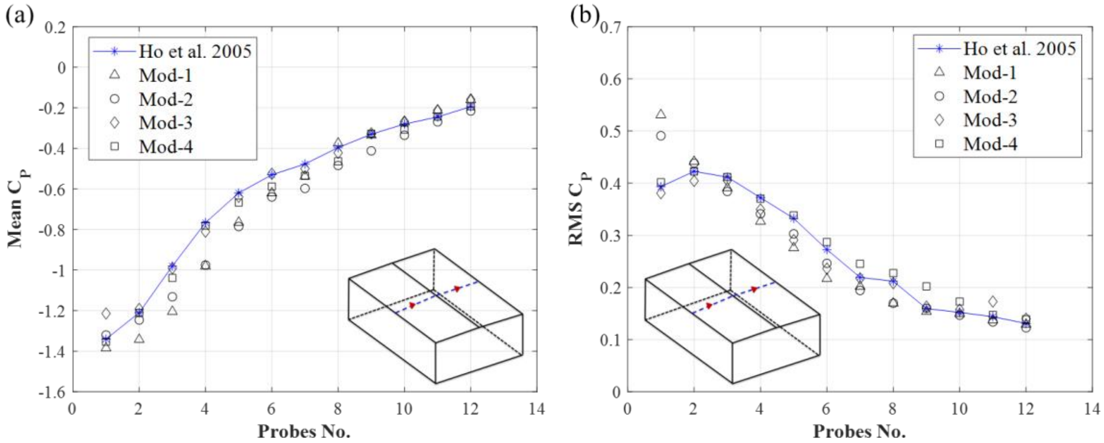

Fig. 4.10 (a) Mean and (b) RMS of the pressure coefficients for probe points across the roof examining the size of the computational domain discretization

4.4.2. Effect of Maximum Turbulence Frequency on Wind Flow and Pressure Distribution

This section explores the impact of varying maximum frequency values used to generate synthetic turbulent flow that simulates the Atmospheric Boundary Layer (ABL). All the numerical models developed for this study adopted the same computational domain size and spatial discretization. The inflow is generated using multiple values of f_{max}, to correlate the maximum frequency employed in the synthetic turbulence method to the accuracy of the wind load evaluation compared to the wind tunnel test experiment.

According to previous studies, the maximum frequency expected to impact the wind load on low-rise buildings ranges from 0.3 to 30 Hz [15]. Hence, input values for the inflow generator for f_{max} ranges from 0.5, 1, 10, 25, and 100 Hz are examined. Fig. 4.11 presents a comparison between numerical wind profiles generated at various maximum frequencies of 0.5 Hz and 100 Hz at the inlet with those obtained from the experimental wind tunnel study. As it can be noticed, the wind profile generated using an f_{max} of $0.5\ Hz$ displayed smoother velocity variations, reflecting the influence of lower-frequency, larger, and slower-moving eddies that cause more gradual changes in the flow. These larger eddies are less disruptive, resulting in a wind profile with lower turbulence intensity, as the flow has fewer small-scale, high-energy fluctuations. Conversely, the wind profile generated with a higher frequency input, such as f_{max} of $100\ Hz$, captured a greater number of smaller, faster eddies, which led to rapid fluctuations in the velocity profile. This dynamic behavior, characterized by localized and fast-changing variations in wind velocity, contributed to an increase in turbulence intensity, as seen in the more chaotic nature of the flow. The greater range of smaller eddies included in the high-frequency wind profile amplifies the chaotic motion of the air, which can significantly influence the resulting wind loads. This distinction between the profiles is clearly depicted in Fig. 4.12, where the increased turbulence intensity is evident in the higher-frequency simulation.

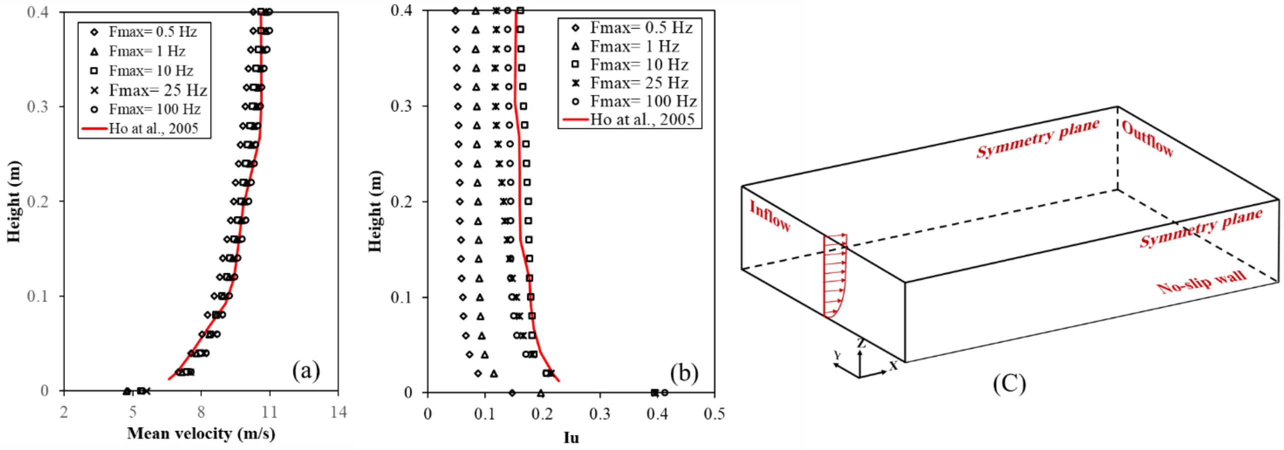

Fig. 4.11 Wind profile at the inlet for various f_{max} for an empty computational domain (a) mean wind velocity, (b) turbulence intensity, and (c) aerodynamic profile location.

To study further the impact of the flow's energy distribution and turbulent characteristics, Fig. 4.12 highlights the effect of different maximum frequencies injected into the wind profiles and their influence on the cut-off frequency at the inlet. Upon examining the spectra profile at a height of 9.75 m, the results indicate a noticeable decrease in energy for the wind profile generated using an $\mathrm{f}_{\mathrm{max}}$ of 0.5 Hz. This decrease suggests that the turbulent energy associated with eddies at frequencies lower than 0.5 Hz is not fully maintained in the flow. Essentially, the lower f_{max} fails to capture smaller, faster-moving eddies, resulting in a reduced range of turbulent scales being resolved. Conversely, profiles with higher f_{max} such as 100 Hz, maintained energy across a broader spectrum. In this case, the cut-off frequency is much higher as more energy is preserved in the flow, ensuring that the simulated wind profile can resolve the full range of turbulent fluctuations impacting the structure. The energy maintenance of capturing the wide range frequencies in the longitudinal spectrum is evidently correlated with the grid resolution and f_{max}. The cut-off frequencies are found to increase with the increase in the maximum frequency used in the turbulence generator. The latter is found to be caused by the increased energy of the streamwise velocity fluctuations. Generally, it can be deduced that the maximum cut-off frequency is 6 Hz for numerical models adopted f_{max} of 100 Hz, as an input in the turbulence generator. This finding aligns with a study conducted by Al-Chalabi et al. (2024), where the maximum dimensional frequency is correlated to grid resolution [15].

To examine the computational discretization efficiency in resolving the turbulence flow generated, the wind flow profiles (i.e., mean velocity and turbulent intensity) at each corresponding height are computed from LES at the building location (i.e., at 0.6 m from the inlet in an empty domain), as shown in Fig. 4.13. The latter profiles are injected into the computational domain to simulate wind flow in an open terrain setup. It is worth mentioning that identical grid refinement zones are selected for all the examined cases for a consistent comparison and to demonstrate their efficacy in resolving large and small eddies velocity spectra. Wind flow profiles for the probe line located at the building location in the computational domain undergo considerable evolution as the values of the maximum frequency increase. In other words, the turbulent intensity keeps growing from what is supplied at the inlet. A similar trend is observed for mean velocity profile cases. Broadly concluding, the LES cases with turbulence generated at frequencies higher than 25 Hz show a good correlation between the experimental and numerical mean velocity and turbulence intensities. Besides, it can be noticed that the high-frequency end of the simulated velocity spectra possesses lower energy because of grid filtering. Moreover, upon using low $\boldsymbol{f_{max}}$, We neglected (filtered) part of the turbulence magnitude, and therefore, the wind speed profiles injected at the inlet are adjusted to a smoother profile to reflect the lower turbulence intensity. Hence, it is crucial to precisely model the proper turbulence by selecting f_{max} and a suitable grid resolution.

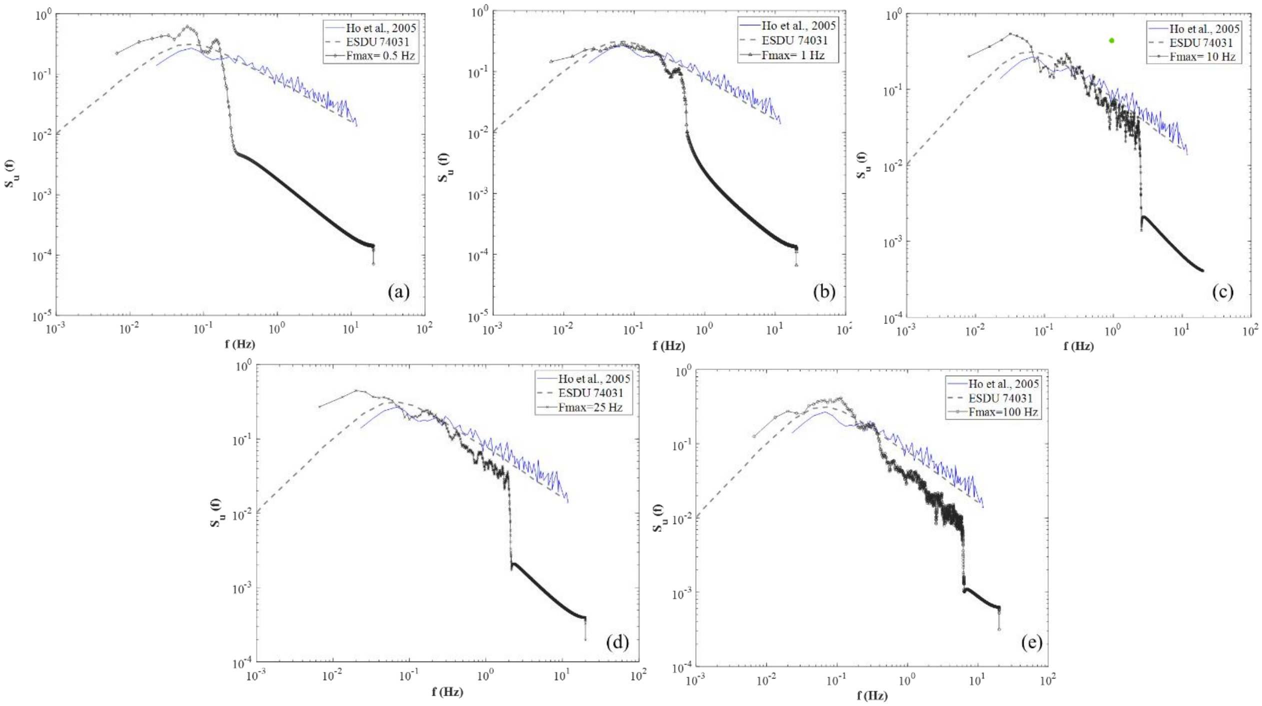

Fig. 4.12 Longitudinal frequency spectrum at a height of 9.75m (full-scale) for maximum frequency of (a) 0.5 Hz, (b)1 Hz, (c)10 Hz, (d) 25 Hz, and (e) 100 Hz

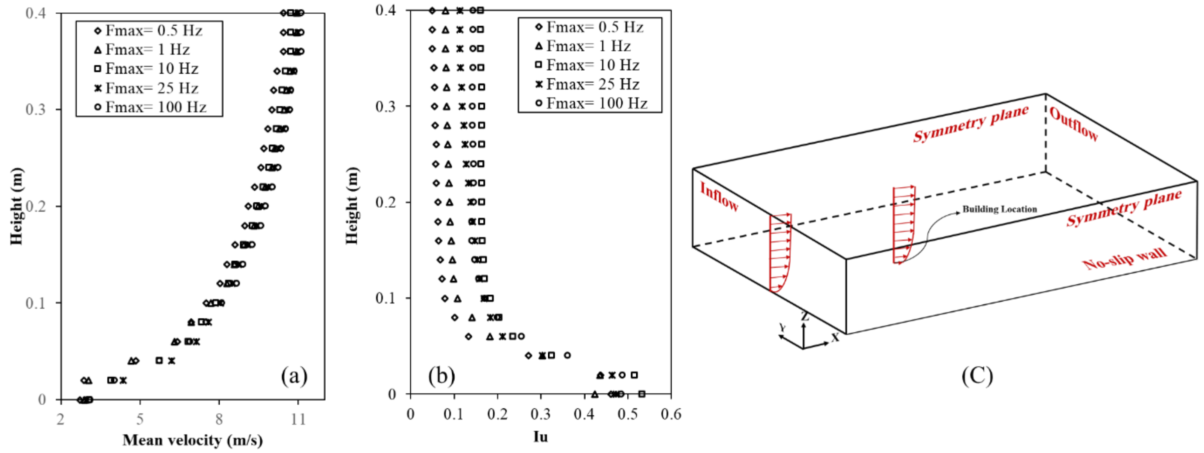

Fig. 4.13 Wind profile at building location for various f_{max} for an empty computational domain (a) mean wind velocity, (b) turbulence intensity, and (c) aerodynamic profile location.

Fig. 4.14 illustrates the velocity Root Mean Square (RMS) across the computational domain for different input maximum frequencies, providing valuable insights into how the inflow turbulence evolves within the domain. For lower input frequencies (e.g., f_{max} of 0.5 Hz), the velocity RMS exhibits smoother variations, indicating a more gradual and sustained turbulent flow, dominated by larger, slower-moving eddies. This is due to the limited range of resolved frequencies contributing to the turbulence. As the input frequency increases (e.g., f_{max} of 10 Hz to 100 Hz), the velocity RMS shows more pronounced fluctuations, particularly in regions closer to the surface, reflecting the presence of smaller, high-energy eddies that are captured by the higher frequency input. The increase in velocity RMS values corresponds to a higher turbulence intensity, as the broader spectrum of turbulent structures contributes to more dynamic flow conditions. This suggests that higher input frequencies more accurately resolve small-scale turbulence, leading to greater variability in the wind flow across the computational domain.

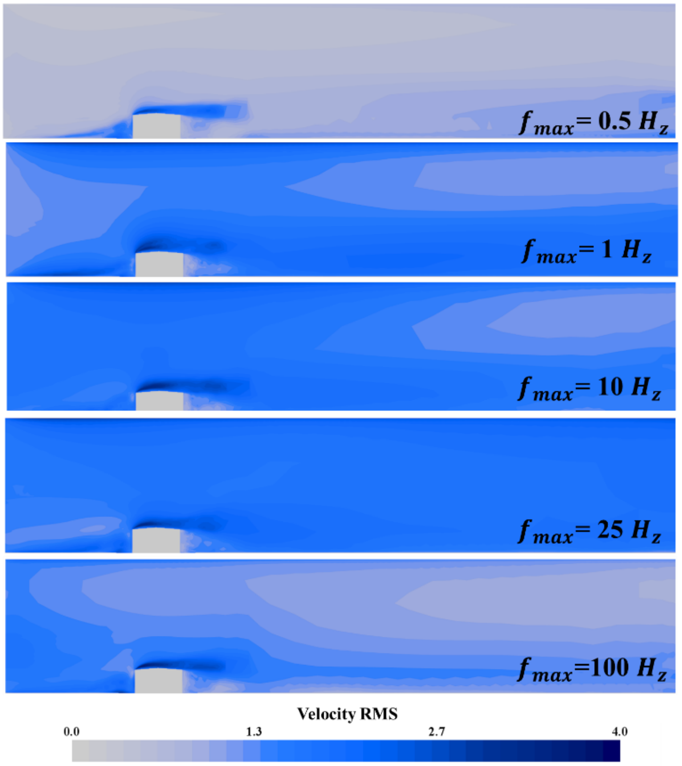

Fig. 4.14 Velocity fluctuation throughout the computational domain.

The velocity spectra agreement with ESDU formulation over the low-frequency part is very encouraging for the computation of the peak pressure on low-rise buildings in future studies using this numerical CFD model. Both Fig. 4.15 and Fig. 4.16 depict the mean and RMS fluctuations on building roof surfaces for different maximum frequencies which offer critical insights into the impact of turbulent inflow on wind-induced pressure distribution. For lower f_{max} values, the mean pressure distribution appears relatively uniform across the roof surfaces, indicating smoother wind flow. This is because the lower frequency inflow is dominated by large-scale eddies that interact less dynamically with the roof, leading to more stable pressure values. The corresponding RMS fluctuations are also subdued, reflecting the reduced turbulence intensity in the flow. This smoother interaction is typical of flows with fewer small-scale turbulent structures, resulting in less variation in the wind pressure over time. In contrast, for higher f_{max}values, both the mean and RMS pressure distributions show greater variability across the roof surfaces. The mean pressure values become more localized and exhibit more distinct gradients, reflecting the influence of smaller, faster eddies generated by the higher frequency inflow. These eddies cause more rapid and localized changes in wind pressure, leading to a more complex pressure distribution pattern. Additionally, the RMS fluctuations are significantly higher, indicating an increase in turbulence intensity. The presence of high-frequency eddies causes greater variability in the wind loads on the roof surfaces, leading to stronger pressure fluctuations over time. A qualitative and quantitative assessment is presented in Fig. 4.17 which shows that in models simulated using frequencies ranging between 0.5 Hz and 100 Hz, both the mean and pressure fluctuation on the roof encountered minimal changes with a high degree of accuracy compared to the wind tunnel test. The RMSE recorded for the mean and pressure fluctuating are 3.1% and 2.6% for a model with a maximum frequency input of 100 Hz, respectively. In contrast, the mean pressure is found to be estimated with RMSE n of >13%, while the pressure fluctuation error is found to be >8 % when the utilized input values of F_{max} the turbulence generator is 0.5 Hz.

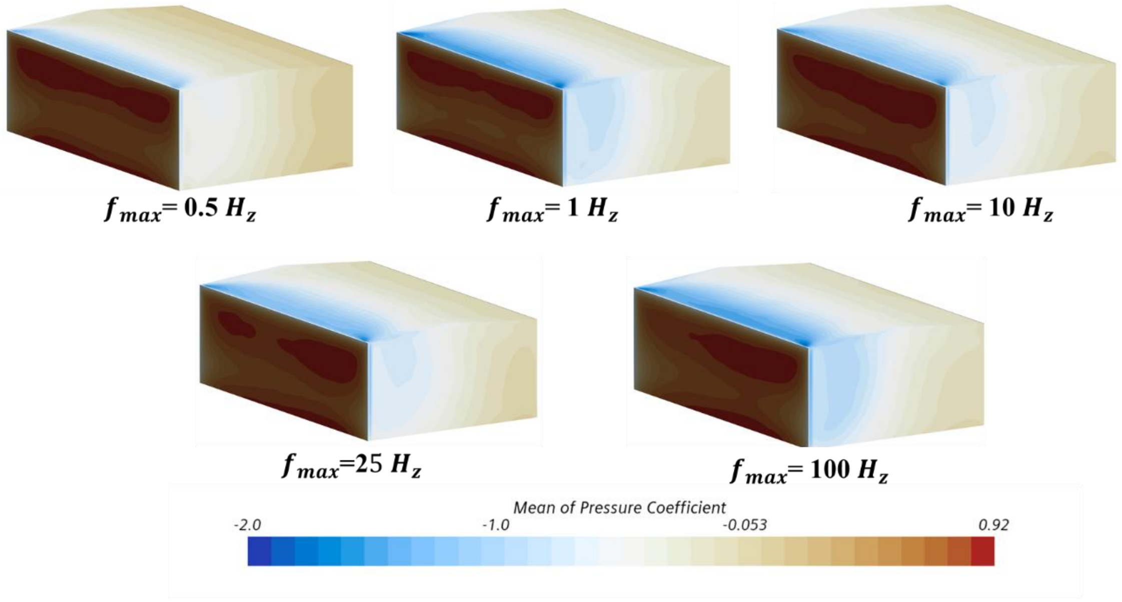

f_{max}= 0.5 H_z f_{max}= 1 H_z f_{max}= 10 H_z

f_{max}=25 H_z f_{max}= 100 H_z

Fig. 4.15 Mean pressure on the building surfaces.

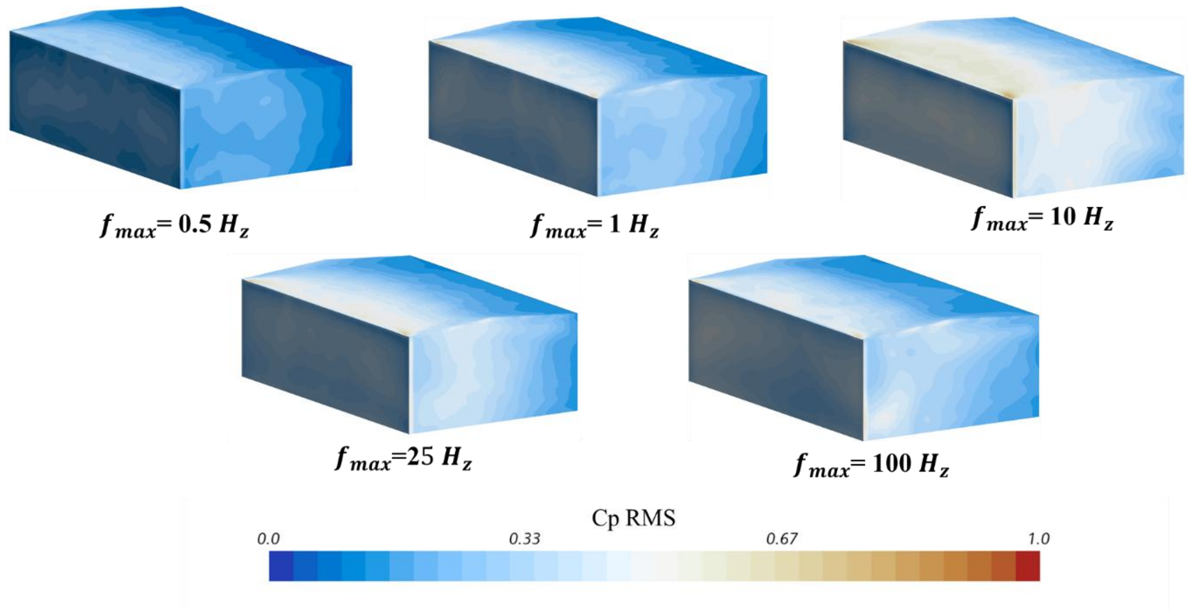

Fig. 4.16 Cp RMS of the pressure on the building surfaces.

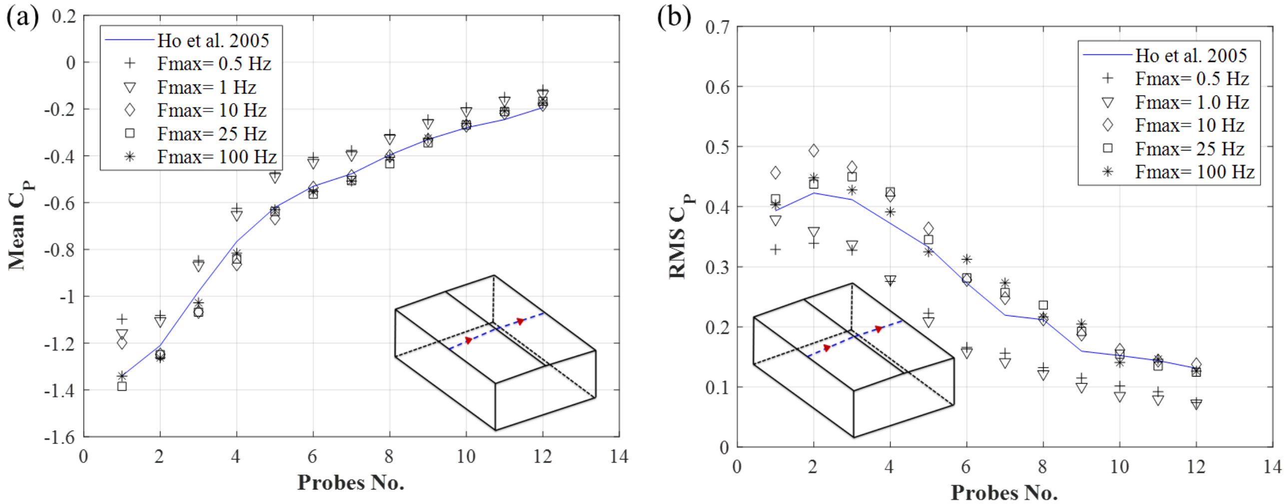

Fig. 4.17 (a) Mean and (b) RMS of the pressure coefficients for probe points across the roof examining a range of maximum turbulent frequencies.

4.5. Summary and Conclusion

This study explored the influence of maximum frequency values f_{max} used in the inflow generation of synthetic turbulent flows within the Atmospheric Boundary Layer (ABL) and their impact on wind load evaluations for low-rise buildings. By employing numerical models using LES, the investigation assessed how variations in f_{max} affected the generation of turbulent inflow and the subsequent wind pressure distributions on building surfaces. The findings revealed that lower values of f_{max} (e.g., 0.5 Hz) resulted in smoother wind profiles with reduced turbulence intensity, primarily due to the presence of larger, slower-moving eddies. These profiles exhibited less variation in velocity and turbulence, which, while more stable, did not adequately capture the smaller, higher-frequency eddies that contribute to more dynamic wind behaviour. On the other hand, higher values of f_{max} (up to 100 Hz) generated more turbulent flows with increased fluctuation in wind velocity, replicating the smaller, faster-moving eddies in the flow. This resulted in higher turbulence intensity and a more accurate representation of wind pressures, particularly on roof surfaces. A significant outcome of the study is the strong correlation between f_{max} and the accuracy with load evaluations on low-rise buildings and the aerodynamic profile injected into the computational domain. Higher f_{max} values led to more accurate mean and RMS pressure distributions on building surfaces. In conclusion, the analysis highlighted the importance of carefully selecting maximum frequency values in synthetic turbulence generation for LES-based wind load evaluations. These findings underscore the need for precise inflow generation techniques in computational wind engineering to ensure that low-rise structures are designed to withstand wind-induced forces in various terrain conditions. The study's recommendations contribute to improved computational efficiency and more reliable wind load evaluations, leading to safer and more resilient building designs.

4.6. References

[1] R.N. Banks, D. and Meroney, A model of roof-top surface pressures produced by conical vortices: Evaluation and implications, Wind Struct. 4(4), p.2 (2001).

[2] H. Kawai, G. Nishimura, Characteristics of fluctuating suction and conical vortices on a flat roof in oblique flow, J. Wind Eng. Ind. Aerodyn. 60 (1996) 211–225. https://doi.org/10.1016/0167-6105(96)00035-9.

[3] D. Surry, J.X. Lin, The effect of surroundings and roof corner geometric modifications on roof pressures on low-rise buildings, J. Wind Eng. Ind. Aerodyn. 58 (1995) 113–138. https://doi.org/10.1016/0167-6105(95)00016-K.

[4] Y. Tominaga, T. Stathopoulos, Numerical simulation of dispersion around an isolated cubic building: Model evaluation of RANS and LES, Build. Environ. 45 (2010) 2231–2239. https://doi.org/10.1016/J.BUILDENV.2010.04.004.

[5] Y. Tominaga, T. Stathopoulos, CFD modeling of pollution dispersion in a street canyon: Comparison between LES and RANS, J. Wind Eng. Ind. Aerodyn. 99 (2011) 340–348. https://doi.org/10.1016/J.JWEIA.2010.12.005.

[6] P. Gousseau, B. Blocken, T. Stathopoulos, G.J.F. van Heijst, CFD simulation of near-field pollutant dispersion on a high-resolution grid: A case study by LES and RANS for a building group in downtown Montreal, Atmos. Environ. 45 (2011) 428–438. https://doi.org/10.1016/J.ATMOSENV.2010.09.065.

[7] M. Ricci, L. Patruno, S.D.M.-E. Structures, undefined 2017, Wind loads and structural response: Benchmarking LES on a low-rise building, Elsevier. (n.d.). https://www.sciencedirect.com/science/article/pii/S0141029617312774 (accessed October 25, 2023).

[8] K. Nozawa, T. Tamura, Large eddy simulation of the flow around a low-rise building immersed in a rough-wall turbulent boundary layer, J. Wind Eng. Ind. Aerodyn. 90 (2002) 1151–1162. https://doi.org/10.1016/S0167-6105(02)00228-3.

[9] A.M. Aly, H. Gol-Zaroudi, A.M. Aly, G. Zaroudi, Peak pressures on low rise buildings: CFD with LES versus full scale and wind tunnel measurements, 30 (2020) 99–117. https://doi.org/10.12989/was.2020.30.1.099.

[10] R. Al-Chalabi, A. Elshaer, Aerodynamic mitigation of low-rise building with complex roof geometry, Front. Built Environ. 9 (2023) 1200383. https://doi.org/10.3389/FBUIL.2023.1200383/BIBTEX.

[11] Y. Tominaga, A. Mochida, R. Yoshie, H. Kataoka, T. Nozu, M. Yoshikawa, T. Shirasawa, AIJ guidelines for practical applications of CFD to pedestrian wind environment around buildings, J. Wind Eng. Ind. Aerodyn. 96 (2008) 1749–1761. https://doi.org/10.1016/J.JWEIA.2008.02.058.

[12] A.K. Dagnew, G.T. Bitsuamlak, Computational evaluation of wind loads on a standard tall building using les, Wind Struct. An Int. J. 18 (2014) 567–598. https://doi.org/10.12989/WAS.2014.18.5.567.

[13] M. Ricci, L. Patruno, I. Kalkman, S. de Miranda, B. Blocken, Towards LES as a design tool: Wind loads assessment on a high-rise building, J. Wind Eng. Ind. Aerodyn. 180

(2018) 1–18. https://doi.org/10.1016/J.JWEIA.2018.07.009.

[14] A. Elshaer, H. Aboshosha, G. Bitsuamlak, A. El Damatty, A. Dagnew, LES evaluation of wind-induced responses for an isolated and a surrounded tall building, Eng. Struct. 115 (2016) 179–195. https://doi.org/10.1016/J.ENGSTRUCT.2016.02.026.

[15] R. Al-Chalabi, A. Elshaer, H. Aboshosha, Enhancing LES efficacy in wind load evaluation of low-rise buildings using synthesized inflow turbulence, J. Build. Eng. 95 (2024) 110233. https://doi.org/10.1016/J.JOBE.2024.110233.

[16] R.H. Kraichnan, Diffusion by a random velocity field, Phys. Fluids. 13 (1970) 22–31. https://doi.org/10.1063/1.1692799.

[17] A. Li, G. Ahmadi, R.G. Bayer, M.A. Gaynes, Aerosol particle deposition in an obstructed turbulent duct flow, J. Aerosol Sci. 25 (1994) 91–112. https://doi.org/10.1016/0021-8502(94)90184-8.

[18] J. Fung, J. Hunt, … N.M.-J. of F., U. 1992, Kinematic simulation of homogeneous turbulence by unsteady random Fourier modes, J. Fluid Mech. 281-318. (1992).

[19] A. Smirnov, S. Shi, I. Celik, Random flow generation technique for large eddy simulations and particle-dynamics modeling, J. Fluids Eng. 123 (2001) 359–371.

[20] P. Batten, U. Goldberg, S. Chakravarthy, Interfacing Statistical Turbulence Closures with Large-Eddy Simulation, Https://Doi.Org/10.2514/1.3496. 42 (2012) 485–492. https://doi.org/10.2514/1.3496.

[21] M. Klein, A. Sadiki, J. Janicka, A digital filter based generation of inflow data for spatially developing direct numerical or large eddy simulations, J. Comput. Phys. 186 (2003) 652–665. https://doi.org/10.1016/S0021-9991(03)00090-1.

[22] N. Jarrin, S. Benhamadouche, D. Laurence, R. Prosser, A synthetic-eddy-method for generating inflow conditions for large-eddy simulations, Int. J. Heat Fluid Flow. 27 (2006) 585-593. https://doi.org/10.1016/j.ijheatfluidflow.2006.02.006.

[23] H. Tieleman, Wind tunnel simulation of wind loading on low-rise structures: a review, J. Wind Eng. (2003). https://www.sciencedirect.com/science/article/pii/S0167610503001326.

[24] H. Aboshosha, A. Elshaer, G.T. Bitsuamlak, A. El Damatty, Consistent inflow turbulence generator for LES evaluation of wind-induced responses for tall buildings, J. Wind Eng. Ind. Aerodyn. 142 (2015) 198–216. https://doi.org/10.1016/j.jweia.2015.04.004.

[25] J. Chen, A. Elshaer, H. Aboshosha, G. Pedro, Calibrated consistent flow generator for tall building aerodynamics using large eddy simulation, Results Eng. 16 (2022) 100634.

[26] M. Alanani, A. Elshaer, ANN-based optimization framework for the design of wind load resisting system of tall buildings, Eng. Struct. 285 (2023) 116032. https://doi.org/10.1016/J.ENGSTRUCT.2023.116032.

[27] Q. Yang, T. Wang, B. Yan, T. Li, M.L.-J. of W.E. and, undefined 2021, Nonlinear motion-induced aerodynamic forces on large hyperbolic paraboloid roofs using LES, Elsevier. (n.d.). https://www.sciencedirect.com/science/article/pii/S0167610521001859 (accessed October 25, 2023).

[28] W.H. Melbourne, Turbulence Effects on Maximum Surface Pressures - A Mechanism and Possibility of Reduction, Zement-Kalk-Gips. 1 (1980) 541–551. https://doi.org/10.1016/B978-1-4832-8367-8.50055-3.

[29] M.J. Morrison, G.A. Kopp, Effects of turbulence intensity and scale on surface pressure fluctuations on the roof of a low-rise building in the atmospheric boundary layer, J. Wind Eng. Ind. Aerodyn. 183 (2018) 140–151. https://doi.org/10.1016/J.JWEIA.2018.10.017.

[30] H.W. Tieleman, Wind tunnel simulation of wind loading on low-rise structures: a review, J. Wind Eng. Ind. Aerodyn. 91 (2003) 1627–1649. https://doi.org/10.1016/J.JWEIA.2003.09.021.

[31] T.C.E. Ho, D. Surry, D. Morrish, G.A. Kopp, The UWO contribution to the NIST aerodynamic database for wind loads on low buildings: Part 1. Archiving format and basic aerodynamic data, J. Wind Eng. Ind. Aerodyn. 93 (2005) 1–30. https://doi.org/10.1016/J.JWEIA.2004.07.006.

[32] J.M. Denmark, Atmospheric turbulence, Breeze.Colorado.EduJ MannDTU Wind Energy, Tech. Univ. Denmark, Denmark, DK, 2012 (2012). https://breeze.colorado.edu/ftp/RSWE/Jakob_Mann.pdf.

[33] R.A. Sanni, D. Surry, A.G. Davenport, Wind loading on intermediate height buildings, Can. J. Civ. Eng. 19 (1992) 148–163. https://doi.org/10.1139/L92-015.

[34] R. Courant, K. Friedrichs, H. Lewy, Über die partiellen Differenzengleichungen der mathematischen Physik, Math. Ann. 100 (1928) 32–74. https://doi.org/10.1007/BF01448839.

[35] M.J. Morrison, G.A. Kopp, Effects of turbulence intensity and scale on surface pressure fluctuations on the roof of a low-rise building in the atmospheric boundary layer, J. Wind Eng. Ind. Aerodyn. 183 (2018) 140–151.

CHAPTER 5

The influence of terrain roughness on parapet efficiency in mitigating wind loads on low-rise buildings: An experimental study

5.1. Introduction

The significance of buildings' aerodynamic performance has grown in recent decades, primarily due to the heightened intensity and frequency of windstorms [1]. Most low-rise buildings are traditionally constructed with limited consideration of wind loads, and therefore more vulnerable to windstorms [2]. The fluctuating nature of wind patterns, specifically within urban environments, along with the added variability caused by the disrupted wind flow due to interaction with buildings can result in significant pressure fluctuations influenced by the flow dynamics and building geometrical configuration [3]. A substantial number of post-disaster damage studies and insurance revealed that damage in low-rise buildings is initiated by roof damage hence, it is considered the leading cause of damage to residential dwellings [4]. According to recent studies, in Ontario, Canada, the percentage of low-rise building damages caused by wind events exceeded 72%, whereas, in 2018, damages cost suppressed the 300 million dollars [5]. Wind load distribution and magnitude on low-rise buildings depend on many factors, which can be mostly summarized as the building geometry and the upstream flow characteristics [6]. These factors significantly influence the response of building components, impacting their structural integrity and performance [7]. A wide range of variables are involved in wind load magnitude on low-rise building roofs and walls, such as terrain roughness, incidence angle, and structural details (i.e., roof shape) [8].

Numerous studies have examined the impact of wind load on low-rise buildings where the most critical mean and peak suction are observed on roof corners near the edge for oblique wind directions caused by the existence of conical vortices resulting from flow detachment at edges and corners as depicted in Fig. 5.1 [9–13]. These vortices can lead to a chain of failures in the building structure that may start from the dislodging of the roof component to total roof connection failure, hence failing the entire system [14], as demonstrated in Fig. 5.2. Improving the resiliency of low-rise buildings can be achieved by adding aerodynamic mitigation techniques located at the roof edges and corners. Though most are solid and straight, there is an infinite variety of parapet geometries. Solid parapets can displace the corner vortices away from the roof surface, reducing the peak suctions at the corner. Building codes, such as NBCC, based on testing of isolated low-rise buildings, have recommended using perimetric parapets at a height of 1.0 m on low-rise buildings to allow the reduction of design pressure on the roof to up to 18%.

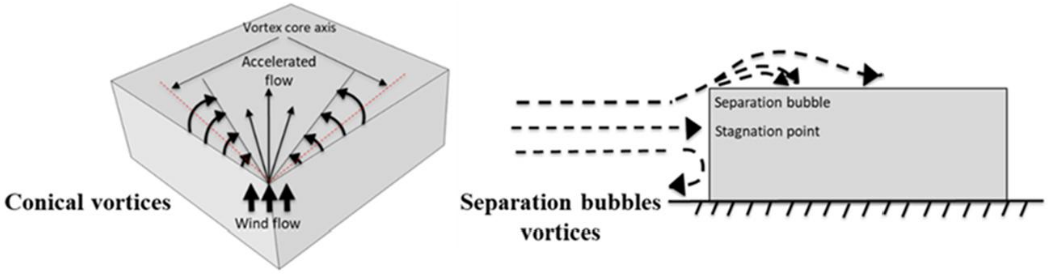

Fig. 5.1 Schematic view of conical vortices developing on the top surface of a bluff body subjected to the oblique fluid flow [15].

Over the past few decades, numerous numerical and experimental studies have examined the aerodynamic efficiency of the parapets installed at various locations on the roof surfaces of low-rise buildings in an open terrain exposure. These studies have helped to understand better and predict the working mechanism of aerodynamic mitigation techniques in reducing the wind pressures on mainly the roof surfaces of low-rise buildings. Several studies have found that the efficacy of a parapet in reducing the magnitude of wind pressures highly depends on the parapet's height and wind direction [9,16,17]. Some studies concluded that roof geometrical configurations are critical in determining the parapet's efficiency in reducing the pressure's mean and RMS [18,19]. Other studies examined the impact of parapet's porosity installed on gable roofs of low-rise buildings embedded in open terrain on their aerodynamic mitigation efficiency [20,21]. Furthermore, to alleviate the impact of flow separation at edges, previous studies have examined the addition of spoilers and soffits on a low-rise building roof [8,22,23].

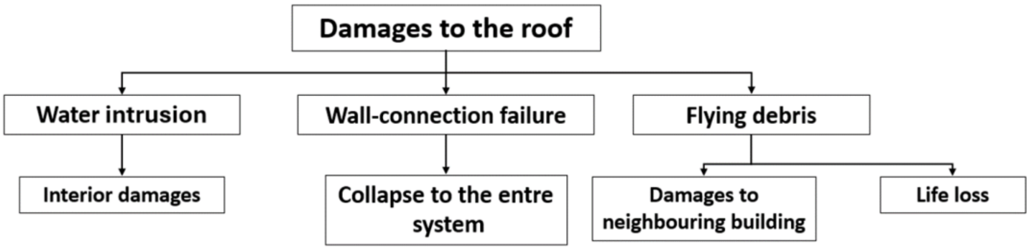

Fig. 5.2 Damages to low-rise buildings during wind event

The low-rise building is located in the lower of the atmospheric boundary layer. Hence, the impact of terrain roughness is more notable due to elevated turbulence. Terrain configuration, among other factors, as underscored in Davenport's wind loading chain, can impact wind-induced pressure, introducing uncertainties in wind loads [24]. Very few studies have discussed the effect of terrain complexity on wind loads. Previous studies examined wind pressure coefficients and flow fields around isolated low-rise buildings through wind tunnel tests, numerical simulations, and full-scale measurements utilizing uniform terrain conditions [25–29]. The current design codes for wind loads are evaluated, while the aerodynamic pressure coefficients are based on wind-tunnel measurements on isolated buildings [30,31]. Isolated buildings are rare, particularly for low-rise buildings, normally arranged in groups in populated areas. The existence of nearby buildings disrupts wind flow and hence alters the pressure distribution variations compared to those observed in isolated low-rise structures [32]. Studies by Tamura [28] and Wang and Stathopoulos [33] have emphasized the influence of upwind terrain within a range of 500 m to 1000 m from buildings, highlighting the importance of considering broader terrain configurations in wind load assessments. To meticulously understand the impact of examining how wind pressure varies on low-rise buildings located in a real-life urban condition, a series of wind tunnel experimental studies are conducted by Ho et al. [30] and Chang and Meroney [34]. Their research highlights the intricate relationship between nearby buildings and the resulting pressure patterns, showing significant fluctuations in surface pressure caused by neighbouring structures. Ho et al. studied the effects of three types of immediate upstream surroundings on wind loads on flat-roof low-rise buildings for open and suburban exposures [35]. They found higher wind loads in smoother terrains due to increased peak wind speeds. Conversely, peak pressure coefficients can be higher in rougher terrains due to reduced mean wind speeds and increased turbulence intensity. Chang and Meroney investigated the effect of surrounding buildings arranged in various symmetric configurations with different separation distances. They concluded that shielding impacts are significant, especially when the street canyon is narrow, and the effects are greater in urban cases than in open country cases [34]. Lee-Sak An et al. conducted a series of wind tunnel tests using 50 actual terrain morphology to evaluate the impact of terrain complexity on wind pressure across low-rise buildings [36]. The roof contour examination revealed that reattachment length in complex terrain is longer than in homogeneous terrain due to higher turbulence intensity, which reduced the shear layer's curvature. The findings apply to the minimum mean and RMS of the pressure coefficients across the roof.

While extensive research has focused on the impact of parapet placement in reducing wind loads on buildings in open terrain, there has been less exploration of the effectiveness of low-height parapets in mitigating wind loads in suburban areas, which is common in urban settings. Accordingly, this study aims to address three key areas: (a) unlike most previous studies that have focused on a 3:12 roof slope, this research seeks to explore aerodynamic mitigation for low-sloped gable roofs; (b) while prior investigations have primarily examined corner and perimeter parapets on roofs in open terrain, this study will assess the performance of these parapets in both open and suburban terrains; and (c) previous studies typically used parapets with full-scale heights ranging from 0.75 to 0.9 m, whereas this study employs a more practical parapet height of 0.6 m. The research will evaluate the effectiveness of parapets in reducing wind pressures on structures under two different terrain roughness conditions and with two parapet configurations added to the benchmark model: perimetric parapets (M1) and corner parapets (M2). The parapet's performance will be assessed using the mean, RMS, and peak pressures induced on the building façade, especially at critical locations where post-damage surveys have shown damage initiation. All models are tested at wind angles of attack ranging from 0° to 90° with 10° increments.

The current study is divided into five sections. Section 1 (this section) discusses the main motive behind this study. Section 2 provides a detailed methodology framework to examine the low-height parapet's efficiency in various terrain setups. Section 3 presents an overview of the experimental wind tunnel testing setup, including the utilized wind aerodynamic profile for open and suburban terrains. In addition, details of the utilized test model geometrical configuration and the tap arrangement are presented, and the details of the geometrical configuration of the various parapets are tested. The following section, section 4, provides the experimental results of modified and non-modified models in various terrains to examine the parapet's efficiency in terms of the mean, RMS, and the peak of the pressure, mainly on the roof of a low-rise building. A subsection for a numerical analysis using Large Eddy Simulation (LES) is added to investigate the reason for the reduced parapet efficiency in suburban terrain further. Section 5 presents a summary and conclusion for the findings and recommendations for utilizing parapets in wind load mitigation on low-sloped gable roofs of low-rise buildings located on various terrains.

Methodology Framework

To meet the objectives of this study, the benchmark model (i.e., BM) is tested for the open (i.e. O.T.) and suburban terrains (i.e., S.T.) for all wind angles of attack (i.e., $0°$ to $90°$ with $10°$ increments). A total of 186 pressure taps are utilized and connected to the Data Acquisition System (DAS) to collect surface pressure. Mean fluctuation and peak pressure on the building surface are obtained to assess the pressure magnitude and distribution and examine the added aerodynamic modification efficiency. The critical wind angle of attack is obtained based on the highest suction values on the roof surface. Modification techniques (i.e., perimetric and corner parapets) are added to the benchmark model and tested at all wind angles of attack, where only the critical wind angle of attack results will be displayed for comparison with the BM model. The flow chart explains the method followed in this study and is presented in Fig. 5.3.

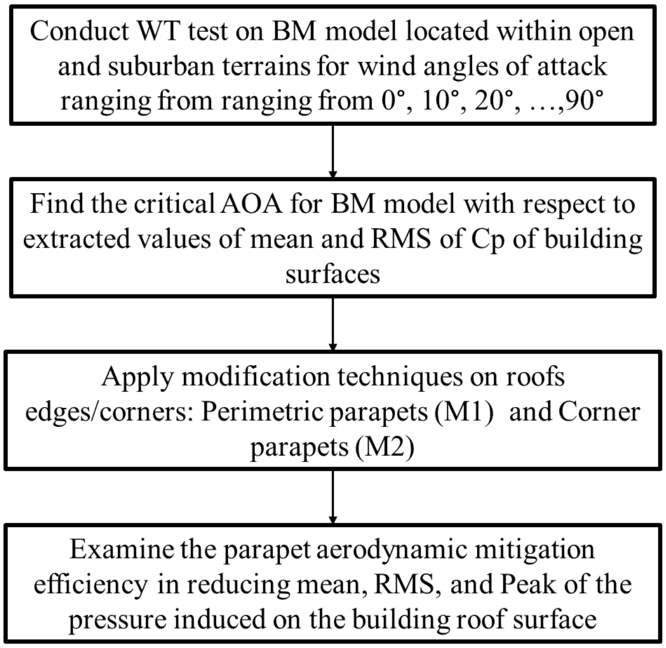

Conduct WT test on BM model located within open and suburban terrains for wind angles of attack ranging from ranging from 0°, 10°, 20°, …,90°

Find the critical AOA for BM model with respect to extracted values of mean and RMS of Cp of building surfaces

Apply modification techniques on roofs edges/corners: Perimetric parapets (M1) and Corner parapets (M2)

Examine the parapet aerodynamic mitigation efficiency in reducing mean, RMS, and Peak of the pressure induced on the building roof surface

Fig. 5.3 Flow chart showing the methodology followed in this study.

5.2. Experimental Wind Tunnel Test Setup

The wind tunnel test is conducted at Toronto Metropolitan University (TMU), which produces a smooth flow. To generate turbulence, the system uses horizontal slats fixed on four Spiers along with 6 rows of staggered roughness blocks of 100 mm height, as shown in Fig. 5.4. The test setup at TMU-WT is validated using the TTU building, and low-rise buildings [37,38]. One rigid arm is used to fix four pitot tubes upstream of the models at heights ranging from $0.067\ m$ to $0.75\ m$

(model scale) to measure the mean wind flow during the test. The benchmark low-rise building model has model-scale dimensions of $0.152\,m$ (width) × $0.23\,m$ (length) × $0.067m$ (height) fabricated at a length scale of $1{:}\,60$ and a gable roof with a slope of $0.25{:}\,12$. Special attention is given to the roof edges and corners; hence more pressure taps are installed in these regions. A total of 186 tabs are used to measure pressure distributions on the low-rise building model surfaces, most of which are located on the roof, as illustrated below. The tabs are connected to the data acquisition (DAQ) system mounted under the turntable. Each pressure tab was linked to a corresponding channel using a tube measuring $1.3\,m$ long with an inner diameter of $1.28\,mm$.

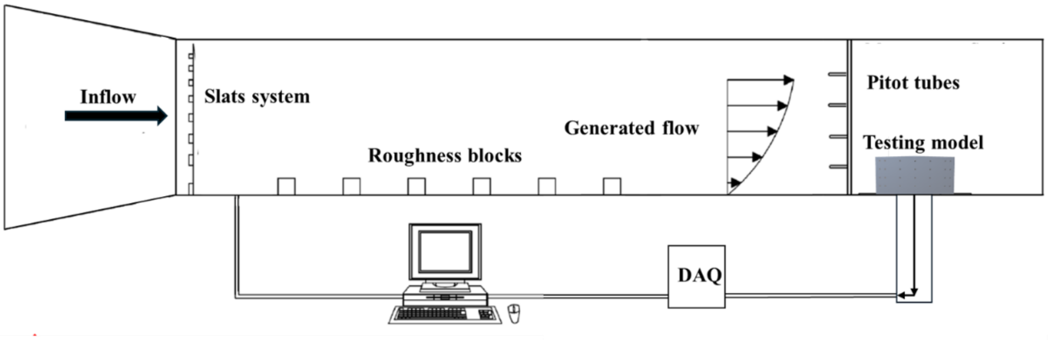

Fig. 5.4 Wind tunnel testing facility at TMU.

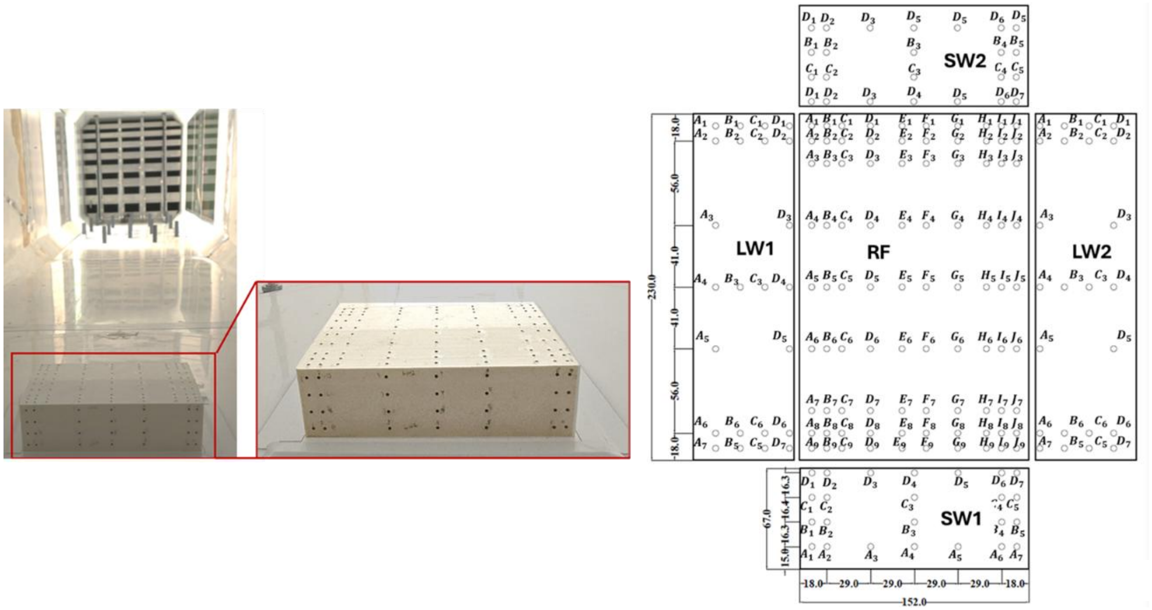

Fig. 5.5 The building model and the layout of the pressure taps on the surfaces.

Two boundary layer flows are simulated in the wind tunnel using a combination of turbulence-generating elements for different terrain types (i.e., open and suburban terrains). According to building codes, the roughness of open terrain conditions ranges from $0.01\,m$ to $0.15\,m$. The suburban terrain exposure roughness lengths range between $0.15\,m$ and $0.7\,m$. The turbulence production mechanism is adjusted to achieve wind profile characteristics of open terrain z_o of $0.03\,m$ and for suburban terrain of $0.25\,m$. The measured mean velocity and turbulence profiles show good agreement with the ESDU using the Power Law (i.e., Eq. (1)) for the mean wind velocity. The U_{10} refers to the wind velocity at $10\,m$ height. The z refers to the height in meters corresponding to the reference wind velocity. The turbulence intensity is calculated for the target profile using the equation below (Eq. (2)).

$$U_z = U_{10}(\frac{z}{10})^{1/\alpha} \tag{1}$$

$$I_u = c_u \left(\frac{z_{ref}}{z}\right)^{bu} \tag{2}$$

The mean wind velocity profiles have been normalized by the velocity at $10\,m$ (full-scale). The resulting turbulence intensities (I_u) at the mean roof height ($4.0\,m$ in full-scale) are equal to approximately 15% and 21%, respectively. The mean velocity and turbulence intensity profiles are in reasonable agreement with the target profiles from the ESDU, as depicted in Fig. 5.6. The surface pressure is collected at a sampling rate of 520 Hz for the wind angle of attacks ranging from 0° to 90° with 10° increments, the total testing time is 2 hours, and 30 minutes corresponds to 15 minutes for every wind increment (full-scale). This direction is then estimated by measuring the angle between the tunnel airflow and the building model's roof ridge. The same setup is repeated to test two aerodynamically mitigated models using parapets. All the details of the wind tunnel setup are presented in Table 5.1. Both parapet configurations added have the same height and width but vary in location and length, as demonstrated in Fig. 5.7. The pressure coefficient is obtained by referencing the data to the dynamic pressure at mean roof height (i.e., $4m$ in full scale). The dynamic pressure coefficient referenced to mean roof height is given by, $C_p = P/q_h$. Hence, P is the pressure difference measured between the pressure time history measured on the model surface and the reference static pressure (i.e., $P_i(t) - P_{tab}$), while q_h is the reference dynamic pressure given by $\frac{1}{2}\rho\, U_{ref}^2$ at mean roof height at an air density, ρ, of $1.2929\ kg/m^3$.

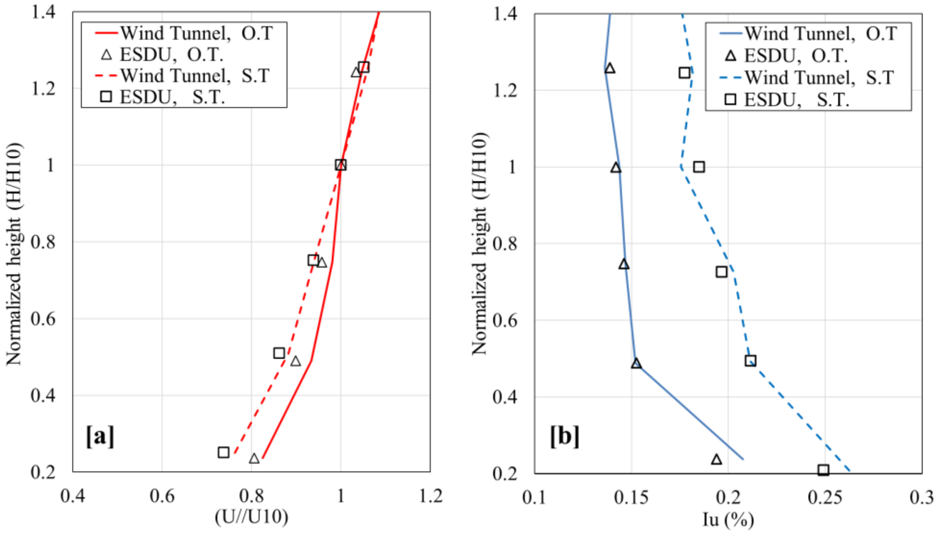

Fig. 5.6 (a) Normalised mean wind velocity profile and (b) Turbulence intensity profiles.

Table 5.1 Measurement configurations and parameters

Test setup	Open Terrain	Suburban Terrain
Length scale	1:60	
Time scale	1:15	
Velocity scale	1:4	
Pitot tube heights	0.067, 0.25, 0.45, and 0.75m	
Wind angle of attack	0°, 10°, 20°, …., 90°	
Roof reference height (H)	0.067 m	
Test duration	30 seconds	
Sampling frequency	520 Hz	
Reference velocity at H	12.9 (full-scale)	10.4 m/s (full scale)
Roughness length (z_o)	0.03m	0.25m

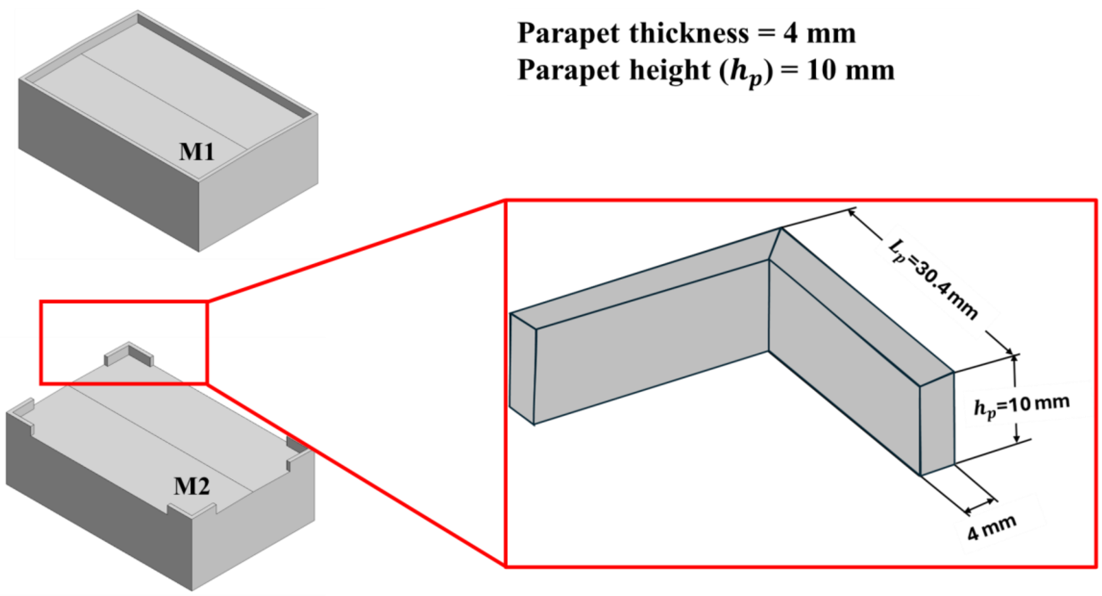

Fig. 5.7 Modified models using perimetric (M1) and corner parapets (M2).

5.3. Results and Discussion

A 60-second (model-scale) test is run for benchmark and modified models for each wind angle of attack where peak, mean, and pressure fluctuation are measured on the building surfaces for open and suburban terrain exposures. The results presented here offer a set of data that provides a qualitative delineation of the influence of approach flow conditions on parapet efficiency in altering and reducing pressure distribution and magnitude at different terrains.

5.3.1. Identification of critical wind angle of attack

The test model is placed on the test floor, with the ridgeline facing the wind direction (i.e., 0°), as depicted in Fig. 5.3 (a). To further examine the impact of the terrain on the pressure magnitude and distribution on the benchmark roof surface, the mean and RMS of the pressure values for pressure taps located at the edges (i.e., $\mathrm{RF}-\mathrm{A}_5,\mathrm{A}_7,\mathrm{A}_9$), reference height (i.e., $\mathrm{RF}-\mathrm{C}_5,\mathrm{C}_7,\mathrm{C}_9$), and at the centre close to the ridgeline (i.e., $\mathrm{RF}-\mathrm{E}_5,\mathrm{E}_7,\mathrm{E}_9$) are presented in Fig. 5.7, Fig. 5.8, and Fig. 5.10, respectively. The solid and dotted lines show the differences between the values of open and suburban terrain readings, respectively.

Following the testing of the benchmark model, the differences between mean and RMS C_p values for the benchmark model are apparent, especially on taps located at the leading edge near the corner. For suburban flow conditions with higher turbulence levels, the value of mean pressure is lower compared to smooth flow conditions (i.e., open terrain). The latter is caused by the rapid decrease in velocity of the approached flow in the rough terrain compared to smoother ones. It can be noticed that the minimum values of the mean pressure are located at the edges when the flow approaches the benchmark model at an oblique wind direction of 50°. This is because strong conical vortices are formed at the roof's edges due to the incident approached flow at the leading edge of the roof surface, where the rolling of the separated shear layer can induce a peak suction when the gust attacks the building from an oblique direction. The contour plot for the mean and RMS of the pressure for the benchmark model located in an open terrain is presented in Fig. 5.11(b) and (b). In particular, the maximum suction ($Cp = -2.8$) for tap A_7 in open terrain, the suction for the same tap is almost doubled compared to that for suburban terrain. It can be depicted that for the benchmark model in an open terrain oriented at 50°, the peak suction at the location on the longer side of the roof parallel to the ridgeline occurred at a distance of $x = 8\,mm$, $y = 8\,mm$ away from the leading corner, while for the shorter side, perpendicular to the ridgeline, it occurred at distance $x = 8mm$, $y = 68mm$, away from the leading corner. The maximum suction occurs at a point a slightly away from the roof corner with a magnitude inversely proportional to the conical vortices height as found by previous studies [39]. This can indicate that reducing suction can be achieved by modifying edges/corners aerodynamically. In addition, the precise location of the peak suction pressure can be used to guide the effective length of the discontinuous corner parapets (L_p). In contrast, it is also found that the pressure fluctuation is amplified remarkably by the approaching of particularly turbulent flow (i.e., in suburban terrain). Previous studies found that for buildings with flat roofs, the suction fluctuation near the roof corner can reach three times larger in the turbulent flow than in the smooth flow [40]. Even though the present study focuses on the pressure magnitude and distribution on the roof surface, the cp distribution on all building surfaces is presented in Fig. 5.10. The latter results depict the mean and standard deviation of the roof surface contour plots of the 6 pressure taps on the benchmark model orientated at 50° with respect to the flow. At the same oblique wind angle of attack, the mean and RMS of the pressure on all the building surfaces are presented in Fig. 5.11(a) and (b). The mean pressure contours are stretched along the flow direction, and high suction pressures are noted near the leading corner and edges. In addition, the mean Cp for interior roof zones and edges of the descending roof surface is low. This is probably related to the reattachment of the separated shear layer on the roof of the low-rise building. The flow is on the surface more perpendicularly oriented to the incoming flow where the stagnation area is larger and the respective Cp values are higher. On the contrary, the vertical surfaces oriented toward the negative x- and y-coordinate are characterized by nearly uniform suction.

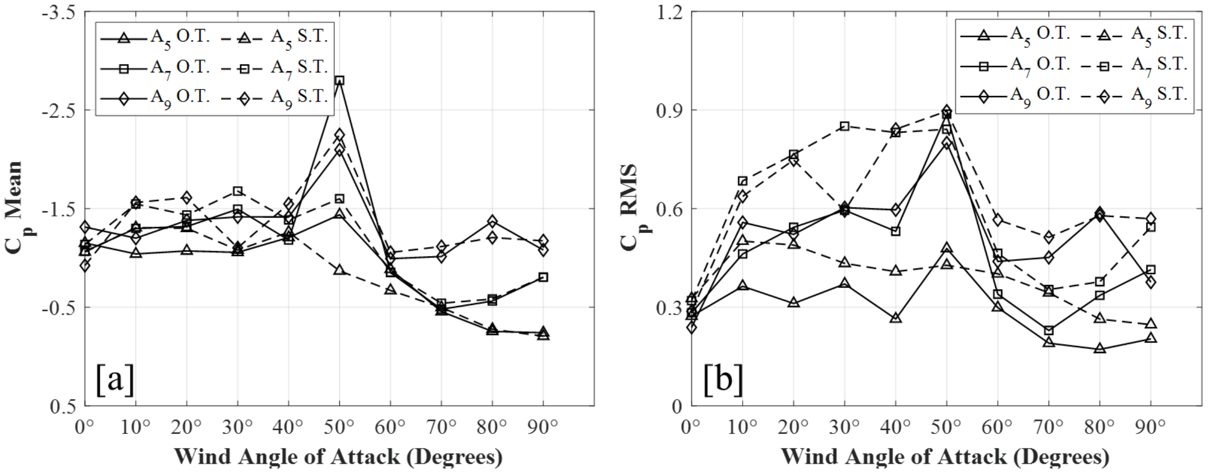

Fig. 5.8 Pressure reading for taps located at edge parallel to the ridgeline (a) mean and (b) RMS of the pressure coefficient.

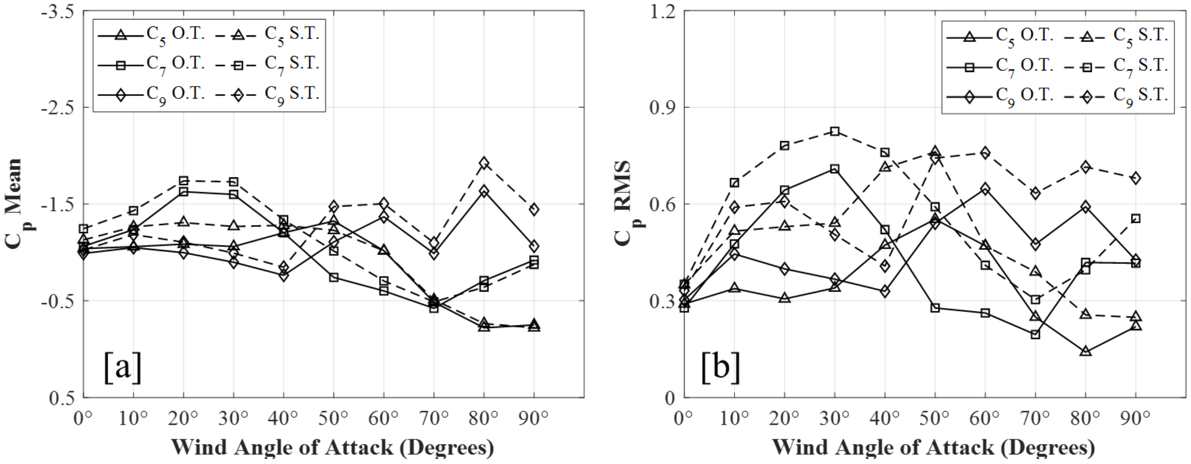

Fig. 5.9 Pressure reading for taps located at reference roof height and parallel to the ridgeline (a) mean and (b) RMS of the pressure coefficient.

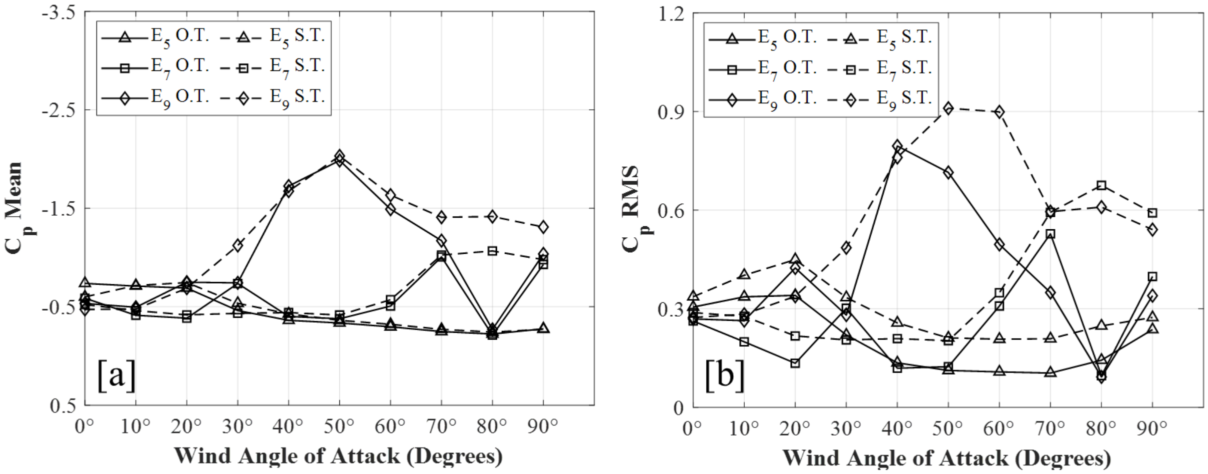

Fig. 5.10 Pressure reading for taps located parallel and close to the ridgeline (a) mean and (b) RMS of the pressure coefficient.

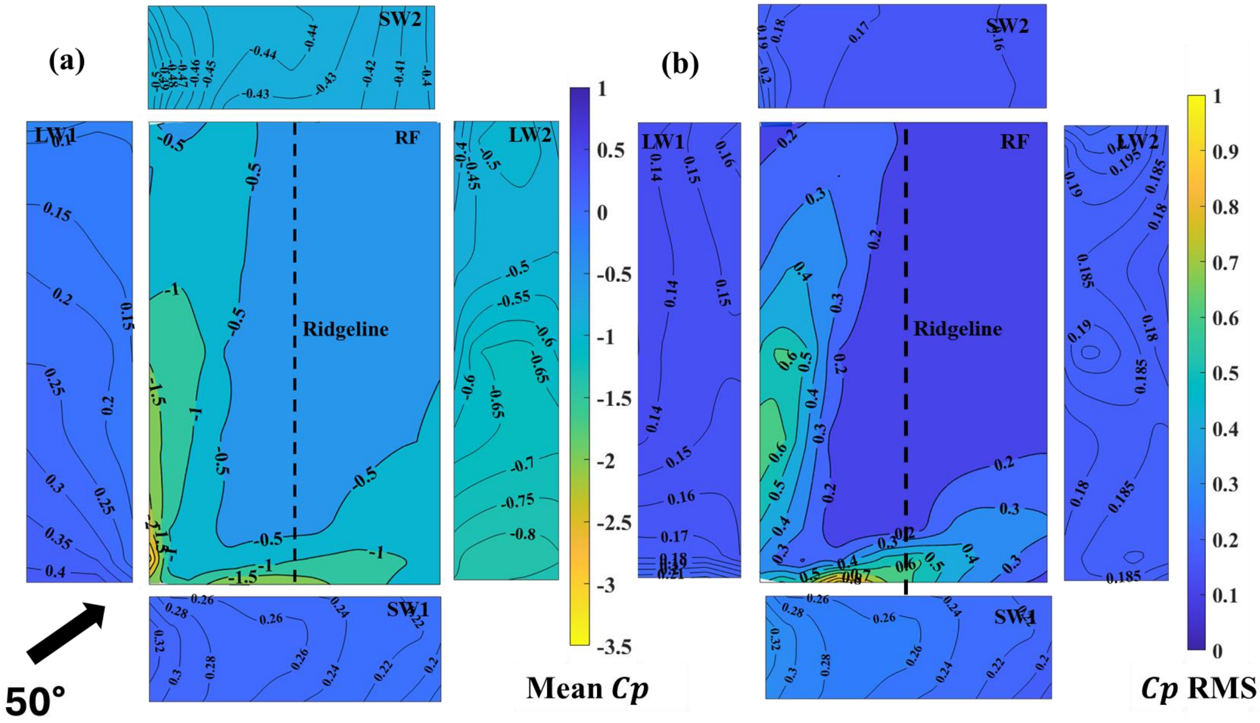

Fig. 5.11 Pressure contours for the BM model located in an open terrain setup (a) mean and (b) RMS of the pressure coefficient.

5.3.2. *Modified models using perimetric and corner parapets*

Overall, it is known that adding a parapet can reduce the pressure's mean and fluctuation, preventing the cladding's dislodging during wind events. The NBCC has recommended the reduction of pressure on low-sloped gable roofs by up to 18% if perimetric parapets exist at heights $\geq 1m$. This suggestion is based on wind tunnel testing for a building model at an isolated (i.e., open terrain) setup. To investigate further the impact of suburban terrain (real-life scenario) on the efficiency of low-height parapets, this study compares the efficiency of parapets installed at low-sloped gable roofs in reducing the pressure on the roof surfaces by employing the most common configuration of parapets (i.e., perimetric, M1 and corner, M2). Since it is found that terrain can amplify the peak pressure, which can lead to initiating the damage at a specific instant, instantaneous peak pressure values will be presented along the mean and fluctuation of the pressure [25]. The contour of the mean and RMS of the pressure for the non-modified and modified models are presented in, Fig. 5.12 and Fig. 5.13. The dotted lines around the modified models refer to the parapet's locations. Reattachment (i.e., downward acting pressure) is noted for the rear roof regions after introducing perimetric parapets for both terrains. Conversely, down-acting pressure regions are found to be significantly limited when introducing corner parapets. Overall, the contour plots show very low pressures in the interior region of the roof, and reductions in the magnitude of negative pressures are magnified at the edges with the introduction of perimetric parapets under the direction of 50°.

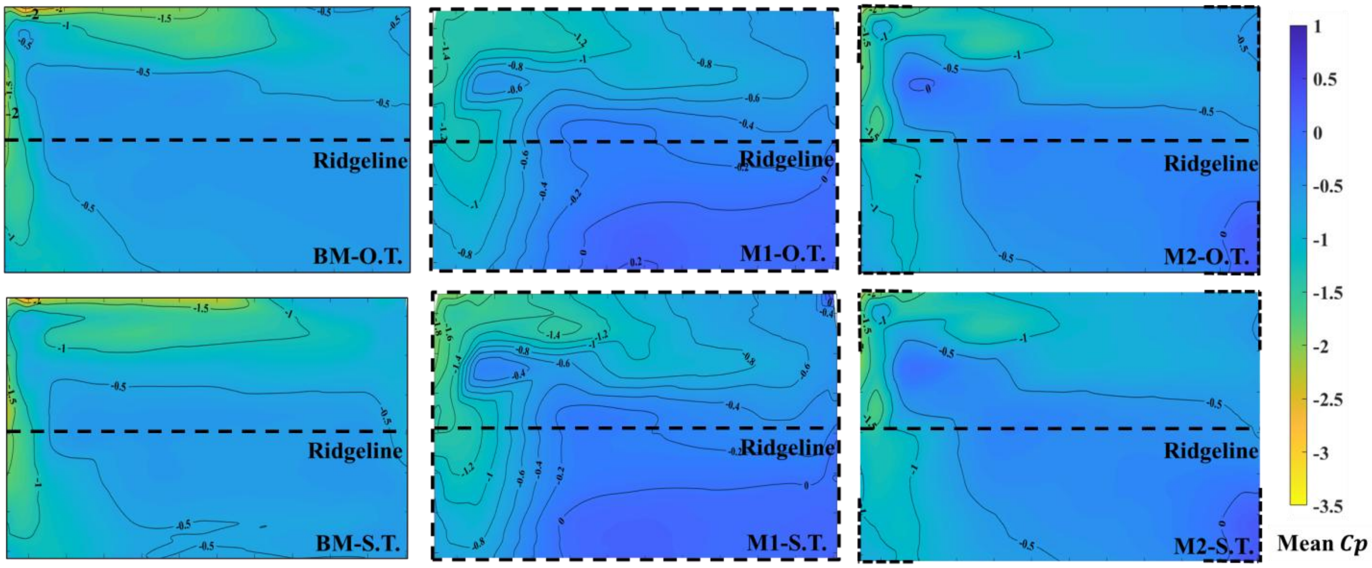

Fig. 5.12 Mean Cp variation for benchmark and modified models located in open terrain and suburban terrain exposures.

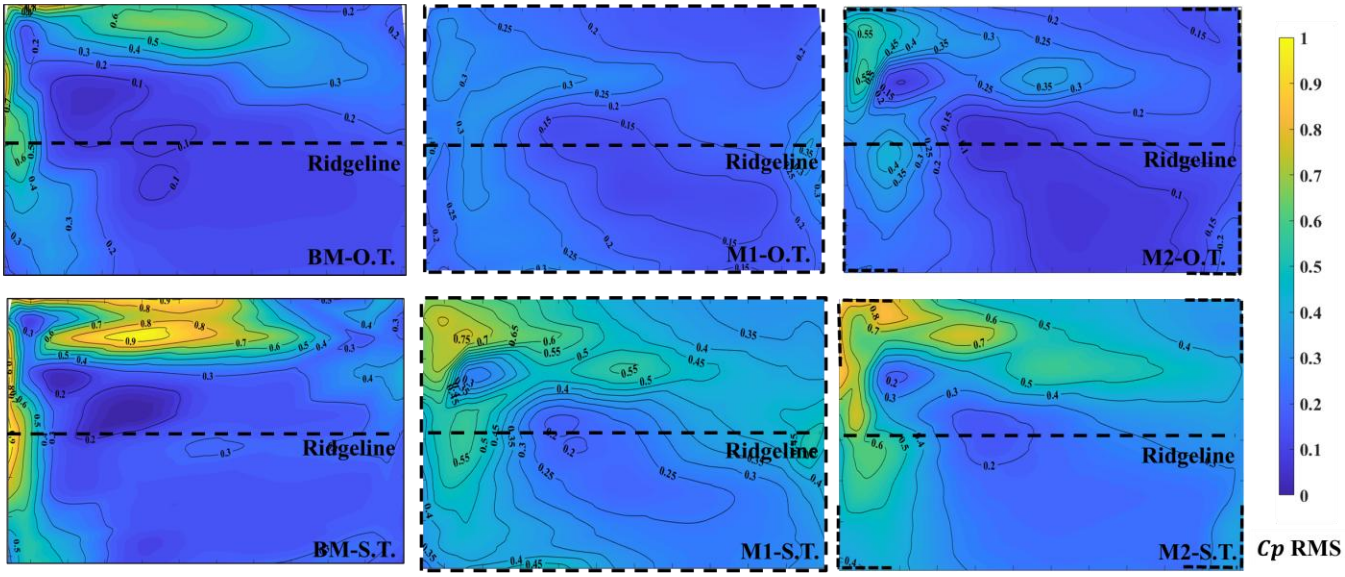

Fig. 5.13 RMS of Cp variation benchmark and modified models located in open and suburban terrain exposures.

To further analyze the parapet impact, a total of 48 taps at 4 locations on the roof surface are selected where a high suction zone can be found, as shown in Fig. 5.13. Point pressures are compared between the bare-roof case and those with parapets to understand their effects in reducing localized pressures. For the open terrain case, the suction pressure along the diagonal and the leading edges decreases with the presence of the parapet. For suburban flow conditions with a higher level of turbulence, a reduction in the value of mean pressures is noted in the case of the perimetric parapet. A perimetric parapet influences pressure recovery, resulting in flow reattachment in the rear region of the roof (i.e., descending roof surface). Introducing a higher level of turbulence (i.e., suburban terrain) led to a decrease in the efficiency of the corner parapets, particularly at the edges. In particular, in Fig. 5.14, by comparing the mean pressure found at the tap A_8 of the open to the suburban terrain, it is found that they are close in value to approximately -2.0, which can serve as an indication that may not influence the corner parapets' efficiency in reducing mean pressure. In summary, it is observed that the highest suction pressure decreases for both flow conditions in the case of the perimetric parapets. The decrease in the mean pressure is relatively more pronounced for open country flow than suburban flow.

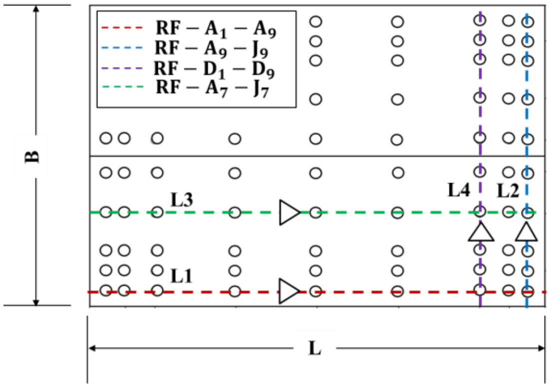

Fig. 5.14 Taps locations selected for mean, RMS and peak pressure comparisons.

For a safe cladding and structural design, mean pressure alone is insufficient to ensure structures' safety. Hence, pressure fluctuations and peak values are obtained. It is noticed that the parapet's efficiency in reducing the pressure fluctuation has significantly varied from open to suburban terrain. In the case of the benchmark model located in open terrain, the standard deviation Cp values ranged from 0.2 to 0.8. In contrast, with the addition of the perimetric parapet, the standard deviation Cp varied from 0.1 to 0.46. It is noticed that the introduction of the perimetric parapet reduces the standard deviation Cp on the roof, as shown in Fig. 5.15. The latter parapets are reduced in some areas, especially at the leading corner, for the cases of 55% and 20% for tap A_8. The only exception is found for the interior zones, whereby introducing suburban terrain suppressed the pressure fluctuation on the benchmark model as depicted in Fig. 5.15 (c). Upon adding the corner parapets on the benchmark model located in rough terrain, it is found to be not efficient in reducing the standard deviation of roof pressures, specifically at tap A_8. This indicates that corner parapets may not reduce roof pressures under oblique wind directions. Corner parapets that have increased in length may reduce the increased turbulence resulting from a cultured build-up environment.

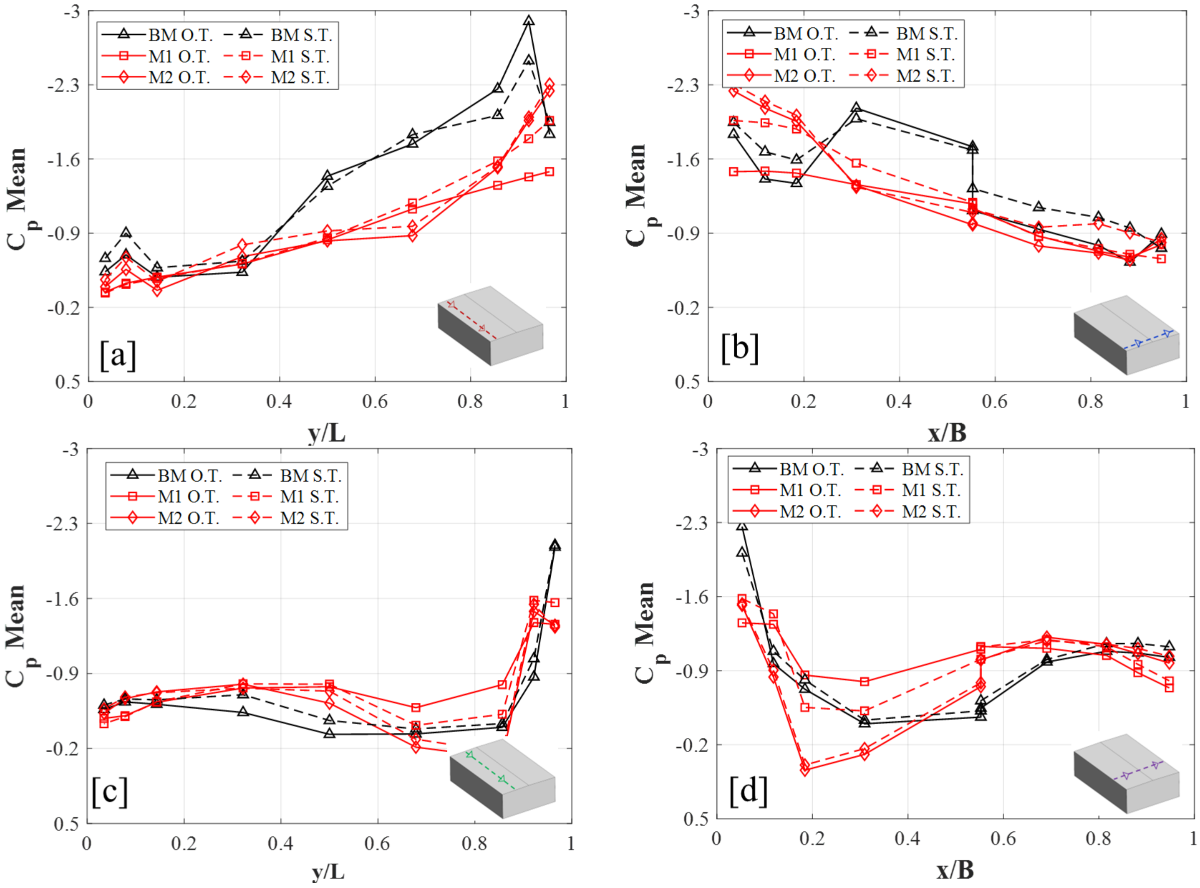

Fig. 5.15 Mean pressure reading for taps located along the ridgeline at (a) L1, and (b) L2 and perpendicular to the ridgeline at (c) L3, and (d) L4.

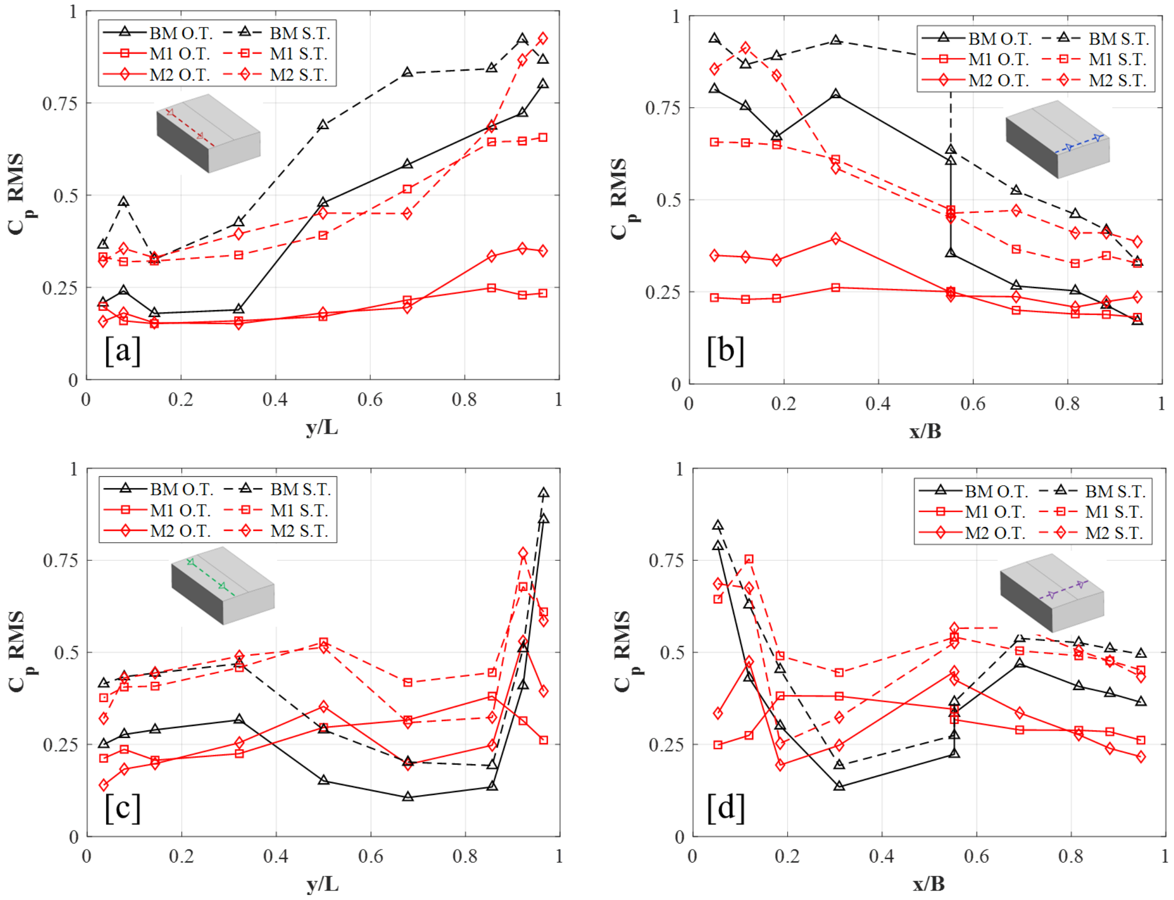

Fig. 5.16 RMS pressure reading for taps located along the ridgeline at (a) L1, and (b) L2 and perpendicular to the ridgeline at (c) L3, and (d) L4.

It is noticed that the standard deviation of Cp values for the taps on the benchmark are higher than those of the roof with a parapet, which means there is a reduction in turbulence at the roof edges with the introduction of the parapet. Accordingly, the peak pressures are also reduced. Perimetric parapets yielded greater reductions in peak pressures. The corner and edge zones experienced high minimum pressures as can be seen in Fig. 5.17. The tap located on the leading corner of the roof has a minimum localized pressure coefficient. In fact, the taps on the corner of the roof in suburban terrain had a peak Cp of nearly -8.84, which is reduced to -3.66 in the case of the perimetric parapet compared to -5.0 for corner parapets. Tap A_8 and B_9 are selected to present the impact of terrain on the parapet's efficiency in reducing the pressure. These taps are located at the edges of the test model; hence a high suction region of the roof is expected. Table 5.2 shows the best benefit in reducing localized pressures at 50° wind direction.

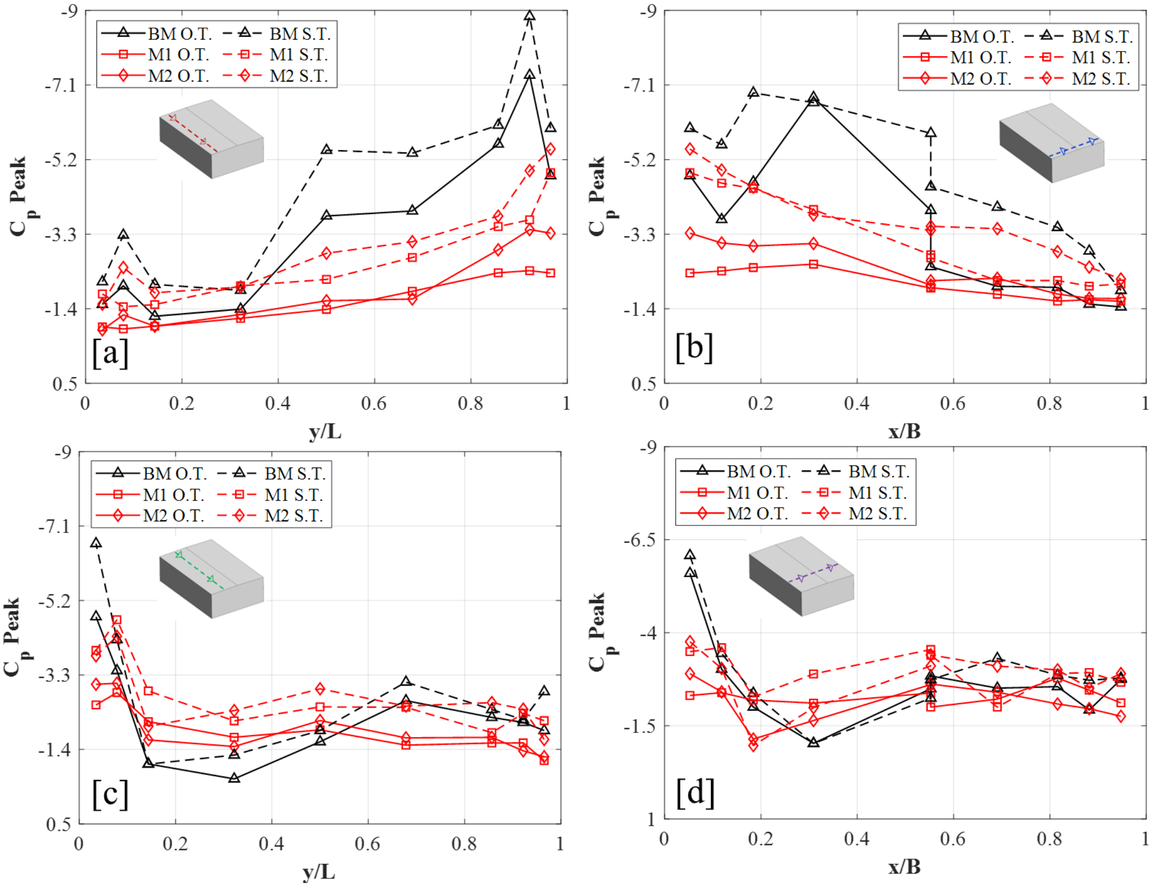

Fig. 5.17 Peak pressure reading for taps located along the ridgeline at (a) L1, and (b) L2 and perpendicular to the ridgeline at (c) L3, and (d) L4.

Table 5.2 Pressure values for Tap A8 and B_9 at 50° wind direction

Configuration	**Tap A_8**			**Tap B_9**		
	Mean	**RMS**	**Peak**	**Mean**	**RMS**	**Peak**
BM O.T.	-2.89	0.722	-7.34	-1.411	0.75	-3.67
BM S.T.	-2.52	0.923	-8.84	-1.66	0.826	-5.57
M1 O.T.	-1.43	0.23	-2.37	-1.48	0.229	-2.36
M1 S.T.	-1.79	0.64	-3.67	-1.94	0.655	-4.6
M2 O.T.	-1.96	0.355	-2.37	-2.1	0.26	-3.07
M2 S.T.	-1.994	0.867	-4.92	-2.145	0.912	-4.49

5.4. Flow visualization to the impact of terrain on parapets efficiency using LES

To further understand the reason for the parapet's reduced efficiency in aerodynamically mitigating pressure induced on the roof of low-rise buildings impacted by the terrain, Large Eddy Simulation (LES) is conducted using the benchmark model using STAR-CCM+ 2024 (19.04.009). A computational domain of dimensions of $3.4\ m \times 2.5\ m \times 0.7\ m$ (in model scale) can clarify the process and mechanism of these non-periodic and localized phenomena because of their abundant detailed data. The boundary conditions at the top and side surfaces of the computational study domain are set as symmetry plane boundary conditions. The ground and building surfaces are defined as a non-slip wall boundary condition, while the outlet surface is defined as an outflow. The simulations adopted the previous setup published by Al-Chalabi et al. [15]. For the benchmark model located at an angle of attack of 50°, 3D iso-surface view of the flow topology and mean pressure coefficient obtained by LES for non-modified(BM) and modified models (M1 and M2) for open and suburban terrains are depicted Fig. 5.18 (a) to (f). The iso-surface represents the Q-criterion, defined as the second invariant of the instantaneous velocity gradient. It can be noticed that the peak suction occurs at the leading corner as the longitudinal component of the velocity increases considerably, particularly near the right side of the leading edge for the open and suburban terrains. Two zones immediately downstream of the leading edges of the top cube surface characterized by strong suctions can be clearly observed. Upon adding perimetric parapets, it can be seen that it is successful in displacing away the separated flow along the leading edges. In contrast, the corner parapets are only effective in displacing the flow away at a distance from the corner equal to the paper's length.

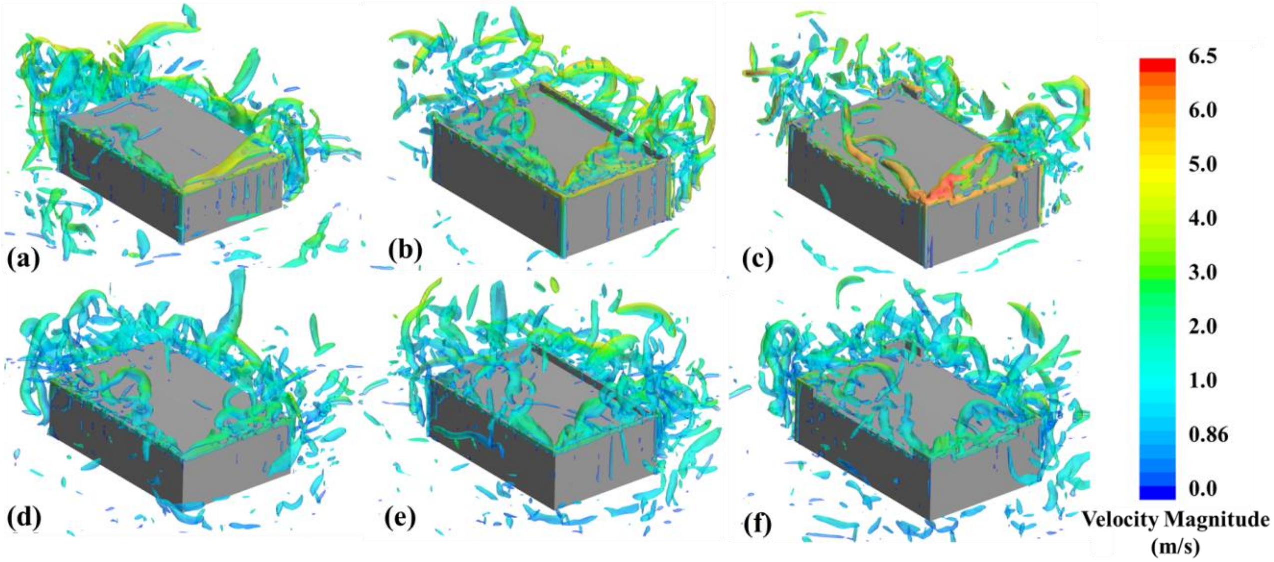

Fig. 5.18 3D views iso-surface of the flow topology at 50° wind angle of attack models model in open terrain (a) BM, (b) M1, and (c) M2, and suburban terrain (d) BM, (e) M1, and (f) M2.

5.5. Summary and Conclusion

Aerodynamic testing is carried out on a low-sloped gable roof building with a footprint of $152 \times 230\,mm$. A 1:60 length scale benchmark model is tested at open and suburban terrain. Tests are conducted in a boundary layer wind tunnel under simulated flow conditions representing open country and suburban flow conditions. The highest suction pressure is observed near the leading edges of the roof close to the upwind corner for wind approaching 50°. The edges and corners of the benchmark model are then modified using low-height parapets (i.e., perimetric and corner). The objective is to understand the effects of introducing suburban terrain (real-life scenario) on parapets' efficiency in altering pressure distribution and magnitude on the roofs compared to open terrain setups. Overall, it is found that the parapets assist in alleviating peak suction pressure. The effectiveness of perimeter parapets in reducing suction pressure coefficients decreased with increasing terrain roughness. The presence of the parapet significantly reduces the magnitude of wind pressure, influences pressure recovery, and results in flow reattachment. This happens because the parapet wall raises the position of corner vortices, which causes reductions in the negative pressures. The results reveal that parapets can reduce roof pressures and alter the pressure distribution on the roof. Hence, installing a parapet above the roof surface at the edges can be an aerodynamic mitigation technique. In general, the results indicated the following:

Upon testing the benchmark models in open and suburban terrains for all wind angles of attack (i.e., form 0° to 90°). At 50°, the mean suction is the highest for the open terrain, and the pressure function is higher for suburban terrain caused by conical vortices. The difference in the value of the mean is amplified at the edges, where tap A_8, showed a reduction of 30% in mean pressure for benchmark in suburban terrain. On the contrary, the peak pressure at the same location is found to be amplified when introducing the benchmark to high turbulence, representing a build-up environment. Mean pressure on the internal roof zones is found to be not altered when introducing rough terrain. On the contrary, the pressure fluctuations on the internal zones of the roof surfaces for the benchmark model are found to increase in some locations by over 60%.

At the longer leading edge of the study building, the mean, peak and fluctuation of the pressure at the heights reaching the tap A_8 magnitudes of perimetric parapets have successfully reduced for both terrains. However, the reduction rate for mean and pressure fluctuation is almost 50% less for suburban terrain than open terrain. Corner parapets for the same tap are found to have an efficiency in reducing pressure fluctuation that decreased from 50% for the open terrain to 6% for the suburban terrain. In addition, the corner parapets' efficiency in reducing the peak pressure is reduced by 30% compared to suburban terrain.

5.6. References

[1] A.M. Aly, N. da Fonseca Yousef, High Reynolds number aerodynamic testing of a roof with parapet, Eng. Struct. 234 (2021) 112006. https://doi.org/10.1016/J.ENGSTRUCT.2021.112006.

[2] A.M. Aly, G. Bitsuamlak, Aerodynamics of ground-mounted solar panels: Test model scale effects, J. Wind Eng. Ind. Aerodyn. 123 (2013) 250–260. https://doi.org/10.1016/J.JWEIA.2013.07.007.

[3] T. Stathopoulos, C. Baniotopoulos, Wind effects on buildings and design of wind-sensitive structures, Springer Science & Business Media, 2007.

[4] Insurance of Bureau of Canada, Welcome to Insurance Bureau of Canada, (2022). http://www.ibc.ca/on/ (accessed July 25, 2022).

[5] M. Hadavi, L. Sun, D. Romanic, Normalized insured losses caused by windstorms in Quebec and Ontario, Canada, in the period 2008–2021, Int. J. Disaster Risk Reduct. 80

(2022) 103222. https://doi.org/10.1016/J.IJDRR.2022.103222.

[6] G.A. Kopp, D. Surry, C. Mans, Wind effects of parapets on low buildings: Part 1. Basic aerodynamics and local loads, J. Wind Eng. Ind. Aerodyn. 93 (2005) 817–841. https://doi.org/10.1016/J.JWEIA.2005.08.006.

[7] G.A. Kopp, M.J. Morrison, D.J. Henderson, Full-scale testing of low-rise, residential buildings with realistic wind loads, J. Wind Eng. Ind. Aerodyn. 104–106 (2012) 25–39. https://doi.org/10.1016/J.JWEIA.2012.01.004.

[8] A.M. Aly, J. Bresowar, Aerodynamic mitigation of wind-induced uplift forces on low-rise buildings: A comparative study, J. Build. Eng. 5 (2016) 267–276. https://doi.org/10.1016/j.jobe.2016.01.007.

[9] G.A. Kopp, C. Mans, D. Surry, Wind effects of parapets on low buildings: Part 2. Structural loads, Undefined. 93 (2005) 843–855. https://doi.org/10.1016/J.JWEIA.2005.08.005.

[10] T. Stathopoulos, A. Baskaran, P.A. Goh, Full-scale measurements of wind pressures on flat roof corners, J. Wind Eng. Ind. Aerodyn. 36 (1990) 1063–1072. https://doi.org/10.1016/0167-6105(90)90103-J.

[11] R. Al-Chalabi, A. Elshaer, Aerodynamic mitigation of low-rise building with complex roof geometry, Front. Built Environ. 9 (2023) 1200383. https://doi.org/10.3389/FBUIL.2023.1200383/BIBTEX.

[12] W. Suaris, P. Irwin, Effect of roof-edge parapets on mitigating extreme roof suctions, J. Wind Eng. Ind. Aerodyn. 98 (2010) 483–491. https://doi.org/10.1016/J.JWEIA.2010.03.001.

[13] D. Surry, J.X. Lin, The effect of surroundings and roof corner geometric modifications on roof pressures on low-rise buildings, J. Wind Eng. Ind. Aerodyn. 58 (1995) 113–138. https://doi.org/10.1016/0167-6105(95)00016-K.

[14] Y. Uematsu, T. Yambe, H. Ikeda, Experimental study of wind-induced dynamic response and collapse of a mechanically-attached membrane roofing system installed on metal substrate of flat-roofed low-rise steel building, J. Build. Eng. 63 (2023) 105401.

https://doi.org/10.1016/J.JOBE.2022.105401.

[15] R. Al-Chalabi, A. Elshaer, H. Aboshosha, Enhancing LES efficacy in wind load evaluation of low-rise buildings using synthesized inflow turbulence, J. Build. Eng. 95 (2024) 110233. https://doi.org/10.1016/J.JOBE.2024.110233.

[16] G.A. Kopp, D. Surry, C. Mans, Wind effects of parapets on low buildings: Part 1. Basic aerodynamics and local loads, J. Wind Eng. Ind. Aerodyn. 93 (2005) 817–841. https://doi.org/10.1016/j.jweia.2005.08.006.

[17] C. Mans, G.A. Kopp, D. Surry, Wind effects of parapets on low buildings: Part 3. Parapet loads, J. Wind Eng. Ind. Aerodyn. 93 (2005) 857–872. https://doi.org/10.1016/J.JWEIA.2005.08.007.

[18] W. Shan, Q. Yang, K. Guo, Y. Tamura, Effects of slope curvature, ridge height and layered roofs on wind pressures on traditional-Chinese-style gable-hip and gable roofs, J. Build. Eng. 70 (2023) 106300. https://doi.org/10.1016/J.JOBE.2023.106300.

[19] G.T. Bitsuamlak, W. Warsido, E. Ledesma, A.G. Chowdhury, Aerodynamic Mitigation of Roof and Wall Corner Suctions Using Simple Architectural Elements, J. Eng. Mech. 139 (2013) 396–408. https://doi.org/10.1061/(ASCE)EM.1943-7889.0000505/ASSET/AF3E3219-D5EB-4BA1-AA81-3AC28CD3F26F/ASSETS/IMAGES/LARGE/FIGURE21.JPG.

[20] W. Suaris, P. Irwin, Effect of roof-edge parapets on mitigating extreme roof suctions, J. Wind Eng. Ind. Aerodyn. 98 (2010) 483–491. https://doi.org/10.1016/j.jweia.2010.03.001.

[21] Z. Azzi, F. Habte, A. Elawady, A. Gan Chowdhury, M. Moravej, Aerodynamic Mitigation of Wind Uplift on Low-Rise Building Roof Using Large-Scale Testing, Front. Built Environ. 5 (2020) 149. https://doi.org/10.3389/FBUIL.2019.00149/BIBTEX.

[22] S. Gan, G. Li, Z. Dong, H. Li, M. Zhao, Numerical study on aeroelastic behavior of spoiler on low-rise building based on fluid-structure interaction method, J. Build. Eng. 59 (2022) 105115. https://www.sciencedirect.com/science/article/pii/S2352710222011238 (accessed October 25, 2023).

[23] Y. Weng, S.G. Paal, Extrapolating wind pressures on roof soffits of low-rise buildings

using few-shot learning, J. Build. Eng. 82 (2024) 108110. https://doi.org/10.1016/J.JOBE.2023.108110.

[24] A.G. Davenport, Past, present and future of wind engineering, J. Wind Eng. Ind. Aerodyn. 90 (2002) 1371–1380. https://doi.org/10.1016/S0167-6105(02)00383-5.

[25] T.C.E. Ho, D. Surry, D. Morrish, G.A. Kopp, The UWO contribution to the NIST aerodynamic database for wind loads on low buildings: Part 1. Archiving format and basic aerodynamic data, J. Wind Eng. Ind. Aerodyn. 93 (2005) 1–30. https://doi.org/10.1016/J.JWEIA.2004.07.006.

[26] A. Hunt, Wind-tunnel measurements of surface pressures on cubic building models at several scales, J. Wind Eng. Ind. Aerodyn. 10 (1982) 137–163. https://doi.org/10.1016/0167-6105(82)90061-7.

[27] B.K. Suresh Kumar, T. Stathopoulos, Wind Loads on Low Building Roofs: A Stochastic Perspective, J. Struct. Eng. 126 (2000) 944–956. https://doi.org/10.1061/(ASCE)0733-9445(2000)126:8(944).

[28] Y. Tamura, H. Kikuchi, K. Hibi, Extreme wind pressure distributions on low-rise building models, J. Wind Eng. Ind. Aerodyn. 89 (2001) 1635–1646. https://doi.org/10.1016/S0167-6105(01)00153-2.

[29] P.L. Fernández-Cabán, F.J. Masters, Experiments in a Large Boundary Layer Wind Tunnel: Upstream Terrain Effects on Surface Pressures Acting on a Low-Rise Structure, J. Struct. Eng. 146 (2020) 04720002. https://doi.org/10.1061/(ASCE)ST.1943-541X.0002690/ASSET/A51F567F-1F93-4879-875C-4DAB63D40D58/ASSETS/IMAGES/LARGE/FIGURE9.JPG.

[30] X.J. Wang, Q.S. Li, J.W. Yang, Nonstationary near-ground wind characteristics and wind-induced pressures on the roof of a low-rise building during a typhoon, J. Build. Eng. 53 (2022) 104492. https://doi.org/10.1016/J.JOBE.2022.104492.

[31] H. Kiefer, E.J. Plate, Modelling of mean and fluctuating wind loads in built-up areas, J. Wind Eng. Ind. Aerodyn. 74–76 (1998) 619–629. https://doi.org/10.1016/S0167-6105(98)00056-7.

[32] S. Kim, N. Alinejad, S. Jung, H.K. Kim, The effect of open-to-suburban terrain transition on wind pressures on a low-rise building, J. Build. Eng. 85 (2024) 108651. https://doi.org/10.1016/J.JOBE.2024.108651.

[33] K. Wang, T. Stathopoulos, The Impact of Exposure on Wind Loading of Low Buildings, Proc. Struct. Congr. Expo. 2006 (2006) 1–10. https://doi.org/10.1061/40889(201)9.

[34] C.H. Chang, R.N. Meroney, The effect of surroundings with different separation distances on surface pressures on low-rise buildings, J. Wind Eng. Ind. Aerodyn. 91 (2003) 1039–1050. https://doi.org/10.1016/S0167-6105(03)00051-5.

[35] T.C.E. Ho, D. Surry, A.G. Davenport, Variability of low building wind loads due to surroundings, J. Wind Eng. Ind. Aerodyn. 38 (1991) 297–310. https://doi.org/10.1016/0167-6105(91)90049-3.

[36] L.S. An, N. Alinejad, S. Kim, S. Jung, Experimental study on wind characteristics and prediction of mean wind profile over complex heterogeneous terrain, Build. Environ. 243 (2023) 110719. https://doi.org/10.1016/J.BUILDENV.2023.110719.

[37] T. Ghazal, J. Chen, M. Aboutabikh, H. Aboshosha, S. Elgamal, Flow-conditioning of a subsonic wind tunnel to model boundary layer flows, Wind Struct. 30 (2020) 339–366. https://doi.org/10.12989/WAS.2020.30.4.339.

[38] T. Ghazal, A. Elshaer, H. Aboshosha, Wind load evaluation on storm shelters using wind tunnel testing and North American design codes, Eng. Struct. 254 (2022) 113821. https://doi.org/10.1016/J.ENGSTRUCT.2021.113821.

[39] D. Banks, R. Meroney, P. Sarkar, Z.Z.-J. of W., undefined 2000, Flow visualization of conical vortices on flat roofs with simultaneous surface pressure measurement, Elsevier. (n.d.). https://www.sciencedirect.com/science/article/pii/S0167610599000446 (accessed August 12, 2024).

[40] H. Kawai, G. Nishimura, Characteristics of fluctuating suction and conical vortices on a flat roof in oblique flow, J. Wind Eng. Ind. Aerodyn. 60 (1996) 211–225. https://doi.org/10.1016/0167-6105(96)00035-9.

CHAPTER 6

Sensor Placement Optimization for Low-rise Buildings Using Multi-resolution Dynamic Mode Decomposition technique

6.1. Introduction

6.1.1. Challenges in Accurate Wind Load Measurement

Low-rise buildings are susceptible to wind-induced forces, which often lead to initiate damages to cladding and, in severe cases, can lead to wall connection failure and, hence, the total collapse of the system [1]. Accurately evaluating wind loads, uplift forces, and the effects of surrounding terrain, designers can enhance the resilience of structures, improving safety, comfort, and cost-effectiveness in mitigating wind-related risks. In Canada, the construction industry relies on the National Building Code of Canada (NBCC) [2]. According to the NBCC, a wind tunnel test is required to evaluate a building's wind load for dynamically sensitive and very sensitive structures to ensure stable and safe design during wind events. Hence, wind tunnel testing remains a crucial benchmark for evaluating wind loads because it provides empirical data by simulating real-world wind conditions. It is particularly beneficial for optimizing the design of low-rise buildings in regions prone to high winds or extreme weather, such as hurricanes and tornadoes. Therefore, pressure distribution must be analyzed across buildings' exterior surfaces to ensure structural integrity and serviceability. A critical aspect of experimental testing for low-rise buildings is the number of pressure sensors, and their placement on the building surfaces is crucial to extracting information needed to design wind-resistant buildings. Therefore, a reliable approach is required to enhance data collection procedures in the Boundary Layer Wind Tunnel test (BLWT). Initially, sensor placement methodologies deployment, utilization and management are proposed for structural diagnosis (i.e., structural health monitoring), particularly in the design phase [3] and field measurement [4,5]. In the field of structural health monitoring, Yuan et al. and Worden et al. suggested using advanced techniques like optimization algorithms and machine learning to determine optimal sensor locations. In these studies, sensors are placed sequentially at positions that provide high entropy values in model predictions, improve the performance of the system and avoid the use of an additional number of sensors and the related wiring that can add significant weight to the system, which can directly affect the operating costs [5–7].

Driven by the need to balance the cost and the amount of information required when deciding on sensor positions, Optimal Sensor Placement (OSP) is a central challenge in predicting, estimating, and controlling high-dimensional systems, particularly in fields such as wind engineering [8]. Optimal sensor placement allows for accurate estimation of the full state of the system, such as identifying pressure fluctuations while maximizing data quality and minimizing redundancy [9,10]. In applications like wind load evaluation on building surfaces, capturing the most critical pressure points using a limited number of sensors can significantly reduce both the cost and complexity of experimental setups [11]. Turbulence is a crucial high-dimensional system that demonstrates multiscale phenomena, making it essential for optimizing sensor placement in the study of wind load evaluations on low-rise buildings [12]. However, determining which sensor locations will yield the most accurate and representative data without oversampling remains a difficult problem, especially when dealing with the complex pressure fields induced by turbulent wind flows [13]. According to the literature, sensor locations are often chosen based on bluff body aerodynamics, using heuristics and intuition derived empirically through engineering judgment and past experience; for low-rise buildings, previous wind experiments allocated sensors primarily at critical locations identified through post-damage surveys, where damage is likely to initiate due to vortex formation at flow separation points. However, if sensor placement misses a critical location, a significant amount of information is lost, commonly referred to in other studies as the sensor placement problem. The number of sensors, though it varies according to the application and the structure to be monitored, is often constrained by the high cost of sensors and the time-consuming task of deploying them [14]. Coupled with the fact that, on some occasions, placing sensors in critical locations can be challenging due to limited accessibility and the complex geometry of the model tested at various length scales. Hence, placing limited numbers of sensors in the optimal locations to extract the most information about the wind pressure or speed field can be challenging. The number of pressure sensors used in wind tunnel experiments typically ranges from 150 to 600, with a significant portion placed at critical locations such as corners and edges, where wind-induced pressures are often the highest due to flow separation effects.

6.1.2. Approaches to Sensor Placement and Data Decomposition in Fluid Dynamics

To optimize the process of sensor placement, automation can be crucial in efficiently selecting sensor positions that provide the most valuable data while minimizing expenses. One can determine the optimal sensor placement by employing automated techniques, such as optimization algorithms or machine learning, thus ensuring comprehensive data collection at a reduced cost. This strategy can be employed to capture the most critical pressure points and provide valuable insights into the wind pressure distribution and the corresponding aerodynamic loads on buildings [15,16]. Previous studies have proposed a sensor optimization framework to establish the optimal number and placement of pressure sensors for applying wind load evaluations on tall buildings and in aerodynamic wind measurements in city blocks based on wind tunnel data [4,5,17]. These studies have utilized decomposition techniques based on data collected to extract actionable insights, reduce complexity, and build efficient models, whether for understanding fundamental behaviour, improving the design, or predicting future outcomes.

Data decomposition techniques are powerful tools for capturing critical data and effectively analyzing and interpreting complex systems for various fields. In fact, these techniques have gained rapid popularity across various fields, including aerospace and wind engineering, the oil and gas industry, and medicine[18]. In fluid dynamics, these techniques are foundational for addressing complex fluid mechanics problems, as they enable the reduction of high-dimensional flow data into coherent modes that capture essential flow features and predict their future behaviour [17]. Different techniques can be used for decomposition, such as equation-based and data-based. Data-based techniques can provide a linear representation of nonlinear dynamical systems by governing the evolution of scalar observables in the state space. In other words, the data-driven techniques operate without explicit knowledge of the equations and instead extract patterns or dynamics directly from observed data [19]. Equation-based techniques, as they rely fundamentally on the governing equations of the physical system, such as Spectral Methods and Resolvent Analysis (RA). The latter techniques are primarily equation-based, not inherently data-driven, as they rely on the linearized governing equations of the system to construct the resolvent operator. The RA developed by Herrmann et al. in 2021, making an impact in the field of fluid mechanics by being employed in research aiming toward new applications of flow control [20]. Luhar et al. reformulated the resolvent analysis to generate predictions for the fluctuating pressure field in turbulent pipe flow. They used their proposed approach to show how the obtained response modes reconcile many of the key relationships among the velocity field, coherent structures, and high-amplitude wall-pressure events [21]. Chavarin et al. considered using a temporal filter to limit the time horizon and conducted a global resolvent analysis on the baseline turbulent mean flow to identify the actuation frequency and wavenumber that provide large perturbation energy amplification [22].

Data-driven decomposition techniques, such as Fast Fourier Transform, Proper Orthogonal Decomposition (POD) and Dynamic Mode Decomposition (DMD), are the most widespread methods, especially in the field of fluid dynamics. The Fast Fourier Transform decomposes a signal into its frequency components by representing a function as a sum of sines and cosines (or complex exponentials), each with a specific frequency and amplitude, while assuming stationarity. It does require time-series or spatial data to provide a frequency-domain representation of the data. however, it cannot effectively handle time-varying frequencies or transient dynamics [23]. Another decomposing technique is the Proper Orthogonal Decomposition (POD), which is employed to identify the principal modes of pressure fields based on their energy content. Higher-order modes capture features with progressively lower energy, but these features can still contain valuable information. It can assist in reducing the dimensionality of data while preserving the essential features of pressure distributions [24]. In addition to the fact that POD is a linear technique, it captures dominant spatial patterns based on energy content but does not separate different frequencies [25]. As a result, multiple frequencies can be mixed within a single mode, leading to a loss of detailed frequency information. This makes it less suitable for analyzing time-varying or transient phenomena where frequency dynamics are important [26,27]. Smith et al. used POD to build low-dimensional models for turbulent fluid flow [28]. Willcox and Peraire combined POD with concepts from balanced realization theory for the reduction of high-order systems, including a computational fluid dynamics (CFD) model that describes the unsteady linearized motion of a two-dimensional airfoil [29]. A recent extension of POD is Spectral POD (SPOD), which was developed to overcome the difficulties classical POD faces when the relevant coherent structures occur at low energies or at multiple frequencies [30].

A well-known data-based decomposition technique is the DMD. Right after introducing the DMD algorithm in 2010, Schmid et al. published a new work to demonstrate the potential of Dynamic mode decomposition (DMD) is a data-driven technique used to identify coherent structures within a fluid flow, decomposing complex flow fields into simpler, oscillatory modes, which are useful for analyzing dominant flow features contributing to the overall pressure field [31,32]. This technique decomposes complex pressure fields into modes that capture the dominant temporal and spatial patterns. Unlike POD, which focuses on variance and energy, DMD is an equation-free method that analyzes dynamic data by decomposing it into modes with distinct temporal frequencies [33,34]. It is known to be closely linked to the spectral analysis of the Koopman operator, allowing it to capture both spatial and temporal structures in time-resolved data [35]. This makes DMD particularly useful for analyzing transient dynamics and identifying dominant frequencies in unsteady pressure fields [36]. However, standard DMD struggles to approximate transient dynamics or data that contain multiple timescales, making it susceptible to missing subtle, localized, or time-varying behaviours [18,31]. The latter is attributed to the fact that DMD operates as a single-step analysis, directly decomposing the entire dataset without iterative refinement or frequency removal [37]. This makes it suitable for capturing coherent structures and their temporal behaviour in systems with well-represented dynamics, but it may be less effective for multiscale or localized phenomena, which require an iterative approach [38,39]. Hence, standard DMD, originally developed for full-state measurements of high-dimensional fluid vector fields, may not yield accurate results or may even fail when applied to localized flow fields with limited spatial dimensions [40,41].

To address the limitations of standard DMD, a more advanced technique called Multi-resolution Dynamic Mode Decomposition (mrDMD) has been developed. mrDMD enhances the capability of DMD by analyzing data across multiple time scales, allowing it to capture transient and intermittent dynamics more effectively [42]. It enhances standard DMD by using hierarchical time windows to analyze data at multiple scales, capturing both long-term trends and short-term transients. It employs adaptive resolution for efficient analysis, separates data into components representing different temporal behaviours, and extends the spectral analysis to cover a broader range of dynamic features. The latter enables mrDMD to handle multi-scale and transient dynamics effectively, providing a more detailed understanding of complex systems [43]. Climaco et al. proposed an approach for damage detection in wind turbine gearboxes using the mrDMD technique. Gearbox generates signals under varying load conditions, which were analyzed using mrDMD, resulting in the identification of important features related to the damage [44]. Gonzales et al. created a continuous-time model of the pressure profile over the fluttering airfoil using mrDMD in order to provide higher temporal resolution information about the system [45]. The mrDMD algorithm was able to isolate the behaviour of an oscillating shock wave over the surface of the fluttering airfoil and to determine the frequency of the amplitude oscillations of the shock wave [45]. Traditional optimization techniques are commonly used to determine optimal sensor placements and can be computationally intensive. These techniques, including QR Pivoting, sequential sensor placement, and genetic algorithms (GAs), are used for optimizing sensor locations [46,47]. Heuristic approaches can efficiently solve complex optimization problems but depend heavily on pre-defined hyperparameters. Selecting appropriate hyperparameters can be challenging and may lead to suboptimal results. QR decomposition techniques are generally efficient, exploring novel methods like con-vex relaxation [48]. Although QR Pivoting techniques are computationally intensive, they offer stronger optimality guarantees and are often used in conjunction with heuristics to balance efficiency and solution quality [49].

6.1.3. Study Objectives

This research aims to optimize sensor placement for pressure measurements on the roof surfaces of low-rise buildings with gable and complex geometries, specifically in open terrain conditions. Where Computational Fluid Dynamics (CFD) can be valuable for providing pressure time histories for different building locations as long as it is carefully validated with experimental testing [50]. The objective of the present study is twofold: the goal is to reduce the number of pressure sensors needed while maintaining accurate wind load evaluations, ultimately enhancing the resilience of buildings against wind-induced damage. This research uses multi-resolution Dynamic Mode Decomposition (mrDMD) to decompose multiscale wind pressure data into modes representing different timescales. QR pivoting then identifies key dynamic modes that best capture the pressure field's dynamics. Together, these techniques can help identify sensor locations that minimize the required sensors while ensuring accurate pressure field reconstruction.

This article consists of five sections. **Section 1** (this section) provides the background and literature review, highlighting the existing gap in the field of optimal sensor placement for an effective wind load evaluation on low-rise buildings. **Section 2** presented a validation for the numerical wind load evaluation for a gable roof building with an experimental wind test using both mean and pressure on the building surfaces. **Section 3** showcases the overall methodology framework, which is followed by this study to fulfill the full objectives. **Section 4** presents a comprehensive review of the DMD, mrDMD, and QR Pivoting techniques followed in this study to reduce the placement of the sensor effectively. The reconstructed pressure values (i.e., predicted pressure data) on the roof of low-rise buildings are compared against the simulated data (i.e., true pressure) and present a case study for practical applications on complex roof geometry of low-rise buildings for efficient wind load monitoring on low-rise buildings. **Section 5**, summarizes the study contributions, emphasizing how optimized sensor placement improves wind load evaluation on low-rise buildings by reducing costs and sensor requirements. It will highlight the practical applicability of the findings.

6.2. Numerical model validation

This section presents the validation of the numerical model for the flow aerodynamics and pressure distribution across the roof of a low-rise building. The CFD model is validated against the experimental tests conducted at Toronto Metropolitan University by Al-Chalabi et al. [51]. Following the validation, the CFD model will be a benchmark for determining the sensors' optimal number and placement. The study model replicates the wind tunnel experimental setup, adopting a length scale of $1{:}\,60$ and a timescale of $1{:}\,15$. The structure used for validation is a low-rise building with a gable roof featuring a roof slope of $1{:}\,1/4$, footprint dimensions of $13.8\ \times\ 9.0\ m^2$, and a total roof height of $4.0\ m$ in full scale. Validation is achieved by comparing the mean and RMS pressure coefficient values recorded by 18 sensors distributed across the front, roof, and rear surfaces of the building, as shown in Fig. 6.1. The mean velocity and turbulence intensity profiles are tailored to represent an open-terrain exposure with a roughness height (z_o) of $30\ m$ in full scale.

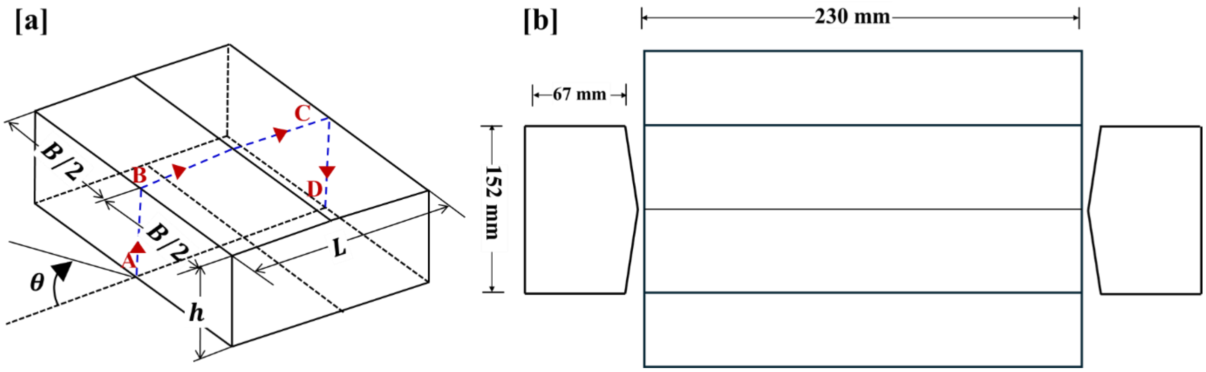

Fig. 6.1 (a) 3D model showing the locations of the sensors used for validation and (b) Exploded view of the study model building showing dimensions in model scale.

The equations proposed and published by the Engineering Sciences Data Unit (ESDU) are followed in this study to compare vertical profiles for mean velocity and turbulence intensity [52,53]. This study's velocity and intensity profiles agree with the wind tunnel experimental data using the Power Law (i.e., Eq. 1) for the mean wind velocity. The $\overline{U}_{10}$ refers to the wind velocity at $10\ m$ height with a value of $15.4\ m/s$. The z refers to the height in meters corresponding to the reference wind velocity, while the terrain roughness for open exposure ($1/\alpha$) is 0.13. The turbulence intensity is calculated for the target profile using the equation below (Eq. 2).

$$U_z = \overline{U}_{10}\left(\frac{z}{10}\right)^{1/\alpha} \tag{1}$$

$$I_u = c_u\left(\frac{z_{ref}}{z}\right)^{bu} \tag{2}$$

To validate the numerical model, STAR-CCM+ 2020.2 (15.04.008-R8) is employed, and Large Eddy Simulation (LES) is utilized to conduct the numerical wind load evaluation. A computational domain of dimensions of $2.2\ m \times 2.61\ m \times 0.4\ m$ (in model scale) is adopted following the finding by Al-Chalabi et al. [38], as shown in Fig. 6.2**Error! Reference source not found.**. The boundary conditions at the top and side surfaces of the computational study domain are set as symmetry plane boundary conditions. The ground and building surfaces are defined as a non-slip wall boundary condition, while the outlet surface is defined as an outflow. Consistent discrete random flow generation (CDRFG) is utilized to generate the inflow [54]. The inlet wall is defined as a time-varying inlet velocity boundary condition using the CDRFG technique described by Aboshosha et al. and later adopted by Elshaer et al. [54,55]. The building is placed $0.6\ m$ away from the inlet. Hence, pressure data collection started after 1200-time steps to stabilize the flow. The Reynolds number (Re) utilized in the CFD is calculated using $U_H H/\nu$, where the viscosity, ν, is $1.3 \times 10^{-5} m/s^2$. Accurate near-wall modelling is crucial for CFD simulation because the solution gradients are high in a wall-bounded flow; thus, y+ values are considered to find the most suitable first cell height from the adjacent wall for a value less than 5 [56]. The computational domain is discretized into three zones using hexahedral mesh cells. Zone 1 adopted a base mesh size of $10\ mm$, while $7\ mm$ and 3.3 mm for Zone 2 and Zone 3, respectively, which yielded $3.31\ M$ of the total mesh cells, as presented in Fig. 6.3. The sub-grid model WALE is employed as it is found by previous studies to reduce the computational time by about 35 to 60% compared to other SGS models without affecting the accuracy of the simulation [57–59]. This is due to its ability to correctly model the asymptotic behaviour of turbulent eddy-viscosity near the walls and generate ABL flow with accuracy comparable to LES with the dynamic one-equation SGS model [58].

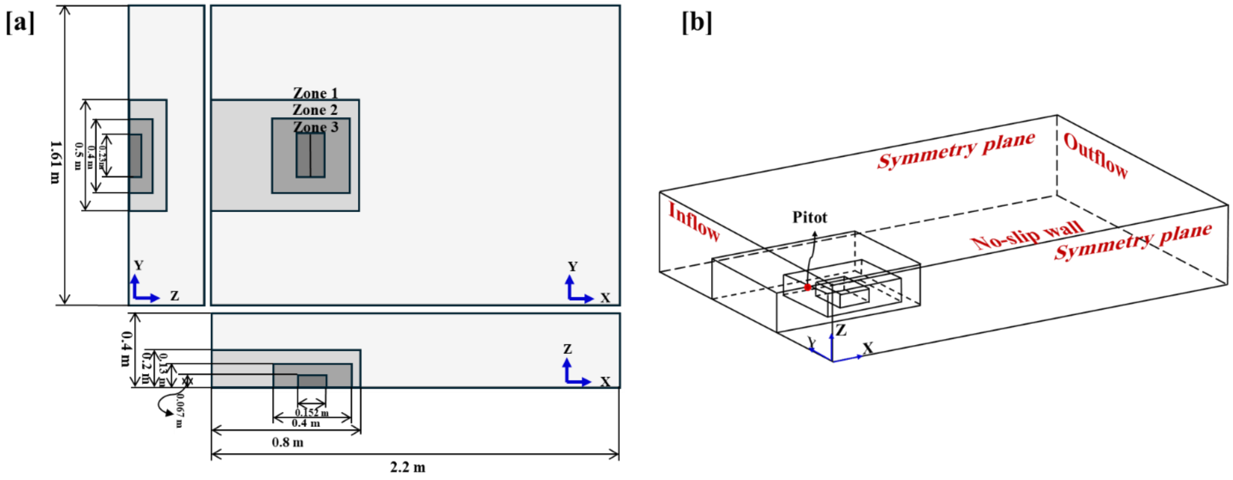

Fig. 6.2 (a) Computational domain and mesh zones dimensions (model-scale) and (b) boundary conditions

The mean wind velocity and turbulence intensity profiles adopted in the wind tunnel experiment compared to numerical profiles showed good agreement with wind tunnel data presented in Fig. 6.4. The simulation duration is 8.0 seconds (in model scale) with a time-step of 0.7 milli-seconds and a total time-step of 16,000. The time step is selected based on the velocity scale and the minimum cell size to satisfy the Courant-Friederichs-Lewy (CFL) number to be below unity to ensure the solution convergence (see Eq. (1)) [60]. As for the reference pressure used to calculate Cp, a probe point is placed in the domain at the midpoint of the inlet before the building at the height of 0.067 m (model scale). After running the validation model, the mean and RMS of the pressure coefficient across the ridgeline are compared to the wind tunnel test, as shown in **Error! Reference source not found.** Fig. 6.5a and Fig. 6.5b, respectively. The validation model results show a good agreement between the reading numerical and experimental pressure parameters, where the mean Cp results showed RMSE of 2%, while the pressure fluctuations showed a 3% difference when compared to the experimentally obtained data.

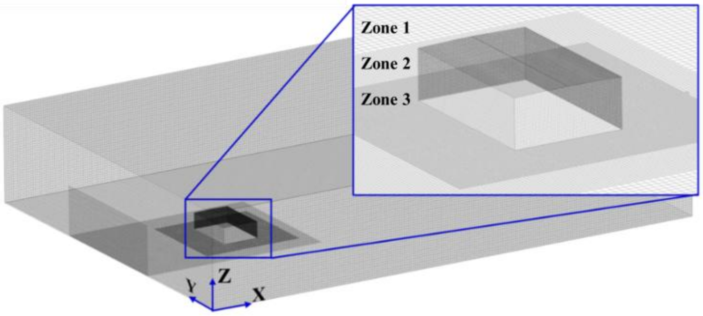

Fig. 6.3 Mesh discretization of the validation model.

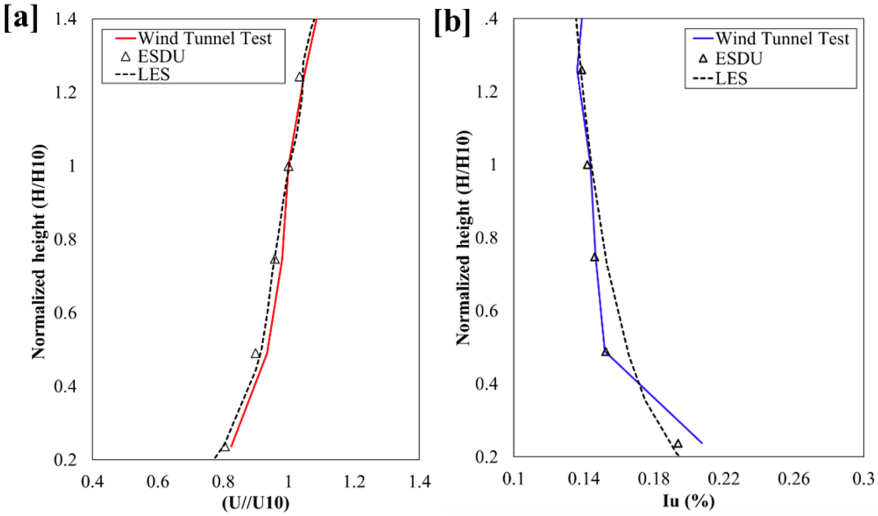

Fig. 6.4 (a) Mean velocity profile and (b) Turbulence intensity profile.

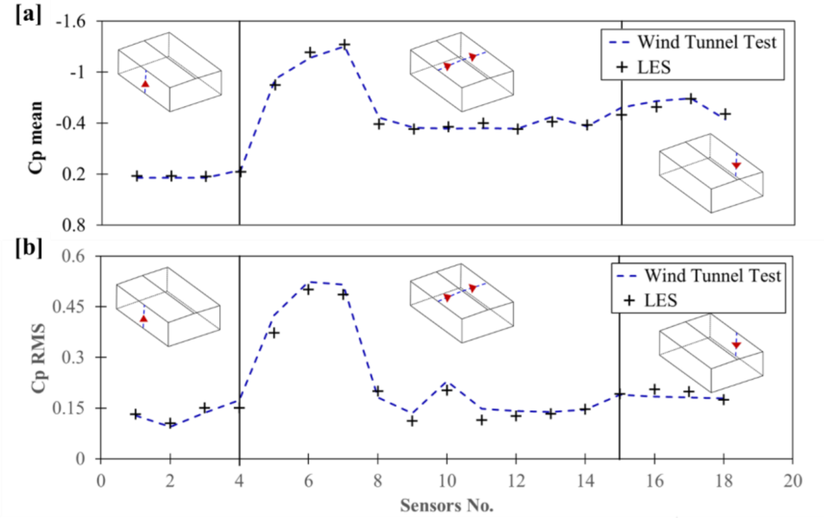

Fig. 6.5 (a) Mean and (b) RMS of the pressure for probes located at the building roof.

6.3. Methodology

The study framework utilizes Multi-Resolution Dynamic Mode Decomposition (mrDMD) to extract critical features from complex, multiscale wind pressure data, enabling the identification of dominant trends and transient behaviours in the pressure field over the roof of a building. The methodology begins with data preparation, where time-history wind pressure data is generated for the roof surface at various wind angle of attack ($0^{\circ}, 30^{\circ}, 60^{\circ}, 90^{\circ}$). Each snapshot represents wind pressure values across the roof's mesh cells at specific time intervals. In addition, a case study for optimal sensor placement on complex roof geometry is presented where the building is tested at all AOA ($0^{\circ}$to 360° with 90° increment). Given the high resolution of the computational mesh, a spatial constraint of 5 mm is applied to reduce computational costs while preserving essential pressure features. This step ensures the dataset is manageable while maintaining accuracy. A time-delay matrix is constructed to capture both spatial and temporal dynamics, incorporating temporal evolution into the spatial data. This enables the methodology to represent transient and unsteady wind pressure patterns effectively. Singular Value Decomposition (SVD) is then applied as part of the Multi-resolution Dynamic Mode Decomposition (mrDMD) process to analyze the wind load snapshots. Dominant spatial and temporal modes are identified, capturing both low-frequency trends (steady wind pressure patterns) and high-frequency variations (transient gusts). Irrelevant low-frequency components are filtered out, while transient high-frequency features are retained for further analysis. A sensitivity analysis is conducted during this stage to optimize key parameters, including cycle frequency, decomposition levels, and truncation rates.

Following the mrDMD analysis, the QR pivoting algorithm is applied to select optimal sensor locations by identifying the most representative spatial-temporal variations. This step prioritizes sensors that capture critical dynamic features efficiently. A common number of sensors is determined to ensure consistency across all wind angles of attack. Finally, the reduced sensor data is combined with the dominant modes extracted from mrDMD to reconstruct the full pressure field on the roof. Specifically, the reduced sensor matrix is multiplied by these modes to recreate the pressure distribution across the roof surface. The reconstruction performance is evaluated using the Root Mean Square Error (RMSE), defined in equation (3). The framework followed by this study is presented in Fig. 6.6. below. To study the performance of the reconstruction method, a regression plot is developed to compare the accuracy of the predicted pressures over the roof surface compared to true (i.e. target) ones.

$$RMSE = \sqrt{\frac{1}{mn}\sum_{j=1}^{m}\sum_{i=1}^{n}(P_{pred,i,j} - P_{true,i,j})^2} \tag{3}$$

where m represents the number of time steps (or instances), n represents the number of spatial points (e.g., pressure measurement locations), $P_{pred,i,j}$is the predicted pressure coefficient at the i-th point and j-th time step, and $P_{true,i,j}$ is the observed coefficient at the i-th point and j-th time step. The following sections detail the methodology used in this study, focusing on the application of Multiresolution Dynamic Mode Decomposition (mrDMD) and QR Pivoting techniques.

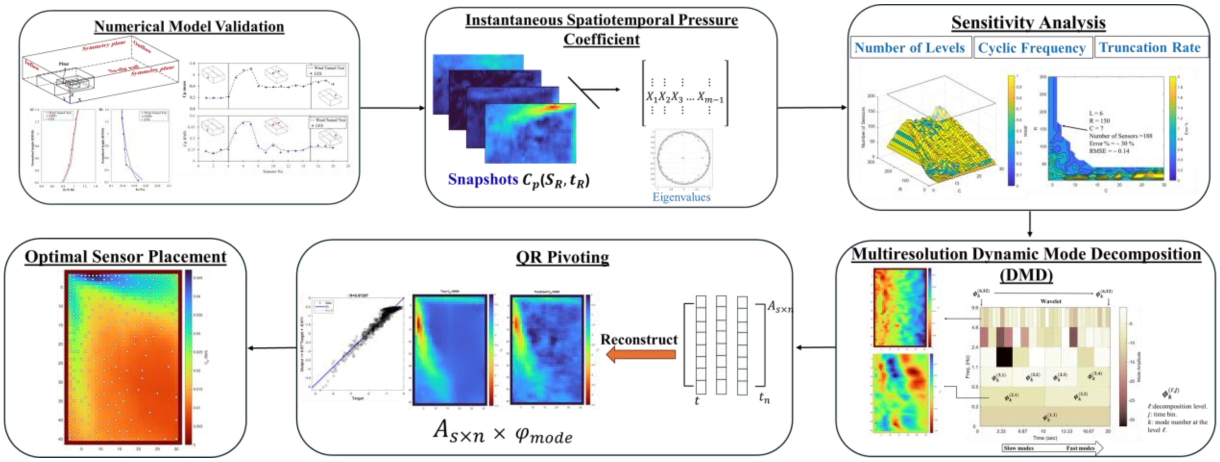

Fig. 6.6 The framework followed in this study.

6.3.1. Multiresolution Dynamic Mode decomposition (mrDMD)

Wind loads on structures vary significantly over different timescales. Large-scale winds can cause overall wind direction changes or long-duration gusts, affecting the building's average load distribution over extended periods. Meanwhile, smaller, faster dynamics, such as turbulent eddies or short gusts, induce rapid, high-frequency fluctuations in pressure on different parts of the structure. To capture these multiscale dynamics, Multi-resolution Dynamic Mode Decomposition (mrDMD) is employed. mrDMD extends the standard Dynamic Mode Decomposition (DMD) by applying it iteratively across multiple levels, each corresponding to a specific timescale, to extract dominant flow structures (modes) contributing to the pressure distribution over time. The time-history data in this study consists of snapshots, where each snapshot represents the pressure distribution on the building's roof at a specific time step. mrDMD begins by dividing the time series into coarse intervals to capture slow, large-scale flow features. At each level, low-frequency components are removed, and the remaining data is split into smaller subsequences. This recursive process isolates high-frequency dynamics localized in time, enabling a time-frequency analysis to detect elements widely separated in scale. The hierarchical decomposition continues until the entire dataset is processed as shown in Fig. 6.7. In this manner, a time-frequency analysis is performed that is capable of and effective at detecting elements in the data sequence that are localized in time and widely separated in scale. The removal-splitting step is continued until the entire data sequence is processed.

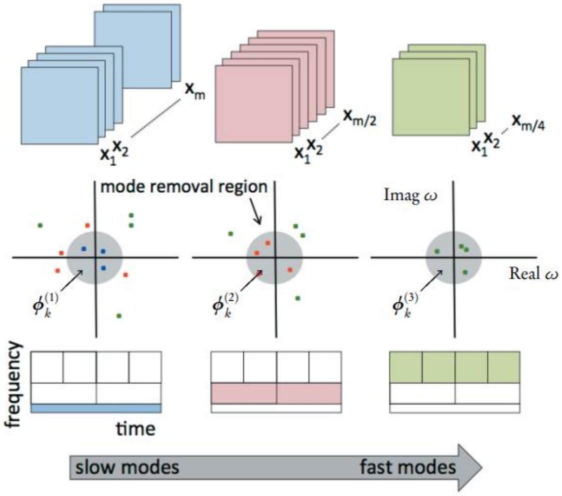

Fig. 6.7 The mrDMD approach successive sampling of the data with m snapshots and decreasing by a factor of two at each resolution level [32].

Assume a set of snapshot data $x_1, x_2, \ldots, x_m$, where each $x_i \in \mathbb{R}^n$ represents the pressure field data from CFD simulations at the time t_i. Assuming that m snapshots of data are available, the input is arranged into two data matrices as follows, where each column represents a state of the system at a discrete time step:

$$X = [x_1, x_2, \ldots, x_{m-1}] \text{ and } X' = [x_2, x_3, \ldots, x_m] \qquad (4)$$

Assuming that $X \in \mathbb{C}^{n\times(m-1)}$ contains the original snapshots while $X' \in \mathbb{C}^{n\times(m-1)}$ contains the shifted snapshots. This step will ensure an analysis of how the system evolves from each state. The time embedding can be used to augment the spatial information by taking advantage of a temporally consistent sequence of the measured data. This technique mitigates data distortion caused by noise and augments the spatial details within the input matrix. The time snapshots of high-dimensional system states are used directly to construct a spatiotemporal decomposition. To find the best-fit linear operator $A \in \mathbb{R}^{n\times n}$ such that $X' = AX$ based on the least-squares minimization of the Frobenius norm of the error. This minimization ensures that A captures the dynamics in a way that best approximates the transition from each state in X to the subsequent state in X' [31].

$$A = arg\ min_A \|X' - AX\|_F = X'X^{\dagger} \quad (5)$$

Where$\| \|_F$ Frobenius norm, and † is the Moore–Penrose pseudoinverse. $A = X'X^{\dagger}$ represents the approximate linear transformation that maps X to X'. The pseudo-inverse of X can be calculated using $X^{\dagger} = (X^T X)^{-1}X^T$. However, it is found that by using truncated single value decomposition (SVD), instead of the pseudoinverse, the data decomposition gives a more stable and efficient way to approximate $X^{\dagger}$ in the reduced space. Hence, this study employs SVD to decompose A and analyze the system's modes. The truncated SVD captures the main system dynamics in a reduced-dimensional space, making DMD a practical tool for analyzing large systems efficiently without unnecessary computation on less significant modes. The matrix A represents the system's approximate linear dynamics, and this step is used to reveal the system's temporal and spatial patterns. By performing an eigen decomposition, A can be expressed in terms of its eigenvalues and eigenvectors as:

$$X = U\sum V^{*} \quad (6)$$

where $*$ denotes the conjugate transpose, U$\in \mathbb{C}^{n\times n}$ is the left singular vectors (i.e., spatial modes), $\sum \in \mathbb{C}^{n\times(m-1)}$ are singular values representing the energy of each mode, $V^{*} \in \mathbb{C}^{(m-1)\times(m-1)}$ is the conjugate transpose of the right singular vectors (i.e., temporal modes). To approximate the system's dynamics efficiently, The SVD is truncated to retain only the most significant r modes, resulting in the reduced matrices:

$$U_r \in \mathbb{C}^{n\times r}, \Sigma_r \in \mathbb{C}^{r\times r}, V_r^{*} \in \mathbb{C}^{r\times(m-1)} \quad (7)$$

r is the rank truncation parameter in DMD, which controls the number of modes (i.e., dimensions or components) retained in the decomposition and assists in avoiding overfitting, especially when dealing with noisy data. Selecting a lower rank r leads to reducing the dimensionality of the data, focusing only on the most significant patterns. With Truncated SVD, the direct pseudoinverse is replaced with the reduced representation, as demonstrated in equation (7). To perform eigenvalues decomposition of the matrix $\tilde{A}$ (depicted in equation (8)). This step is critical for extracting the temporal dynamics of the system.

$$\tilde{A} = U_r^* X' V_r \sum {}_r^{-1} \tag{8}$$

$$\tilde{A}W = W\Lambda \tag{9}$$

Where W is the matrix of eigenvectors obtained from the eigen decomposition of $\tilde{A}$ representing the dynamic structures associated with each mode present how the system evolves over time. Each column of W corresponds to a mode that captures specific features of the system's behaviour. In another word, W represents a spatial pattern in the data that is dominant over time. While Λ is the diagonal of eigenvalues with elements λ_k that represents each mode's growth or decay rates and oscillations over time. The computation of DMD modes is then conducted by:

$$\Phi = X' V_r \Sigma_r^{-1} W \tag{10}$$

Where X' is the matrix of shifted, which contains the system snapshots at successive time intervals. V_r the matrix of right singular vectors from the truncated SVD. They are derived from the SVD of the snapshot matrix X and are truncated to retain only the top r modes. Σ_r^{-1} is the inverse of the truncated diagonal matrix of singular values. This step involves inverting the matrix of singular values, which allows us to weigh the contribution of each mode appropriately during the computation of the DMD modes. The detailed process of DMD can introduce systematic bias in the eigenvalue computation of noisy data [61]. To correct for this, a weighted approximation of A is employed, which incorporates both forward $X' = A_f X$ and backward $X = A_b X'$ time. The following flowchart, as demonstrated in Fig. 6.9, explains the process followed in this study.

The mrDMD solution expansion can be expressed as:

$$x_{mrDMD}(t) = \sum_{\ell=1}^{L} \sum_{j=1}^{J} \sum_{k=1}^{m_L} f_{\ell,j}\,(t) b_k^{(\ell,j)} exp\left(\omega_k^{(\ell,j)} t\right) \tag{11}$$

where L is the total number of decomposition levels, J is the number of time bins at each level, and m_L is the number of modes extracted at each level. The indicator function $f_{(\ell,j)}t$ is only nonzero in the interval, or time bin, associated with the value j. The latter ensures the isolation of the data corresponding to each time bin before applying DMD. This isolation is crucial for recursively extracting dominant modes at progressively finer timescales.

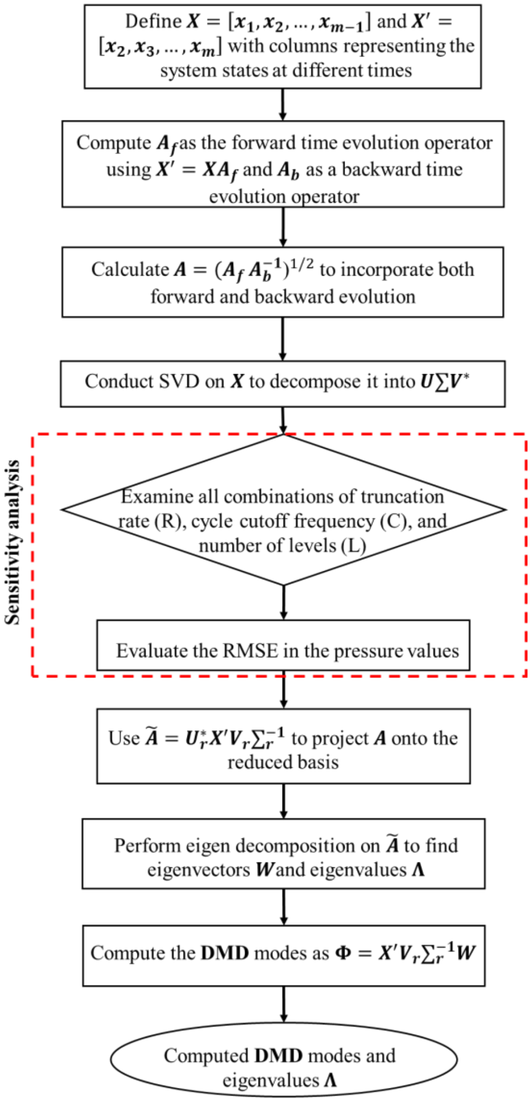

Fig. 6.8 mrDMD framework used in the study.

$$f_{(\ell,j)}t = \begin{cases} 1, & t \in [t_j^\ell, t_{j+1}^\ell] \\ 0, & elsewhere \end{cases} \quad \text{with } j = 1,2,\dots,2^{(\ell-1)} \tag{12}$$

Where $t_j^\ell, t_{j+1}^\ell \in \mathbb{R}^+$ determines the interval of the jth time bin at the ℓth decomposition level (i.e., a variable index that runs through each level from 1 to L, representing the level at which the specific DMD components are computed). It is worth mentioning that by using the indicator function $f_{(\ell,j)}t$, time series relies on the hard cut-off. In other words, the function this function is abruptly switched from 0 to 1 (or vice versa) at the boundaries of the time intervals, leading to the introduction of very high-frequency fluctuations which may not be part of the actual dynamics in the data but are simply caused by the abrupt changes in the indicator function. Wavelets like the

Haar wavelet can be used to smoothen the transition between segments to prevent aggressive boundaries at time intervals, preventing these artificial oscillations. In this study, the authors chose to use a Haar-like windowing function because it is computationally efficient while still addressing the oscillation problem to some degree [62].

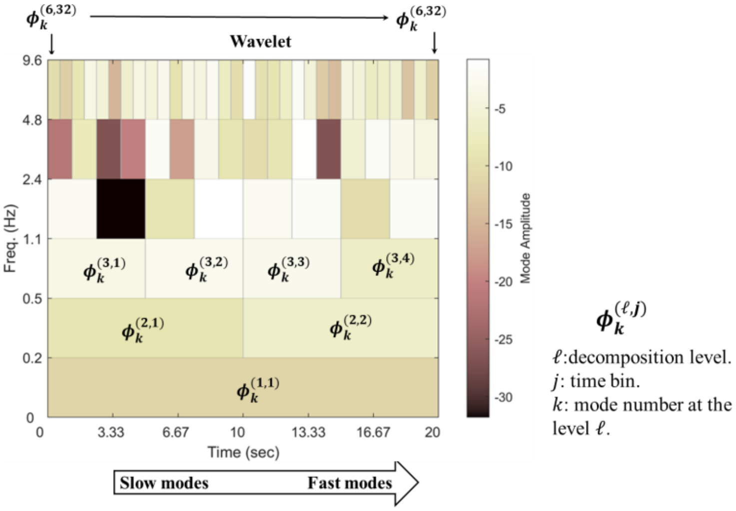

Fig. 6.9 Illustration of the mrDMD hierarchy.

6.3.1. QR Pivoting Technique for Optimal Sensor Placement

This study explores the pivoted QR decomposition technique, which is defined as standard mathematical method employed to break down complex data systems into more manageable components. The primary application in this study is to optimize sensor placement by identifying the best locations for capturing the most informative data about wind-induced pressure fields. This is done algorithm at each step to identify the column with the highest norm (or largest entry). This selection maximizes the determinant of the matrix, effectively choosing the column that will add the most significant new information at that iteration. This step ensures that each additional sensor placement captures new and uncorrelated information. By using multi-resolution Dynamic Mode Decomposition (mrDMD), the system dynamics are decomposed into a set of spatial modes and their temporal evolution. These modes, which represent dominant flow structures and dynamics, form the basis for constructing a library of modes represented by a matrix. The QR decomposition is then applied to this matrix of modes resulted from applying mrDMD, which represent dominant flow structures and dynamics to select a small set of sensors that can capture critical information with minimal error. The resulting QR pivoting matrix is then used to reconstruct the pressure field by multiplying it with the effective modes extracted from mrDMD. This reconstruction ensures that the selected sensors provide sufficient spatial and temporal information to approximate the pressure distribution with minimal error. By leveraging this approach, the study not only optimizes sensor placement but also validates the effectiveness of the chosen sensors in representing the underlying dynamics of the system. It is worth mentioning that the number of sensors for all cases was constrained to 200.

Using multi-resolution Dynamic Mode Decomposition (mrDMD), the system dynamics are decomposed into a set of spatial modes and their temporal evolution. The library of modes is represented by the matrix:

$$\Phi = \left[\phi_k^{(1,1)}, \phi_k^{(2,1)}, \phi_k^{(2,2)}, \phi_k^{(3,1)}, \dots, \phi_k^{(\ell,j)}\right] \tag{13}$$

where each $\phi_k^{(\ell,j)}$ represents the modes indexed by ℓ and j. These modes capture the dominant dynamics in the system. The high-dimensional state vector $X(t)$, which represents the pressure field at each time t, can be approximated by a linear combination of these modes:

$$X(t) = \phi \, a(t) \tag{14}$$

where $a(t)$ is a vector of time-dependent coefficients for each mode. In order to estimate the full state from a few strategically placed sensors by leveraging dominant modes from mrDMD, a linear relationship is established between the high-dimensional state $X(t)$ and a limited set of sensor measurements y.

$$y = CX + \eta = CXa + \eta \tag{15}$$

Where, $C \in \mathbb{R}^{p \times n}$ is the measurement matrix, encoding the locations of the sensors. If $p \ll n$, then the number of sensors used is far fewer than the dimensions of the system. η is additive white noise. To reconstruct the state vector X from measurements, the maximum likelihood of the estimated coefficient a can be used as follows:

$$\hat{a} = (C\Phi_r)^{\dagger} y \tag{16}$$

where Φ_r contains the dominant mrDMD modes with amplitude exceeding a threshold ε , defined as $r \coloneqq \{i \in [1, \dots, r] \, |b_i| \, > \epsilon\}$. This estimate will allow to reconstruct the state:

$$X = \Phi_r \hat{a} = \Phi_r (C\Phi_r)^{\dagger} y \tag{17}$$

To define the optimal sensor placement criterion for determining the best sensor locations, the aim is to minimize the estimation error for the coefficients $a - \hat{a}$. The error covariance is given by:

$$\Sigma = Var\,(a - \hat{a}) = \sigma^2[(C\Phi_r)^T(C\Phi_r)]^{-1} \tag{18}$$

Where σ^2 is noise variance. The optimal sensor placement is then formulated to maximize the log determinant of $(C\Phi_r)^T(C\Phi_r)$ as expressed by [63] is :

$$\gamma^* = argmax_c \log\det[(C\Phi_r)^T(C\Phi_r)] \tag{19}$$

The measurement matrix C is designed to capture measurements at specific locations corresponding to sensor positions. It is represented as:

$$C = \left[e_{\gamma 1}\ e_{\gamma 2} \ldots\ e_{\gamma p}\right]^T \tag{20}$$

where $\gamma = \left\{\gamma_1,\ \gamma_2, \ldots, \gamma_p\right\}$ is the set of sensor locations, and each $e_{\gamma j}$is a canonical basis vector with a 1 in the position corresponding to a sensor location and 0s elsewhere. This matrix structure ensures sparse measurement, where each sensor only measures a single point in the domain. QR Factorization with Column Pivoting: The process begins with a matrix $A \in \mathbb{R}^{m\times n}$ where QR Pivoting is performed. This decomposition transforms A into:

$$AC^T = QR \tag{21}$$

Q is an orthogonal matrix (meaning $Q^TQ = I$ for real matrices), R is the upper matrix, and C is a permutation matrix that reorders the columns of A to improve factorization. When the factorization is applied to the transposed mode matrix Φ_r^T, the equation developed to the following:

$$|\det \Phi_r^T C^T| = |\det(Q)|.|\det(R)| \tag{22}$$

Since Q is orthogonal, $\det(Q) = \pm 1$, so the determinant depends solely on R. With the QR factorization applied to Φ_r^T, the following determinant can be simplified as:

$$|\det \Phi_r^T C^T| = |\det Q|\,|\det R| = \prod_i |R_{ii}| \tag{23}$$

This results in the following diagonal dominance structure in R:

$$|R_{ii}|^2 \geq \sum_{j=i}^{k} \left|R_{jk}\right|^2, 1 \leq i \leq k \leq r \tag{24}$$

The R_{ii} is the diagonal entries of R. This means that maximizing $\prod_i |R_{ii}|$ is effectively maximizing the determinant, which is the criterion for optimal sensor placement. Using the results from the equation above, the $\log\det[(C\Phi_r)^T(C\Phi_r)]$ can be expressed as follows:

$$\log\det[(C\Phi_r)^T(C\Phi_r)] = \log(\textstyle\prod_{i=1}^{r} R_{ii}^2) = \log R_{11}^2 + \log R_{22}^2 + \ldots + \log R_{rr}^2 \tag{25}$$

The goal is to choose p (pivot points) that best characterize the dominant dynamical modes Φ_r. This can be done with at least $p = r$ sensors (where r is the rank of the mode matrix Φ_r). Although oversampling with additional sensors can add robustness, the following equation defines the optimization criterion for sensor placement.

$$\gamma^* = argmax_{\gamma,|\gamma|=p}\big(\log\det[(C\Phi_r)^T(C\Phi_r)] - \lambda R_g(\gamma)\big) \tag{26}$$

where $Rg(\gamma)$ is the regularization function, and λ is the tuning parameter that controls the strength of the regularization. The pivoting procedure yields the following decomposition at the kth iteration:

$$\Phi_r^T P = QR = Q\begin{Bmatrix} R_{11}^{(k)} & R_{12}^{(k)} \\ 0 & R_{22}^{(k)} \end{Bmatrix} \tag{27}$$

where $R_{11}^{(k)} \in \mathbb{R}^{k\times k}$ represent the upper triangular matrix with the most significant information about the columns selected so far in the pivoting process.

The magnitude of these diagonal entries is maximized at each step, helping ensure that the selected columns provide the most robust coverage of the dominant modes in Φ_r^T. $R_{12}^{(k)} \in \mathbb{R}^{k\times(n-k)}$ submatrix contains the interactions between the columns already selected ($R_{11}^{(k)}$) and the remaining columns. While it doesn't contain the main information of the selected columns, it provides a relationship between what has already been chosen and the remaining possible choices. This part of R is essential for managing the dependencies and ensuring that each newly selected sensor adds unique information to the set. $R_{22}^{(k)} \in \mathbb{R}^{(m-k)\times(n-k)}$ represents the part of R corresponding to the columns not yet selected. Each iteration adds one new column to $R_{11}^{(k)}$, updating the permutation matrix $P \in \mathbb{R}^{n\times n}$ to reflect the sensor placement that maximizes information coverage. As this process continues, $R_{11}^{(k)}$ grows to encompass the most informative subset of Φ_r, iteratively maximizing the determinant in the objective function. This expanded form reveals the contribution of each sensor location while balancing it against any imposed constraints, optimizing the selection process under both maximum information gain and system constraints. In the constrained QR pivoting process, the selection of columns differs from the unconstrained approach by limiting choices to a specific subset of indices that meet the required constraints. This adjustment means that instead of simply picking the column with the maximum two-norm from $R_{22}^{(k)}$, only the columns that fulfill the imposed constraints are considered. This approach maintains the objective of prioritizing columns with large two-norms, thus preserving the informativeness of the selected columns within the constraints. Additionally, by limiting the selection in the last $r - s$ steps of the pivoting process (where s represents the allowable indices or predetermined sensors within the constrained region), the largest terms in the objective function's expansion remain relatively unaffected. This ensures that the constrained QR pivoting still closely matches the information-maximizing goals of the unconstrained approach. Therefore, Equation (24) is modified for the constrained case to include both the determinant term and the regularization penalty, balancing information content and constraint adherence.

$$\log\det\left[(C\Phi_r)^T(C\Phi_r)\right] \; - \lambda R_g(\gamma) = log\left(\prod\nolimits_i^r R_{ii}^2\right) - \lambda R_g(\gamma) =$$

$$logR_{11}^2 \; logR_{22}^2 + \ldots + logR_{(r-s)(r-s)}^2 + \ldots + logR_{rr}^2 - \lambda R_g(\gamma) \tag{28}$$

It is worth mentioning that although the minimal allowable number of sensors p=r can be considered, additional sensors can be added for redundancy and robustness through oversampling optimization [64]. The pseudocode of the QR pivoting without constraints is presented Fig. 6.10 below.

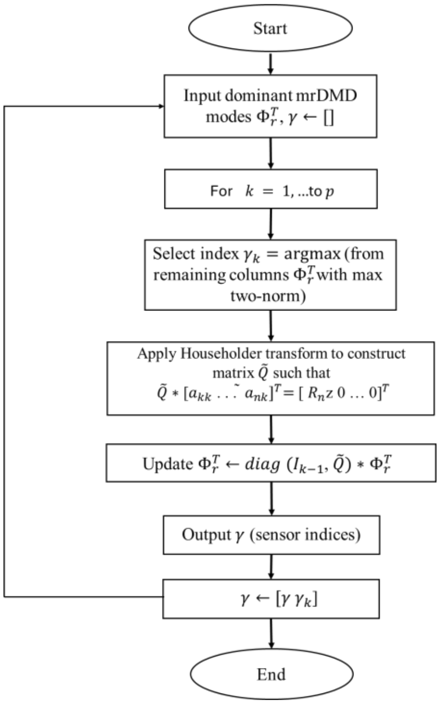

Fig. 6.10 Pseudo-algorithm for the QR pivoting.

6.4. Results and Discussion

The upcoming sub-sections demonstrate the process of data decomposition using the mrDMD technique and QR Pivoting for sensor placement for a low-rise building with a gable roof geometry constructed for all wind angles of attack. In addition, a case study for a complex roof geometry is presented to demonstrate the framework's effectiveness in optimal sensor placement for complex roof design for wind angle of attack ranging from 0° to 360° with 90° increments.

6.4.1. Optimal Sensor Placement Framework with Sensitivity analysis

In this subsection, a set of parameters that influence the accuracy of the reconstructed data and the resulting number of sensors for the tested models is specified. Given the high number of mesh cells (each representing a potential sensor location) and to avoid sensor placement in challenging areas, interpolation is applied to exclude cells located within 5 mm of one another. This step ensures that sensors are not redundantly placed while preserving data integrity in critical regions. The accuracy of the multiresolution Dynamic Mode Decomposition (mrDMD) in data decomposition is determined by balancing resolution and precision in capturing the system’s dynamics. Key parameters, such as cycle frequency (C), truncation rate (R), and number of levels (L), are interdependent, and their optimal combination varies based on the characteristics of the system being analyzed. To address this, a sensitivity analysis algorithm was employed to optimize sensor placement by identifying the ideal combination of R, C, and L that minimizes the number of sensors while ensuring the accurate reconstruction of Cp values across all angles of attack.

The comparison across levels 4, 5, and 6 presented in Fig. 6.11 reveals a progressive tightening of the range of input combinations for optimizing sensor placement. At level 4, a broad range of truncation rates (R) and cycle cutoff frequencies (C) provides valid solutions that satisfy the 200 sensors constraint while maintaining low RMSE values. The solutions are more forgiving at this level, meaning slight deviations in the chosen values of R and C still yield acceptable results. At level 5, the range of explored values becomes narrower, with valid combinations of R and C concentrated in a more specific region. For instance, truncation rates below 200 and cycle cutoff frequencies between 10 and 20 dominate the valid solutions. Deviations outside this range either exceed the sensor threshold or increase RMSE, demonstrating increased sensitivity to input values compared to level 4. By level 6, the valid range of input combinations becomes significantly restricted. Only a small subset of truncation rates ($R < 100$) and cycle cutoff frequencies (C between 10 and 20) result in solutions that meet both the sensor threshold and acceptable RMSE levels. Deviating from these ranges, even slightly, leads to a rapid increase in RMSE or a dramatic rise in the number of sensors, showing that higher levels demand much more precise input tuning to achieve the desired outcomes.

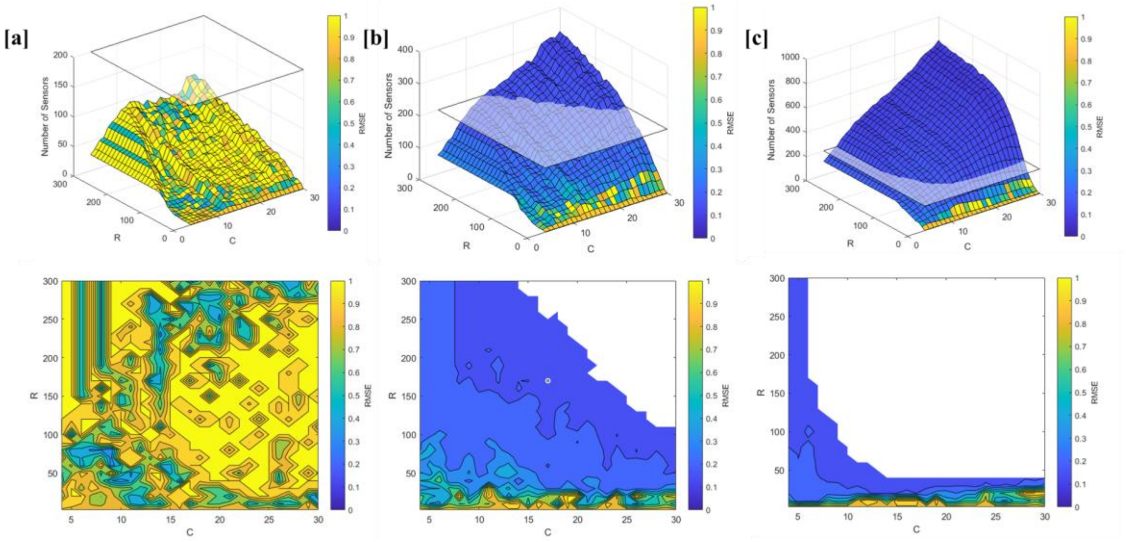

Fig. 6.11 Optimization results for levels (a) L=4, (b) L=5, and (c) L=6 show the relationship between truncation rate (R), cycle cutoff frequency (C), and the number of sensors with RMSE.

The contour plots (i.e., Fig. 6.12) of the true and predicted Cp distributions visually represent the pressure fields on the gable roof. The contours display the spatial variation of Cp, highlighting areas of high and low pressure across the roof surface for each AOA. A good match between the true and predicted Cp contours is indicated by the similarity in the contour patterns, gradients, and critical pressure zones. This suggests that the sensitivity analysis successfully identified parameters that capture the dominant aerodynamic behavior on the roof. However, noticeable discrepancies, such as shifts in pressure zones or differences in contour sharpness, indicate areas where the model struggles to accurately replicate the true Cp distribution, particularly in regions with flow separation, reattachment, or other complex aerodynamic phenomena.

The scatter plots on the right column provide a quantitative assessment of the regression model's performance in capturing the correlation between true and predicted Cp values. The correlation coefficient (R^2), displayed on each plot, measures how well the predicted Cp values correspond to the true values. High R^2 values indicate that the sensitivity analysis optimization effectively tuned the cycle frequency, truncation rate, and level to predict Cp with high accuracy. Conversely, lower R^2 values or significant scatter deviations suggest limitations in capturing certain pressure characteristics, possibly due to insufficient parameterization or challenges in modelling localized flow features unique to specific AOAs. The variation in performance across different AOAs provides insights into the robustness of the sensitivity analysis optimization process. For some AOAs, the predicted Cp contours and scatter plots show strong agreement, indicating that the optimized parameters generalize well to those flow conditions. However, for AOAs with more complex flow dynamics (e.g., involving strong vortices or asymmetric flow patterns), discrepancies in the contours and lower R^2 values suggest that the model may require further refinement, such as incorporating additional parameters or improving the representation of turbulence effects. Overall, the analysis reveals that the sensitivity analysis optimization demonstrates varying levels of success in predicting Cp distributions on the gable roof. While strong correlations and similar pressure contours in some AOAs highlight the model's effectiveness, discrepancies in others underscore the need for further improvements. This emphasizes the importance of systematically refining the cycle frequency, truncation rate, and level to enhance predictive accuracy across a wide range of aerodynamic conditions.

Wind angle	**True C_P**	**Predicated C_P**	**Regression model**
0°	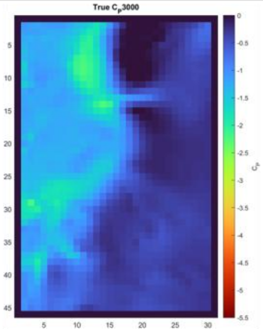	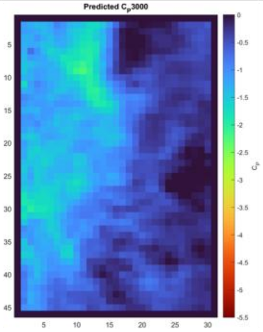	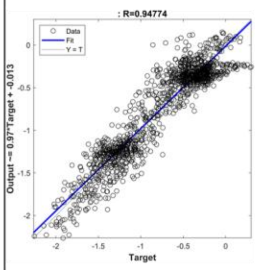
30°	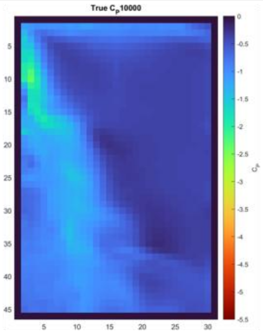	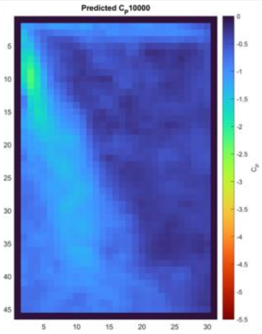	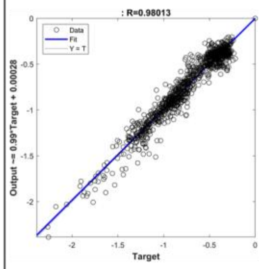
60°	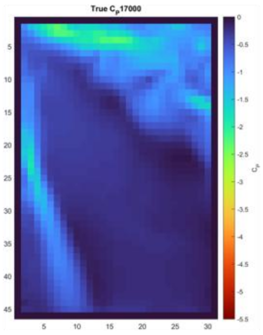	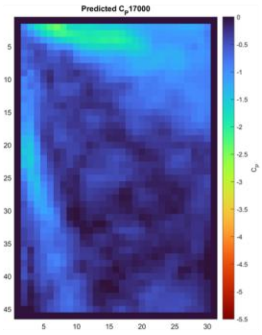	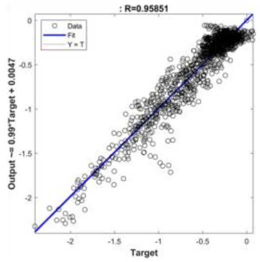
90°	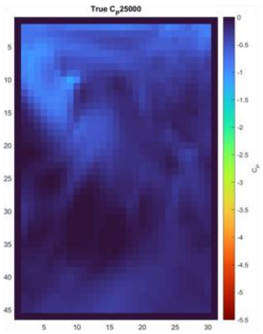	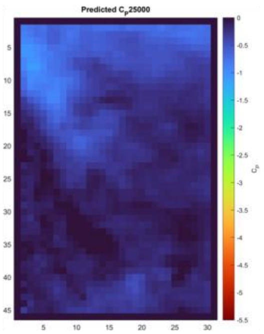	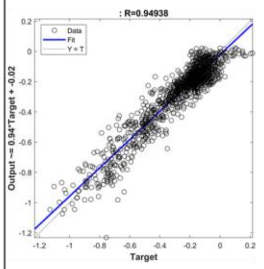

Fig. 6.12 Reconstructed pressure data on the roof of low-rise buildings along with a regression model for each AOA.

Fig. 6.13 illustrates the comparison between the true and predicted mean pressure coefficients (Cp) for wind angles of attack at 0°, 30°, 60°, and 90°. The comparison includes spatial contour plots for both predicted and true Cp fields, as well as regression models, to assess the accuracy of the predictions. For an angle of attack of 0°, the predicted and true pressure distributions exhibit excellent agreement across the entire roof surface. The contours show a uniform pressure gradient typical of wind flowing perpendicularly to a simple surface. The regression model highlights this accuracy, with an R^2 value of 0.99991, confirming good correlation between the predicted and true values. The minimal scatter observed in the regression plot further demonstrates the precision of the reconstruction process. At 30°, the pressure field becomes more complex due to the oblique wind direction, introducing localized regions of higher suction near the leading edges and separation zones. Despite these complexities, the predicted pressure contours closely align with the true distribution, accurately capturing the key aerodynamic features. The regression plot yields an R^2 value of 0.99975, reflecting strong agreement and minimal reconstruction error. For an angle of attack of 60°, the pressure variations intensify, particularly near the leading roof edges where significant gradients occur due to flow separation and reattachment. The predicted and true Cp fields remain consistent, with slight deviations observed in regions of complex flow interactions. The regression model confirms the accuracy of the reconstruction, with an R^2 value of 0.99916, indicating a strong correlation between predicted and true values. At 90°, the flow stagnates on the windward face, leading to sharp pressure drops and turbulence downstream. This results in an asymmetrical pressure distribution, with pronounced regions of flow separation on the trailing side of the roof. Despite the increased complexity, the reconstructed Cp fields match the true fields effectively. The regression analysis yields an R^2 value of 0.99838, demonstrating the robustness of the reconstruction method even under challenging aerodynamic conditions.

Fig. 6.14 Compares the true and predicted Root Mean Square (RMS) values of the pressure coefficient for wind angles of at ,30°, 0°, 30°, 60°, and 90°. The results are presented as spatial contour plots for both true and predicted fields alongside regression models to evaluate prediction accuracy. At 0°, the predicted RMS values closely align with the true data, displaying a near-uniform gradient across the surface. The regression plot confirms this agreement with a high R^2 value of 0.99938, demonstrating minimal error and excellent correlation. For 30°, the pressure distribution becomes more complex, with regions of higher RMS values near leading edges due to oblique wind flow. Despite this complexity, the predicted and true contours remain consistent, with an R^2 value of 0.9955 indicating strong accuracy. At $60°$ the RMS values show greater variability, particularly near separation regions where localized peaks are observed. The predicted RMS fields capture the key features effectively, though slight deviations appear in high-gradient areas. The regression analysis yields an R^2 value of 0.9866, reflecting a slight reduction in accuracy but maintaining reliable performance. For 90° the RMS distribution is influenced by flow stagnation on the windward face and turbulence on the leeward side. The predicted results match the overall pattern well, with an R^2 value of 0.9804, confirming the robustness of the reconstruction under complex aerodynamic conditions.

Fig. 6.15 Illustrates the optimized placement of sensors on the surface of a gable roof, accounting for pressure variations across all angles of attack (AOAs). The contours represent the eigenvector distributions of the pressure coefficient (Cp), with cooler colours (blues and greens) indicating regions of higher variability and warmer colours (yellows and reds) corresponding to areas of lower variation. The sensors, represented by white markers, are strategically distributed to ensure comprehensive coverage of critical zones with significant pressure fluctuations, such as leading edges and areas prone to flow separation. Conversely, regions with minimal variability require fewer sensors, reflecting an efficient and resource-conscious optimization. The optimization process for combining all AOA cases uses Level 6 ($L = 6$) analysis, with a truncation rate ($R = 150$) and a maximum cycle cutoff ($C = 7$). These parameters balance data complexity and accuracy by retaining key aerodynamic information while filtering out higher-frequency noise. The truncation rate is selected to ensure sufficient data retention to capture the dominant pressure patterns, while the cycle cutoff focuses on significant frequency components, improving measurement reliability. Considering all AOAs, the sensor layout provides robust and accurate coverage for varying wind conditions. High sensor density in regions of high Cp ensures critical aerodynamic phenomena are captured while minimizing redundant sensors in less dynamic areas, reducing resource usage. This optimized layout enhances the reliability of pressure measurements, supporting accurate wind load predictions and structural assessments. By ensuring high-resolution data collection across critical zones, this approach contributes to better computational models and informs safer, more efficient structural designs.

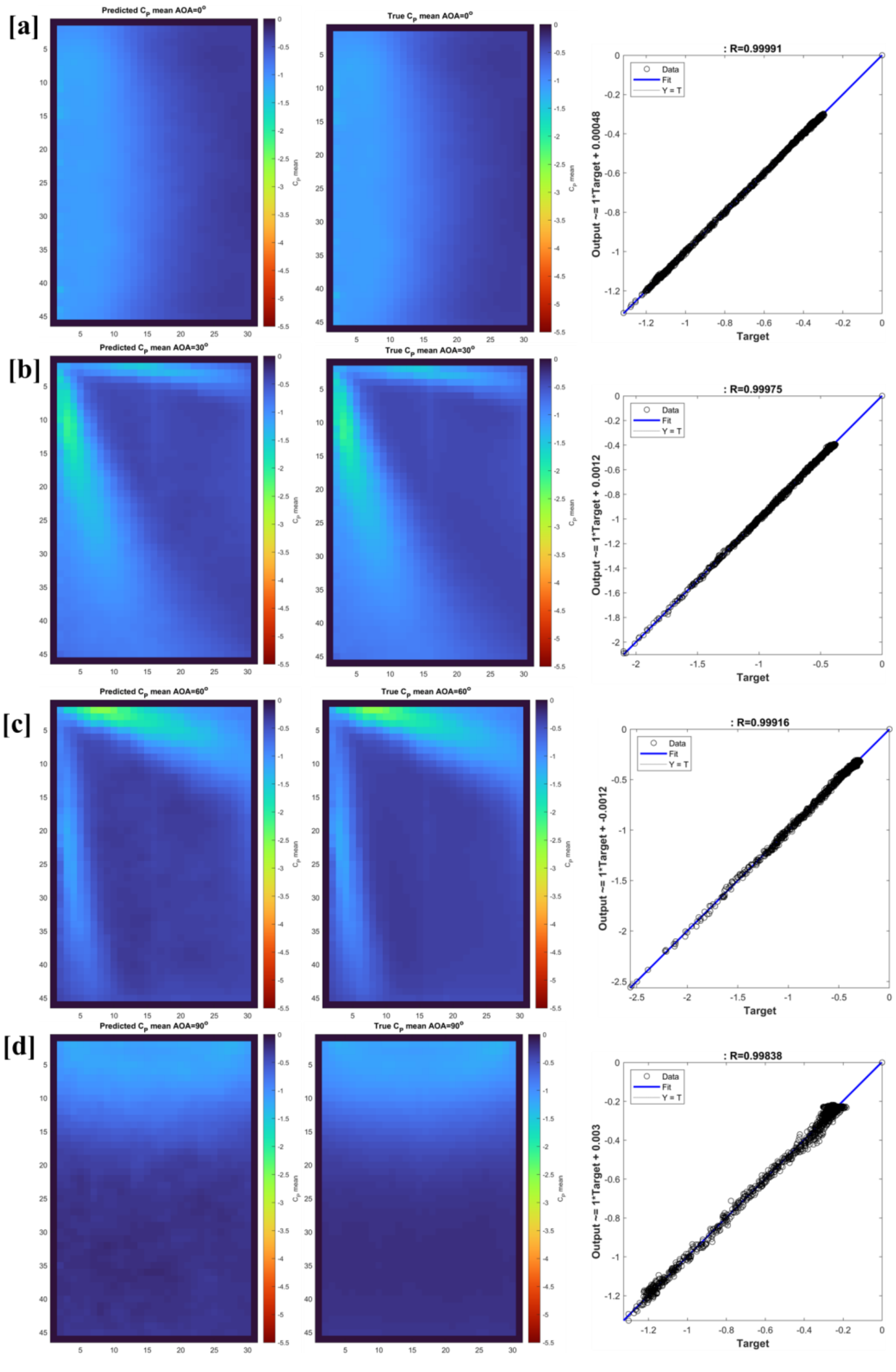

Fig. 6.13 Comparison between true and predicated mean pressure coefficient and regression model for wind angle of attack (a)0^o, (b) 30^o, (c) 60^o, and (d) 90^o.

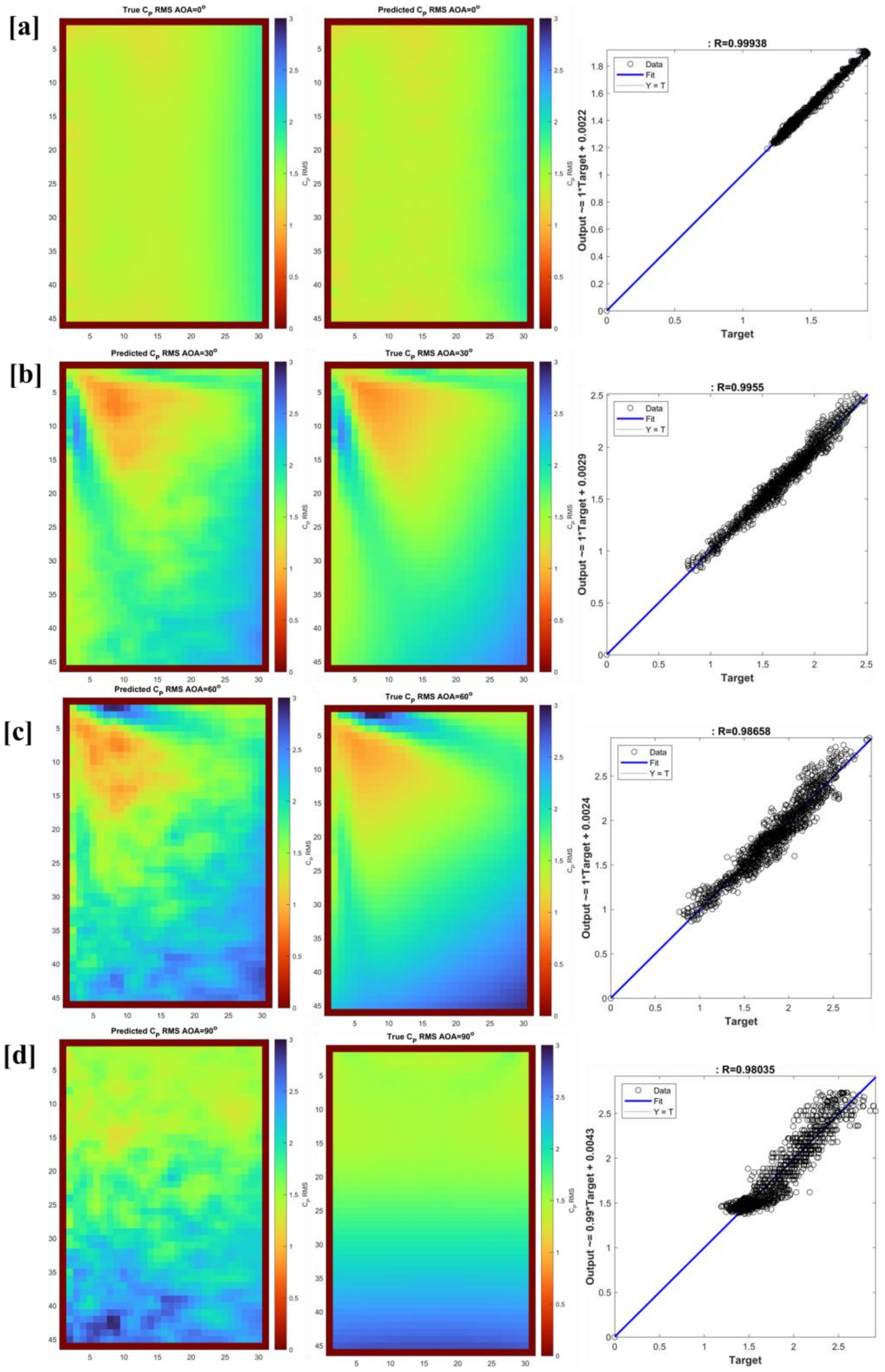

Fig. 6.14 comparison between true and predicated RMS of pressure coefficient and regression model for wind angle of attack (a) 0^o, (b) 30^o, (c) 60^o, and (d) 90^o.

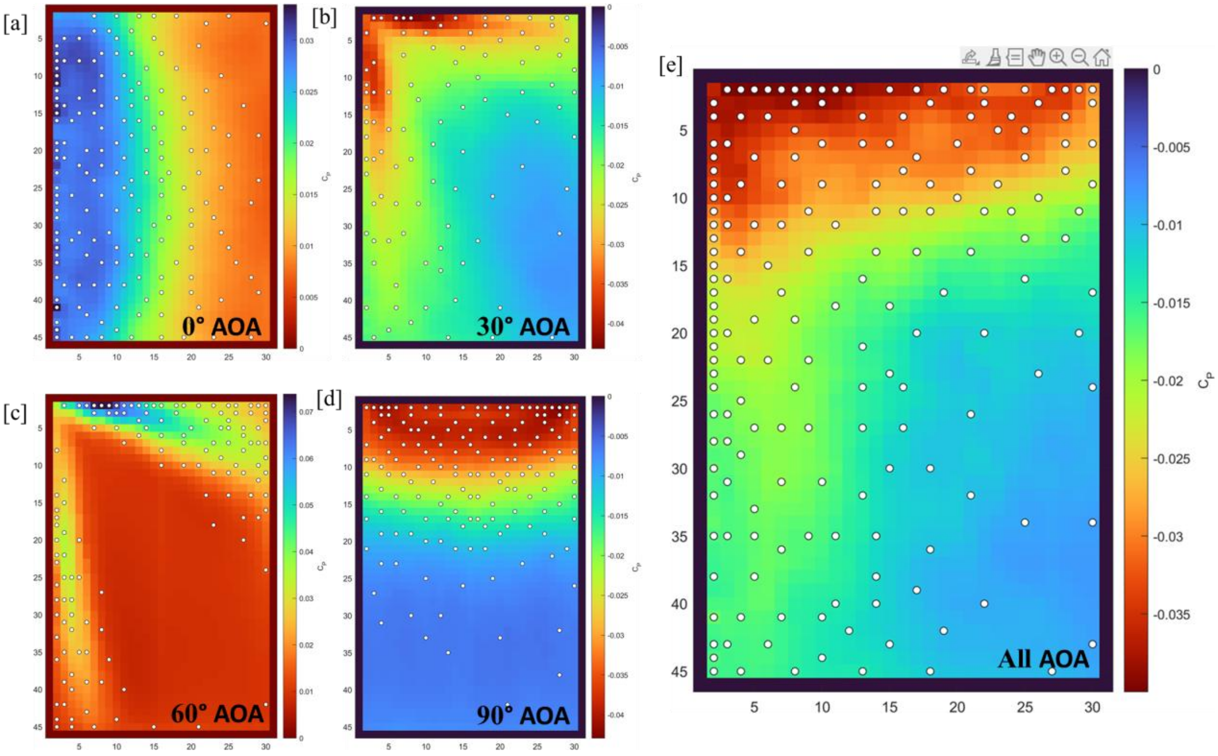

Fig. 6.15 Optimized sensor placement across (a) 0°, (b) 30°,(c) 60°,(d) 90°, and (e) combined all AOAs, illustrating eigenvector distributions of pressure coefficients (Cp) and highlighting critical regions of pressure variation with strategically placed sensors for accurate and efficient data collection.

6.4.2. Optimal Sensor Placement for Complex roof geometry of low-rise building

The aerodynamic behavior of complex roof geometries introduces significant challenges due to the development of intricate flow phenomena such as flow separation**,** reattachment, and vortex formation regions. Unlike simple roof geometries, which exhibit relatively uniform pressure distributions, complex roof designs create highly localized pressure variations, leading to areas of high suction and significant flow disturbances. This behavior is particularly critical in modern residential buildings, where intricate architectural features, such as multiple slopes and roof ridges, influence the wind load distribution. For this case study, a real-world-inspired design adapted from the Kopp and Gavanski model was analyzed, with full-scale dimensions of $\mathbf{20.88}\,\boldsymbol{m} \times \mathbf{21.7}\,\boldsymbol{m} \times \mathbf{5.5}\,\boldsymbol{m}$ (Fig. 6.16). The geometry included multiple ridges, intersections, and varied roof slopes, reflecting the increasing complexity in contemporary residential construction [65].

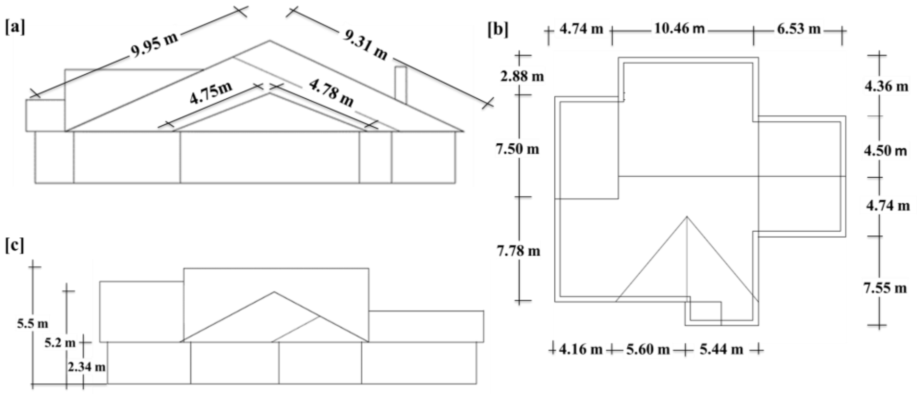

Fig. 6.16 Complex roof geometry layout and dimensions in full scale (a) Side view illustrating roof slope and ridge measurements, (b) Front elevation view of the roof structure, and (c) Top view (roof plan) displaying overall roof geometry and dimensions.

To analyze the wind-induced pressures, a Large Eddy Simulation (LES) was performed under an open terrain inflow profile to resolve the flow turbulence accurately. The LES results provided spatiotemporal data for pressure coefficient (Cp) fields across the building surface, which exhibited significant variations near roof ridges and intersections due to flow separation and reattachment. Using the LES-generated data, multi-resolution Dynamic Mode Decomposition (mrDMD) is applied to extract the dominant spatial modes of the pressure fields across different time scales. The mrDMD technique effectively identified critical areas of pressure variation, capturing the most influential aerodynamic features of the flow. Following the mrDMD analysis, QR pivoting is employed to optimize sensor placement by identifying the most influential spatial points for data reconstruction. The reconstructed pressure fields, illustrated in Fig. 6.17, present time snapshots of the reconstructed and true pressure fields (Cp) at three distinct time steps, 3000, 10000, and 25000, for an attack (AOA). The predicted pressure fields, obtained using optimized sensor placements, align closely with the true LES data, effectively capturing critical flow phenomena such as flow separation, reattachment regions, and zones of significant pressure gradients. The regression plots validate the accuracy of the reconstruction, showing minimal deviation from the ideal line and consistently high R^2 values $0.9985, 0.9979$, and 0.9987. These results confirm that the spatial modes extracted through mrDMD capture the dominant pressure dynamics, while the optimized sensor placements ensure accurate reconstruction over time. The close agreement between predicted and true fields across all snapshots demonstrates the methodology's effectiveness in handling both spatial and temporal variations of the pressure field for complex roof design.

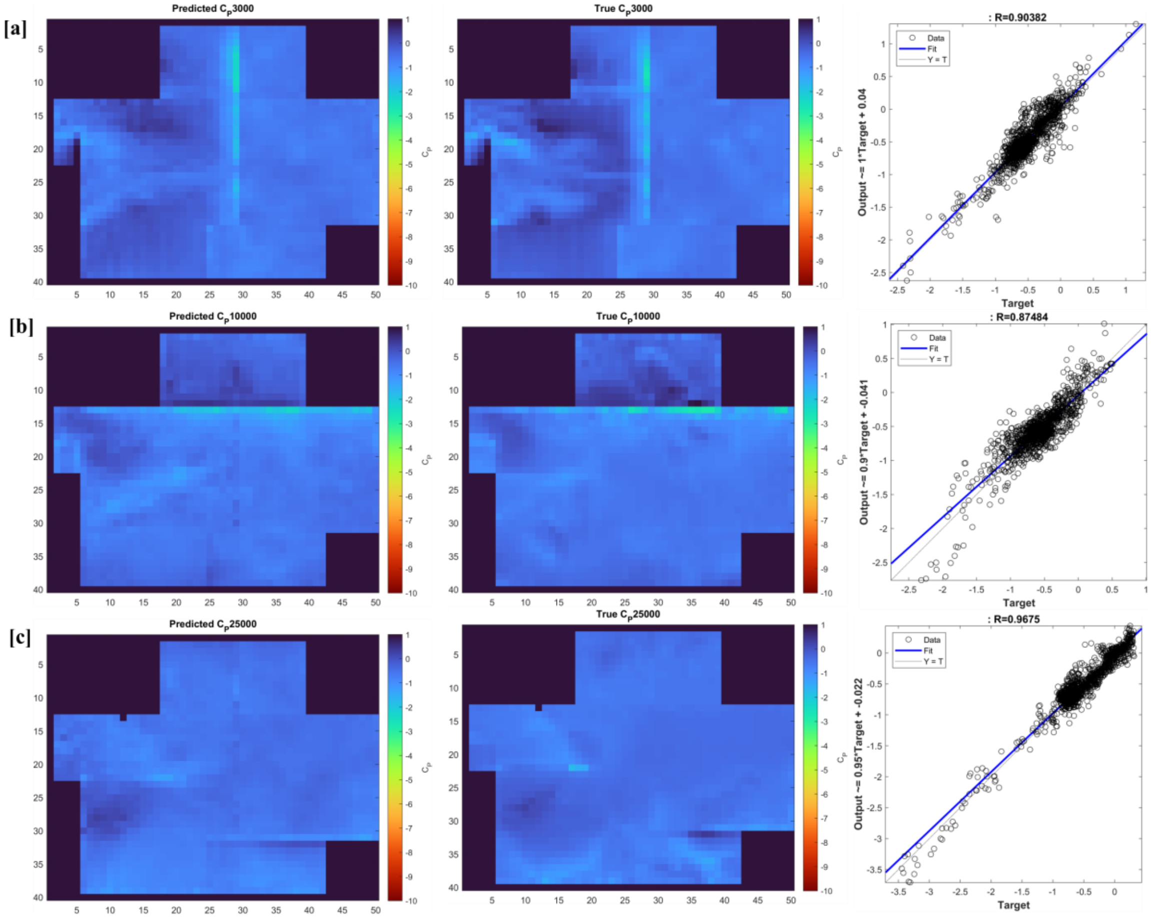

Fig. 6.17 Reconstructed pressure data on the roof of low-rise buildings along with a regression model for all AOA.

The optimization results for various truncation levels and cycle cutoff frequencies, shown in Fig. 6.18, highlight the trade-off between sensor count and reconstruction error (RMSE). showing the relationship between truncation rate (R), cycle cutoff frequency (C), and the number of sensors (Z) with the associated Root Mean Square Error (RMSE). The top row of 3D surface plots illustrates how the number of sensors and reconstruction accuracy depends on the truncation rate and cycle cutoff frequency. At lower truncation rates, the required sensors increase significantly to achieve acceptable accuracy. As the truncation rate increases, fewer sensors are needed, with the RMSE gradually stabilizing, indicating that higher truncation rates contribute diminishing improvements to reconstruction quality. Similarly, the cycle cutoff frequency influences the sensor count and accuracy. Higher values of C improve accuracy, as reflected in the lower RMSE values, but require a larger number of sensors. The bottom row of 2D contour plots provides a clearer visualization of the trade-offs between truncation rate, cycle frequency, and accuracy. The plots highlight regions where the RMSE is minimized, corresponding to an efficient balance between sensor count and reconstruction performance. At low truncation rates, the RMSE remains high due to insufficient mode capture. However, as R and C increase, the RMSE reduces significantly, forming distinct regions where the reconstruction error is minimized. Progressing from Level 4 to Level 6, the total number of sensors decreases considerably while maintaining high reconstruction accuracy. Level 6, in particular, achieves the most efficient optimization, with RMSE values stabilized close to zero and a significant reduction in sensor count. The findings underscore the importance of selecting appropriate truncation rates and cycle cutoff frequencies to achieve cost-effective and efficient sensor placement for monitoring aerodynamic pressures on complex roof surfaces. Finally, the optimized sensor placement for combined AOAs is shown in Fig. 6.19, where the eigenvector distributions of pressure coefficients (Cp) reveal the critical regions of pressure variation. The strategically placed sensors effectively captured the aerodynamic behavior while significantly reducing measurement redundancy. This case study demonstrates the effectiveness of combining LES, mrDMD, and QR pivoting to address the challenges posed by complex roof geometries. The methodology ensures a robust, cost-effective approach to wind load evaluation while maintaining high accuracy. These findings are particularly valuable for improving modern residential buildings' design and structural resilience with increasingly intricate roof designs.

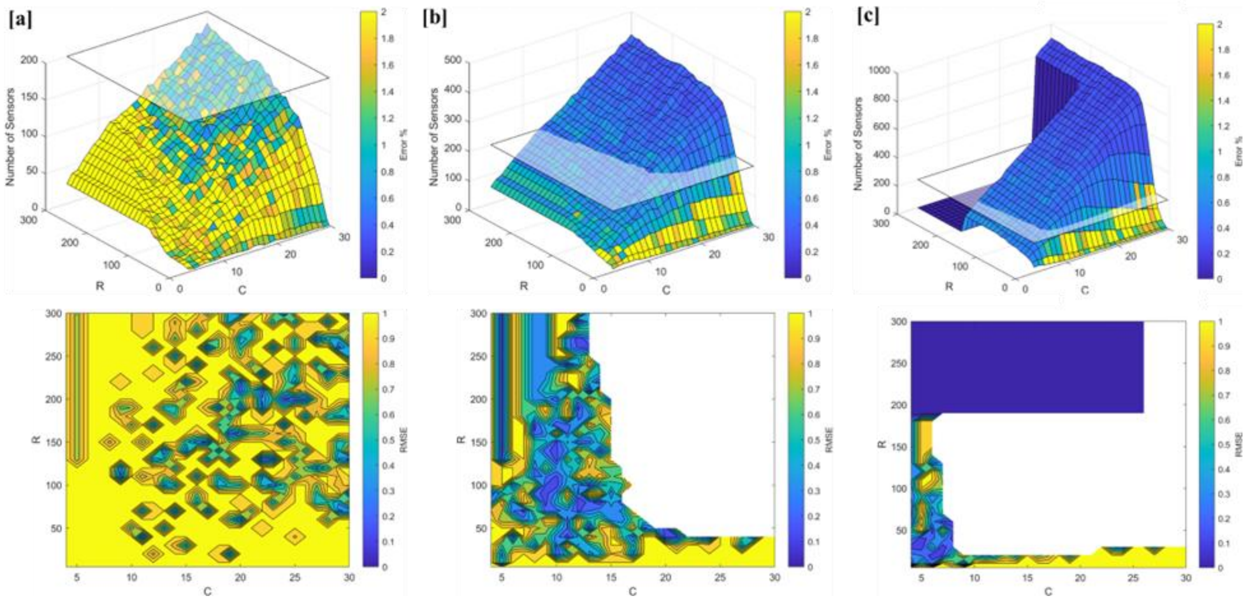

Fig. 6.18 Optimization results for levels (a) L= 4, (b) L= 5, and (c) L= 6 show the relationship between truncation rate (R), cycle cutoff frequency (C), and the number of sensors with RMSE.

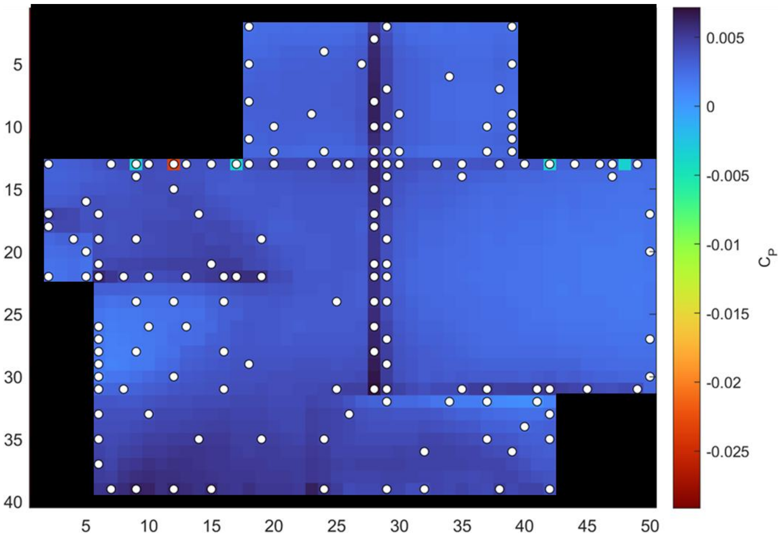

Fig. 6.19 Optimized sensor placement for the combined AOAs, illustrating eigenvector distributions of pressure coefficients (Cp) and highlighting critical regions of pressure variation with strategically placed sensors.

6.5. Summary and Conclusion

This study examines the aerodynamic behaviour of low-rise buildings with complex roof geometries, addressing challenges such as wind-induced pressures, flow separation, and vortex formation. Using large eddy simulation (LES), high-fidelity pressure data were generated to capture critical aerodynamic features, including localized suctions and pressure gradients near ridges and leading edges. A combined multi-resolution dynamic mode decomposition (mrDMD) and QR pivoting approach was applied to optimize sensor placement, reducing sensor count by up to 80 percent while maintaining accuracy. The methodology was validated through time snapshots and RMS comparisons across various wind angles of attack, achieving high correlation values above 0.98 and minimal errors. The results effectively captured spatial and temporal pressure variations while illustrating trade-offs between truncation rates, sensor count, and accuracy. The main contributions of this study include:

I. Sensors were strategically placed to capture critical aerodynamic features, such as leading edges and flow separation zones for both case studies (i.e., gable and complex roof geometry).

II. A truncation rate ($R < 100$) and cycle cutoff frequency ($10 \leq C \leq 20$) achieved minimal RMSE and reduced sensor requirements, balancing accuracy and cost, showcasing efficient Trade-offs in Optimization

III. It is found that the gable roof geometry requires fewer sensors due to uniform pressure distribution, with Level 4 optimization providing sufficient accuracy. On the other hand, the complex roof geometry needed higher sensor density to capture localized pressure variations and complex aerodynamic phenomena, especially at Level 6 optimization.

IV. The gable roof geometry achieved minimal reconstruction error across all AOAs, with $R^2 > 0.99$, even at lower optimization levels. On the other hand, Complex Roof geometry maintained high reconstruction accuracy ($R^2 > 0.998$) but exhibited slight deviations in regions with complex flow interactions, such as flow separation and reattachment.

V. In the case of the gable roofs, broader valid ranges of truncation rates (R > 200) and cycle cutoff frequencies ($C > 20$) allowed flexibility, simplifying the optimization process, while it was found that Complex roofs required higher levels (e.g., Level 6), leading to tighter constraints ($R < 100,\ 10 \le C \le 20$) to balance reconstruction accuracy and sensor count, ensuring effective coverage of critical aerodynamic regions.

6.6. Reference

[1] R. Al-Chalabi, A. Elshaer, Aerodynamic mitigation of low-rise building with complex roof geometry, Front. Built Environ. 9 (2023) 1200383. https://doi.org/10.3389/FBUIL.2023.1200383/BIBTEX.

[2] Municipal By-Laws and National Fire Protection Codes, Ontario Building Code, (2012).

[3] S. Hassani, M. Mousavi, A.H. Gandomi, Structural Health Monitoring in Composite Structures: A Comprehensive Review, Sensors 2022, Vol. 22, Page 153. 22 (2021) 153. https://doi.org/10.3390/S22010153.

[4] X. Luo, A. Kareem, S. Yoo, Optimal sensor placement for reconstructing wind pressure field around buildings using compressed sensing, J. Build. Eng. 75 (2023) 106855. https://doi.org/10.1016/J.JOBE.2023.106855.

[5] H. Gao, J. Liu, P. Lin, G. Hu, L. Patruno, Y. Xiao, K.T. Tse, K.C.S. Kwok, An optimal sensor placement scheme for wind flow and pressure field monitoring, Build. Environ. 244 (2023) 110803. https://doi.org/10.1016/J.BUILDENV.2023.110803.

[6] Y. Yuan, F.T.K. Au, D. Yang, J. Zhang, Active learning structural model updating of a multisensory system based on Kriging method and Bayesian inference, Comput. Civ. Infrastruct. Eng. 38 (2023) 353–371. https://doi.org/10.1111/MICE.12822.

[7] K. Worden, C.R. Farrar, G. Manson, G. Park, The fundamental axioms of structural health monitoring, Proc. R. Soc. A Math. Phys. Eng. Sci. 463 (2007) 1639–1664. https://doi.org/10.1098/RSPA.2007.1834.

[8] Y. Ma, Y.B. Zheng, S.Y. Wang, Y.D. Wong, S.M. Easa, Virtual-real-fusion simulation framework for evaluating and optimizing small-spatial-scale placement of cooperative roadside sensing units, Comput. Civ. Infrastruct. Eng. 39 (2024) 707–730. https://doi.org/10.1111/MICE.13167.

[9] J.P. Amezquita-Sanchez, M. Valtierra-Rodriguez, H. Adeli, Wireless smart sensors for monitoring the health condition of civil infrastructure, Sci. Iran. 25 (2018) 2913–2925. https://doi.org/10.24200/SCI.2018.21136.

[10] Z. Bai, S.L. Brunton, B.W. Brunton, J.N. Kutz, E. Kaiser, A. Spohn, B.R. Noack, Data-Driven Methods in Fluid Dynamics: Sparse Classification from Experimental Data, Whither Turbul. Big Data 21st Century? (2017) 323–342. https://doi.org/10.1007/978-3-319-41217-7_17.

[11] X. Xie, J. Cai, H. Wang, Q. Wang, J. Xu, Y. Zhou, B. Zhou, Sparse-sensing and superpixel-based segmentation model for concrete cracks, Wiley Online Libr. Xie, J Cai, H Wang, Q Wang, J Xu, Y Zhou, B ZhouComputer-Aided Civ. Infrastruct. Eng. 2022•Wiley Online Libr. 37 (2022) 1769–1784. https://doi.org/10.1111/mice.12903.

[12] J. Harlim, A.J. Majda, B. Gershgorin, Mathematical strategies for filtering turbulent dynamical systems, 27 (2010) 441–486. https://doi.org/10.3934/dcds.2010.27.441.

[13] C. Malings, M. Pozzi, Value of information for spatially distributed systems: Application to sensor placement, Reliab. Eng. Syst. Saf. 154 (2016) 219–233. https://doi.org/10.1016/J.RESS.2016.05.010.

[14] R. Semaan, Optimal sensor placement using machine learning, Comput. Fluids. 159 (2017) 167–176. https://doi.org/10.1016/J.COMPFLUID.2017.10.002.

[15] K. Worden, A.P. Burrows, Optimal sensor placement for fault detection, Eng. Struct. 23 (2001) 885–901. https://doi.org/10.1016/S0141-0296(00)00118-8.

[16] M. Yuan, Y. Geng, B. Lin, H. Tang, Y. Yang, Optimization of indoor temperature sensor deployment in large spaces for multiple building operation scenarios using the genetic algorithm, J. Build. Eng. 96 (2024) 110446. https://doi.org/10.1016/J.JOBE.2024.110446.

[17] R. Snaiki, S.F. Mirfakhar, Multiresolution dynamic mode decomposition approach for wind pressure analysis and reconstruction around buildings, Comput. Civ. Infrastruct. Eng. (2024). https://doi.org/10.1111/MICE.13304.

[18] J.S. Hwang, D.K. Kwon, A. Kareem, A modal-based Kalman filtering framework for mode extraction and decomposition of damped structures, Comput. Civ. Infrastruct. Eng. 38 (2023) 1274–1289. https://doi.org/10.1111/MICE.12963.

[19] J.N.K. and S.L.B. K. Manohar, B. W. Brunton, Data-driven sparse sensor placement for reconstruction: Demonstrating the benefits of exploiting known patterns, IEEE Control Syst. Mag. 38 (2018) 63–86.

[20] B. Herrmann, P.J. Baddoo, R. Semaan, S.L. Brunton, B.J. Mckeon, Data-driven resolvent analysis, J. Fluid Mech. 918 (2021) A10. https://doi.org/10.1017/JFM.2021.337.

[21] M. Luhar, A. Sharma, B.M. Mechanics, On the structure and origin of pressure fluctuations in wall turbulence: predictions based on the resolvent analysis, J. Fluid Mech. 741 (2014) 30–70.

[22] A. Chavarin, M. Luhar, Resolvent analysis for turbulent channel flow with riblets, AIAA J. 58 (2020) 589–599. https://doi.org/10.2514/1.J058205.

[23] H. Shu, W. Song, Z. Song, H. Guo, C. Li, Y. Wang, Multistep short-term wind speed prediction with rank pooling and fast Fourier transformation, Wind Energy. 27 (2024) 667–694. https://doi.org/10.1002/WE.2906.

[24] G. Berkooz, P. Holmes, J.L.-A. review of Fluid, U. 1993, The proper orthogonal decomposition in the analysis of turbulent flows, Annu. Rev. Fluid Mech. 25 (2003) 539–75. https://doi.org/10.1146/annurev.fl.25.010193.002543.

[25] Y. Zhao, M. Zhao, X. Li, Z. Liu, J. Du, A modified proper orthogonal decomposition method for flow dynamic analysis, Comput. Fluids. 182 (2019) 28–36. https://doi.org/10.1016/J.COMPFLUID.2019.01.020.

[26] Q. Zhang, Y. Liu, S. Wang, The identification of coherent structures using proper orthogonal decomposition and dynamic mode decomposition, J. Fluids Struct. 49 (2014) 53–72. https://doi.org/10.1016/J.JFLUIDSTRUCTS.2014.04.002.

[27] T.W. Muld, G. Efraimsson, D.S. Henningson, Flow structures around a high-speed train extracted using Proper Orthogonal Decomposition and Dynamic Mode Decomposition, Comput. Fluids. 57 (2012) 87–97. https://doi.org/10.1016/J.COMPFLUID.2011.12.012.

[28] T.R. Smith, J. Moehlis, P. Holmes, Low-dimensional modelling of turbulence using the proper orthogonal decomposition: A tutorial, Nonlinear Dyn. 41 (2005) 275–307. https://doi.org/10.1007/S11071-005-2823-Y.

[29] K. Willcox, J. Peraire, Balanced model reduction via the proper orthogonal decomposition, AIAA J. 40 (2002) 2323–2330. https://doi.org/10.2514/2.1570.

[30] A. Towne, O. Schmidt, T.C. Mechanics, Spectral proper orthogonal decomposition and its relationship to dynamic mode decomposition and resolvent analysis, J. Fluid Mech. (2018).

[31] P.J. Schmid, Dynamic mode decomposition of numerical and experimental data, J. Fluid Mech. 656 (2010) 5–28. https://doi.org/10.1017/S0022112010001217.

[32] J.N. Kutz, X. Fu, S.L. Brunton, Multiresolution dynamic mode decomposition, SIAM J. Appl. Dyn. Syst. 15 (2016) 713–735. https://doi.org/10.1137/15M1023543.

[33] S.L. Brunton, J.L. Proctor, J.H. Tu, J.N. Kutz, S.L. Brunton, J.L. Proctor, J.H. Tu, J.N. Kutz, Compressed sensing and dynamic mode decomposition, J. Comput. Dyn. 2 (2016) 165–191. https://doi.org/10.3934/JCD.2015002.

[34] P.J. Schmid, Dynamic Mode Decomposition and Its Variants, Annu. Rev. Fluid Mech. 54 (2021) 225–254. https://doi.org/10.1146/ANNUREV-FLUID-030121-015835.

[35] P. Bevanda, S. Sosnowski, S. Hirche, Koopman operator dynamical models: Learning, analysis and control, Annu. Rev. Control. 52 (2021) 197–212. https://doi.org/10.1016/J.ARCONTROL.2021.09.002.

[36] J.H. Tu, C.W. Rowley, D.M. Luchtenburg, S.L. Brunton, J.N. Kutz, On dynamic mode decomposition: Theory and applications, J. Comput. Dyn. 1 (2014) 391–421. https://doi.org/10.3934/JCD.2014.1.391.

[37] C.W. Rowley, I. Mezi, S. Bagheri, P. Schlatter, D.S. Henningson, Spectral analysis of nonlinear flows, J. Fluid Mech. 641 (2009) 115–127. https://doi.org/10.1017/S0022112009992059.

[38] R. Al-Chalabi, A. Elshaer, H. Aboshosha, Enhancing LES efficacy in wind load evaluation of low-rise buildings using synthesized inflow turbulence, J. Build. Eng. 95 (2024) 110233. https://doi.org/10.1016/J.JOBE.2024.110233.

[39] J.D. Holmes, C. Paton, R. Kerwin, Wind Loading of Structures, CRC Press, 2007. https://doi.org/10.4324/9780203964286.

[40] J.H. Tu, C.W. Rowley, J.N. Kutz, J.K. Shang, Spectral analysis of fluid flows using sub-Nyquist-rate PIV data, Exp. Fluids. 55 (2014) 1–13. https://doi.org/10.1007/S00348-014-1805-6.

[41] Y. Yuan, K. Zhou, W. Zhou, X. Wen, Y. Liu, Flow prediction using dynamic mode decomposition with time-delay embedding based on local measurement, Phys. Fluids. 33 (2021). https://doi.org/10.1063/5.0064867/13882694/095109_1_ONLINE.PDF.

[42] J.H. Tu, C.W. Rowley, J.N. Kutz, J.K. Shang, Spectral analysis of fluid flows using sub-Nyquist-rate PIV data, Exp. Fluids. 55 (2014) 1–13. https://doi.org/10.1007/S00348-014-1805-6/FIGURES/14.

[43] J.N. Kutz, X. Fu, S.L. Brunton, Multiresolution Dynamic Mode Decomposition, Https://Doi.Org/10.1137/15M1023543. 15 (2016) 713–735. https://doi.org/10.1137/15M1023543.

[44] P. Climaco, J. Garcke, R. Iza-Teran, Multi-resolution dynamic mode decomposition for damage detection in wind turbine gearboxes, Data-Centric Eng. 4 (2023). https://doi.org/10.1017/dce.2022.34.

[45] J. Gonzales, H. Sakaue, A. Jemcov, Multi-Resolution Dynamic Mode Decomposition Analysis of the Pressure Profile Over a Fluttering Wing, AIAA Sci. Technol. Forum Expo. AIAA SciTech Forum 2022. (2022). https://doi.org/10.2514/6.2022-1661.

[46] T.H. Yi, H.N. Li, M. Gu, Optimal sensor placement for structural health monitoring based on multiple optimization strategies, Struct. Des. Tall Spec. Build. 20 (2011) 881–900. https://doi.org/10.1002/TAL.712.

[47] P. Reed, B. Minsker, D.E. Goldberg, Designing a competent simple genetic algorithm for search and optimization, Water Resour. Res. 36 (2000) 3757–3761. https://doi.org/10.1029/2000WR900231.

[48] B. Błachowski, A. Świercz, M. Ostrowski, P. Tauzowski, P. Olaszek, Ł. Jankowski, Convex relaxation for efficient sensor layout optimization in large-scale structures subjected to moving loads, Wiley Online Libr. Błachowski, A Świercz, M Ostrowski, P Tauzowski, P Olaszek, Ł JankowskiComputer-Aided Civ. Infrastruct. Eng. 2020•Wiley Online Libr. 35 (2020) 1085–1100. https://doi.org/10.1111/mice.12553.

[49] N. Karnik, M.G. Abdo, C.E. Estrada-Perez, J.S. Yoo, J.J. Cogliati, R.S. Skifton, P. Calderoni, S.L. Brunton, K. Manohar, Constrained Optimization of Sensor Placement for Nuclear Digital Twins, IEEE Sens. J. 24 (2024) 15501–15516. https://doi.org/10.1109/JSEN.2024.3368875.

[50] J. Tian, K.R. Gurley, M.T. Diaz, P.L. Fernández-Cabán, F.J. Masters, R. Fang, Low-rise gable roof buildings pressure prediction using deep neural networks, J. Wind Eng. Ind. Aerodyn. 196 (2020) 104026. https://doi.org/10.1016/J.JWEIA.2019.104026.

[51] A. Al-Chalabi, R., Elshaer, Mitigation of Wind Load on Low-rise Buildings Using Roof Parapets: A Numerical and Experimental Study, in: 9th Int. Colloq. Bluff Body Aerodyn. Appl. (BBAA). Birmingham, UK, 2024: p. 4.

[52] J.M. Denmark, Atmospheric turbulence, DTU Wind Energy. (2012).

[53] R.A. Sanni, D. Surry, A.G. Davenport, Wind loading on intermediate height buildings, Can. J. Civ. Eng. 19 (1992) 148–163. https://doi.org/10.1139/L92-015.

[54] H. Aboshosha, A. Elshaer, G.T. Bitsuamlak, A. El Damatty, Consistent inflow turbulence generator for LES evaluation of wind-induced responses for tall buildings, J. Wind Eng. Ind. Aerodyn. 142 (2015) 198–216. https://doi.org/10.1016/j.jweia.2015.04.004.

[55] A. Elshaer, H. Aboshosha, G. Bitsuamlak, A. El Damatty, A. Dagnew, LES evaluation of wind-induced responses for an isolated and a surrounded tall building, Eng. Struct. 115 (2016) 179–195. https://doi.org/10.1016/J.ENGSTRUCT.2016.02.026.

[56] B. Blocken, T. Stathopoulos, J. Carmeliet, CFD simulation of the atmospheric boundary layer: wall function problems, Atmos. Environ. 41 (2007) 238–252. https://www.sciencedirect.com/science/article/pii/S135223100600834X (accessed February 27, 2023).

[57] F. Bazdidi-Tehrani, S. Masoumi-Verki, P. Gholamalipour, M. Kiamansouri, Large eddy simulation of pollutant dispersion in a naturally cross-ventilated model building: Comparison between sub-grid scale models, Build. Simul. 12 (2019) 921–941. https://doi.org/10.1007/S12273-019-0525-5/METRICS.

[58] P. Kakka, K. Anupindi, Assessment of subgrid-scale models for large-eddy simulation of a planar turbulent wall-jet with heat transfer, Int. J. Heat Mass Transf. 153 (2020) 119593. https://doi.org/10.1016/J.IJHEATMASSTRANSFER.2020.119593.

[59] M.F. Khaled, A.M. Aly, A. Elshaer, Computational efficiency of CFD modeling for building engineering: An empty domain study, J. Build. Eng. 42 (2021) 102792. https://doi.org/10.1016/J.JOBE.2021.102792.

[60] R. Courant, K. Friedrichs, H. Lewy, Über die partiellen Differenzengleichungen der mathematischen Physik, Math. Ann. 100 (1928) 32–74. https://doi.org/10.1007/BF01448839.

[61] S.T.M. Dawson, M.S. Hemati, M.O. Williams, C.W. Rowley, Characterizing and correcting for the effect of sensor noise in the dynamic mode decomposition, Exp. Fluids. 57 (2016) 1–19. https://doi.org/10.1007/S00348-016-2127-7/FIGURES/12.

[62] A. Haar, Zur Theorie der orthogonalen Funktionensysteme - Erste Mitteilung, Math. Ann. 69 (1910) 331–371. https://doi.org/10.1007/BF01456326/METRICS.

[63] E. Candès, M. Wakin, An introduction to compressive sampling, IEEE Signal Process. Mag. 25 (2008).

[64] B. Peherstorfer, Z. Drmac, S. Gugercin, Stability of discrete empirical interpolation and gappy proper orthogonal decomposition with randomized and deterministic sampling points, SIAM J. Sci. Comput. 42 (2020) A2837–A2864. https://doi.org/10.1137/19M1307391.

[65] Gregory A. Kopp, Eri Gavanski, Wind tunnel pressure measurements on two FCMP houses, (2010) 1–30. https://scholar.google.ca/scholar?hl=en&as_sdt=0%2C5&q=wind+tunnel+pressure+measurements+on+two+FCMP+houses+&btnG= (accessed January 11, 2022).

CHAPTER 7

Conclusion and Recommendations

7.1. Summary

This thesis addresses critical challenges in evaluating and mitigating wind-induced forces on low-rise buildings by integrating experimental and numerical methods focusing on practical and efficient solutions. The research spans multiple studies to comprehensively investigate the aerodynamic performance of low-rise buildings and propose effective mitigation and optimization strategies. The aerodynamic efficiency of parapets is explored in detail, including their impact on both typical roof geometries (i.e., gable) and complex roof structures in suburban terrains. Experimental and numerical investigations reveal the role of parapets in displacing flow separation zones, reducing wind loads, and mitigating corner suctions. The studies also highlight the potential drawbacks of parapets, including increased interior roof loads and the risks posed by flying debris, emphasizing the need for a balanced design approach.

The thesis advances numerical wind load evaluations using Large Eddy Simulation (LES), with a focus on improving turbulence inflow generation, computational domain specifications, and grid refinement. Key findings include defining optimal parameters, such as the turbulence maximum frequency (f_{max}) and grid resolution, to enhance the accuracy of wind pressure predictions. The results demonstrate the limitations of current computational guidelines and propose improvements to ensure reliable evaluations for low-rise building geometries. The performance of aerodynamic mitigation techniques, including parapets and roof modifications, is assessed across various terrain types, wind directions, and roof slopes. Results emphasize the importance of considering terrain effects and building arrangements in wind load assessments, which are often overlooked in current standards.

An innovative framework for Optimal Sensor Placement (OSP) is developed, leveraging multi-resolution Dynamic Mode Decomposition (mrDMD) and QR pivoting algorithms. This framework identifies optimal sensor locations on building surfaces, significantly reducing the number of sensors required (i.e., over 80%) while maintaining data accuracy. This approach enhances the efficiency and affordability of experimental wind load evaluations, addressing practical constraints such as cost and accessibility.

Through these studies, the thesis contributes to the understanding of wind-induced forces on low-rise buildings, providing practical guidelines for aerodynamic mitigation, sensor optimization, and accurate wind load evaluations. These findings have implications for improving structural resilience, reducing costs, and enhancing the safety of low-rise buildings in diverse environmental conditions, particularly in regions prone to extreme weather events.

7.2. Main Contribution

I. Examining the effectiveness of common of Aerodynamic Mitigation Techniques for Complex Roof Geometries

- Introduced and evaluated corner and ridgeline parapets for low-rise buildings with complex roof geometries using Computational Fluid Dynamics (CFD).
- Demonstrated that corner parapets reduce extreme suction by up to 29%, while ridgeline parapets decrease pressure values at interior roof zones by 53% and overall roof uplift by 5.6%.
- Highlighted the critical role of parapet design in mitigating wind loads while addressing potential risks such as flying debris and water leaks at parapet connections.

II. Advancement in large eddy simulation (LES) accuracy for wind load evaluations

- Systematically defined optimal inflow turbulence parameters, including the maximum turbulence frequency and grid size, to improve LES predictions.
- Guideline to estimate the required mesh size Δx within the computational domain that resolves the turbulence up to the maximum frequency, f_{max} or to determine f_{max} that can be resolved by a pre-designed grid of size Δx.
- Identified that computational domain dimensions, grid refinement zones, and grid discretization schemes significantly impact wind load accuracy on low-rise building, achieving RMSE as low as 3% for mean pressure and 1.5% for pressure fluctuations when optimized parameters are employed.
- Highlighted the limitations of current computational wind load evaluation on low-rise buildings guidelines, particularly for minimum domain width and height, and provided refined recommendations to reduce discrepancies.

III. Evaluation of the efficiency of the aerodynamic mitigation add to low-rise buildings in suburban and open terrains

- Conducted wind tunnel tests on low-sloped gable roofs with perimetric and corner parapets in open and suburban terrain conditions.
- Found that terrain roughness reduces parapet efficiency, with mean and fluctuating pressure reductions 50% lower in suburban terrains compared to open terrains.
- Demonstrated that parapets alter pressure distributions by raising vortex positions and promoting flow reattachment, effectively reducing peak and mean roof pressures.

IV. Identification of terrain-induced variations in wind load patterns
   - Showed that suburban terrain amplifies pressure fluctuations at internal roof zones by over 60% while reducing mean suction at edges by 30%.
   - Highlighted that parapet efficiency in reducing peak and fluctuating pressures varies significantly between terrains, with reduced performance in higher turbulence suburban conditions.
   - Framework for optimal sensor placement (OSP):
   - Proposed a methodology integrating advanced techniques like mrDMD and QR pivoting to optimize sensor placement for wind load evaluation.
   - Anticipated reduction of over 80% in sensor count without compromising accuracy, making experimental setups more cost-effective and scalable.

7.3. Future work and recommendations

I. **Exploration of Flexible Parapets:** Investigate the aerodynamic performance of flexible parapets as an alternative to rigid designs. Flexible parapets may provide adaptive responses to varying wind conditions, potentially reducing extreme pressures and mitigating the risk of structural damage or failure.

II. **Study of Complex Building Arrangements:** Extend the analysis to include low-rise buildings situated in densely populated areas with complex arrangements, focusing on the influence of surrounding structures on wind flow and pressure distribution.

III. **Validation of Mitigation Techniques in Full-Scale Models:** Conduct full-scale testing of aerodynamic mitigation strategies, including parapets and roof modifications, to validate numerical and wind tunnel findings under real-world conditions.

IV. **Dynamic Effects on Roof Components:** Analyze the dynamic effects of wind-induced vibrations on roof components, including cladding and parapets, to better understand fatigue and failure mechanisms.

V. **Development of Hybrid Frameworks:** Develop hybrid frameworks where CFD and experimental results complement each other, leveraging experimental sensor data to refine boundary conditions and turbulence parameters.

VI. **Incorporation of Machine Learning:** Incorporate machine learning to predict optimal sensor configurations for different building geometries and terrain conditions.